Heterogeneous Catalyst Stability in Hydrothermal Media

by

Jennifer N. Jocz

A dissertation submitted in partial fulfillment
of the requirements for the degree of
Doctor of Philosophy
(Chemical Engineering)
in The University of Michigan
2018

Doctoral Committee:

      Professor Emeritus Phillip E. Savage, Co-Chair
      Professor Levi T. Thompson, Co-Chair
      Professor Emeritus Mark Barteau
      Professor Adam Matzger
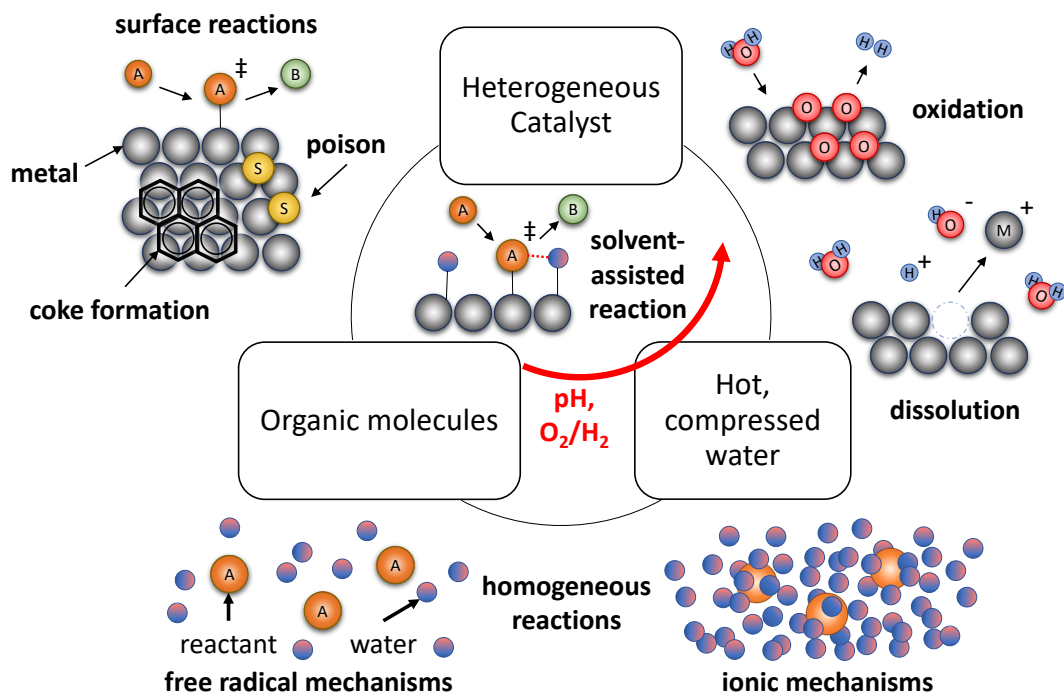
Complexity of molecular interactions during hydrothermal catalysis.

Jennifer N. Jocz

jennjocz@umich.edu

ORCID iD: 0000-0002-0827-9232

For my family (human, equine, canine, and feline).

Their unconditional love and support made this dissertation possible.

ACKNOWLEDGEMENTS

I would like to thank my advisors, Phillip Savage and Levi Thompson, for their support and guidance throughout my time as a graduate student at the University of Michigan. The combination of their expertise supplied me with high quality feedback on my work. From their guidance, I learned a great deal about research, technical writing, and how to spot and ask critical questions. I would also like to thank Mark Barteau and Adam Matzger, the members of my dissertation committee, for their support and input on my dissertation.

I am eternally grateful to my parents for their unwavering support and constant prayers. Through the highs and lows, they were there with love, understanding, and high quality wine and cheese. They taught me that a fruit-forward pinot noir or merlot paired well with a failed experiment and the big, peppery tannins of a nappa valley cabernet paired well with everything and anything else. And no matter the wine, it always tasted better when drank together.

I thank my brother and sisters for their love and support. Mike's visits to my humble office were always welcome and Kathryn's hand drawn cards of encouragement always held positions of honor on my apartment fridge. When Natalie married Mike, she also got me and all my grad school baggage and I am very grateful for her love, patience, and encouragement. I thank my grandmother, Elsie Jocz, for her love, prayers, and for financing my housing in college and grad school. Times 'Awastin (Taxi) literally and figuratively carried me over the hurdles of my first four years of grad school. Although he could no longer continue show jumping, our weekend trail

rides at Forte Farms were the perfect remedy for a stressful week. Rocky made sure I ate breakfast every morning, got fresh air and exercise twice a day, and kept my Frisbee skills sharp. Gracie would remind me of the importance of sleep, as she often did that for most of the day.

I owe a special thanks to Emily Deschenes and Rachael Harrington for their friendship over the past 9 years. Together, we survived and supported each other through our bachelors and masters degrees in chemical engineering at Michigan and during illness and grad school milestones (sometimes concurrent) they brought me food, medicine, encouragement, and distraction. I also owe a special thanks to Joe Quinn, who kept me fed and caffeinated during the last semester of my PhD and for being my Samewise Gamgee, constantly reminding me that "it's only a passing thing this shadow. Even darkness must pass. A new day will come, and when the sun shines, it'll shine out the clearer. Folks with their PhDs had lots of chances of turning back, only they didn't. They kept going, because they were holding on to something. That there is some good in this world, and it's worth fighting for."

I thank the past and present members of the Savage and Thompson Research Groups who helped shape my graduate school experience at the University of Michigan (and for being my friends), including Jacob Dickinson, Thomas Yeh, Allison Franck, Julia Martin (Faeth), Na (Tiffany) Mo, Yuan Chen, Brian Wyvratt, Shawn Eady, David Hietala, Sarah Paleg, and Zixuan Wang. From them, I learned about experimental design, catalyst characterization, and seeing the forest through the trees of data. I especially thank Thomas Yeh for sharing his experimental trouble-shooting expertise, Julia Martin for making the office fun, and David Hietala for introducing me to the powers of Matlab and Mathematica coding. I also thank Joseph Mims for helping run many of the batch experiments.

I thank Susan Montgomery for her support and guidance during my 9 years of undergrad and grad school at Michigan. Thanks to Kelly Raickovich, Susan Hamlin,

TABLE OF CONTENTS

LIST OF FIGURES

LIST OF TABLES

LIST OF APPENDICES

Appendix

LIST OF ABBREVIATIONS

SCW supercritical water

GC-MS gas chromatography with mass spectrophotometer

GC-TCD gas chromatography with thermal conductivity detector

XRD X-ray diffraction

ICP-OES inductively coupled plasma with optical emission spectroscopy

SEM scanning electron microscopy

WPF whole pattern fitting

HKF Helgeson-Kirkham-Flowers equation of state

R-HKF revised Helgeson-Kirkham-Flowers equation of state

SAA Sue-Adschiri-Arai equilibrium model

SCWO supercritical water oxidation

SCWG supercritical water gasification

DI deionized

BET Brunauer-Emmett-Teller method

HDN hydrodenitrogenation

HDO hydrodeoxygenation

STP standard temperature and pressure

AICc Akaike Information Criterion with correction for finite sample size

TGA thermogravimetric analysis

HTL hydrothermal liquefaction

ABSTRACT

Catalytic reactions in hydrothermal media are important for the conversion of biomass-derived species to useful chemicals and the destruction of environmental pollutants, however these aqueous solutions are aggressive and can degrade heterogeneous catalysts. This dissertation describes the study of heterogeneous catalyst stability during hydrothermal reactions and the application of thermodynamic modeling to predict dissolution of catalysts and changes in their oxidation states. Agreement between experimental results for catalytic materials (Co, Ni, Pd, Ru, CeO_2, TiO_2, ZrO_2, Mo_2C, W_2C, MoN, WN) in supercritical water at 400 °C and 24-40 MPa and the revised Helgeson-Kirkham-Flowers thermodynamic model showed that the model is a good predictor of the oxidation and dissolution behavior of metal, oxide, carbide and nitride catalytic materials in supercritical water reactor systems.

The model was applied to additional hydrothermal temperatures and pressures (150-550 °C, 22-50 MPa) and catalytic materials and the results were used to identify relationships between material properties and catalyst solubility. The solubility of metals at 400 °C and 50 MPa correlated strongly with electronegativity and the solubility of oxides at 400 °C and 50 MPa was correlated with cation electronegativity, ionic-covalent parameter, and polarizing power. These relationships suggest that changes to the composition of the catalyst which alter these properties (e.g., alloying, doping) may improve stability.

Catalyst stability is also affected by the pH and oxygen fugacity of hydrothermal

solutions, which are controlled by the reactants and products present in solution. The pH and oxygen fugacity can also change during a reaction as various solutes are generated or consumed and their concentrations change. Oxygen fugacity-pH diagrams were constructed using the revised Helgeson-Kirkham-Flowers thermodynamic model and were used to predict catalyst stability as a function of temperature, pressure, pH, and oxygen fugacity. Equilibrium calculations were also performed on different concentrations of solutes that are common in hydrothermal reactions (e.g., CO_2, CH_4, NH_3, formic acid) to predict the pH and oxygen fugacity of the overall solution. Using these tools, one can learn how best to engineer the composition of the catalyst and the hydrothermal medium to ensure catalyst stability. As an illustration, Pt/TiO_2 was predicted to be hydrothermally stable at the temperatures, pressures, and solution compositions typical of hydrodenitrogenation reactions in supercritical water. Flow experiments in aqueous solutions of formic acid and ammonia at 50 MPa and 380 and 500 °C resulted in little ($\leq$ 2 wt%) or no dissolution of Pt and TiO_2 and verified the predicted stability. While Pt/TiO_2 did not undergo dissolution or changes in oxidation state, flow experiments in aqueous solutions of formic acid and either propylamine or pyridine at 420 °C and 30 MPa showed that Pt/TiO_2 was only active for denitrogenation of propylamine.

CHAPTER I

Introduction

1.1 Reactions in Hot, Compressed Water

The hydrothermal environment offers a potentially "greener" reaction medium than many alternative solvents because water is non-toxic, inexpensive, and environmentally benign. Moreover, the properties of hot, compressed water can strongly influence reaction rates and selectivities [2]. The dielectric constant of subcritical (200 °C $< T <$ 374 °C) water is lower than that of water at ambient conditions and there are fewer and less-persistent hydrogen bonds, resulting in an increased solubility of organic compounds. In addition, the ion product (K_W) at these conditions is several orders of magnitude higher than that for ambient water. Above the critical point of water (374 °C, 22.1 MPa), the density, ion product and dielectric constant are tunable with temperature and pressure. Many permanent gases and most organic compounds are soluble in supercritical water (SCW) because of the decreased dielectric constant and the absence of interphase transport limitations allows for a single homogeneous fluid phase at reaction conditions. As a result of these changes in solvent properties, hot compressed water can support ionic, polar non-ionic, and free-radical reactions. These solvent properties as a function of temperature and pressure are shown in Figure 1.1. In SCW, increases in temperature and decreases in pressure (or density) decrease the ion product and dielectric constant.
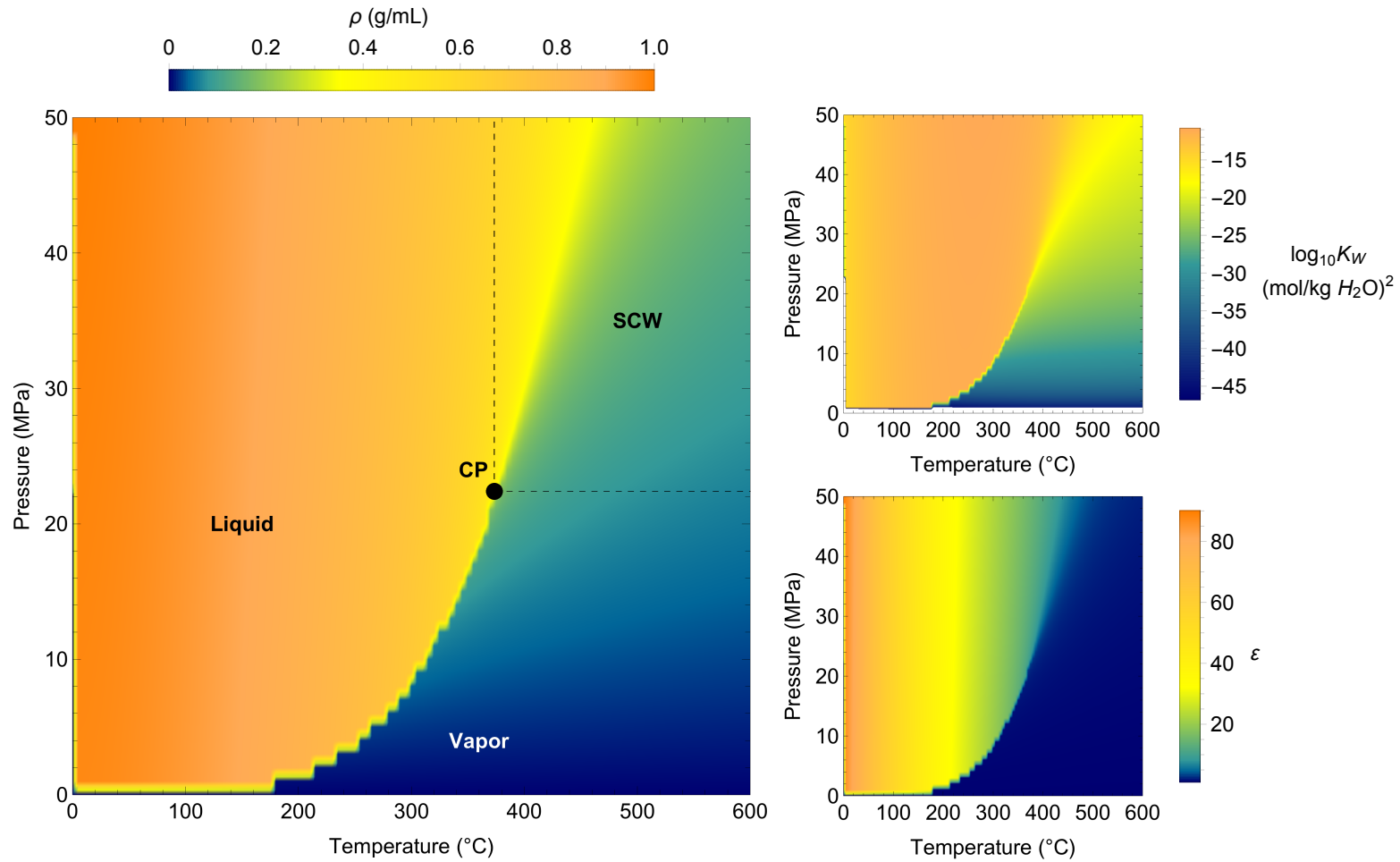
Figure 1.1: H_2O density (ρ), ion product (K_W), and dielectric constant (ϵ) as a function of temperature and pressure. The critical point (CP) at 374 °C, 22.1 MPa denotes the lower limits of temperature and pressure for the supercritical phase. Temperature-pressure-density data was obtained from Steam Tables, K_W was calculated using the Marshall and Franck correlation [3] and ϵ was calculated using Johnson and Norton equations [4].

1.2 Catalysis in Hydrothermal Media

While rates for homogeneous hydrothermal reactions can be high, techno-economic analysis suggest that improvements via the use of catalysts will be required for greater industrial adoption [5–7]. Indeed, catalysis in sub- and supercritical water SCW can be used to improve rates and selectivities for chemical synthesis, gasification of wet biomass, biofuel production, desulfurization of heavy crude oil, and oxidation of pollutants [5, 8–13].

Many heterogeneous catalysts, however, are not stable in hot water. Although the properties of sub- and supercritical water benefit organic chemical reactions, these properties are also responsible for the corrosion of inorganic materials like heterogeneous catalysts and reactor walls and tubing [14–17]. Catalysts subjected to hydrothermal reaction conditions can undergo changes in oxidation state, migration and leaching of active metals, structural changes such as sintering and loss of surface area, and dissolution, in addition to deactivation mechanisms commonly observed in gas-phase reactions such as poisoning, coking, and thermally induced solid state transformations [5, 18, 19]. Temperature, pressure, and composition of the hydrothermal solution all play a role in influencing the oxidation state of the catalyst. Changes in the oxidation state can result in loss of catalytic activity and increased dissolution of heavy metals into the effluent [18].

The fragmentary understanding of hydrothermal catalyst stability limits the widespread application of heterogeneous catalysis for hydrothermal reactions. A 2011 review of heterogeneous catalysts for hydrothermal biomass gasification concluded that while catalytic activity during supercritical water gasification (SCWG) has been well studied, very few studies focused on understanding or enhancing the stability of the heterogeneous catalysts [10]. Similarly, Yeh et al concluded in their review of hydrothermal catalytic processing of aquatic biomass that there have been only a handful of studies on hydrothermal catalyst stability and activity maintenance [5].

Research on the sintering and dissolution of supported active metals is restricted to Ru and Ni gasification catalysts. The authors identify support stability, active metal stabilization, and resistance to sulfur poisoning as key areas for future research to improve hydrothermal catalysts for algal biomass processing. A more recent 2014 review focused on the physical stability of various heterogeneous catalysts under hydrothermal conditions for biomass conversion reactions [19]. The review addresses changes in the physical structure (surface area and framework) of the catalysts observed after treatment in superheated steam, liquid water below 200 °C, liquid water above 200 °C, and supercritical water. The review also describes recent approaches for improving hydrothermal catalyst stability. However, the reviewed research does not explain why some catalysts, especially active metals, experience better hydrothermal stability than others. While hydrothermal heterogeneous catalysis is a promising route for achieving a number of chemical transformations, a key challenge is the limited understanding of catalyst stability as a function of changes in the solvent properties and also as a function of the catalyst structure and composition.

1.3 Hydrothermal Inorganic Chemistry in Other Research Fields

Although our understanding of hydrothermal catalyst stability is still developing, other research fields including geological sciences, corrosion science, and material synthesis have more thoroughly explored inorganic chemistry in hydrothermal environments. Tanger and Helgeson performed rigorous empirical and theoretical analysis on the thermodynamic and transport properties of aqueous inorganic species at high temperatures and pressures to improve predictions of fluid-rock interactions in the Earth's crust [20]. Their analysis resulted in revision of the Helgeson-Kirkham-Flowers equation of state (HKF) which significantly improved the accuracy of predicting standard

partial molal properties of aqueous ions and electrolytes for temperatures to 450 °C and pressures to 500 MPa.

In the decades following its initial publication in 1988, the revised Helgeson-Kirkham-Flowers equation of state (R-HKF) received an increase in the temperature validity to ≤ 1000 °C, several important additions to the database of material parameters including platinum-group and rare-earth element species [21–26] and also a modification by Sue et al. to extend the valid SCW density range of the model from ≥ 0.35 g/mL to densities ≥ 0.2 g/mL [27]. Sue, Adschiri, and Arai also published a simplified model, the Sue-Adschiri-Arai equilibrium model (SAA), with fewer material-dependent parameters (derived from the R-HKF model) for calculating reaction equilibrium constants of aqueous inorganic species [27]. However a recent comparison of the R-HKF and SAA models against experimental solubility data for several inorganic salts of varying magnitudes of solubility revealed that the R-HKF model was consistently more accurate [28].

The R-HKF and SAA thermodynamic solubility models have supplemented material stability experiments aimed at understanding corrosion of reactor walls and tubing for supercritical water oxidation (SCWO) reactors and nuclear reactors that use SCW as working fluid [14–16, 29, 30]. We refer the reader to several excellent reviews for more details on current advances in hydrothermal corrosion science. Stainless steels and Ni-based alloys are often the focus of these studies and titanium, tantalum, and noble metals are sometimes used as reactor and tubing liners or additives doped into the structural alloys. These materials contain significant amounts of Fe, Cr, and Ni and as a result much is already known about these elements and their oxides during exposure to hydrothermal conditions.

The solubility of other metal oxide materials including CuO, CeO_2, TiO_2, and ZrO_2 (to name only a few) and their salt precursors have been studied experimentally and using thermodynamic models for the goal of engineering nano-materials

using "green" synthesis processes [31–33]. By understanding the dramatic decrease in solubility for metal ions around the critical point and the reactivity of different salt precursors, the precipitation of nanomaterials with specific morphologies and surface functionalities can be carefully controlled. This process has also been explored in combination with SCWO, which overall produces metal or metal oxide nanoparticles from the hydrothermal treatment of two wastewaters: one containing metal ions and the other containing organic compounds.

1.4 Research Motivation and Summary

To date, the hydrothermal stability of several metals and metal oxides has been studied in geological science and for corrosion reduction and nanoparticle synthesis, however it is unclear if the results from these studies translate to hydrothermal catalysis applications. For many hydrothermal catalyst material candidates, the temperature and pressure conditions previously studied do not correspond to the range of conditions typical for hydrothermal reaction processes. Furthermore, it is also unclear how catalyst composition and reaction solution composition influence oxidation and dissolution in sub- and supercritical water and which material properties, if any, are responsible for controlling hydrothermal stability.

The following chapters address several of these gaps in the literature concerning catalyst stability and the role of catalyst and solution composition. In Chapter II, a combination of batch experiments and thermodynamic modeling was employed to examine the hydrothermal stability of four different classes of catalytic materials (transition metals, oxides, and transition metal carbides and nitrides). Comparison between experimental and model results were used to test the usefulness of the model for describing catalyst stability in practical SCW reaction systems. The thermodynamic model was successful in describing the experimentally observed changes in the catalysts and captured the underlying thermodynamic driving forces behind cat-

alytic oxidation and dissolution. By using thermodynamic models to estimate each catalyst's thermodynamic equilibrium for oxidation and dissolution, the "worst case scenario" for the catalyst could be determined (i.e., if the kinetics for oxidation and dissolution are fast, the catalyst would quickly reach its new equilibrium state, but total oxidation and dissolution would not exceed the equilibrium limit). Chapters III and IV further explore thermodynamic modeling for determining catalyst stability in water at all potential (and practical) hydrothermal reaction conditions (150-550 °C and 22-50 MPa). Chapter III correlates material properties with hydrothermal stability and Chapter IV examines methods for determining the influence of pH and oxygen fugacity, which vary with the concentrations of different reaction solutes, on the catalyst stability. Chapter V tests the stability estimations methods by designing and testing a stable catalyst (Pt/TiO_2) for hydrodenitrogenation (HDN) reactions in SCW. Finally, Chapter VI contains the conclusions of all work in this dissertation and recommendations for future work.

CHAPTER II

Effect of Supercritical Water Density on Catalyst Oxidation and Dissolution

This chapter discusses the use of thermodynamic models to predict catalyst oxidation and dissolution in SCW and the experimental results used to assess the viability of the models for practical SCW reaction systems. The transition metals (Co, Ni, Pd, Ru), oxides (CeO_2, TiO_2, ZrO_2), carbides (Mo_2C, W_2C), and nitrides (Mo_2N, WN) examined in this study represent a broad range of catalytic and chemical properties which yield different stabilities in SCW. At the time the contents of this chapter were published [34], this was the first study to examine nitride catalysts in SCW. The thermodynamic calculations predicted oxidation and dissolution of Co, Ni, carbides and nitrides in SCW at 400 °C, and evidence for oxidation and dissolution of these materials was observed experimentally. The overall qualitative agreement between predicted and experimental oxidation and dissolution show that thermodynamic modeling is an effective tool for efficiently screening the stability of catalytic materials in SCW and for estimating long-term hydrothermal catalyst stability.

2.1 Introduction

The hydrothermal stability and thermodynamics of several metals and metal oxides have been studied in geological science [20–26] and for corrosion reduction [14–16, 29, 30] and nanoparticle synthesis [31–33], however these studies often test electrolyte solutions, temperatures, pressures, and timescales that differ from those required (and practical) for SCW catalysis applications. In addition, the hydrothermal cells in these studies [35] are lined in Au or another inert material and can have fluid flow patterns that differ from those in the steel, inconnel, or hastelloy reactors used for catalyzed reactions in SCW so it is unclear if the results from these studies will translate to the conditions employed for SCW catalysis. In this chapter, a combination of batch experiments and thermodynamic modeling are compared to study and predict catalyst oxidation and dissolution as a function of SCW density. The models elucidate the underlying thermodynamic driving forces behind oxidation and dissolution in the SCW environment and predict material stability at long timescales. The batch experiments test the efficacy of these models for predicting catalyst stability in real reaction systems by screening four different classes of catalytic materials in the reactor environments and at the timescales commonly used during hydrothermal catalytic biomass conversion and upgrading studies [5, 10–12].

The transition metals, oxides, carbides, and nitrides chosen for this study represent a broad range of catalytic and chemical properties and allow for the elucidation of important property-stability relationships. The transition metals (Pd, Ru, Ni, Co) and oxides (CeO_2, TiO_2, ZrO_2) represent a subset of the catalysts that have been used in SCW reactions [5, 10–13]. Interest in carbides (Mo_2C, W_2C) and nitrides (Mo_2N, WN) has been growing as a consequence of their catalytic performance for fast pyrolysis bio-oil upgrading [36, 37]. Their application will likely expand to hydrothermal bio-oil upgrading systems. Several studies have already examined the catalytic activity of Mo_2C in SCW [38–41] and W_2C in sub-critical water [42], however, to the

best of our knowledge, nitride catalysts have not yet been studied in SCW. For simplicity, the SCW stability of the individual, bulk materials (particle size $\gg 1~\mu$m) was evaluated because the metal/support combinations are numerous and several of these materials can serve as catalyst supports as well as dispersed active materials. Information regarding the bulk material stabilities in SCW provides an important basis for comparison among the materials without nano size or support-metal effects.

The results presented in this chapter show that these calculations successfully capture the catalyst stability trends observed experimentally and therefore we propose using thermodynamic modeling to complement future hydrothermal catalyst stability studies. The thermodynamic models used herein could also be used to screen catalyst material candidates prior to running experiments. The work in this chapter represents a step toward improved heterogeneous catalyst stability for hydrothermal reactions.

2.2 Experiment Design and Methods

This section describes the experimental and computational methods for examining oxidation and dissolution of catalytic materials in SCW.

2.2.1 Batch Experiments

Particles of Ru, CeO_2, TiO_2, and ZrO_2 (Alfa Aesar), Ni (Acros), Co (QSI-Nano), and Pd (Sigma-Aldrich) were all obtained in high purity ($> 99.5\%$) and used as received. Mo_2C, W_2C, Mo_2N and WN were synthesized using well-developed temperature-programmed-reaction procedures [43–47]. Briefly, the oxide precursors (sieved to 125-250 μm) were loaded into a tubular quartz reactor and secured in a vertical furnace. After the temperature program was completed, the reactor was rapidly cooled to room temperature. Because of their pyrophoricity, the carbide and nitride samples were then passivated with 1% O_2/He mixture (Cryogenic Gases) flowing at 20 mL/min for 7 hours to prevent bulk oxidation upon exposure to air.

Figure 2.1: Photograph of a batch reactor with the gas valve attachment.

Experiments were conducted in batch reactors at 400 °C and 60 minutes with different catalyst materials and SCW densities. The batch reactors were assembled from 316 stainless steel Swagelok tube fittings (3/8 in. port connector, cap, and 3/8 in. to 1/8 in. reducing union). The reducing union was connected with 8 in. of Swagelok tubing (1/8 in. o.d.) to a two-way angle high pressure gas valve rated to 15,000 psi (High Pressure Equipment Company) which allowed for the exchange of gases in the reactor headspace. The assembled reactor (see Figure 2.1) had a total internal reactor volume of 2.32 mL. After assembly, the reactors were loaded with 0.4 g deionized (DI) water (prepared in house) and heated to 400 °C for 60 minutes. This step exposed the reactor walls to the hydrothermal environment and allowed the SCW to remove any residual material on the reactor walls prior to use.

For each stability experiment, 50 mg of catalyst (10 mg for Ru) and either 0, 0.3 or 1.2 g of deionized water (argon-sparged) were loaded into the reactor. The materials were used without any pretreatment. After loading catalyst and water, the gas valve attachments were coupled to the reactors and the connection was tightened with a torque wrench to seal the reactors. The valves were connected to a gas manifold containing a vacuum pump and a He cylinder (ultra high purity grade, Cryogenic Gases) and then the reactor valves were opened. A schematic of the gas manifold was published previously [48]. The air in the reactor was removed with the vacuum pump and the headspace was repeatedly flushed with He to ensure air removal. Control experiments revealed that pulling vacuum on the reactors and exchanging the gas in the headspace led to no loss of solid catalysts and less than 3 wt% evaporative

11

Density (g/mL)	Pressure (MPa)	Ion Product (logK$_W$) [a]	Dielectric Constant (ϵ)
0[b]	2	n.a.[c]	1.0
0.15	24	-20.13	2.5
0.52	40	-12.48	9.6

[a] mol^2/kg^2 [b] Gas phase control experiment.   [c] not applicable (n.a.)

Table 2.1: Values for pressure, ion product (K$_W$), and dielectric constant (ϵ) at 400 °C and the water densities used in the batch experiments. For experiments with water, pressure was from the steam tables, K$_W$ was calculated using the Marshall and Franck correlation [3] and ϵ was calculated using Johnson and Norton equations [4].

losses of the water. The reactors were then pressurized to 8 bar with He, which served as an internal standard for quantifying gas phase reaction products. After pressurization, the reactor valves were closed to seal the contents and then detached from the gas manifold. The loaded reactors were immersed in a pre-heated, fluidized sand bath (Techne IFB-51 with a Eurotherm 3216 PID controller) at 400 °C for 60 minutes. Upon heating to 400 °C, the different water loadings result in different SCW conditions, listed in Table 2.1. At 60 minutes, the diffusion lengths for the self-diffusion of SCW[49] at 400 °C and 0.15 and 0.5 g/mL are 5.5 cm and 3.2 cm, respectively, which is sufficient for water molecules to repeatedly traverse the reactor diameter (0.7 cm) during the experiment. In reality, diffusion transport is assisted by convection currents generated as the reactor is heated from the outer walls to the interior. After 60 minutes, the reactors were quenched in cold water and allowed to equilibrate at room temperature for another 60 minutes.

An Agilent 6890N gas chromatograph with a Carboxen 1000 packed column and a thermal conductivity detector (GC-TCD) separated and analyzed gaseous products using a procedure outlined previously [50]. Gas calibration standards purchased from Grace Davison that contained H_2, He, CO, CO_2, CH_4, C_2H_2, C_2H_4, and C_2H_6 were used to identify the resulting peaks and determine molar fractions. The molar quantities of the gases in the mixture were determined using the GC analysis along with

the amount of He loaded into the reactor, which was calculated using the ideal gas law.

The reactors were then opened and the contents collected by flushing the reactors with 8 mL of DI water. The catalyst-water solution was centrifuged to separate out the catalyst and the aqueous phase was collected for analysis. The aqueous phase was diluted with DI water to achieve a total of 10 mL and then analyzed for metal content by inductively coupled plasma optical emission spectroscopy inductively coupled plasma with optical emission spectroscopy (ICP-OES) using a Varian 710-ES. The solids were dried in a vacuum oven at 70 °C overnight with the exception of the carbide and nitride samples. These materials were dried at room temperature overnight by flowing 1% O_2/He (Cryogenic Gases) over the vials. This procedure served to re-passivate any active material and prevent bulk oxidation upon exposure to air.

The fresh materials and the dried materials recovered from the reactors were characterized with X-ray diffraction (XRD) and scanning electron microscopy (SEM). The XRD data were collected using a Rigaku 600 Miniflex set at 40 kV and 15 mA ($K_\alpha = 1.5406$ Å) and the diffraction patterns were analyzed using Jade. Compositions of the crystalline fractions were calculated using the whole pattern fitting (WPF) function in Jade. The precise amount of amorphous material was unknown and therefore the sample compositions provide relative comparisons instead of absolute mass fractions. The SEM images were collected using a Philips XL30FEG. Powder samples were adhered to the SEM posts using carbon tape and nonconducting samples were sputter coated with gold for 60 seconds. In addition, surface areas of CeO_2, TiO_2, and ZrO_2 before and after stability experiments were measured using N_2-physisorption (Micromeritic ASAP 2010) and the Brunauer-Emmett-Teller method (BET). All experiments were performed at least in triplicate to determine experimental variability, which is reported herein as standard error.

2.2.2 Catalyst Oxidation Calculations

The thermodynamic oxidation state of each catalyst in SCW at 400 °C and 0.15 and 0.52 g/mL SCW density (ρ_{H_2O}) was determined by calculating the change in free energy of the redox reactions (ΔG_{rxn}). The solid redox reactions follow the forms in Equations (2.1) and (2.2) where Equation (2.1) is oxidation of a metal $M_{(s)}$ by H_2O and Equation (2.2) is reduction of an oxide $MO_{2(s)}$.

$$M_{(s)} + xH_2O \leftrightarrow MO_{x(s)} + xH_{2(aq)} \tag{2.1}$$

$$2MO_{2(s)} + H_2O \leftrightarrow M_2O_{3(s)} + H_{2(aq)} + O_{2(aq)} \tag{2.2}$$
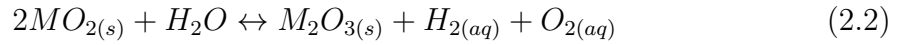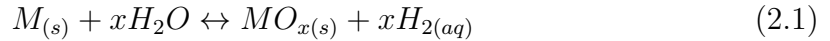
The values for $\Delta G_{rxn}(T, \rho_{H_2O})$ were calculated using Equation (2.3) where ν_j is the stoichiometric coefficient of species j in the reaction (positive for products and negative for reactants) and $\Delta G_f(T, \rho_{H_2O})_j$ is the apparent standard partial molar Gibbs free energy of formation of species j at $T = 400$ °C and $\rho_{H_2O} = 0.15$ or 0.52 g/mL.

$$\Delta G_{rxn}(T, \rho_{H_2O}) = \sum_j \nu_j \Delta G_f(T, \rho_{H_2O})_j \tag{2.3}$$

$\Delta G_f(T, P)_{H_2O}$ was obtained from values tabulated in the Steam Tables. For the solids, $\Delta G_f(T, \rho_{H_2O})_j$ was calculated using the differential expression for apparent standard partial molar Gibbs free energy in Equation (2.4) where S is molar entropy and V is molar volume.

$$dG = -SdT + VdP \tag{2.4}$$

Integration of both sides from standard temperature and pressure (STP) to 400 °C and $P = 240$ or 400 bar (pressures corresponding to $\rho_{H_2O} = 0.15$ and 0.52 g/mL at 400 °C, respectively) yields the expression in Equation (2.5) where ΔG_f^o is the standard partial molar Gibbs free energy of formation of a species from the elements in their stable form at the standard reference temperature and pressure STP of 298.15

K and 1 bar. To evaluate the pressure integral in Equation (2.5), we assumed the solid catalysts were incompressible.

$$\Delta G_f(T, P) - \Delta G_f^o = - \int\limits_{298.15K}^{673.15K} S(T)dT + \int\limits_{1bar}^{P} VdP \tag{2.5}$$

Eq. 2.6 gives $S(T)$ where S^o is molar entropy at STP and C_P is molar heat capacity. $C_P(T)$ is a polynomial function where the coefficients were obtained from NIST [51] or fitted from tabulated $C_P(T)$ data [52] (unless otherwise cited) and are listed in Table B.1 in Appendix B.

$$S(T) = S^o + \int\limits_{298.15K}^{T} \frac{C_P(T)}{T}dT \tag{2.6}$$

$\Delta G_f(T, \rho_{H_2O})$ for H_2 and O_2 in Equations (2.1) and (2.2) were calculated using the R-HKF equation of state in Equation (2.7) since these species are miscible in H_2O at the SCW conditions examined in this work [20].

$$
\begin{aligned}
\Delta G_f(T, \rho_{H_2O}) = {} & \Delta G_f^o - S^o(T - T_r) - c_1\left(T\ln\left(\frac{T}{T_r}\right) - T + T_r\right) \\
& + a_1(P - P_r) + a_2\ln\left(\frac{\Psi + P}{\Psi + P_r}\right) \\
& - c_2\left[\left(\left(\frac{1}{T - \Theta}\right) - \left(\frac{1}{T_r - \Theta}\right)\right)\left(\frac{\Theta - T}{\Theta}\right) - \frac{T}{\Theta^2}\ln\left(\frac{T_r(T - \Theta)}{T(T_r - \Theta)}\right)\right] \\
& + \left(\frac{1}{T - \Theta}\right)\left(a_3(P - P_r) + a_4\ln\left(\frac{\Psi + P}{\Psi + P_r}\right)\right) \\
& + \omega\left(\frac{1}{\epsilon} - 1\right) - \omega_{P_r,T_r}\left(\frac{1}{\epsilon_{P_r,T_r}} - 1\right) + \omega_{P_r,T_r}Y_{P_r,T_r}(T - T_r)
\end{aligned}
\tag{2.7}
$$

In Equation (2.7), a_1, a_2, a_3, a_4, c_1, and c_2 represent species-dependent nonsolvation parameters, T_r and P_r represent the reference temperature (298.15 K) and reference pressure (1 bar), respectively, ϵ is the dielectric constant of H_2O which can

be calculated using equations published by Johnson and Norton [4], Ψ and Θ are solvent parameters equal to 2600 bars and 228 K, respectively, ω is the conventional Born coefficient given by Equation (2.8) and Y is a Born function given by Equation (2.9). In Equation (2.8), $\eta = 6.94657 \times 10^5$ J/mol, Z is the charge, r_e is the effective electrostatic radius, and g is a temperature- and pressure-dependent solvent function given by Shock et al. [23]. The Born coefficient is constant (ω_{T_r,P_r}) with T and P for nonionic species.

$$\omega_{T,P} = \eta\Big(\frac{Z^2}{r_e + |Z|g} - \frac{Z}{3.082 + g}\Big) \tag{2.8}$$

$$Y = \frac{1}{\epsilon}\Big(\frac{\partial \ln \epsilon}{\partial T}\Big)_P \tag{2.9}$$

Values for a_1, a_2, a_3, a_4, c_1, c_2, and ω were obtained or correlated from the work by Shock et al [21, 25, 26] and are listed in Tables B.2 and B.4 in Appendix B.

2.2.3 Catalyst Dissolution Calculations

The equilibrium metal concentrations in SCW for each catalyst were calculated from the equilibrium constants (K_{eq}) of the dissolution reactions. The dissolution reactions involve the solid reacting with H_2O, H^+, and/or OH^- to form aqueous inorganic species. The specific dissolution reactions considered in the calculations are listed in Tables C.1 to C.5 and C.7 to C.10 in Appendix C. The equilibrium constants (K_{eq}) were calculated using Equation (2.10) where R is the universal gas constant.

$$K_{eq}(T, \rho_{H_2O})_i = exp\left(\frac{-\Delta G_{rxn}(T, \rho_{H_2O})_i}{RT}\right) \tag{2.10}$$

As with the redox reactions, $\Delta G_{rxn}(T, \rho_{H_2O})_i$ values for the dissolution reactions were calculated from Equation (2.3) and $\Delta G_f(T, P)_{H_2O}$ values were obtained from the Steam Tables. $\Delta G_f(T, \rho_{H_2O})_j$ values for the solid species were calculated from

Equations (2.5) and (2.6) and $\Delta G_f(T, \rho_{H_2O})_j$ values for the aqueous inorganic species were calculated using the R-HKF equation of state in Equation (2.7). By convention, $\Delta G_f(T, \rho_{H_2O})_{H^+_{(aq)}}$ was set as the reference for all aqueous species and equal to zero at all conditions. $\Delta G_f(T, \rho_{H_2O})_{OH^-_{(aq)}}$ values were calculated using Equation (2.11) where K_W is the ion product of H_2O. Values for K_W at 400 °C and $\rho_{H_2O} = 0.15$ and 0.52 g/mL were calculated using the Marshall and Franck correlation [3].

$$\Delta G_{f,OH^-} = -RT \times ln(K_W) + \Delta G_{f,H_2O} - \Delta G_{f,H^+} \tag{2.11}$$

Combined, K_W and $K_{eq}(T, \rho_{H_2O})_i$ for the dissolution reactions were used to calculate the molal concentration m_j (mol/kg H_2O) of all of the species in solution for a given catalyst at 400 °C and $\rho_{H_2O} = 0.15$ and 0.52 g/mL. The expression in Equation (2.12) relates the equilibrium constants to the thermodynamic activity of each species (a_j) and the species concentrations (m_j).

$$K_{eq}(T, \rho_{H_2O})_i = \prod_j a_j^{\nu_j} = \prod_j \left(\gamma_j \frac{m_j}{m_\Theta} \right)^{\nu_j} \tag{2.12}$$

The activity coefficients (γ_j) of neutral aqueous species and the activities (a_j) of solid phases and H_2O are taken to be unity. The γ_j of charged aqueous species are calculated using the Davies extension of the Debye-Hückel equation [53] in Equation (2.13) where Z_j is the charge on the jth species, A_Φ is the Debye-Hückel parameter calculated from Equation (2.14) and I is the ionic strength of the solution calculated from Equation (2.15). Extensions of the Debye-Hückel equation work well when the aqueous solution ionic strength is low (less than 0.2 mol/kg H_2O). Since the ionic strength of the modeled hydrothermal systems never exceeded 0.2 mol/kg H_2O, Equation (2.13) was assumed to be a good approximation. The treatment of activities and activity coefficients herein is consistent with previous work on modeling

hydrothermal solutions [20, 25, 28, 53].

$$\ln \gamma_j = -\frac{Z_j^2 A_\Phi I^{1/2}}{1 + I^{1/2}} + 0.2 A_\Phi I \tag{2.13}$$

$$A_\Phi = \frac{1.8246 \times 10^6 (\rho_{H_2O}/1.00)^{1/2}}{(\epsilon T)^{3/2}} \tag{2.14}$$

$$I = \frac{1}{2} \sum_j^N m_j Z_j^2 \tag{2.15}$$

For a solution of N total aqueous species (H^+, OH^-, and N-2 metal-containing species dissolved from the catalyst) with a concentration-dependent ionic strength, there are N+1 unknown variables (N concentrations m_j plus ionic strength I) and so there must be N+1 equations to solve for these unknowns. We combined the equilibrium expressions (Equation (2.12)) for the independent dissolution reactions (one for each for each aqueous metal-containing species) with the equilibrium equation for the water dissociation reaction, the definition of ionic strength in Equation (2.15), and the electro-neutrality condition in Equation (2.16) and then solved simultaneously using Matlab's nonlinear least-squares solver function (lsqnonlin).

$$0 = \sum_j^N m_j Z_j \tag{2.16}$$

For systems of reactions that also contain dissolved H_2 and O_2, two additional equations were incorporated into the solution: the equilibrium equation for H_2O splitting into dissolved H_2 and O_2 and atomic mass balances for hydrogen (H) and oxygen (O) in Equations (2.17) and (2.18). $(\Delta h)_j$ is the net H gain on aqueous metal species j and $(\Delta o)_j$ is the net O gain on aqueous metal species j (relative to the initial molar composition of the solid).

$$2[H_2O]_{initial} = 2[H_2O]_{final} + 2m_{H_{2(aq)}} + m_{OH^-} + m_{H^+} + \sum_j (\Delta h)_j m_j \tag{2.17}$$

18

$$[H_2O]_{initial} = [H_2O]_{final} + 2m_{O_{2(aq)}} + m_{OH^-} + \sum_j (\Delta o)_j m_j \qquad (2.18)$$

Eq. 2.18 and 2.17 combine to give Equation (2.19):

$$0 = 2m_{H_{2(aq)}} - 4m_{O_{2(aq)}} - m_{OH^-} + m_{H^+} + \sum_j ((\Delta h)_j - 2(\Delta o)_j)m_j \qquad (2.19)$$

2.3   Results and Discussion

The beginning of this section summarizes the oxidation and dissolution results from the experiments and the thermodynamic calculations. Subsequent sections then discuss the results in detail according to material type with metals appearing first, then oxides, followed by carbides and nitrides. Table 2.2 summarizes the pre- and post-experiment catalyst composition and H_2 formation from each catalyst. It shows that the carbide and nitride catalysts underwent the greatest extent (complete) of oxidation in SCW, followed by Co, Ni, and then Pd. The Ru and oxide catalysts did not undergo any bulk changes in oxidation during any of the experiments. All catalysts except for Co had undetectable amounts (< 1 mg/L) of metal ions in the water recovered from the reactors. There was no Fe, Cr, Ni, and Mo detected in the water after 60 minute control experiments with only SCW and He (no catalysts) and there was not visible evidence of reactor corrosion. Therefore, the recovered aqueous solutions were not affected by dissolution of the stainless steel walls. We hypothesize that any aqueous metal species in solution under supercritical conditions precipitated out of solution as an oxide of lower solubility or upon quenching of the batch reactors to room temperature. The XRD data and SEM images for all the catalysts are in Appendix A.

The results of the thermodynamic oxidation and dissolution calculations are summarized in Tables 2.3 and 2.4, respectively. Overall, the calculated ΔG_{rxn} results in

Catalyst	Phase	XRD composition (Mass %)				H$_2$ formed (mmol/mol catalyst)		
		Fresh catalyst	He (no SCW)	$\rho_{H_2O} = 0.15$	$\rho_{H_2O} = 0.52$	He (no SCW)	$\rho_{H_2O} = 0.15$	$\rho_{H_2O} = 0.52$
Pd	Pd	96.3	95.0	89.9	87.2	n.d.	0.24±0.19	0.18±0.14
	PdO	3.7	5.0	10.1	22.8			
Ru	Ru	100	100	100	100	10.3	22±9	17±4
	RuO$_2$	0	0	0	0			
Ni	Ni	100	100	100	93.9	2.9±0.5	15±9	6.5±1.0
	NiO	0	0	0	6.1			
Co	Co	92.1	91.5	57.3	61.0	60±9	13±4	40±3
	CoO	7.9	8.5	42.7	39.0			
CeO$_2$	cubic	100	100	100	100	n.d.	n.d.	n.d.
TiO$_2$	anatase	100	100	100	100	n.d.	n.d.	n.d.
ZrO$_2$	monoclinic	-	54.9	75.8	76.5	n.d.	n.d.	n.d.
	tetragonal	-	45.1	24.2	23.5			
Mo$_2$C	α-Mo$_2$C	100	65.6	1.6	0	170	2,800	12,000
	MoO$_2$	0	34.4	98.5	100			
W$_2$C	ϵ-W$_2$C	100	100	34.7	0	110	8,000	2,800
	WO$_2$	0	0	28.4	0			
	WO$_3$	0	0	36.9	100			
Mo$_2$N	Mo$_2$N	93.3	68.5	0	0	9.4	260	380
	MoO$_2$	6.7	31.5	100	100			
WN	WN	85.2	43.3	3.6	0	1.1	430	560
	WO$_3$	14.8	56.7	96.4	100			

Table 2.2: Catalyst composition and H$_2$ production after batch experiments with catalysts in He, 0.15 g/mL SCW, and 0.52 g/mL SCW at 400 °C for 60 min. The catalyst composition represents the crystalline fraction and was determined by XRD. H$_2$ production was determined by GC-TCD. (n.d. = not detected)

Solid oxidation/reduction reactions	$\Delta G_{rxn}\|_{400°C,\rho_{H_2O}}$ (kJ/mol)	
	$\rho_{H_2O} = 0.15$	$\rho_{H_2O} = 0.52$
$Pd + H_2O \leftrightarrow PdO + H_{2(aq)}$	144.2	175.7
$Pd + \frac{1}{2}O_{2(aq)} \leftrightarrow PdO$	-8.4	-38.8
$Ru + 2H_2O \leftrightarrow RuO_2 + 2H_{2(aq)}$	159.9	222.8
$Ru + O_{2(aq)} \leftrightarrow RuO_2$	-145.4	-206.2
$Ni + H_2O \leftrightarrow NiO + H_{2(aq)}$	-4.0	27.4
$Ni + \frac{1}{2}O_{2(aq)} \leftrightarrow NiO$	-156.6	-187.1
$Co + H_2O \leftrightarrow CoO + H_{2(aq)}$	-13.1	18.3
$Co + \frac{1}{2}O_{2(aq)} \leftrightarrow CoO$	-165.8	-196.2
$3Co + 4H_2O \leftrightarrow Co_3O_4 + 4H_{2(aq)}$	42.9	168.7
$3Co + 2O_{2(aq)} \leftrightarrow Co_3O_4$	-567.7	-689.3
$2CeO_2 + H_2O \leftrightarrow Ce_2O_3 + H_{2(aq)} + O_{2(aq)}$	426.6	519.6
$2CeO_2 + H_{2(aq)} \leftrightarrow Ce_2O_3 + H_2O$	121.2	90.6
$2CeO_2 \leftrightarrow Ce_2O_3 + \frac{1}{2}O_{2(aq)}$	273.9	305.1
$2TiO_2 + H_2O \leftrightarrow Ti_2O_3 + H_{2(aq)} + O_{2(aq)}$	432.4	524.7
$2TiO_2 + H_{2(aq)} \leftrightarrow Ti_2O_3 + H_2O$	127.0	95.7
$2TiO_2 \leftrightarrow Ti_2O_3 + \frac{1}{2}O_{2(aq)}$	279.7	310.2
$ZrO_2 + 2H_2O \leftrightarrow Zr + 2H_{2(aq)} + 2O_{2(aq)}$	1,232.4	1,417.0
$ZrO_2 + 2H_{2(aq)} \leftrightarrow Zr + 2H_2O$	621.8	560.0
$ZrO_2 \leftrightarrow Zr + O_{2(aq)}$	927.1	988.0
$Mo_2C + 5H_2O \leftrightarrow 2MoO_2 + CO_{(aq)} + 5H_{2(aq)}$	N/A	N/A
$Mo_2C + 6H_2O \leftrightarrow 2MoO_2 + CO_{2(aq)} + 6H_{2(aq)}$	-212.1	-20.0
$Mo_2C + 8H_2O \leftrightarrow 2MoO_3 + CO_{2(aq)} + 8H_{2(aq)}$	-83.3	171.9
$Mo_2C + 4H_2O \leftrightarrow 2MoO_2 + CH_4 + 2H_{2(aq)}$	-207.7	-97.6
$Mo_2C + 6H_2O \leftrightarrow 2MoO_3 + CH_4 + 4H_{2(aq)}$	-78.9	94.3
$2Mo_2C + 8H_2O \leftrightarrow 4MoO_2 + C_2H_6 + 5H_{2(aq)}$	-337.0	-119.9
$2Mo_2C + 12H_2O \leftrightarrow 4MoO_3 + C_2H_6 + 9H_{2(aq)}$	-79.4	263.9
$MoC + 4H_2O \leftrightarrow MoO_2 + CO_{2(aq)} + 4H_{2(aq)}$	-120.7	8.5
$MoC + 2H_2O \leftrightarrow MoO_2 + CH_{4(aq)}$	-116.3	-69.1
$W_2C + 5H_2O \leftrightarrow 2WO_2 + CO_{(aq)} + 5H_{2(aq)}$	N/A	N/A
$W_2C + 6H_2O \leftrightarrow 2WO_2 + CO_{2(aq)} + 6H_{2(aq)}$	-249.5	-57.3
$W_2C + 8H_2O \leftrightarrow 2WO_3 + CO_{2(aq)} + 8H_{2(aq)}$	-306.4	-51.1
$W_2C + 4H_2O \leftrightarrow 2WO_2 + CH_4 + 2H_{2(aq)}$	-245.1	-134.9
$W_2C + 6H_2O \leftrightarrow 2WO_3 + CH_4 + 4H_{2(aq)}$	-302.0	-128.7
$2W_2C + 8H_2O \leftrightarrow 4WO_2 + C_2H_6 + 5H_{2(aq)}$	-411.7	-194.6
$2W_2C + 12H_2O \leftrightarrow 4WO_3 + C_2H_6 + 9H_{2(aq)}$	-525.6	-182.2
$WC + 4H_2O \leftrightarrow WO_2 + CO_{2(aq)} + 4H_{2(aq)}$	-115.6	13.8
$WC + 2H_2O \leftrightarrow WO_2 + CH_{4(aq)}$	-111.2	-63.8
$Mo_2N + 4H_2O \leftrightarrow 2MoO_2 + NH_{3(aq)} + \frac{5}{2}H_{2(aq)}$	-169.8	-84.7
$Mo_2N + 6H_2O \leftrightarrow 2MoO_3 + NH_{3(aq)} + \frac{9}{2}H_{2(aq)}$	-41.0	107.2
$MoO_2 + H_2O \leftrightarrow MoO_3 + H_{2(aq)}$	64.4	96.0
$MoO_2 + \frac{1}{2}O_{2(aq)} \leftrightarrow MoO_3$	-88.2	-118.5
$WO_2 + H_2O \leftrightarrow WO_3 + H_2$	-28.5	3.1
$WO_2 + \frac{1}{2}O_{2(aq)} \leftrightarrow WO_3$	-181.1	-211.4

Table 2.3: Free energy changes calculated for potential catalyst oxidation reactions in 0.15 and 0.52 g/mL SCW at 400 °C.

	Solubility (μmol/kg H_2O)		
Catalyst	25 °C, 1 bar	$\rho_{H_2O} = 0.15$	$\rho_{H_2O} = 0.52$
Pd	8.7×10^{-34}	7.2×10^{-3}	4.8×10^{-4}
Ru	2.6×10^{-10}	5.0×10^{-6}	1.8×10^{-5}
RuO_2	1.0×10^{-20}	3.3×10^{-9}	1.3×10^{-9}
Ni	3.0×10^{-7}	300	13
NiO	4.5	0.044	0.023
Co	3.9×10^{-6}	4,000	170
CoO	16	1.6	0.78
Co_3O_4	6.7×10^{-8}	0.37	0.044
CeO_2	8.1×10^{-7}	2.1×10^{-4}	2.6×10^{-5}
TiO_2	0.011	3.1×10^{-7}	2.0×10^{-7}
ZrO_2	5.2×10^{-5}	2.2×10^{-4}	1.0×10^{-4}
MoO_2	2.2×10^{-5}	15	0.69
MoO_3	240	22	13
WO_2	4.7	340	74
WO_3	5.3	7.3×10^{-4}	0.012

Table 2.4: Catalyst solubilities in water at ambient conditions and in SCW at 400 °C and $\rho_{H_2O} = 0.15$ and 0.52 g/mL calculated using the revised Helgesen-Kirkham-Flowers equation of state.

Table 2.3 for the Ru, Ni, Co and the oxide, carbide, and nitride redox reactions predict oxidation states that agree with the phases observed by XRD after exposure to SCW (Table 2.2). Values of ΔG_{rxn} for metal oxidation suggest that the PdO, NiO, and CoO observed after exposure to SCW were formed from reactions with $O_{2(aq)}$ ($\Delta G_{rxn} < 0$) rather than reactions with H_2O ($\Delta G_{rxn} > 0$). The solubility model results in Table 2.4 predict significant dissolution ($\geq 1\mu$mol/kg H_2O) for Ni, Co, CoO, WO_2, and Mo oxides in both low and high SCW densities. Evidence supporting these predictions is the observed formation of surface crystallites and nanowires on the catalysts, shown in the following sections. The remaining materials are predicted to have equilibrium aqueous metal concentrations well below 1μmol/kg H_2O and the detection limit of the ICP-OES. On the basis of calculated solubility for the metals and oxides and the observed oxidation and dissolution for the carbides and nitrides, catalyst stability in SCW follows $TiO_2 >$ Ru $> CeO_2 \approx ZrO_2 >$ Pd $>$ Ni $>$ Co $>$ carbides $\approx$ nitrides.

2.3.1 Pure Metals

Pd, Ni, and Co underwent oxidation to PdO, NiO, and CoO, respectively, and Ru was unchanged in the presence of SCW (Table 2.2). Negligible oxidation occurred for Pd, Ru, Ni, and Co after 60 minutes in He at 400 °C, demonstrating that the experimental protocol was successful in removing O_2 from the reactor headspace. For Pd and Ni, the fraction of oxidized material was greater after exposure to high-density (0.52 g/mL) SCW compared to low-density (0.15 g/mL) SCW. One explanation for this difference is that the increased H_2O partial pressure at higher SCW density increases the oxidation rate.

The values of ΔG_{rxn} in Table 2.3 predict that oxidation of Pd, Ru, Ni, and Co by H_2O is unfavorable in high-density SCW (or high- and low-density SCW) at 400 °C ($\Delta G_{rxn} > 0$). Oxidation by $O_{2(aq)}$, however, will occur spontaneously ($\Delta G_{rxn} < 0$). At these SCW conditions, the equilibrium constant for the water-splitting reaction is greater than at room temperature and the equilibrium concentrations of $O_{2(aq)}$ at $\rho_{H_2O} = 0.15$ and 0.52 g/mL are $\approx 8 \times 10^{-9}$ mol/kg H_2O and 5×10^{-12} mol/kg H_2O, respectively. The presence of $O_{2(aq)}$ at concentrations approaching these equilibrium values may be sufficient for the metal oxidation reactions to proceed to some extent, producing the partially oxidized catalysts observed experimentally. The ΔG_{rxn} values for metal oxidation by $O_{2(aq)}$ are lower at high ρ_{H_2O} than at low ρ_{H_2O} so the thermodynamic driving force for metal oxidation by $O_{2(aq)}$ increases with increasing SCW density. The reverse trend is observed for oxidation by H_2O, however, because $H_{2(aq)}$ formation becomes less thermodynamically favorable at high pressure (high SCW density).

A comparison of ΔG_{rxn} values (Table 2.3) for metal oxidation by $O_{2(aq)}$ and oxide reduction by $H_{2(aq)}$ shows that Pd, Ru, NiO, and CoO are the thermodynamically favored oxidation states for these metals in SCW. In addition, the difference between the free energies of metal oxidation and reduction in SCW ($\Delta G_{rxn,Ox} - \Delta G_{rxn,R}$)

increases in the following order: Co < Ni < Ru < Pd. With the exception of Pd, this ranking follows trends regarding the nobility or susceptibility to oxidation. In all experiments, the PdO formation was greater than the NiO formation. Pd also produced less H_2 than the experiments with Ni and Ru. Of course, we expect H_2 to be a product of metal oxidation with H_2O. Visual comparison of the fresh Pd, Ni, and Ru SEM images (Figures A.2, A.4 and A.6, respectively) shows that the Pd particles have higher surface areas and visible pores while the Ni and Ru particles are smooth and relatively non-porous. A plausible explanation for the PdO formation is that Pd contained more residual oxygen in the pores and on the surface compared to the other metals. During reactor loading, the water in the reactor may have prevented the exchange of gases in the Pd pores. Excess oxygen added to the system would result in PdO formation without the production of H_2. Although Pd is the thermodynamically favored oxidation state in SCW, future experiments with Pd catalysts in SCW should ensure that oxygen is completely removed prior to the experiment to prevent oxide formation. Other oxygen sources in the system (e.g. feedstock) should be identified and balanced with H_2.

For several experiments with Ru, Ni, and Co, oxidation of the metal was not observed but H_2 was detected in the reactor headspace. One explanation for this result is that H_2 is formed from surface oxidation of the metal particle, which then goes undetected by XRD. Another possible source for the H_2 is from impurities adsorbed on the metal surface that react to form H_2 upon heating to 400 °C. The production of small amounts of H_2 in experiments with no added H_2O supports this hypothesis.

For the remainder of the Ni and Co experiments that resulted in H_2 formation, the measured H_2 was only 4-16% of the amount that would correspond with the extent of oxidation measured by XRD. The difference between H_2 measured and H_2 expected could be due to H_2 losses such as diffusion into the stainless steel reactor walls or

adsorption on the reactor walls and the catalysts. Any residual O_2 adsorbed on the reactor walls or dissolved in the Ar-sparged water that was loaded into the reactors could also cause catalyst oxidation without the formation of H_2.

For Co, the amount of H_2 produced was greater in high-density SCW compared to low-density SCW, which is not consistent with the trend in the XRD data for oxidation via H_2O. On the contrary, the other pure metals had less H_2 measured after exposure to high-density SCW compared to low-density SCW but the large error on the H_2 measured after 0.15 g/mL SCW render this difference statistically insignificant.

With the exception of the experiments with Co, the water recovered from the reactors did not contain any detectable amounts of aqueous metal species. The water recovered from the SCW experiments with Co contained $\sim$0.1 mg/L of aqueous Co species for both SCW conditions. SEM images of the recovered Co (Figure A.8) and Ni catalysts (Figure 2.2), however, show the formation of submicron surface crystallites. These crystallites likely formed from dissolution of the metals in SCW at 400 °C followed by precipitation of the oxide or during the quenching of the batch reactor to room temperature. Dissolution at these SCW conditions is supported by the calculated solubilities of Ni and Co (Table 2.4), which predict the aqueous metal contents to exceed 1μmol/kg H_2O. Precipitation is supported by the calculated solubilities of NiO and CoO in SCW and Ni and Co at 25 °C, all of which are several orders of magnitude lower than those of Ni and Co in SCW.

One might expect metal solubility at 400 °C to increase with increasing SCW density because as K_W and ϵ also increase, the solvent can support more ions. For many species in Table 2.4, however, the calculated solubility is lower in high-density SCW. The solubility for those catalysts is lower in high-density SCW because the total dissolved metal concentration is controlled by neutral aqueous species and at constant temperature, these neutral species become less soluble as ρ_{H_2O}, K_W, and ϵ

(a) Fresh Ni particles   (b) After 0.15 g/mL SCW   (c) After 0.52 g/mL SCW
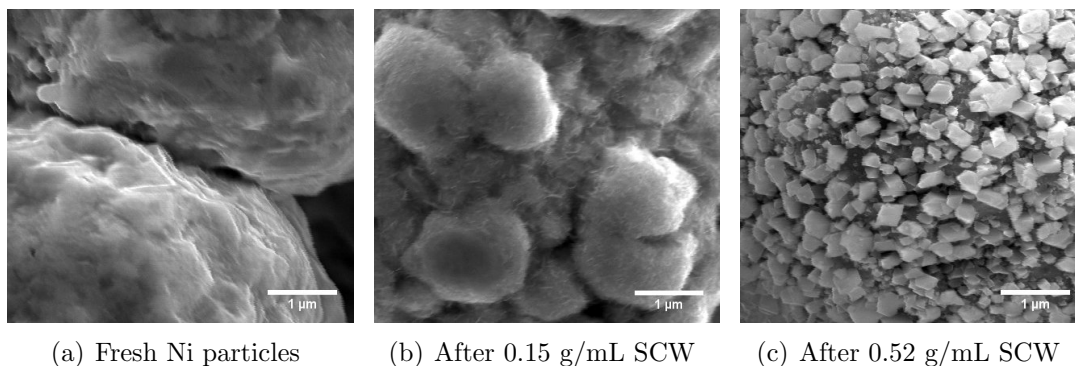
Figure 2.2: SEM images of Ni particles before and after exposure to SCW at 400 °C for 60 min. Scale bar is 1 micron. The images were collected with 15 kV accelerating voltage and spot size 3.

increase. Figure 2.3 shows the concentrations of the aqueous species used to model CoO and WO_3 solubility as a function of SCW density at 400 °C. As expected, the concentrations of the charged species increase as SCW density increases, however these ions are in much lower concentration than the neutral aqueous species. For CoO, the concentration of $CoO_{(aq)}$ decreases with increasing SCW density, resulting in an overall lower CoO solubility at high SCW densities. The concentration of the neutral aqueous species for WO_3 ($H_2WO_{4\ (aq)}$) increases with increasing SCW density, resulting in an overall higher WO_3 solubility at high SCW densitites. The behavior of these neutral aqueous species is strongly dependent on the conventional Born coefficient, one of the species-dependent model parameters.

The calculated solubility for Ni is higher at low SCW density than at high SCW density, however evidence of dissolution was only observed at high SCW density. This result suggests that Ni dissolution rates are higher in high-density SCW than in low-density SCW. Without a way to accurately measure total dissolved metal in situ after 60 minutes, however, the relative rates of dissolution for other catalysts as a function of SCW density cannot be determined.

In summary, Co and Ni will dissolve in SCW, given enough time. The solubilities of Pd and Ru in SCW are many orders of magnitude lower. Co, Ni, and Pd are

26
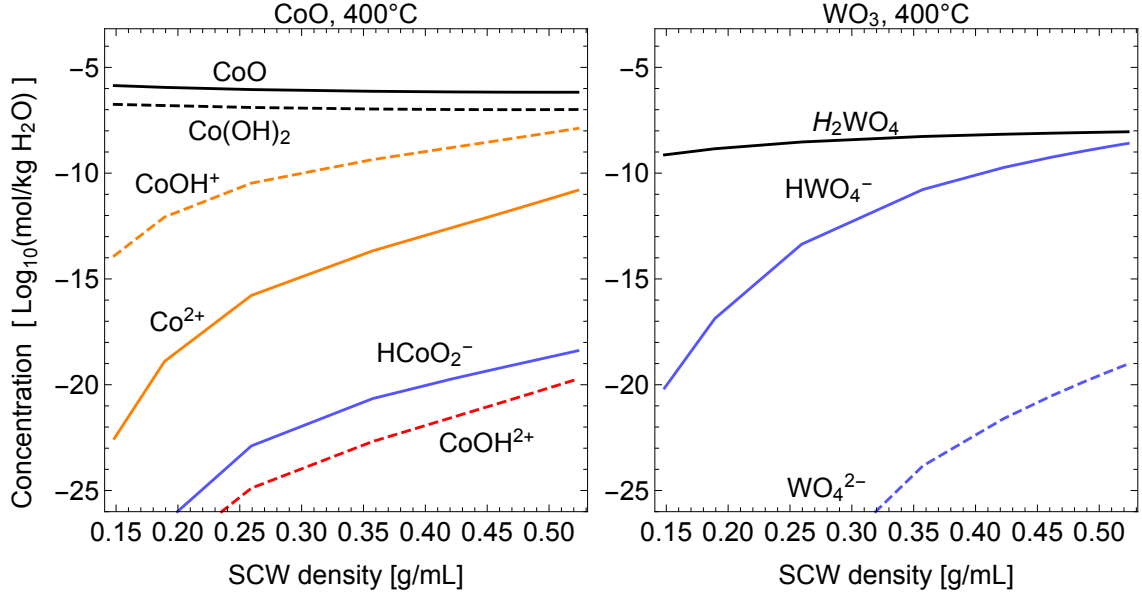
Figure 2.3: Calculated equilibrium concentrations of aqueous metal ions from CoO (left) and WO$_3$ (right) dissolution in SCW at 400 °C as a function of SCW density.

susceptible to oxidation, Ru less so. Since PdO is not thermodynamically favored in pure SCW, PdO is likely an artifact of residual oxygen in the system originating from the large Pd surface area and in the pores. Of the four pure metals tested, Ru is the one that provides the best resistance to both oxidation and dissolution.

2.3.2 Metal Oxides

The experimental results for CeO$_2$ and TiO$_2$ in Table 2.2 show no significant changes in composition or crystal structure after exposure to SCW. The literature reports that TiO$_2$ undergoes a phase change from anatase to rutile in SCW after 120 hours on stream [54]. The 60 minute experiment duration may not have been sufficient time to observe this phenomenon. Table 2.3 lists the calculated ΔG_{rxn} as > 0 for the reduction reactions of CeO$_2$, TiO$_2$ (rutile), and ZrO$_2$ (monoclinic) in SCW at 400 °C and $\rho_{H_2O} = 0.15$ and 0.52 g/mL. Thus, reduction of these oxides is thermodynamically unfavorable in both low- and high-density SCW at 400 °C. The oxidation states of CeO$_2$, TiO$_2$, and ZrO$_2$ observed after the batch experiments

27

(Table 2.2) are in agreement with this predicted absence of reduction in SCW at 400 °C.

The results for ZrO_2 show that the material was initially amorphous and any crystallites were too small for effective x-ray scattering. After the gas-phase control experiment at 400 °C (no SCW), the ZrO_2 crystallinity increases and the diffraction peaks are more defined. The composition of the crystalline fraction after the gas-phase control experiment was approximately 55% monoclinic and 45% tetragonal. The ZrO_2 crystallinity after the experiments with SCW is also greater than that of the fresh catalyst. The ratio of monoclinic to tetragonal ZrO_2 after exposure to SCW is greater than in the catalyst after the gas-phase control experiment. The elevated temperature of 400 °C for all three experimental conditions likely caused the crystallization since crystal growth was also observed in the absence of water. The presence of SCW, however, accelerates the transformation from the metastable tetragonal phase to the thermodynamically stable monoclinic phase. One possible explanation for this result is that the addition of SCW greatly increases the pressure of the system, thereby increasing the driving force for ZrO_2 to decrease its volume by transforming from the tetragonal structure (ρ = 4.60 g/cm^3) to the monoclinic structure (ρ = 5.56 g/cm^3). Although ZrO_2 underwent initial structural changes, monoclinic ZrO_2 catalysts in SCW are reported to have good hydrothermal stability [55, 56].

The results from the gas phase analysis show that no H_2 was detected from the batch experiments with CeO_2, TiO_2, and ZrO_2, which is consistent with the XRD analysis that showed no further oxidation of the materials. No aqueous metal was detected in the water recovered from the experiments with the metal oxides. In addition, the SEM images of the metal oxide catalysts (Figures A.10, A.12 and A.14) show no significant morphological changes compared to the original particles. These results combined suggest that very little (if any) dissolution of the metal oxides occurred

during the 60 minute experiments in low- and high-density SCW. The predicted solubilities of CeO_2, TiO_2, and ZrO_2 in Table 2.4 are relatively low ($< 1\mu$mol/kg H_2O and below ICP-OES detection limits), further supporting this conclusion.

The surface areas of the fresh CeO_2, TiO_2, and ZrO_2 are 8.9±0.2 m^2/g, 9.6±0.4 m^2/g, and 134±5 m^2/g, respectively. After exposure to high-density SCW at 400 °C for 60 minutes, the surface areas decrease to 6.1±0.2 m^2/g, 9.4±0.3 m^2/g, and 75±2 m^2/g, respectively. The change in surface area for TiO_2 is within the error for the BET surface area analysis, so TiO_2 was essentially unchanged during the experiment. The 44±4% decrease in surface area for ZrO_2 is consistent with the crystal growth and phase transformation discussed above.

2.3.3 Transition Metal Carbides and Nitrides

The results for Mo_2C, Mo_2N, and WN show oxidation after exposure to He at 400 °C for 60 minutes (Table 2.2). The He batch experiments for the other catalyst materials show that O_2 in the reactor headspace is effectively replaced with He prior to heating, so the oxidation of Mo_2C, Mo_2N, and WN is not likely from procedural error during the exchange of overhead gases. One hypothesis is that Mo_2C, Mo_2N, and WN reacted with O_2 species already present on the surface of the materials. After synthesis, the carbide and nitride materials were passivated with 1% O_2/Ar prior to the experiments to allow safe handling of the oxophillic materials in air. These materials also have relatively large surface areas ($50 - 100$ m^2/g) and any O_2 on the surface or trapped within the pores may not have been completely removed during the exchange of overhead gases. As a result, the excess O_2 on the surface reacted with the bulk Mo_2C, Mo_2N, and WN phases upon heating to form oxides.

The results for Mo_2C and W_2C in Table 2.2 show significant oxidation in SCW after only 60 minutes. Gas analysis identified CO, CO_2, CH_4, C_2H_6 and H_2 as products. Table 2.5 lists the amounts of the carbonaceous gases produced. Table 2.3 lists

Catalyst	ρ_{H_2O} (g/mL)	Gas produced (mol/mol M$_2$C)[a]				
		CO	CO$_2$	CH$_4$	C$_2$H$_6$	Total C
Mo$_2$C	0[b]	0	0.145	0.005	0	0.150
	0.15	0.016	0.453	0.059	0.005	0.532
	0.52	0	1.528	0.308	0.011	1.848
W$_2$C	0[b]	0	0.024	0.002	0	0.026
	0.15	0.398	0.938	0.527	0.109	2.080
	0.52	0.129	0.095	0.117	0.009	0.358

[a] mol gas/mol C in loaded catalyst   [b] Gas phase control experiment in He.

Table 2.5: Quantities of carbonaceous gas species produced from Mo$_2$C and W$_2$C in He and SCW at 400 °C for 60 min.

possible overall reactions for the formation of these gases from Mo$_2$C and W$_2$C. Prior calculations of ΔG_{rxn} for carbide oxidation in H$_2$O vapor at 300 °C found oxidation by H$_2$O thermodynamically unfavorable [36], however at 400 °C in SCW, Table 2.3 shows that the majority of these reactions are thermodynamically favorable ($\Delta G_{rxn} < 0$) and explain the MoO$_2$, WO$_2$, and WO$_3$ oxides formed during the experiments. The amounts of H$_2$ produced from carbide oxidation in SCW (Table 2.2) are several orders of magnitude larger than the amount of H$_2$ formed from the metal catalysts and correspond to ∼1-8 mol H$_2$ per mol of Mo or W. The H$_2$ formation for Mo$_2$C also increases with increasing SCW density. These results more closely match the expected H$_2$ formation corresponding with the oxidation measured by XRD. The larger oxide fraction and greater H$_2$ production at ρ_{H_2O} = 0.52 g/mL compared to 0.15 g/mL also suggests that the rate of carbide oxidation increases with ρ_{H_2O}, despite a lower ΔG_{rxn} at ρ_{H_2O} = 0.52 g/mL and therefore a lower thermodynamic driving force for oxidation.

Analysis of the relative gas concentrations suggests that different oxidation reactions dominate depending on the SCW density and the catalyst. For Mo$_2$C in low-density SCW, the CO formation reaction is competitive with the other gas formation reactions. In high-density SCW, Mo$_2$C produces more CO$_2$ and H$_2$ and there

is no CO detected, suggesting that all the CO formed is completely converted to CO_2 through the water-gas shift reaction.

The relatively high amounts of CO, CH_4 and C_2H_6 formed from W_2C in low-density SCW suggest that the reactions for the formation of these species are competitive with CO_2 formation at these conditions. The presence of WO_3 and the large H_2 formation indicate additional oxidation of WO_2. The results for W_2C after high-density SCW show that all of the metal was oxidized to WO_3, however the amounts of all gaseous species formed from W_2C in high-density SCW are lower than the amounts in low-density SCW. This reduction in gaseous species could be attributed to diffusion into the reactor walls or losses during the experiment when gas formation would have forced the system to pressures in excess of 40 MPa. Also, the total gaseous carbon recovered after Mo_2C was tested in low-density SCW and W_2C was tested in high-density SCW accounts for only 53% and 36% of the carbon losses in the solid catalysts, respectively. One possibility for the incomplete carbon balance is the dissolution of gaseous CO_2 and other carbon species in the water after quenching the reactors to room temperature.

H_2 was also measured after Mo_2N and WN were exposed to SCW (Table 2.2) and both materials show nearly 100% conversion to MoO_2 and WO_3, respectively, after 60 minutes in low- and high-density SCW. The oxidation of the Mo_2N was likely from the reactions in Table 2.3 and the oxidation of WN was likely from the reactions in Equations (2.20) and (2.21). We could not calculate ΔG_{rxn} for the reactions in Equations (2.20) and (2.21) due to insufficient thermodynamic data for WN. From the available data for Mo_2N, however, its oxidation to form MoO_2 and NH_3 is thermodynamically favorable at low and high SCW densities (Table 2.3). From the similarities between the ΔG_{rxn} values for Mo_2N and Mo_2C and because $\Delta G_{rxn} < 0$ for the oxidation of MoC and WC, one might expect $\Delta G_{rxn} < 0$ for WN oxidation

reactions.

$$WN + 2H_2O \leftrightarrow WO_2 + NH_3 + 0.5H_2 \tag{2.20}$$

$$WN + (x + 2)H_2O \leftrightarrow WO_2 + NO_x + (x + 2)H_2 \tag{2.21}$$
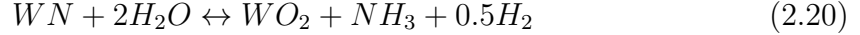
SEM images of the carbide and nitride catalysts after exposure to SCW show the formation of new surface morphologies similar to those observed for Co and Ni. Figure 2.4 shows SEM images of fresh Mo_2C and the Mo_2C samples recovered after the batch experiments. The surfaces of the fresh Mo_2C and the Mo_2C after 60 minutes in He at 400 °C are nearly identical and covered with long, thin macropores 0.5-3 μm long and $\leq$ 300 nm wide. After exposure to low-density (0.15 g/mL) SCW, the Mo_2C surface is rough and covered in spherical surface morphologies 1-2 μm in diameter. After exposure to high-density (0.52 g/mL) SCW, the Mo_2C surface is covered in various different morphologies including disc-shaped particles with dendrites growing from the edges, cube-like particles ($\leq$ 300 nm in diameter), and rod-like particles ($\leq$ 400 nm in diameter). Others have synthesized Mo oxide submicron particles by treating $(NH_4)_6Mo_7O_{24} \bullet 4H_2O$ in water and polyethylene glycol at 180 °C [57] and by treating pure Mo in water at 400 °C and 16-18 MPa [58], so the mechanism for the formation of particles on Mo_2C in SCW may be similar.

The SEM images in Figure 2.5 of W_2C before and after the batch experiments also show new surface morphologies formed after exposure to SCW. The surface of fresh W_2C is rough and porous with the largest pores $\approx$ 900 nm in diameter and the smallest visible pores are $\leq$ 100 nm. The surface of W_2C after 60 minutes in He at 400 °C is similar to that of fresh W_2C with the exception of a few, relatively small needle-like particles on the surface. The surface of W_2C after exposure to low- and high-density SCW is coated in a thick network of whisker-like particles with diameters $\leq$ 100 nm. Mechanisms for WO_{3-x} nanoparticle and whisker synthesis have been proposed [59–61], however they involve different W precursors and treatments

(a) Fresh Mo$_2$C　　　　(b) He (no water)　　　　(c) 0.15 g/mL SCW

(d) 0.52 g/mL SCW　　　　(e) 0.52 g/mL SCW　　　　(f) 0.52 g/mL SCW
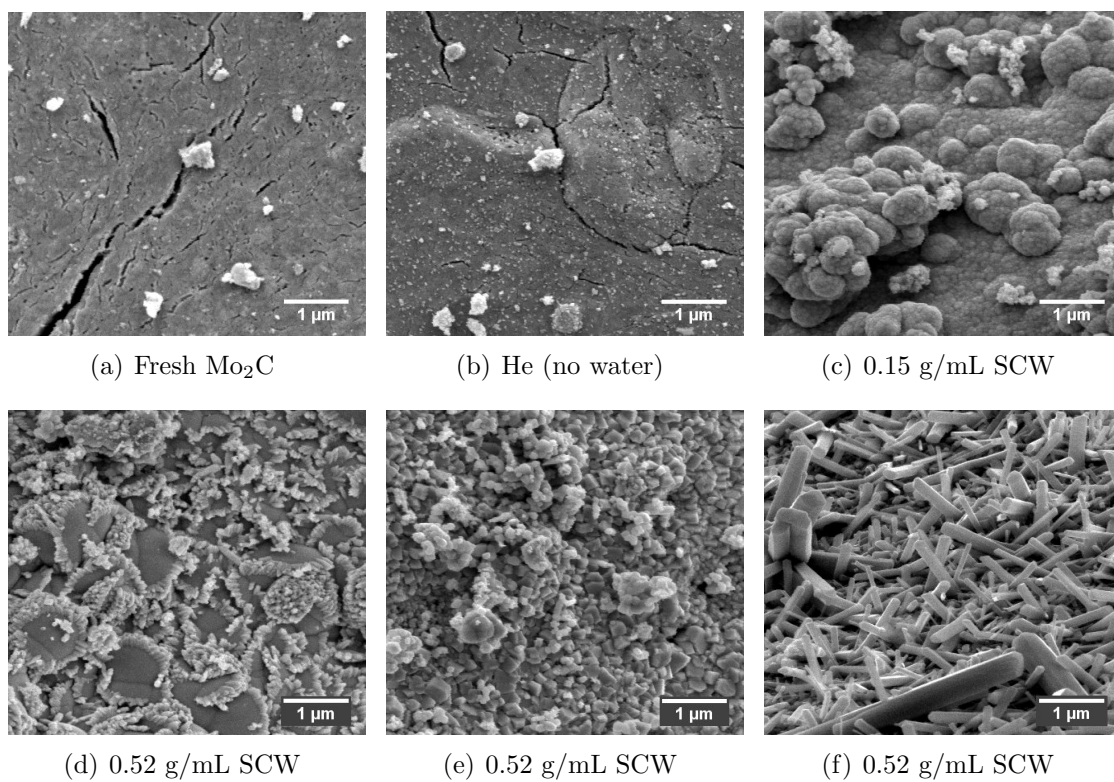
Figure 2.4: SEM images of fresh Mo$_2$C (2.4(a)) and Mo$_2$C after batch experiments at 400 °C for 60 minutes in He (2.4(b)), low-density SCW (2.4(c)), and high-density SCW (2.4(d)-(f)). The images were collected with 5kV accelerating voltage and spot size 3.

(a) Fresh W$_2$C	(b) He (no water)
(c) 0.15 g/mL SCW	(d) 0.52 g/mL SCW
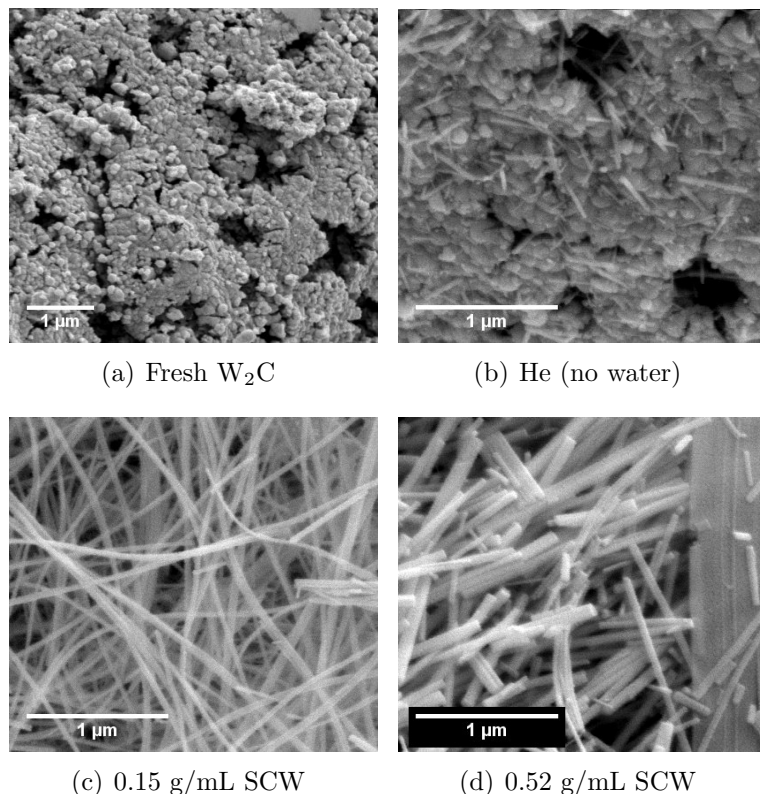
Figure 2.5: SEM images of fresh W$_2$C (2.5(a)) and W$_2$C after batch experiments at 400 °C for 60 min. in He (2.5(b)), low-density SCW (2.5(c)), and high-density SCW (2.5(d)). The images were collected with 10kV accelerating voltage and spot size 3.

than this work.

Another possibility for the formation for these crystallites and whiskers is dissolution under high-density SCW conditions followed by precipitation and anisotropic growth on the particle surface. Indeed, W leaching was previously observed during testing of a WO$_X$/TiO$_2$ catalyst at 400 °C and 33 MPa [62]. Consider that the calculated solubilities of MoO$_2$ and WO$_2$ in SCW (Table 2.4) are relatively large (> 1 μmol/kg H$_2$O) but the calculated solubilities of WO$_3$ in SCW and MoO$_2$ at 25 °C are several orders of magnitude less. For Mo$_2$C and Mo$_2$N, particles at the surface could form when the materials oxidize, which forms aqueous Mo species in solution. Then, these species precipitate when the reactors are quenched to room temperature. For W$_2$C and WN, the aqueous W species formed from WO$_2$ could precipitate in SCW

as WO_3 or upon quenching. Future work should test whether these morphologies are retained after recarburization of the material.

The MoO_2 and MoO_3 solubility models contain some uncertainty due to unavailability of published R-HKF parameters and inconsistencies in reported thermodynamic properties for H_2MoO_4 $_{(aq)}$, the most abundant aqueous-phase Mo-containing species. We took the thermodynamic properties for H_2MoO_4 $_{(aq)}$ from several sources [63–65] and the R-HKF parameters were either fitted from experimental equilibrium data [64] or correlated [25]. In addition, the present model does not include other potential aqueous species such as $MoO_3 \cdot (H_2O)_2$ $_{(aq)}$ and $MoO_3 \cdot (H_2O)_n$ $_{(aq)}$ of higher hydration numbers. Despite this uncertainty, the MoO_3 solubility results in Table 2.4 are in good agreement with experimental solubility measurements in SCW at 400 °C (10-1000 μmol/kg H_2O) [64, 65]. H_2MoO_4 forms gaseous Mo-containing species $(MoO_3 \cdot (H_2O)_n$ $_{(gas)})$ in aqueous vapor at elevated temperatures and the gas-phase Mo concentration increases exponentially with increasing H_2O concentration, including as H_2O transitions from vapor to liquid [65, 66]. This trend in Mo solubility further supports the large Mo concentration predicted by the thermodynamic equilibrium model.

2.4   Conclusion

The ΔG_{rxn} values for catalyst oxidation and the solubility values calculated from the R-HKF equation of state predicted the oxidation and dissolution of carbides, nitrides, Ni, and Co, which was observed after batch experiments in SCW at 400 °C. These materials will lose catalytic activity in SCW and the aqueous metal species could contaminate the reaction products. On the other hand, the model predicted good hydrothermal stability for Ru, CeO_2, TiO_2, and ZrO_2, which was also verified with experiments. From the overall agreement between model and experiments, these thermodynamic calculations should be used to complement future catalyst stability

studies. A continuous flow system or a batch system with *in-situ* measurement capabilities would also prove valuable for measuring catalyst dissolution rates in the future.

The batch experiments with Ni, Co, Mo_2C, W_2C, Mo_2N, and WN in SCW showed that dissolution and re-precipitation formed nano-scale features. Although this phenomena is undesirable for catalysis, SCW processing in batch reactors offers a route to altering the morphology of different materials for other purposes. Additional work is needed to determine whether and how these altered morphologies could lead to functional materials.

CHAPTER III

Structure-Solubility Correlations for the Design of Stable Catalysts in Hot, Compressed Water

This chapter describes a framework for predicting the hydrothermal dissolution of heterogeneous catalyst materials. The revised Helgeson-Kirkham-Flowers thermodynamic equation of state was used to determine the solubilities of metals and oxides in water at 150-550 °C and 22-50 MPa. Design criteria for catalyst compositions were determined through correlations between metal solubility and electronegativity and between oxide solubility and cation electronegativity, ionic-covalent parameter, and polarizing power. These structure-stability relationships, determined from pure compounds, facilitate the design of new alloys and mixed metal oxides as catalytic materials with improved stability during hydrothermal reactions.

3.1   Introduction

Property-stability relationships are essential in the rational design of functional materials, particularly heterogeneous catalysts. Many of the scaling relationships for theory-driven catalyst design focus on the activity of the catalyst for a particular reaction [67]. Volcano plots, for example, are used to predict optimal catalysts for certain chemical reactions by relating the binding energies of various catalytic inter-

mediates across a range of catalytic surfaces. For hydrothermal reactions, however, many catalytic materials become unstable in the hot, compressed water and lose their activity during the reaction [5, 18, 19]. Therefore, designing heterogeneous catalysts for hydrothermal reactions involves two challenges: achieving activity and also stability. In a similar way that scaling relationships are used to relate surface chemistry with catalytic activity or electronegativity and chemical hardness are used to describe conductor, semiconductor, and insulator behavior among electronic materials [1], we aim to identify material descriptors for the rational design of hydrothermally stable heterogeneous catalysts.

In Chapter II, we identified the revised Helgeson-Kirkham-Flowers equation of state (R-HKF) as a successful model for describing catalyst oxidation and dissolution behavior in practical SCW reaction systems. In this chapter, we use the R-HKF model [20] to elucidate the thermodynamic dissolution of common catalytic transition metals and oxides (Au, Co, Cu, Ni, Pd, Pt, Ru, CeO_2, MoO_3, TiO_2, WO_3, ZrO_2) across a large range of sub- and supercritical conditions relevant for hydrothermal organic chemistry (150-550 °C and 22-50 MPa) and correlate key material properties with hydrothermal stability. The equilibrium calculations reported herein predict the most severe outcome for irreversible catalyst deactivation by indicating the maximum possible catalyst dissolution in the system. Furthermore, these methods for analyzing catalyst solubility could be used to determine the relative contributions of heterogeneous catalysis and homogeneous catalysis from dissolved metal ions. Finally, the relationships between material properties and hydrothermal stability reported herein could be used to select or design catalytic materials that experience minimal dissolution.

3.2 Catalyst Dissolution Calculations

The equilibrium aqueous metal concentrations of various materials in hydrothermal solutions from 150-550 °C and 22-50 MPa were calculated from the equilibrium constants (K_{eq}) of the dissolution reactions. The details for calculating K_{eq} and $\Delta G_f(T, P)_j$ at elevated temperatures and pressures using either the R-HKF equation of state [20] for aqueous species or the differential expression for molar Gibbs free energy for solid and gaseous species are discussed in Section 2.2.2. Tables B.1 and B.2 contain the thermodynamic properties necessary for the calculations with references. The accuracy of the thermodynamic properties measured or approximated from these references provides the accuracy for these calculations. The methods for calculating the concentrations of dissolved catalyst species are given in Section 2.2.3. The specific dissolution reactions considered in this chapter are listed in Tables C.1 to C.11.

3.3 Results and Discussion

Figure 3.1 shows the total equilibrium metal concentrations (sum of all aqueous metal-containing species) for several transition metals and oxides in pure water at 150-550 °C and 22-50 MPa calculated using the R-HKF equation of state [20]. Solubilities of 0.01, 10^{-6}, and 10^{-20} mol/kg H_2O correspond to shades of red, yellow, and blue, respectively, in the various figures. In general, the total aqueous metal concentration decreases when moving down a periodic column (e.g., Ni, Pd, Pt) and as the oxidation state of a metal increases (e.g., Co, CoO, Co_3O_4).

The model predicts that Co, CoO, Ni, MoO_3, and WO_2 have the highest solubilities across all hydrothermal conditions modeled in this work. Dissolution ≥ 1 μmol/kg H_2O is also predicted for Cu, CuO, NiO and WO_3 in subcritical water and for Co_3O_4 and MoO_2 in SCW. The remaining materials in Figure 3.1 are predicted to have equilibrium aqueous metal concentrations well below 1 μmol/kg H_2O.
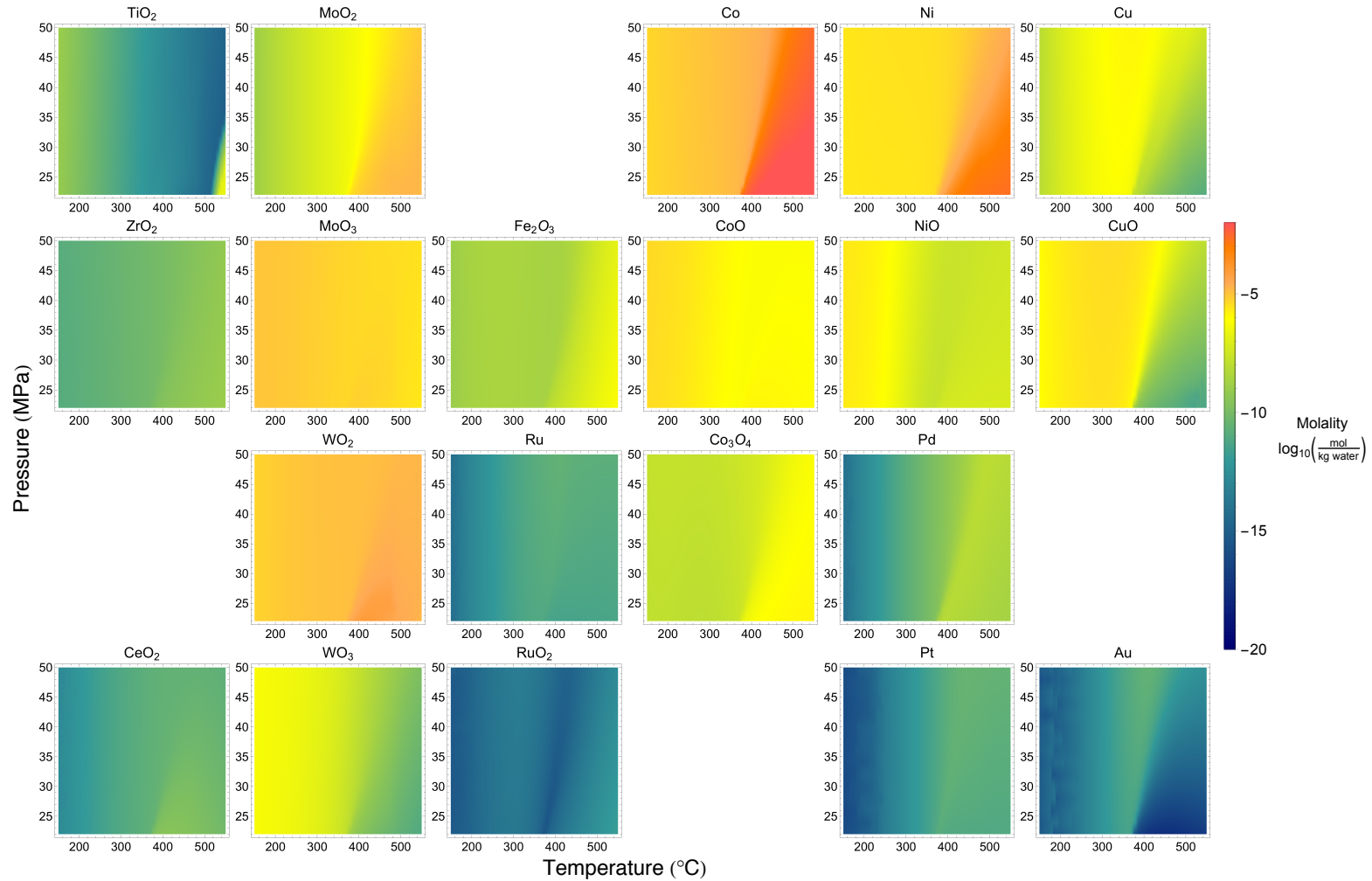
Figure 3.1: Total aqueous metal concentration ($\log_{10}[\text{mol/kg H}_2\text{O}]$) of different materials in pure H_2O at 150-550 °C and 22-50 MPa calculated from the R-HKF equation of state. The materials are arranged according to their approximate location in the periodic table and metals and their oxides appear within the same column.
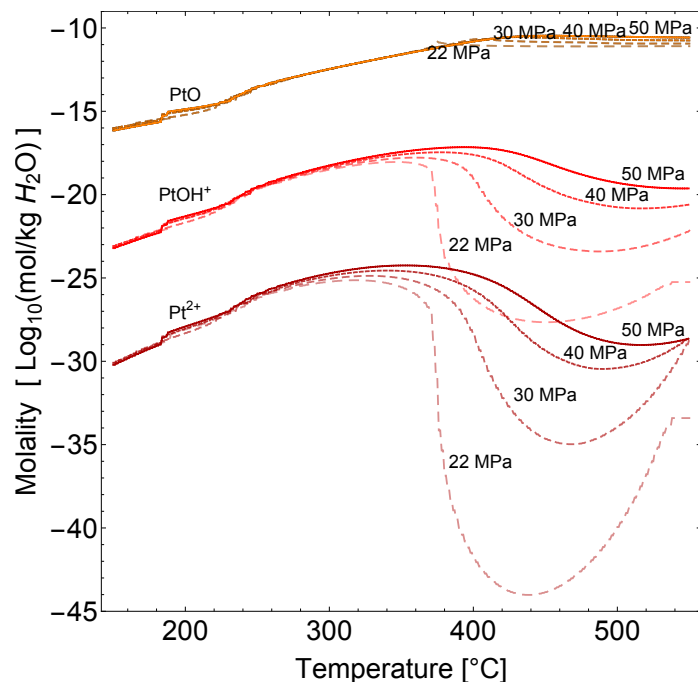
Figure 3.2: Calculated Pt species concentrations: Pt^{2+}, $PtOH^+$, and PtO concentrations in pure H_2O at 22, 30, 40 and 50 MPa and 150-550 °C

A majority of the materials in Figure 3.1 undergo significant changes in solubility on going from sub- to supercritical water which correspond with changes in the solvent properties (Figure 1.1). The solubilities of TiO_2, WO_3, NiO, Cu and CuO decrease because their aqueous species have strong ionic character and the lower dielectric constant in SCW does not support ions as well. On the other hand, the solubilities of MoO_2, Co, Co_3O_4, and Ni increase in low density SCW because their most abundant aqueous species have no charge and negative conventional Born coefficients, which produce an inverse relationship with dielectric constant.

The weak dependence of solubility on temperature and pressure for CoO, MoO_3, Pt, Ru, RuO_2, WO_2, and ZrO_2 is because the aqueous metal concentration is dominated by a neutral aqueous metal species. The solubilities of such species are only weakly dependent on the solvent properties. Figure 3.2 provides an example for the case of aqueous Pt species. The neutral PtO_{aq} species has the highest concentration at all temperatures and pressures, therefore dominating the total Pt solubility. The

41

concentration of PtO_{aq} is a very weak function of temperature and pressure compared to Pt^{2+} and $PtOH^+$. Individual species concentrations for the other materials are plotted with temperature in Appendix D.

3.3.1 Material Properties and Hydrothermal Solubility

The solubilities of the metals and oxides at 400 °C and 50 MPa were fit to models with independent variables representing chemical and electronic properties of the materials. Our objective was to construct a function of material properties that correlated the calculated solubilities with the fewest number of terms. Solubility was chosen as the dependent variable because it is a quantifiable measure of hydrothermal stability that can be used to compare materials.

A strong correlation exists between pure metal solubility (S_m, mol/kg H_2O) and electronegativity (Figure 3.3(a)) and the second-order polynomial in Equation (3.1) captures this effect (χ is electronegativity in Pauling units) for 400 °C and 50 MPa. Because the aqueous metal-containing species are in higher oxidation states than the pure metal and metals with lower electronegativities are (generally) more easily oxidized, the metals are also more easily dissolved as electronegativity decreases.

$$Log_{10}(S_m)|_{400^\circ C, 50MPa} = 15.15\chi^2 - 77.78\chi + 87.96 \qquad (3.1)$$

For the oxide solubility data, we considered a second order polynomial. The base model is shown in Equation (3.2) where α_i represents first order coefficients, β_{ij} represents second order coefficients, and x_i and x_j denote the independent variables (material parameters).

$$Log_{10}(S) = \alpha_0 + \sum_i \alpha_i x_i + \sum_{i,j} \beta_{ij} x_i x_j \qquad (3.2)$$

The independent variables considered for fitting the oxide solubility data (S_x,
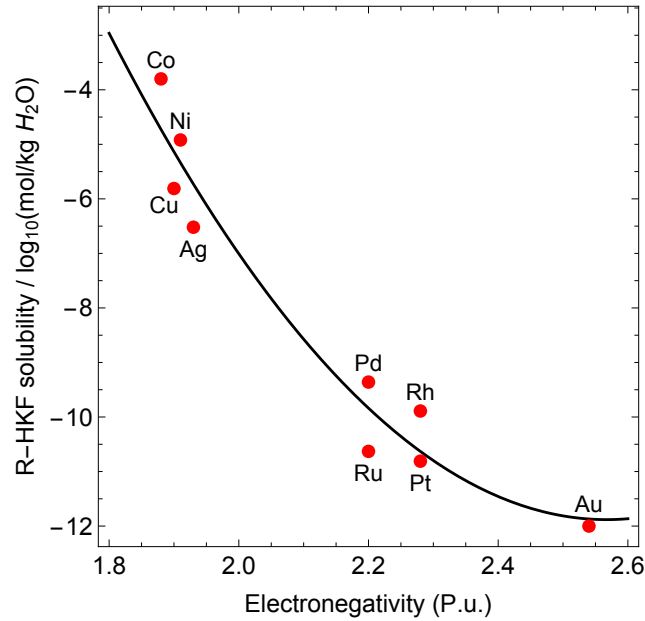
(a) Metal solubility correlation
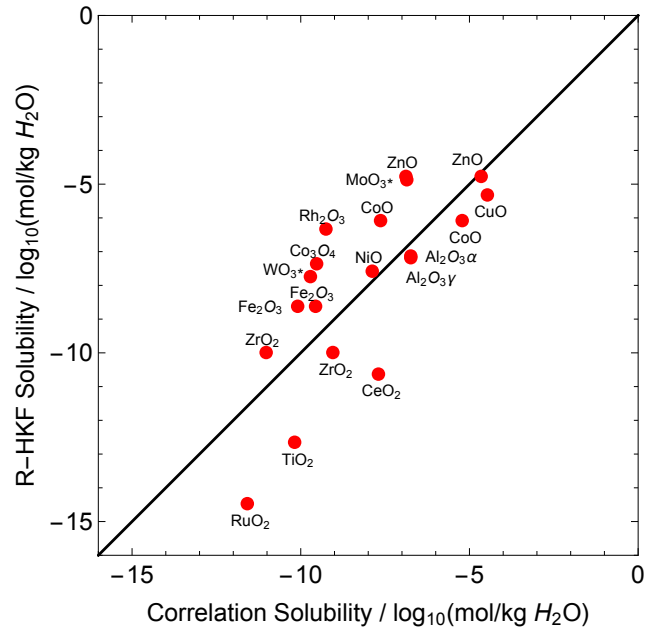
(b) Oxide solubility correlation

Figure 3.3: Catalyst solubility analysis: Figure 3.3(a) compares the calculated solubility of different metals at 400 °C, 50 MPa with a polynomial function of electronegativity (in Pauling units) in Equation (3.1); Figure 3.3(b) compares metal oxide solubility values at 400 °C and 50 MPa obtained from the R-HKF model with the best-fit correlation as a function of polarizing power, cation electronegativity, and ionic-covalent parameter in Equation (3.3).

43

mol/kg H$_2$O) included cation radius (r$_{cation}$, Å), cation electronegativity (χ_{ion}, Pauling units), Ionic-Covalent Parameter (ICP, unit-less), oxide electronegativity (χ_{oxide}, eV), chemical hardness (η, eV), and polarizing power (P, Å^{-2}). These parameters were chosen because they have previously been used to describe other electronic and chemical properties of oxides [1] and are listed in Table 3.1. ICP is related to the acid strength of the cation and the ionic or covalent nature of the metal-oxygen bond. Polarizing power is calculated from z/r^2 where z is the formal charge on the cation and r is the ionic radius. Chemical hardness is defined as half the bandgap of the oxide [1].

We used LinearModelFit in Mathematica to fit Equation (3.2) to the solubility data in Table 3.1 and then we used an iterative function to systematically eliminate terms. The quality of the model was measured on each iteration using the Akaike Information Criterion with correction for finite sample size (AICc). AICc measures the goodness of fit while taking into account model complexity (i.e., number of terms), with lower AICc values representing better models. If the removal of a term decreased the AICc value, then the original model was replaced with the better model of fewer terms. This analysis was repeated until the best model was obtained, shown in Equation (3.3). According to the empirical model expression, an increase in the ionic-covalent parameter (ICP) and a decrease in polarizing power (P) will result in a decrease in oxide solubility. The calculated solubility goes through a maximum with cation electronegativity (χ_{ion}).

$$Log_{10}(S_x)|_{400^oC,50MPa} = -105 - 41(ICP) + 187\chi_{ion} + 74\chi_{ion}^2 + 1.1\chi_{ion}P \qquad (3.3)$$

A comparison between the solubility values obtained from the R-HKF equation of state and the expression in Equation (3.3) is shown in Figure 3.3(b). This is the first general correlation for metal oxide solubility in SCW of which we are aware.

Material	r_{cation} (Å)	χ_{ion} (P.u.)[a]	ICP[b]	χ_{oxide} (eV)[c]	η (eV)[d]	$Log_{10}(S)$[e]
$Al_2O_{3\alpha}$	0.4	1.58	1.16	6.38	4.03	-7.13
$Al_2O_{3\gamma}$	0.4	1.58	1.16	6.38	4.03	-7.18
CeO_2	0.87	1.65	0.52	6.5	1.65	-10.63
Co_3O_4	0.61	1.77	0.53	6.7	1.75	-7.36
CoO	0.745	1.55	0.49	6.7	1.75	-6.08
CoO	0.65	1.58	0.57	6.13	1.56	-6.08
CuO	0.73	1.73	0.26	7.87	0.71	-5.32
Fe_2O_3	0.55	1.84	0.52	6.7	1.39	-8.62
Fe_2O_3	0.645	1.8	0.44	6.7	1.39	-8.62
MoO_3	0.59	1.95	0.62	7	2.04	-4.87
NiO	0.69	1.5	0.62	6.1	2.04	-7.58
Rh_2O_3	0.665	1.71	0.55	5.70	1.67	-6.33
RuO_2	0.62	1.9	0.47	6.87	1.5	-14.47
TiO_2	0.605	1.87	0.52	6.8	1.69	-12.65
WO_3	0.6	2.03	0.49	7.06	1.56	-7.74
ZnO	0.74	1.58	0.45	6.3	1.87	-4.77
ZnO	0.74	1.63	0.45	6.3	1.87	-4.77
ZrO_2	0.72	1.56	0.8	6.4	2.57	-9.99
ZrO_2	0.72	1.49	0.8	6.4	2.57	-9.99

[a] cation electronegativity in Pauling units   [b] ionic-covalent parameter
[c] oxide electronegativity in eV   [d] chemical hardness   [e] solubility data at 400 °C and 50 MPa in mol/kg H_2O

Table 3.1: Values of oxide properties obtained from Matar et al [1] and oxide solubility in SCW at 400 °C and 50 MPa calculated from the R-HKF solubility model. Duplicate material entries account for variations in properties due to high and low spin states, variation in coordination number, and differences in reported property values.

3.4   Conclusion

Results for the calculated solubilities of transition metals and oxides in water at 150-550 °C and 22-50 MPa identified a variety of materials with low hydrothermal solubility (Au, Pt, Pd, Ru, RuO_2, TiO_2, ZrO_2, and CeO_2) which are expected to be stable during hydrothermal reactions. The calculated solubilities also illustrated the "worst case scenario" for catalyst deactivation by dissolution. That is, if oxidation and dissolution rates are fast, the catalyst would quickly reach its new equilibrium state, but total oxidation and dissolution would not exceed the equilibrium limit. Of course, the dissolution kinetics may be slow and more forgiving in practice.

New correlations between the hydrothermal solubilities and readily available material properties allowed for rapid estimation of metal or metal oxide solubility. These correlations could also be used to identify new materials with improved hydrothermal stability. For example, metal alloy catalysts should have large average electronegativities and oxides should have relatively large ionic-covalent parameters and small polarizing power values to minimize dissolution. The property-stability relationships identified in this chapter provide guidance for the design of heterogeneous catalysts with improved hydrothermal stability.

CHAPTER IV

Design of Hydrothermal Solution Properties for Improved Heterogeneous Catalyst Stability

This chapter describes methods for understanding how the composition of hydrothermal reaction solutions influences the oxidation and dissolution of heterogeneous catalyst materials. Design criteria for engineering aqueous solution compositions were determined by constructing oxygen fugacity-pH diagrams, which illustrate material phase changes (i.e., changes in oxidation state and solubility) in response to changes in pH and the oxidative or reductive strength of the solution. These diagrams were constructed using the R-HKF thermodynamic equation of state and were used to determine the oxidation states and solubilities of transition metals and oxides in hydrothermal media at 150-550 °C and 22-50 MPa. Combined with the design criteria for catalyst compositions (Chapter III), these solution criteria facilitate design of stable catalytic materials for hydrothermal reactions.

4.1 Introduction

During hydrothermal reactions, changing concentrations of reactants and products will vary the oxidizing potential and pH of the solution. As a result, the system may be operating under conditions that alter the catalyst. Oxygen fugacity (f_{O_2})-pH dia-

grams are useful for understanding how these changes in acidity and concentrations of oxidizing or reducing species affect catalyst stability, showing regions of thermodynamically favored species in water as a function of pH and f_{O_2}. Pourbaix diagrams are similar in that they also show material phases as a function of pH and potential (V), however, Pourbaix diagrams readily relate to electrochemical systems while f_{O_2}-pH diagrams readily relate to molecular reactions like those in hydrothermal reaction systems. f_{O_2}-pH diagrams can also be used to design conditions that minimize catalyst dissolution and changes in the catalyst oxidation state through addition of buffers to control pH and addition of oxidizers or reducers to control f_{O_2}.

In this chapter, we use the R-HKF equation of state [20] to construct f_{O_2}-pH diagrams to elucidate thermodynamically-favored oxidation states and dissolution of common catalytic transition metal elements (Co, Ni, Pd, Pt, Ru, Ce, Mo, Ti, W, Zr) in hydrothermal reaction solutions at 150-550 °C and 22-50 MPa. These diagrams show the power of thermodynamic modeling for the selection of aqueous solutes and process conditions that minimize changes in catalyst oxidation state and dissolution of metal during hydrothermal reactions.

4.2 Methods for Constructing Oxygen Fugacity-pH Diagrams

Methods for constructing oxygen fugacity (f_{O_2})-pH diagrams of catalytic materials are presented first, followed by the methods for calculating f_{O_2} and pH values for various aqueous solutes in hot, compressed water.

4.2.1 Oxygen Fugacity-pH Diagrams of Catalytic Materials

The redox reactions for each material follow the form in Equation (4.1) where the forward reaction is oxidation of a metal $M_{(s)}$ by O_2 and the reverse reaction is reduction of the corresponding oxide $MO_{x(s)}$. For these reactions, O_2 comes from the water splitting reaction in Equation (4.2). These reactions combined are thermody-

48

namically equivalent to metal oxidation by H_2O and are not necessarily intended to represent the actual oxidation mechanism.

$$M_{(s)} + \frac{x}{2}O_2 \rightleftharpoons MO_{x(s)} \tag{4.1}$$

$$H_2O \rightleftharpoons \frac{1}{2}O_2 + H_2 \tag{4.2}$$

The O_2 fugacity (f_{O_2})-pH diagrams show where different species are thermodynamically favored relative to the oxidizing or reducing character of a solution (f_{O_2}) and its acidic or basic character (pH). A single f_{O_2}-pH diagram corresponds to a single temperature and pressure. The boundaries between solid species define the f_{O_2} conditions for the equilibrium oxidation/reduction. The boundaries between solid and aqueous species define the f_{O_2} and pH conditions for the presence of the aqueous species at some arbitrary fixed activity. These boundaries are expressed by Equation (4.3) where ν_{H^+} and ν_{O_2} are the stoichiometric coefficients of H^+ and O_2 in the reaction, respectively, K_{eq} is the equilibrium constant for the oxidation or dissolution reaction, and a_j is the thermodynamic activity for each species j in the reaction (not O_2 or H^+). Gas activities are expressed as fugacities (f_j, bar). From the standard state convention of the R-HKF equation of state [21], aqueous species have unit activity in a hypothetical one molal solution referenced to infinite dilution and activities of solid phases and H_2O are taken to be unity at any pressure and temperature. If the reaction did not contain O_2 or H_2, Equation (4.3) was solved for pH, instead.

$$log_{10}f_{O_2} = \left(\frac{\nu_{H^+}}{\nu_{O_2}}\right)pH - \left(\frac{1}{\nu_{O_2}}\right)log_{10}\left(\frac{\prod a_j^{\nu_j}}{K_{eq}}\right) \tag{4.3}$$

Equation (4.3) is derived by taking the log_{10} of Equation (4.4). If the equation included a_{OH^-}, it was first converted to an a_{H^+} term by a substitution of Equation (4.5).

Then, the a_{H^+} terms were converted to pH using Equation (4.6).

$$K_{eq}(T,P)_i = \prod_j a_j^{\nu_j} \tag{4.4}$$

$$a_{OH^-} = \frac{K_W}{a_{H^+}} \tag{4.5}$$

$$pH = -log_{10}(a_{H^+}) \tag{4.6}$$

In this work, activities of 10^{-6} or 10^{-8} were used for aqueous boundary construction ($\approx$ 1 or 0.01 μmol/kg H_2O). While any threshold activity can be chosen, we selected 1 ppm as the threshold below which the material could be considered stable because material loss would be negligible for the timescales of lab-scale reactions. For several materials, no dissolved species were present at 1 ppm, so the threshold was reduced to 10 ppb. When a_j are constant ($a_j = C$), Equation (4.3) is a linear relationship between $log_{10} f_{O_2}$ and pH and corresponds to an equilibrium boundary on the diagram. On one side of the boundary is a solid species and on the other side is either another solid species or an aqueous species with $a_j \geq C$. The f_{O_2}-pH boundary equations for all the materials that were modeled are listed in Tables C.1 to C.10.

Each f_{O_2}-pH diagram also shows, for those specific conditions, the f_{O_2} and pH of pure H_2O and where f_{H_2} equals one bar. The pH and f_{O_2} of pure H_2O at T and P were determined using the ion product ($K_W(T,P)$) and the equilibrium constant for the water-splitting reaction in Equation (4.2) ($K_{WS}(T,P)$). From stoichiometry of the water-splitting reaction ($\nu_{H_2} = 2\nu_{O_2}$) and the ideal gas assumption ($f_i = P_i$), $f_{H_2} = 2f_{O_2}$ (in bars) and Equation (4.7) is obtained. Under these conditions, errors from the ideal gas assumption are considered negligible and are discussed in Appendix

B. Equation (4.7) can be solved for $log_{10}f_{O_2}$ of pure H_2O as shown in Equation (4.8).

$$K_{WS} = (f_{H_2})(f_{O_2})^{\frac{1}{2}} = 2(f_{O_2})^{\frac{3}{2}} \qquad (4.7)$$

$$log_{10}f_{O_2} = \frac{2}{3}log_{10}\left(\frac{K_{WS}(T,P)}{2}\right) \qquad (4.8)$$

The value of $log_{10}f_{O_2}$ when f_{H_2} equals one bar was determined by Equation (4.9), which is obtained by substituting $f_{H_2} = 1$ into Equation (4.7).

$$log_{10}f_{O_2}|_{(f_{H_2}=1bar)} = 2log_{10}(K_{WS}(T,P)) \qquad (4.9)$$

4.2.2 Oxygen Fugacity-pH Diagrams of Reaction Solutions

The f_{O_2}-pH diagrams of various aqueous solutes were calculated using a similar method to that used for calculating equilibrium concentrations of aqueous catalyst species in pure H_2O. The pH and f_{O_2} come from the concentrations of H^+ and $O_{2\,(aq)}$, respectively, for each aqueous solution at equilibrium. The equilibrium concentrations in each solution were calculated after identifying all likely reactions of the solutes (CO_2, CH_4, NH_3, formic acid) in water. The reactions used for each solution, including H_2O ion dissociation (K_W) and H_2O splitting (K_{WS}), are listed in Table C.12.

$\Delta G_f(T,P)_j$ values (at T = 150, 370, 380 and 550 °C and P = 22, 24, 30, 40 and 50 MPa) were calculated for all the aqueous species in Table C.12 using Equation (2.7) and the HKF parameters in Table B.4. $K_{eq}(T,P)$ values for each of the reactions in Table C.12 were calculated using Equations (2.3) and (2.10). Matlab was used to solve the following system of equations for the equilibrium concentrations (m_j, in mol/kg H_2O) of each species:

- K_W, K_{WS}, and K_{eq} expressions in Table C.12 where $a_j = \gamma_j m_j/m_\ominus$

  ($m_\ominus$ = 1 mol/kg H_2O, γ_j = 1 for neutral species or determined by Equation (2.13) for charged species)

51

- Ionic strength as a function of m_j, Equation (2.15)

- Charge balance, Equation (2.16)

- Mass balance on H and O, Equation (2.19)

- Mass balance on C (or N) from the solute

Examples of mass balances on C (in CO_2) and N (in NH_3) are in eq. (4.10) and eq. (4.11), respectively, where $m_j|_{in}$ is the initial molal concentration (or loading) of the solute (0.1, 1, or 10 mol/kg H_2O) and $m_j|_{out}$ is the molal concentration of the solute at equilibrium.

$$m_{CO_{2(aq)}}|_{in} = m_{CO_{2(aq)}}|_{out} + m_{HCO_3^-} + m_{CO_3^{2-}} \tag{4.10}$$

$$m_{NH_{3(aq)}}|_{in} = m_{NH_{3(aq)}}|_{out} + m_{NH_4^+} + m_{HNO_2} + m_{NO_2^-} + m_{NO_3^-} \tag{4.11}$$

Once equilibrium concentrations were obtained for a solution at T and P, pH was calculating using m_{H^+} and Equation (4.6). The corresponding coordinate, $log_{10}f_{O_2}$, was calculated using $m_{O_{2(aq)}}$ by considering the phase equilibrium in Equation (4.12):

$$O_{2(aq)} \leftrightarrow O_{2(g)} \tag{4.12}$$

$K_{eq}(T, P)$ values for this reaction were calculated using Equations (2.3) and (2.10) and the K_{eq} expression for this reaction is shown in Equation (4.13).

$$K_{eq} = \frac{f_{O_{2(g)}}}{m_{O_{2(aq)}}} \tag{4.13}$$

Applying log_{10} to both sides of Equation (4.13) and solving for $log_{10}f_{O_2}$ yields the expression in Equation (4.14), which was used to calculate values of $log_{10}f_{O_2}$ for all the solutions.

$$log_{10}f_{O_2} = log_{10}(K_{eq} \times m_{O_{2(aq)}}) \tag{4.14}$$

Once pH and $log_{10} f_{O_2}$ coordinates were obtained for all the solutions at the temperatures and pressures of interest, the solutions were plotted on the f_{O_2}-pH diagrams in Figure E.11.

4.3   Results and Discussion

In an f_{O_2}-pH diagram, the boundaries between solid species indicate the value of f_{O_2} at which the two solids coexist in equilibrium. The diagrams for Co appear in Figure 4.1 as a representative example. Diagrams for additional materials including Ce, Mo, Ni, Pd, Pt, Ru, Ti, W, and Zr and at additional temperatures and pressures are shown in Appendix E. At f_{O_2} values greater or less than these boundaries, only one solid phase is present. For example, the boundaries between $Co(OH)_{2(s)}$ and $Co_3O_{4(s)}$ in Figure 4.1 show the f_{O_2} conditions at which both oxides exist at the system temperatures and pressures indicated above the diagrams. Because H^+ and OH$^-$ do not participate in the redox reactions between solid species, these solid-solid boundaries are independent of pH. Boundaries between solids and neutral aqueous species are also independent of pH for the same reason. As expected, the oxidation state increases with increasing f_{O_2}.

Activities (a_j) of 10^{-6} and 10^{-8} were used to construct boundaries between solids and aqueous metal species (see Section 4.2). The shaded region within the boundaries indicates that $a_j \geq 10^{-6}$ or 10^{-8} for all conditions in the region. For example, Co^{2+} and $CoOH^+$ in Figure 4.1 are bounded by equilibrium reactions with $Co_{(s)}$, $CoO_{(s)}$, and $Co_3O_{4\ (s)}$. Inside these red regions, the ions have activities $\geq 10^{-6}$. From the solubility calculations, the ion activity coefficients γ_j were found to be ≥ 0.95 (the majority of species were ≥ 0.99) among all materials modeled. As these values are very close to unity and $\gamma_j = 1$ for neutral aqueous species, the activities of aqueous metal species are approximately equal to the concentration ($a_j = \gamma_j \frac{m_j}{m_\Theta} \approx \frac{m_j}{m_\Theta}$ where $m_\Theta = 1$ mol/kg H_2O).
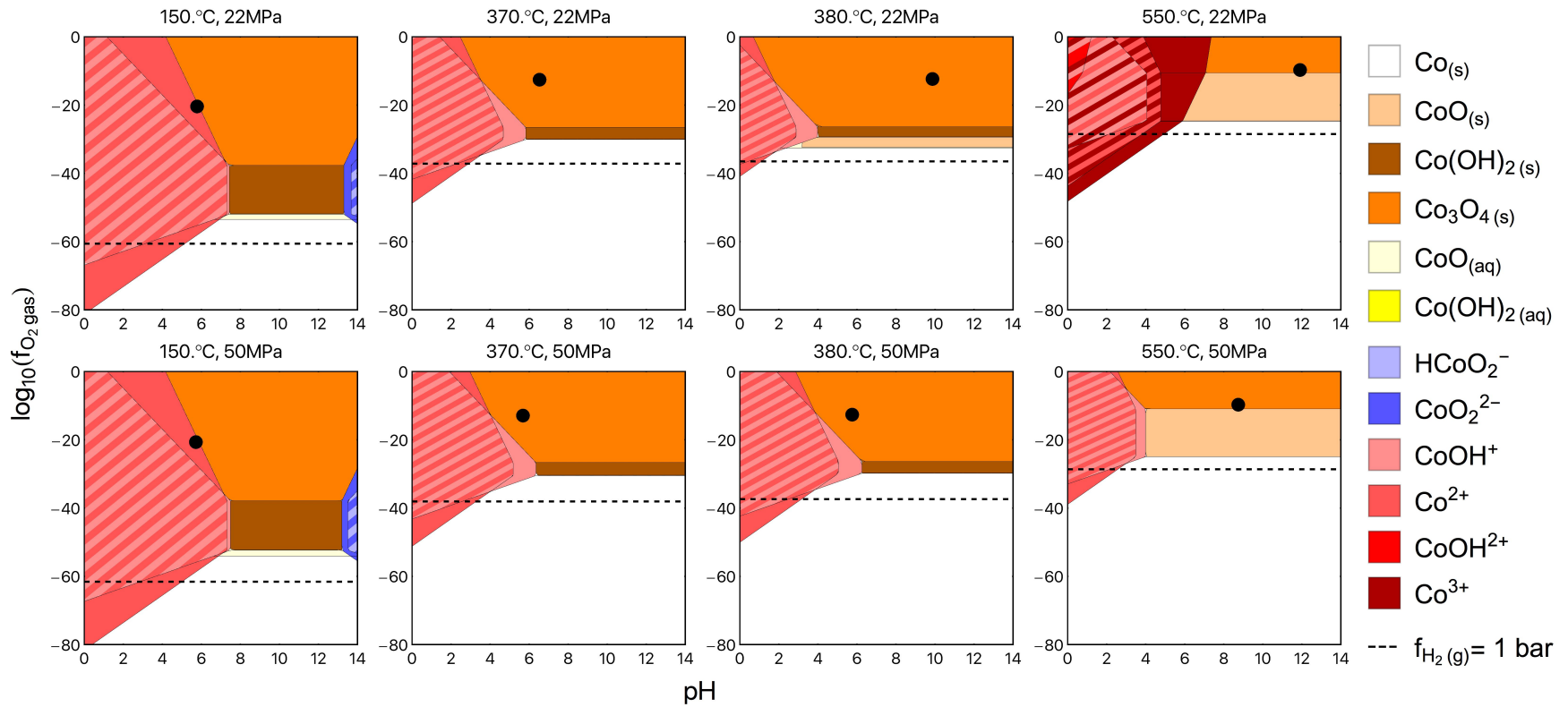
Figure 4.1: f_{O_2}-pH diagrams for Co-H$_2$O system. f_{O_2} is in bar, and pH is in log_{10}(mol/kg H$_2$O). Boundaries for aqueous metal species are defined as $a_j = 10^{-6}$ (≈ 1 μmol/kg H$_2$O) so within the shaded regions $a_j \geq 10^{-6}$. Striped regions indicate the presence of multiple aqueous metal species (e.g. Co^{2+} and CoOH$^+$) with $a_j \geq 10^{-6}$. The f_{O_2} and pH values of pure H$_2$O are plotted as $\bullet$.

All diagrams in this work contain two reference conditions: the f_{O_2} and pH of pure H_2O (• symbol) and the f_{O_2} value at which f_{H_2} is one bar (- - - -) plotted at the system temperature and pressure. A third reference can be made from $log_{10} f_{O_2}$ = zero, where f_{O_2} is one bar. It is important to note that the f_{O_2} and pH of the aqueous solution can change with time during batch operation. For example, the Co-H_2O systems in Figure 4.1 show that at all conditions, the f_{O_2} of pure H_2O is sufficient for Co oxidation. As the O_2 is consumed during Co oxidation (or H_2 is released), however, the f_{O_2} of the system decreases. In batch, this reduction of f_{O_2} will occur until the f_{O_2} of the system reaches the Co/CoO equilibrium boundary (resulting in a partially oxidized catalyst) or until all the Co is oxidized (large H_2O:Co ratio). During flow operation, however, the Co-H_2O system is expected to eventually reach a steady-state f_{O_2} value corresponding with that of the feed (H_2O) and Co will be entirely oxidized to Co_3O_4. Therefore, the pure H_2O reference identifies the dominant species at equilibrium for a catalyst-H_2O flow system.

The f_{O_2}-pH diagrams for Co (Figures 4.1 and E.2) and Ni (Figure E.4) show that both materials form cations ($\geq$ 1 μmol/kg H_2O) at moderate to low pH values and negative ions at very high pH values. In general, Co ions form over a wider range of hydrothermal f_{O_2}-pH conditions than Ni ions. A small decrease in pH (relative to the conditions for pure H_2O) favors formation of Co^{2+} and $CoOH^+$ at concentrations $\geq$ 1μmol/kg H_2O. Across all temperatures and pressures, the reference points for pure H_2O on the Co and Ni diagrams are located in the regions for Co_3O_4 and NiO, respectively. This means that under H_2O flow conditions, Co will form Co_3O_4 and Ni will form NiO, eventually. One strategy for improving the hydrothermal stability of Co and Ni catalysts would be to operate under reducing and slightly basic conditions that correspond to the regions of $Co_{(s)}$ and $Ni_{(s)}$.
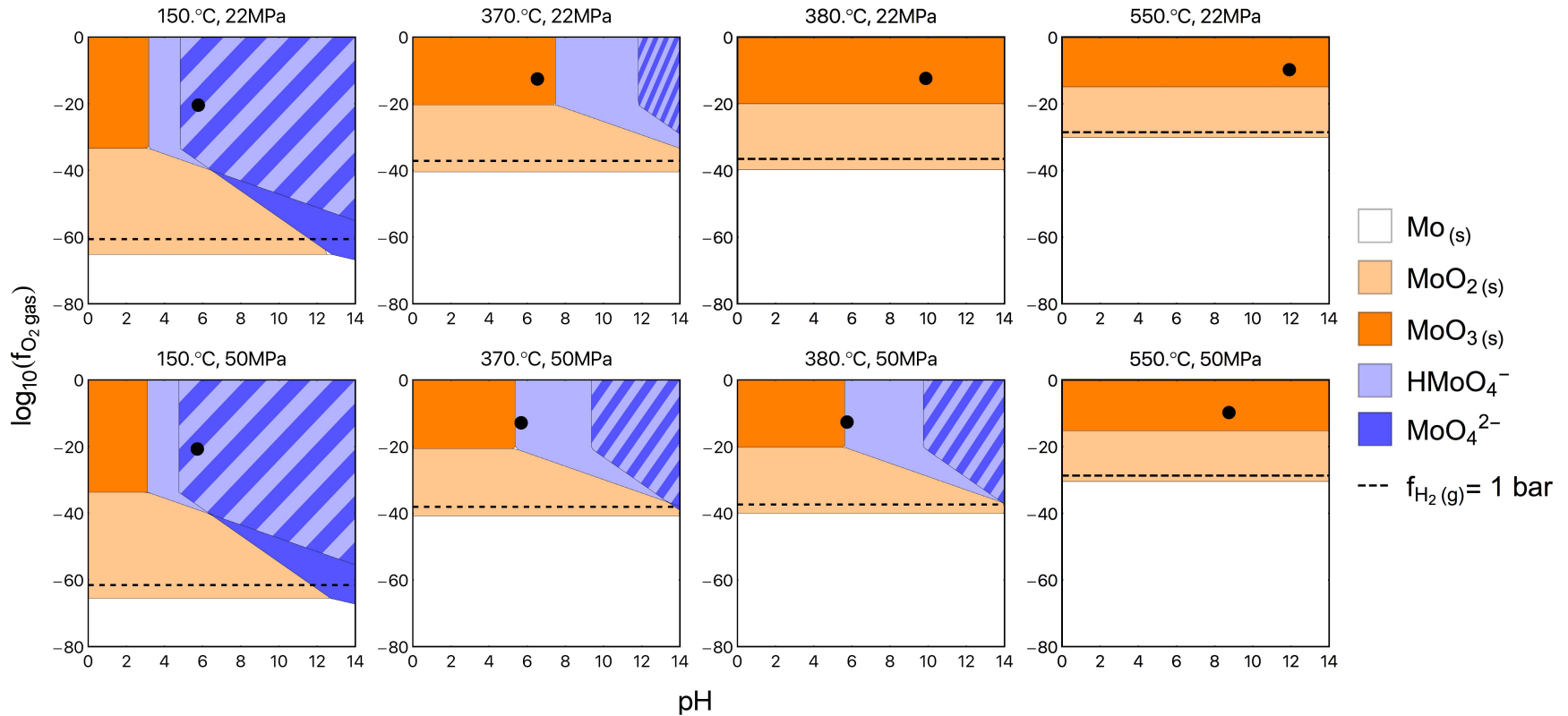
Figure 4.2: f_{O_2}-pH diagrams for Mo-H$_2$O system. f_{O_2} is in bar, and pH is in log_{10}(mol/kg H$_2$O). Boundaries for aqueous metal species are defined as $a_j = 10^{-6}$ (≈ 1 μmol/kg H$_2$O). The striped regions indicate the presence of both HMoO$_4^-$ and MoO$_4^{2-}$ with $a_j \geq 10^{-6}$. The f_{O_2} and pH values of pure H$_2$O are plotted as $\bullet$.

In the f_{O_2}-pH diagrams for the Mo-H_2O system (Figures 4.2 and E.3) and the W-H_2O system (Figure E.9), $H_2MoO_{4(aq)}$ and $H_2WO_{4(aq)}$ species were omitted from the diagrams because the regions for these aqueous neutral species dominate the entirety of the diagram and obscure analysis of the other species. At all conditions, Mo and W (and their oxides) dissolve to form significant (≥ 1 μmol/kg H_2O) amounts of $H_2MoO_{4(aq)}$ and $H_2WO_{4(aq)}$. Additionally, small increases in pH result in further formation of Mo and W anions. In pure H_2O flow, MoO_3 and WO_3 are predicted to be the thermodynamically favored oxidation states. While both Mo and W oxides have very poor hydrothermal stability, the amount of dissolution could be reduced by operating the system under reducing and acidic conditions.

Unlike the results for Co, Ni, Mo, and W, calculations for Pt, Pd and Ru (Figures E.5 to E.7) predict good hydrothermal stability in pure H_2O, other than the predicted formation of RuO_2 in pure H_2O flow. This prediction was not realized in batch experiments, which showed no oxidation of Ru after 60 minutes in SCW at 400 °C and 24-40 MPa [34]. One possible explanation for this discrepancy is that the experiment did not reach equilibrium. Oxygen diffusion in bulk Ru is slow [68, 69], so while a thin film of RuO_2 may form on the surface, subsequent oxidation of the bulk Ru would not be observed during the experiments.

The f_{O_2}-pH stability results for Ce (Figure E.1), Ti (Figures 4.3 and E.8), and Zr (Figure E.10) also predict good hydrothermal stability and $CeO_{2(s)}$, $TiO_{2(s)}$, and $ZrO_{2(s)}$ are the thermodynamically favored oxidation states in pure H_2O at all temperatures and pressures examined in this study. The dissolution of $TiO_{2(s)}$ (shown in Figure 4.3) and $ZrO_{2(s)}$ into aqueous species is insensitive to f_{O_2} and pH with the exception of conditions of high temperatures (≥ 500 °C) and relatively low supercritical pressures. One explanation for this sudden instability could be errors in the $\Delta G_{f,j}$ values for certain ions at high temperatures (≥ 500 °C) and low water densities. Specifically, the aqueous species in highest concentration at high temperatures and
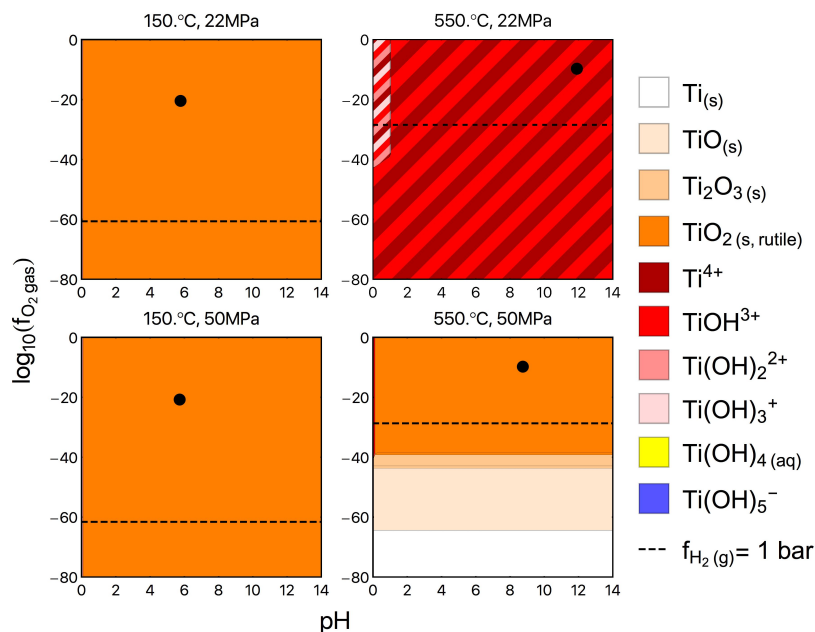
Figure 4.3: f_{O_2}-pH diagrams for Ti-H_2O system. f_{O_2} is in bar, and pH is in log_{10}(mol/kg H_2O). Boundaries for aqueous metal species are defined as $a_j = 10^{-6}$ (≈ 1 μmol/kg H_2O). The striped regions indicate the presence of multiple aqueous species with $a_j \geq 10^{-6}$. The f_{O_2} and pH values of pure H_2O are plotted as ●.

low pressures also had the highest heat capacities. This relationship suggests that the thermal contribution in the calculation of $\Delta G_{f,j}$ becomes more influential at higher temperatures and dominates the small solvent contributions at low SCW densities. While the R-HKF model can be a useful tool for predicting catalyst solubility, it does have limitations if the material-dependent parameters contain large errors and if SCW densities are well below 0.2 g/mL.

4.3.1 Engineering Hydrothermal Solutions to Enhance Catalyst Stability

We calculated the f_{O_2} and pH values of simple solutes (representative of reactants or products for some hydrothermal reactions) in equilibrium with H_2O at different temperatures, pressures, and concentrations to illustrate the effect of these species on the f_{O_2} and pH of the solution and a subset of these results are shown in Figure 4.4 (see Section 4.2.2 for methods and Figure E.11 for all results).
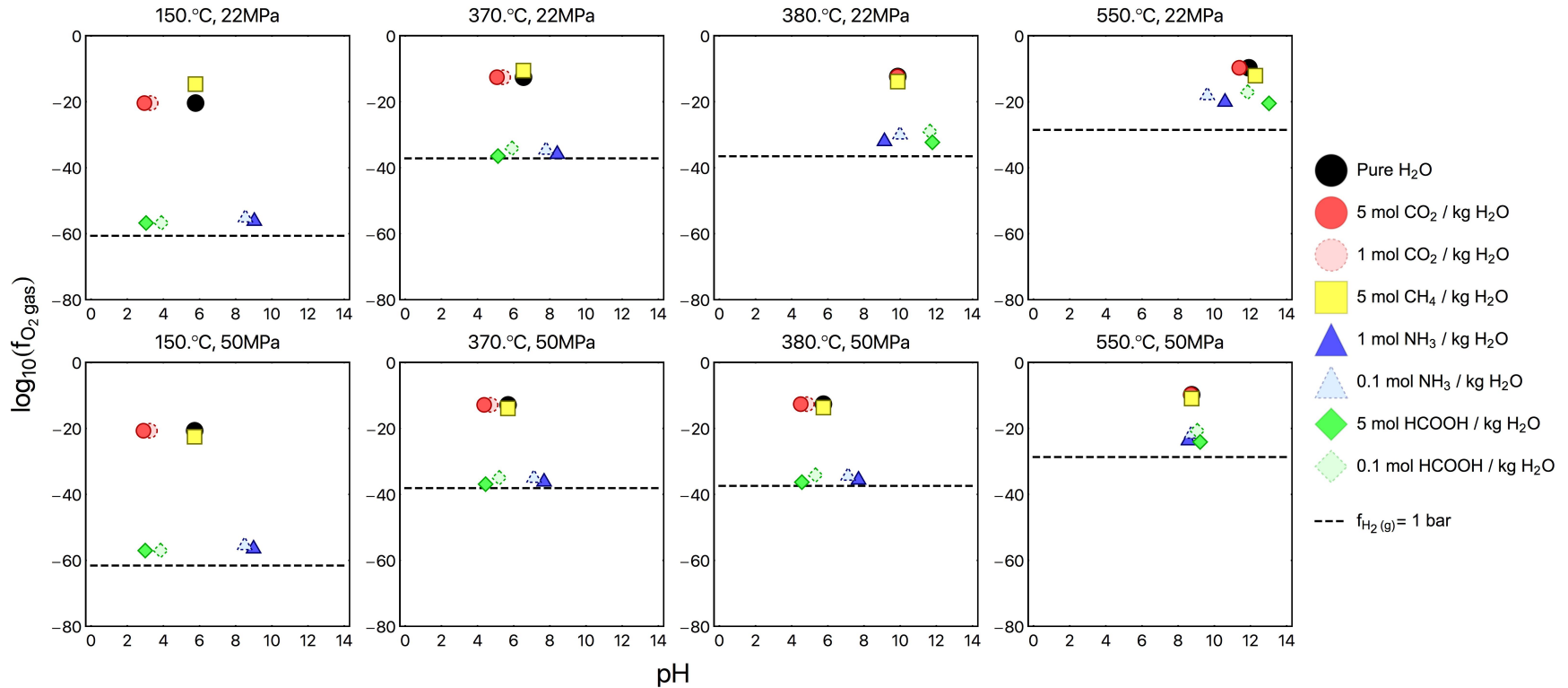
Figure 4.4: f_{O_2}-pH diagrams of aqueous solutions of CO_2, CH_4, NH_3, and formic acid (HCOOH) at equilibrium. f_{O_2} is in bar, and pH is in $log_{10}(mol/kg\ H_2O)$.

The values for these solutions were calculated by finding the reaction equilibrium for the components in the solution (e.g., CO_2 reacts with water to form carbonic acid, bicarbonate, and carbonate) and the corresponding concentrations of O_2 and H^+ at that equilibrium. Overall, the solutes that we modeled have the largest effect on the solution f_{O_2} and pH at 150 °C. As temperature increases, the solution points converge on the point for pure H_2O. The convergence is more significant at 22 MPa than 50 MPa, likely from the lower ion product and dielectric constant at 22 MPa. The presence of CO_2 decreases the pH due to the formation of carbonic acid and the presence of NH_3 increases the pH due to the formation of NH_4^+. Methane (CH_4) has very little effect on the f_{O_2} and pH of the solution, while formic acid significantly reduces the f_{O_2} and slightly decreases pH. This is because formic acid decomposes to H_2 and CO_2.

Figure 4.5 illustrates how the f_{O_2}-pH diagrams can be used to design a hydrothermal reaction system. Consider a Ni/CeO_2 catalyst for a hydrothermal reaction at 400 °C and 30 MPa. The f_{O_2}-pH diagram for Ni (Figure 4.5(a)) shows that $Ni_{(s)}$ is favored at $f_{O_2} < 10^{-30}$ bar. The f_{O_2}-pH diagram for Ce (Figure 4.5(b)) shows that $CeO_{2(s)}$ is stable at $f_{O_2} > 10^{-48}$ bar and pH > 8. By using various solutes, one can engineer a solution wherein both $Ni_{(s)}$ and $CeO_{2(s)}$ are stable. The equilibrium f_{O_2} and pH results for various aqueous solutions at 400 °C and 30 MPa are plotted in Figure 4.5(c). From the options plotted in Figure 4.5(c), a feed with > 0.1 mol/kg H_2O formic acid or ammonia will provide thermodynamically stable flow operation of Ni/CeO_2.
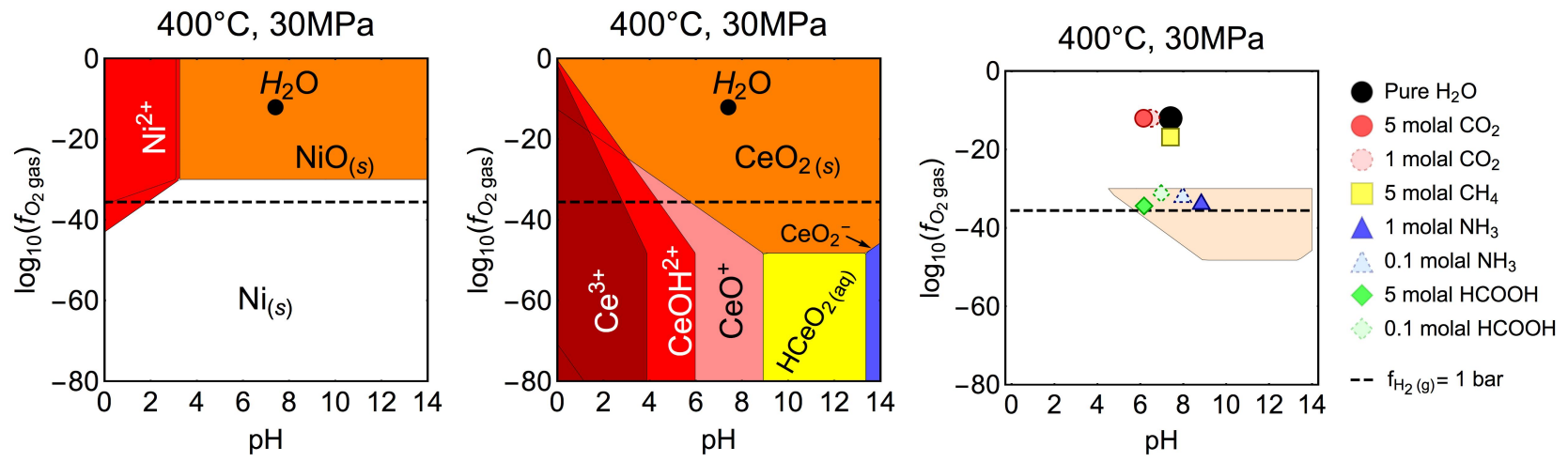
Figure 4.5: f_{O_2}-pH diagrams for Ni, CeO₂, and simple aqueous solutions at 400 °C and 30 MPa. f_{O_2} is in bar, and pH is in log_{10}(mol/kg H₂O). Boundaries for aqueous metal species in 4.5(a) and 4.5(b) are defined as $a_j = 10^{-6}$ (≈ 1 μmol/kg H₂O). In 4.5(c), the solute concentrations are in molal (mol/kg H₂O) and the shaded region indicates the stable operating conditions for a Ni/CeO₂ catalyst.

4.4   Conclusion

The f_{O_2}-pH diagrams predicted phase changes of the catalytic materials in response to changes in the composition of hydrothermal reaction solutions. At subcritical conditions, dissolution of Co, Ni, and their oxides will increase with decreasing pH. Therefore, one strategy for decreasing dissolution of Co and Ni catalysts is to operate under slightly basic conditions. On the other hand, dissolution of Mo and W oxides at subcritical conditions will increase with increasing pH, so decreasing pH will decrease dissolution of Mo and W catalysts. The dissolution of Pt, Pd, Ru, CeO_2, TiO_2, and ZrO_2 catalysts is less sensitive to changes in pH or f_{O_2} and is expected to be low (≤ 1 μmol/kg H_2O at most hydrothermal reaction conditions. Together with f_{O_2} and pH calculations for different solutes in aqueous solution, these diagrams provide the information needed to design hydrothermal solutions (e.g., temperature, pressure, and solute concentration) that improve the catalyst stability.

CHAPTER V

Catalyst Stability During Hydrodenitrogenation in Supercritical Water

In this chapter, the thermodynamic modeling techniques described in earlier chapters were used to identify hydrothermally stable catalytic materials for HDN reactions in SCW. Among the materials assessed with the model, Pt/TiO_2 was chosen for further study as it is not predicted to undergo dissolution or changes in oxidation in the reaction environment. The stability and activity of the Pt/TiO_2 catalyst in the reaction environment was then systematically evaluated in a flow reactor and experiments were designed to isolate specific interactions between the catalyst, the SCW, and the reagents. The catalyst did not exhibit any evidence of oxidation or dissolution during experiments, however HDN activity was only observed for propylamine and no reaction was observed for pyridine. During several experiments, the stainless steel tubing between the reactor inlet and the catalyst bed experienced corrosion and Fe was deposited on the catalyst. Although Pt/TiO_2 did not exhibit the desired HDN activity, the design of experiments applied in this chapter was successful for identifying variables that could be improved for future hydrothermal HDN reactions.

5.1 Introduction

Algae biocrude is an energy-dense material produced from the hydrothermal liquefaction (HTL) of microalgae. Water at HTL conditions (T $\geq$ 200 °C and P $\geq$ 1.6 MPa) has a significantly higher solubility for organic compounds and a higher ion product than water at ambient temperature. Combined, these properties facilitate acid- and base-catalyzed reactions that break down lipids, carbohydrates, proteins, and other algal biomolecules into biocrude containing fatty acids, hydrocarbons, indole derivatives, and phenols [50]. The biocrude is viscous and contains $10-20$ wt% N, O, and S heteroatoms. These heteroatoms must be removed to prevent the formation of NO_x and SO_x upon combustion, to reduce the total acid number, and to increase the energy density. To improve the properties of biocrude while preserving the energy content of the oil, a catalytic treatment of the biocrude in the hydrothermal environment has been proposed. Different catalysts in SCW have been shown to reduce heteroatom content in algae biocrude and lower viscosity and total acid number [5, 70, 71]. The complexity of biocrude makes it difficult to discern the reaction pathways and networks when working with algae biocrude directly. Consequently, studies with model compounds have been undertaken to probe reaction pathways, kinetics, and catalyst stability.

Catalytic hydrothermal liquefaction of soy protein concentrate at 250-400 °C was performed in batch reactors to simplify the analysis of denitrogenation reactions within the protein fraction of algal biomass [72]. The authors screened various catalysts (HZSM-5, sulfided CoMo/γ-Al$_2$O$_3$, Mo$_2$C, MoS$_2$, and 5 wt% Pt, Pd, Ru, supported on carbon or Al$_2$O$_3$) and found that the supported Pt, Pd, and Ru catalysts produced crude bio-oils with less heteroatom content than non-catalytic liquefaction under identical conditions. Additional experiments with Ru/C showed that longer reaction times, higher temperatures, and higher catalyst loadings produced biocrudes with lower nitrogen contents, however increasing H$_2$ loading had a negligible effect

on the biocrude yield. Although the screening experiments identified active catalytic materials for HDN of soy protein and several important process conditions for optimization, the stability and deactivation of the catalyst is unknown since the catalysts were not characterized or reused.

Model compound studies with quinoline in H_2O at 350-450 °C and 25-35 MPa [73] and pyridine in H_2O at 250-400 °C and 20 MPa [39] offer further insight into catalytic HDN of biocrude in hydrothermal media as these heterocyclic nitrogen-containing hydrocarbons and their derivatives are present in algal bio-oils [38, 48, 50]. The authors of both studies observed hydrogenation of the aromatic ring as the first step in the reaction pathway, followed by ring opening and then nitrogen removal. H_2 for the HDN of quinoline in SCW was generated in situ through partial oxidation of heptane and the authors observed up to 85% total nitrogen reduction after batch reactions with a sulfided $NiMo/\gamma\text{-}Al_2O_3$ catalyst [39]. Catalyst deactivation, however, was observed after only one hour and complex oxides were detected in the catalyst. In addition, competitive adsorption between CO, quinoline, and other intermediates on the catalyst surface decreased HDN rates.

The activities of Pt/C, Pd/C, Ru/C, Rh/C, sulfided Pt/C, $Pt/\gamma\text{-}Al_2O_3$, sulfided $CoMo/\gamma\text{-}Al_2O_3$, Mo_2C, MoS_2, and PtO_2 for HDN of pyridine were also tested in batch reactors [39], however the H_2 for these reactions was supplied by pressurizing the batch reactors with gaseous H_2 prior to reaction. While nearly all the catalysts that were tested showed high pyridine conversion, $Pt/\gamma\text{-}Al_2O_3$ had the greatest selectivity for C_{4+5} products. Additional experiments with the $Pt/\gamma\text{-}Al_2O_3$ catalyst varied batch holding time, temperature, catalyst loading, H_2 pressure, and water density and the authors observed a modest loss in activity upon reuse, but no further catalyst characterization was performed.

To date, little is known about catalyst stability for HDN reactions in SCW. Much of the research focus on catalyst activity and stability for heteroatom removal from

biocrude in SCW has focused on catalytic hydrodeoxygenation (HDO) while HDN is much less studied [5, 12]. Catalytic HDN of quinoline [73], pyridine [39], and proteins [72] in SCW identified active catalysts and batch process conditions for nitrogen removal, however the stability of the catalysts was only determined by measuring activity loss upon re-use of the catalyst in secondary batch reactions.

In this work, we used thermodynamic modeling to select a stable catalyst (no dissolution or changes in oxidation) for HDN of pyridine and propylamine in SCW at 380-500 °C and 22-38 MPa. We modeled the stability of Ni, Co, Mo, W in hydrothermal HDN reaction solutions because NiMo, CoMo, NiW, and CoW catalysts are active catalysts for HDN of vapor phase petroleum feeds [74–76]. We also evaluated Pt for an active metal because it was shown to be active for hydrothermal HDN chemistry [39, 72] even though pure Pt is rarely used for vapor phase HDN due to its high activity for additional C-C bond breaking and because it can be poisoned by basic-N compounds [74]. The stabilities of TiO_2 and CeO_2 at SCW conditions for HDN reactions were also evaluated to identify an appropriate support for the active metal.

Using the results of thermodynamic stability analysis in this chapter, we selected Pt/TiO_2 as a stable catalyst candidate for HDN in SCW. The stability and activity of Pt/TiO_2 in the HDN reaction environment were systematically evaluated in a flow reactor. Experiments were designed to isolate specific interactions between the catalyst, the SCW, and the reagents. Formic acid (HCOOH) was used to supply H_2 for the reaction as it rapidly decomposes to H_2 and CO_2 in sub- and supercritical water and was successfully used for HDO of o-cresol [77]. Others have also shown that in situ generation of hydrogenating species by addition of CO or HCOOH was even more effective than added H_2 itself [78]. In addition to testing the catalyst activity in flow experiments with pyridine and propylamine, Pt/TiO_2 stability was monitored in the flow reactor using simple solutions consisting of either 0.4 mol NH_3/kg H_2O or 0.06

mol NH_3/kg H_2O and 0.4 mol HCOOH/kg H_2O. These solutions were designed to test the stability of the catalyst at the expected pH and f_{O_2} of the HDN reactions in SCW without the carbonaceous reagents present. The elimination of many carbonaceous species in these simple solutions allowed us to characterize the catalyst stability without the possibility of coke formation and measure aqueous metal content in the effluent without damaging the ICP-OES instrument. The use of simplified reaction solutions to study hydrothermal catalyst stability described in this work is a new approach for separating influences of reagents and solvent properties on the catalyst stability.

5.2 Materials and Methods

5.2.1 Thermodynamic Calculations for Catalyst Selection

Oxygen fugacity (f_{O_2})-pH diagrams were constructed to predict the stability of different catalytic materials (Co, Ni, Mo, W, Pt, CeO_2, and TiO_2) during HDN reactions in SCW at 380-500 °C and 22-38 MPa. Methods for constructing the diagrams and calculating pH and f_{O_2} of aqueous solutions are described in Sections 4.2.1 and 4.2.2.

5.2.2 Catalyst Synthesis and Characterization

From the results of the thermodynamic stability calculations, Pt/TiO_2 was selected as a stable catalyst material for HDN chemistry in SCW. For synthesis of Pt/TiO_2, the titanium dioxide (TiO_2, Alfa Aesar) support was sieved to a particle size of 170-250 μm in diameter and calcined in air at 500 °C for 10 hours. The surface area and pore volume of the calcined support were determined by N_2 physisorption using a Micromeritics ASAP 2020. Platinum in the form of $H_2PtCl_6 \cdot 6\,H_2O$ (Sigma Aldrich) was deposited onto the support using a dry impregnation method, which has been previously described [79]. In summary, enough $H_2PtCl_6 \cdot 6\,H_2O$ for 6 Pt atoms

67

per nm^2 of TiO_2 surface was dissolved in an amount of DI water equal to the TiO_2 pore volume. The solution was added to the TiO_2 drop-wise and then the material was dried under vacuum at 110 °C for 12 hours and calcined in air at 450 °C for 4 hours.

The TiO_2 and Pt/TiO_2 recovered from the stability and reactivity experiments were characterized with XRD, thermogravimetric analysis (TGA), and CO chemisorption. The XRD data were collected using a Rigaku 600 Miniflex set at 40 kV and 15 mA (K_α = 1.5406 Å) and the diffraction patterns were analyzed using Jade. Mass data for the TGA were collected on a TA Instruments Q50 while the sample was heated in air (90 mL/min) to 1,000 °C with a ramp rate of 10 °C/min. Surface Pt was measured with CO chemisorption. First, the catalyst was pretreated in a flow of H_2 at 300 °C for 60 minutes. Surface H_2 was then removed by flowing N_2 across the material at 300 °C for 60 minutes. The catalyst was cooled to 35 °C in flowing N_2 and then 0.5 mL of 5% CO/N_2 was pulsed across the catalyst in 5 minute intervals. The composition of the effluent gas was analyzed with mass spectrometry to quantify the CO adsorption on the surface.

5.2.3 Flow Experiments

The hydrothermal stability of Pt/TiO_2 in simple solutions of NH_3 and HCOOH and real HDN solutions of HCOOH and propylamine or pyridine was tested in a flow reactor which has been previously described [77]. For this study, modifications were made to the flow reactor which included reduction of the inlet tubing diameter from 1/8 in. o.d. to 1/16 in. o.d. and the sandbath used to heat the reactor was replaced with a vertical tube furnace. For each experiment, Pt/TiO_2 was loaded into a 4 in. long catalyst bed constructed from 1/4 in. o.d. 316 S.S. tubing. TiO_2 was used as diluent in the catalyst bed for different Pt/TiO_2 loadings. Hastelloy frits with 5 μm pores were installed at both ends of the catalyst bed to keep the catalyst

in place. Once the catalyst bed was installed in the reactor, the assembly was leak tested with H_2 at 200 bar (the highest pressure available from the H_2 regulator). The catalyst was reduced in the reactor by flowing H_2 at 300 °C and 1 atm for 60 minutes. After pretreatment, the catalyst was heated in N_2 to the experiment set point temperature. Aqueous solutions were fed into the reactor to build pressure once the desired temperature was achieved.

Solutions consisting of either 0.4 mol NH_3/kg H_2O or 0.06 mol NH_3/kg H_2O and 0.4 mol formic acid (HCOOH)/kg H_2O were prepared to test the stability of the catalyst at the expected pH and f_{O_2} of the HDN reactions in SCW. These solutions allowed us to characterize the catalyst stability without possible poisoning or coke formation from the reagents and measure any metal content in the effluent without damaging the ICP-OES instrument with large carbonaceous species. The NH_3/HCOOH solution experiments were run for 6 hours at 38 MPa and 380 or 500 °C. These solutions were fed into the reactor at a constant flow rate of 3 mL (STP)/min which corresponded to Reynolds numbers in the catalyst bed of 30 and 60 at 380 and 500 °C, respectively. A solution of 1% HNO_3/H_2O was fed at 1 mL/min into the effluent after the heat exchanger and before the back pressure regulator. The purpose of the nitric acid solution was to prevent precipitates from clogging the reactor and allow accurate measurement of aqueous metal content in the reactor effluent by stabilizing any aqueous metals in solution prior to depressurization.

At the completion of the experiment, the catalyst was dried overnight in N_2 and characterized with XRD, TGA, and CO chemisorption. An Agilent 6890N gas chromatograph with a Carboxen 1000 packed column and a thermal conductivity detector (GC-TCD) was used to separate and analyze the H_2 and CO_2 (produced from the formic acid) using a procedure outlined previously [50]. NH_3 concentrations in the effluent were measured using HACH reagent kits and a GENESYS 20 Visible Spectrophotometer. Analytical NH_4OH standards were used to calibrate absorbance with

NH_3 concentration. The remaining solution from the reactor (1.4-1.5 L) was distilled to approximately 20 mL and analyzed for aqueous Pt and Ti using ICP-OES. During ICP-OES analysis, characteristic wavelengths for Fe, Ni, and Mo were also analyzed to test for corrosion of the 316 S.S. tubing. An aqueous Cu internal standard was used to compare the metal concentrations in solution before and after distillation.

Catalyst pretreatment and reactor preparation for HDN experiments at 420 °C and 30 MPa in the flow reactor were executed in a similar method. A solution of 0.2 mol formic acid/kg H_2O was used generate H_2 for the reaction in situ. Aqueous solutions of 10 wt% pyridine or propylamine reagents were fed to the reactor and mixed with the formic acid solution just prior to the catalyst bed. The flow rates of the formic acid and reagent feeds were controlled to ensure molar ratios of 5:1 for formic acid and pyridine or 1:1 for formic acid and propylamine. Tetrahydrofuran was fed into the reactor effluent just prior to the back pressure regulator to prevent separation of aqueous and organic phases. An Agilent 6890N gas chromatograph equipped with a Porapak packed column and a thermal conductivity detector (GC-TCD) separated and analyzed gaseous products directly from the reactor outlet. Liquid samples were collected every 30 minutes and analyzed at a later time by gas chromatography with mass spectrophotometer (GC-MS).

5.3   Results and Discussion

Thermodynamic modeling results in Section 5.3.1 were used to identify Pt/TiO_2 as a hydrothermally stable catalyst candidate for HDN reactions. Section 5.3.2 presents experimental results for the stability of Pt/TiO_2 in SCW solutions of HCOOH and NH_3. These solutions were designed to simulate the f_{O_2} and pH conditions of real hydrothermal HDN reactions but without the possibility of catalyst coking or poisoning from the reaction. Section 5.3.3 reports the activity of Pt/TiO_2 for HDN of pyridine and propylamine in SCW at 420 °C and 30 MPa.

5.3.1 Predicted Catalyst Stability during HDN in SCW

We used f_{O_2}-pH diagrams to evaluate the thermodynamic stability of Ni, Co, Mo, W, Pt, TiO_2, and CeO_2 at SCW conditions relevant for HDN chemistry. The equilibrium f_{O_2} and pH values of different aqueous solutions of HCOOH and NH_3 were calculated as models for real hydrothermal solution conditions containing H_2 and basic N-containing compounds. Diagrams for Ni, Co, Mo, W, and CeO_2 in Figure 5.1 identify reaction conditions with HCOOH and NH_3 that may result in oxidation and dissolution of these materials. The diagram for CeO_2 in Figure 5.1 predicts Ce dissolution during HDN reactions at 380 °C and 38 MPa. At most HDN reaction conditions from 380-500 °C and 22-38 MPa, Ni, Co, Mo, and W are expected to eventually form oxides. From the f_{O_2} of the modeled solutions, the amount of H_2 that is generated in situ from formic acid (HCOOH) is insufficient to inhibit this metal oxidation. In addition, Mo and W (and their oxides) are expected to form significant $H_2MoO_{4(aq)}$ and $H_2WO_{4(aq)}$ in SCW. These species were omitted from the diagrams, however, as they have concentrations ≥ 1 μmolal at all SCW conditions and obscure analysis of the other phases. As a result of the predicted oxidation or dissolution of Ni, Co, Mo, W, and CeO_2 during HDN in SCW, these materials were no longer considered for use as catalysts for the flow reaction experiments in this study. Future studies, however, could examine the rates of these oxidation and dissolution mechanisms and determine whether the hydrothermal stability of these materials is sufficient enough for practical applications.

Figures 5.2 and 5.3 show f_{O_2}-pH diagrams for Pt and TiO_2, respectively, with f_{O_2} and pH coordinates plotted for different mixtures of HCOOH and NH_3 to illustrate the changes in the solution as HDN reactants are consumed and NH_3 is formed. In these diagrams, Pt and TiO_2 are both predicted to be stable at all SCW conditions that were modeled to represent HDN chemistry and as a result, a Pt/TiO_2 catalyst was selected for further stability and activity characterization in a SCW flow reactor.
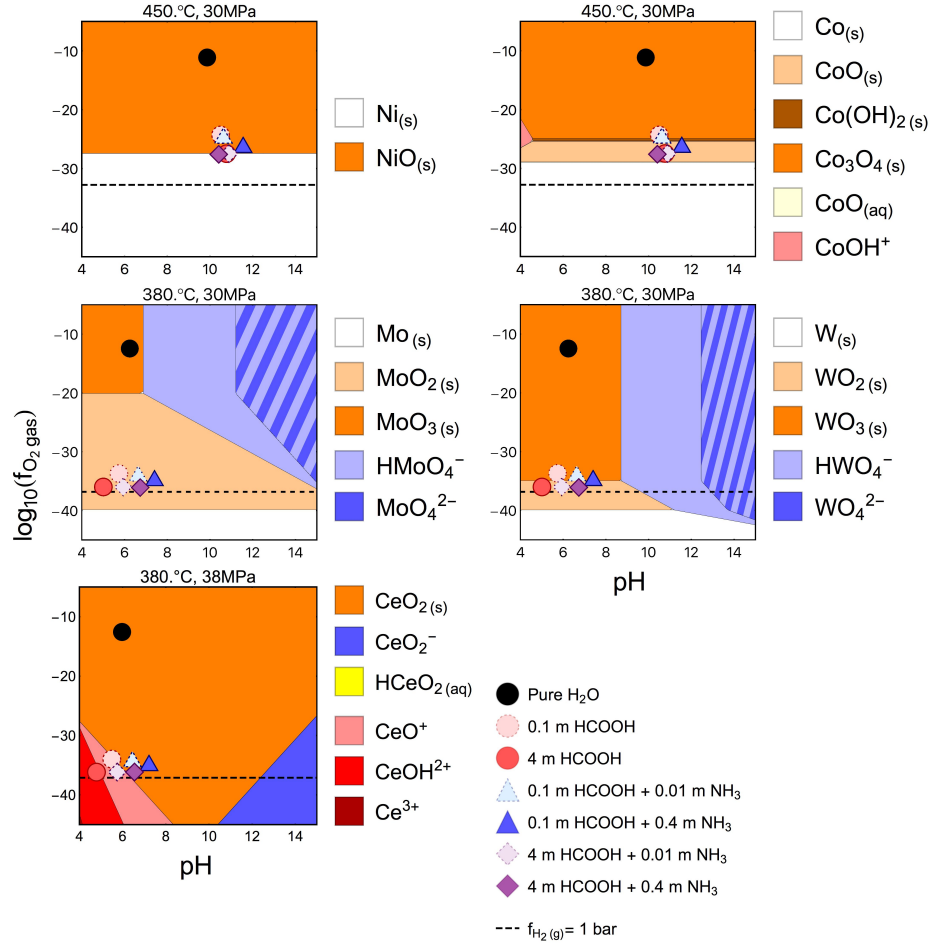
Figure 5.1: f_{O_2}-pH diagrams of Ni, Co, Mo, and W at SCW conditions which predict oxidation or dissolution during HDN reactions. f_{O_2} is in bar, and pH is in log_{10}(mol/kg H_2O). Boundaries for aqueous metal species are defined as $a_j = 10^{-6}$ (≈ 1 μmol/kg H_2O) so within the shaded regions $a_j \geq 10^{-6}$. Striped regions indicate the presence of multiple aqueous metal species (e.g. $HMoO_4^-$ and MoO_4^{2-}) with $a_j \geq 10^{-6}$. The equilibrium f_{O_2} and pH values of different aqueous solutions of HCOOH and NH_3 (m is mol/kg H_2O) are plotted as circle, triangle, and diamond markers on each diagram. For diagram clarity, H_2MoO_{4aq} and H_2WO_{4aq} were omitted as these species have concentrations ≥ 1 μmolal at all SCW conditions.
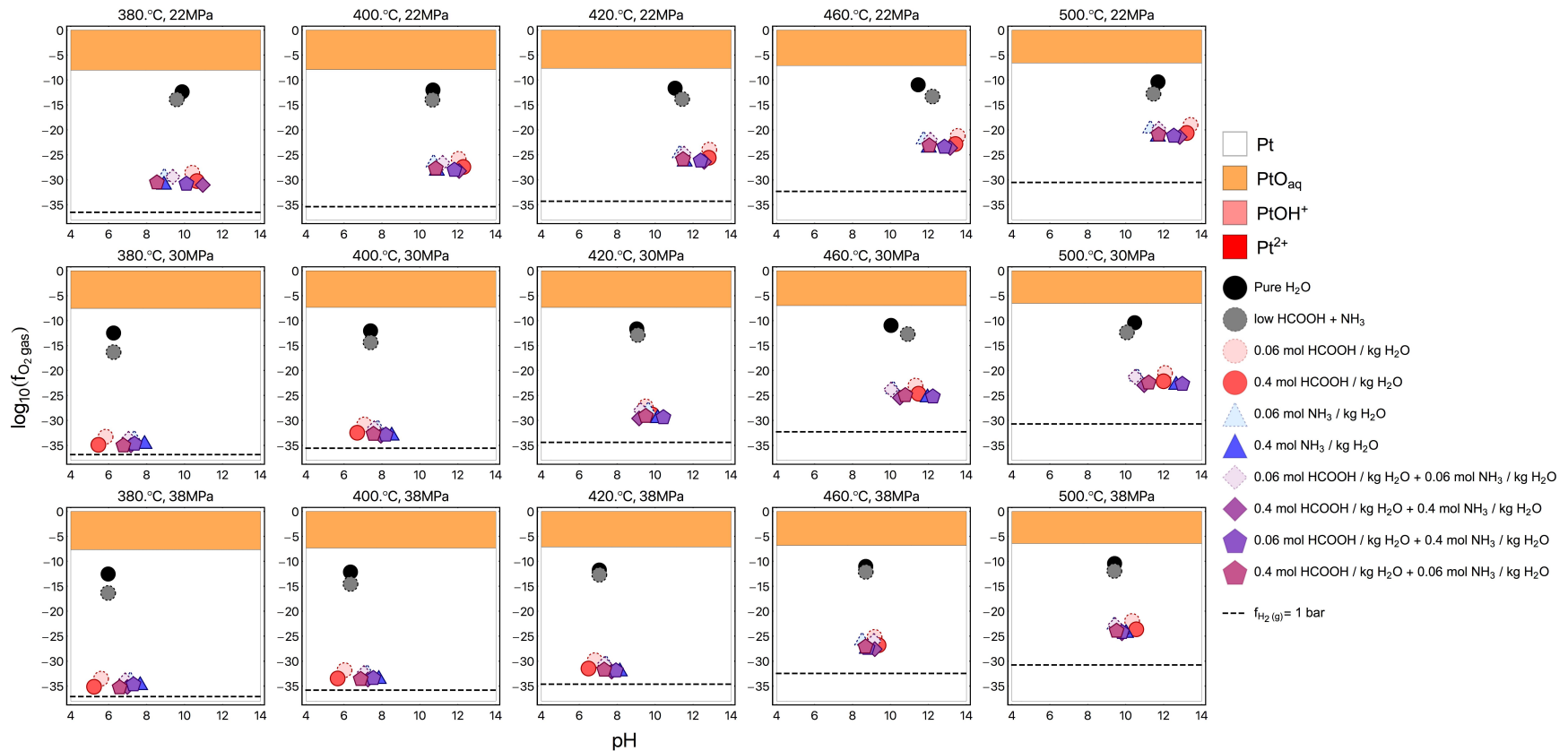
Figure 5.2: f_{O_2}-pH diagrams diagrams showing Pt stability at hydrothermal HDN reaction conditions. f_{O_2} is in bar, and pH is in log_{10}(mol/kg H_2O). Boundaries for aqueous metal species are defined as $a_j = 10^{-8}$ (≈ 0.01 μmol/kg H_2O) and plot markers represent equilibrium f_{O_2} and pH values of solutions with various NH_3 and HCOOH concentrations. The low HCOOH + NH_3 solution marker represents HCOOH and NH_3 concentrations of 10^{-10} mol/kg H_2O.
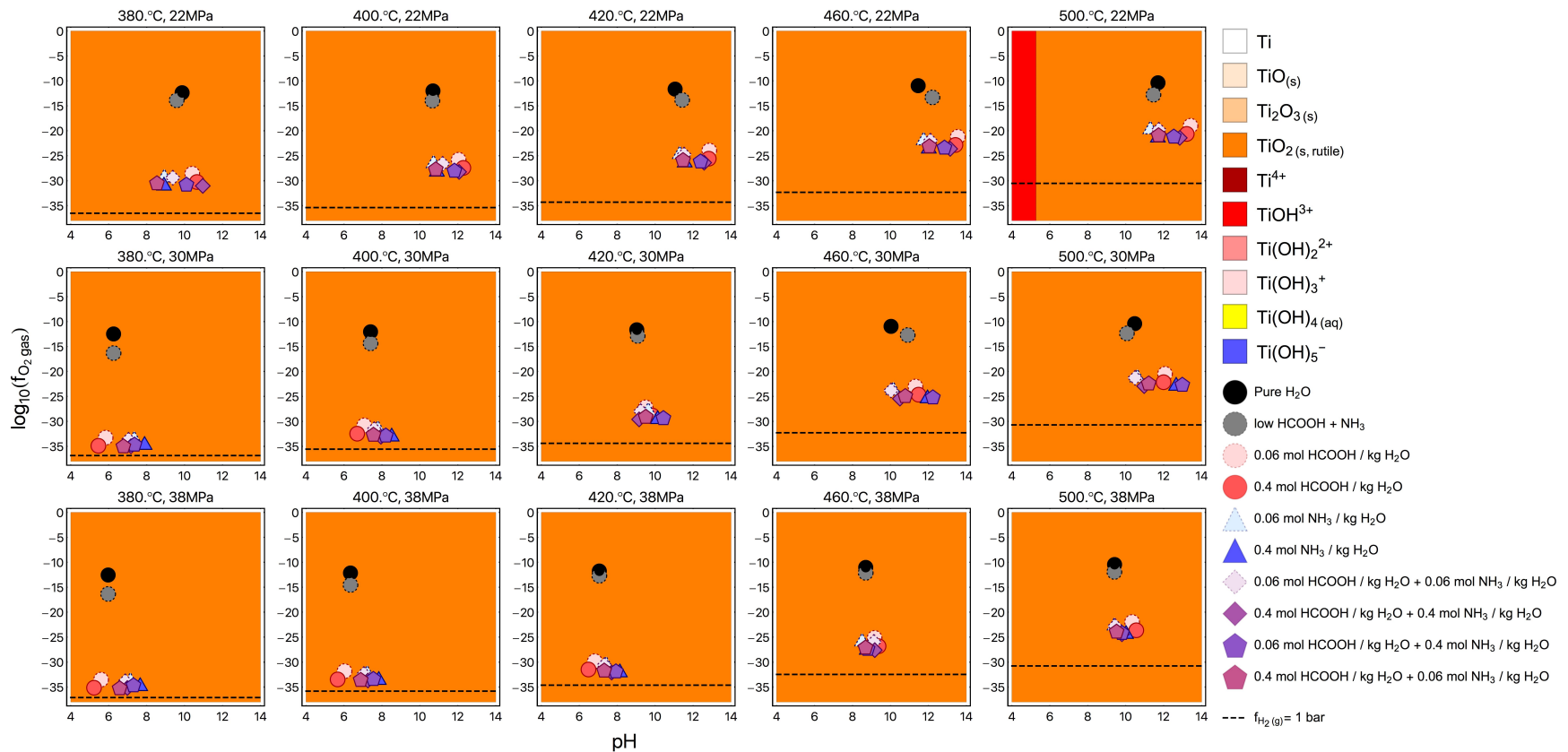
Figure 5.3: f_{O_2}-pH diagrams diagrams showing TiO_2 stability at hydrothermal HDN reaction conditions. f_{O_2} is in bar, and pH is in log_{10}(mol/kg H_2O). Boundaries for aqueous metal species are defined as $a_j = 10^{-8}$ (≈ 0.01 μmol/kg H_2O) and plot markers represent equilibrium f_{O_2} and pH values of solutions with various NH_3 and HCOOH concentrations. The low HCOOH + NH_3 solution marker represents HCOOH and NH_3 concentrations of 10^{-10} mol/kg H_2O.

5.3.2   Catalyst Stability in Solutions of Formic Acid and Ammonia

Table 5.1 shows results from the flow experiments with Pt/TiO_2 in aqueous NH_3 and $NH_3/HCOOH$ solutions. For all experiments, NH_3 recovery was approximately 75%. Small amounts of H_2 were produced during the experiments with 0.4 mol NH_3/kg H_2O, likely from decomposition of NH_3 to N_2 and H_2, however the amount of H_2 measured does not account for the missing NH_3. From analysis of the Henry's Law constants for NH_3 in water [51], it is more likely that NH_3 losses occurred from evaporation. We were unable to identify or quantify NH_3 using the GC-TCD methods for analysis of the reactor gas, however the Henry's Law constants for NH_3 in water [51] estimate equilibrium NH_3 pressures of 0.004-0.02 bar. If vapor-liquid equilibrium is achieved at these NH_3 partial pressures, the molar flow rate of NH_3 in the N_2 gas (16 mL/min), which served as an internal standard, would be greater than the molar flow rate of NH_3 in the aqueous solution (3 mL/min).

During analysis of aqueous metal content, the Cu internal standards confirmed that aqueous metals remained in solution during distillation. Although distillation allowed us to increase aqueous metal concentrations by a factor of 60-80, Ti concentrations were below the limits of detection for the ICP-OES and Pt concentrations were $\leq 2\%$ of the total Pt loaded into the reactor. Measurable concentrations of Fe and Ni were detected, however, and their concentrations are tabulated in Table 5.1. The Fe and Ni likely originated from corrosion of the 316 stainless steel reactor tubing. Similar corrosion products have been reported for hydrothermal experiments with HCOOH [80, 81]. Visual inspection of the reactor tubing after the flow experiment at 380 °C with 0.4 m HCOOH and 0.06 m NH_3 confirmed the presence of reddish brown solid deposits at the exit of the pre-heating zone. The Fe and Ni were likely corroded at a section of the tubing where the solution temperature was subcritical and the pH at that temperature was very low. The damaged tubing was replaced and a 10% nitric acid solution was used in-between flow experiments to clean and

	0.4 m NH$_3$		0.4 m HCOOH + 0.06 m NH$_3$	
T (°C)	380	500	380	500
NH$_{3,\text{feed}}$ [a]	1.2	1.2	0.18	0.18
HCOOH$_{\text{feed}}$ [a]	0	0	1.2	1.2
NH$_3$ Recovery (%)	74.7 ± 0.2	78.1 ± 0.2	77.3 ± 0.3	75.8 ± 0.3
mmol H$_2$/min	0.003±0.001	0.004±0.001	0.32 ± 0.01	0.34 ± 0.07
mmol CO$_2$/min	n.d.[b]	n.d.	0.27 ± 0.01	0.26 ± 0.04
μmol Pt/L	0.4 ± 0.01	0.03 ± 0.08	0.3 ± 0.1	0.08 ± 0.09
μmol Ti/L	0.1 ± 0.3	0.1 ± 0.3	−0.05 ± 2	−0.04 ± 1
μmol Fe/L	2 ± 0.01	0.3 ± 0.2	20 ± 0.1	1 ± 0.05
μmol Ni/L [c]	3	2	4	2
μmol Mo/L	0.08 ± 0.02	0.3 ± 0.01	0.1 ± 0.02	0.07 ± 0.001

[a] mmol/min [b] none detected [c] Error not available from single wavelength analysis

Table 5.1: Quantities of gaseous products, aqueous metals, and NH$_3$ measured in the product streams from flow experiments of Pt/TiO$_2$ in SCW solutions of NH$_3$ and HCOOH. For all experiments, Pt/TiO$_2$ loading in the reactor was 250 mg, SCW pressure was 38 MPa and the solution flow rate was 3 mL/min (STP) which corresponded to Re of 30 and 60 at 380 °C and 500 °C, respectively.

re-passivate the stainless steel as per manufacturer recommendations.

To further study the corrosion at the reactor inlet, f_{O_2}-pH diagrams for Fe at 150 and 370 °C and 22 and 40 MPa were constructed (Figure 5.4). These diagrams show the influence of a 0.4 mol/kg H$_2$O formic acid feed on the stability of Fe, the major component of stainless steel tubing. Although stainless steel is composed of additional elements including Cr, Ni, and Mo that improve the corrosion resistance of Fe at different conditions, the f_{O_2}-pH diagrams in Figure 5.4 provide a simple analysis for studying corrosion of the reactor tubing. The diagrams in Figure 5.4 for Fe at 150 °C and 22-40 MPa show that at equilibrium, Fe^{2+} and FeOH$^+$ are present in concentrations greater than 1 μmol/kg H$_2$O. When the solution temperature is increased to 370 °C, however, the concentrations of these ions drop below 1 μmol/kg H$_2$O and the feed conditions shift toward Fe$_3$O$_4$. This result is in agreement with the observation of corrosion in the reactor tubing prior to the catalyst bed.
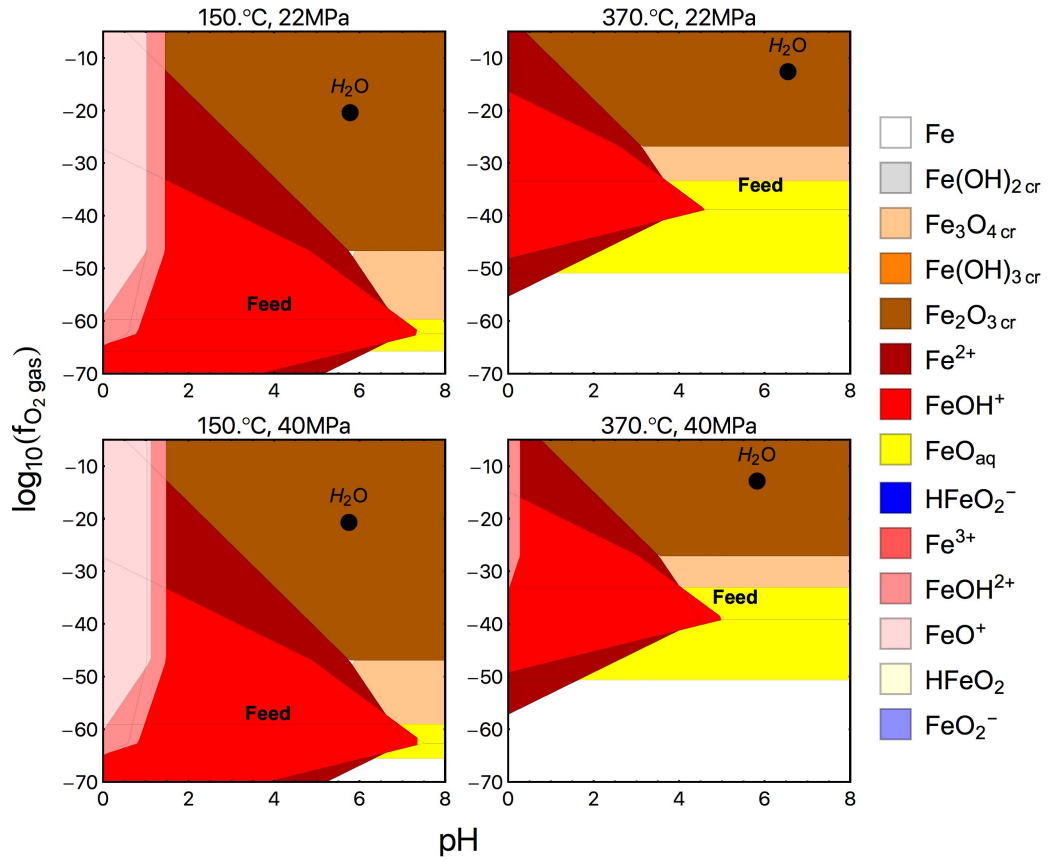
Figure 5.4: f_{O_2}-pH diagrams diagrams showing Fe stability in the preheating section of the SCW reactor. f_{O_2} is in bar, and pH is in $log_{10}(\text{mol/kg H}_2\text{O})$. Boundaries for aqueous metal species are defined as $a_j = 10^{-6}$ ($\approx$ 1 μmol/kg H$_2$O). Coordinates labeled "Feed" represent the f_{O_2} and pH values of the 0.4 m HCOOH feed solutions.

Sample ID	T ($^{\circ}$C)	[NH$_3$]^a	[HCOOH]^a	Pt atoms/nm^2	Dispersion^b
TiO$_2$	-	-	-	0	-
A	-	-	-	0.22	0.37
B	380	0.4	0	0.01	0.02
C	500	0.4	0	0.04	0.07
D	380	0.06	0.4	0.02	0.04
E	500	0.06	0.4	0 ^{c}	-

^{a} mol/kg H$_2$O ^{b} surface Pt atoms/total Pt atoms ^{c} Negligible CO uptake

Table 5.2: Pulse CO chemisorption measurements of Pt dispersion on bare TiO$_2$ support and fresh (sample A) and used (samples B-E) Pt/TiO$_2$ recovered after 6 h flow experiments in SCW solutions of NH$_3$ and HCOOH at 38 MPa. NH$_3$ and formic acid (HCOOH) feed concentrations in mol/kg H$_2$O.

Table 5.2 lists the results of the pulse CO chemisorption measurements. The fresh catalyst had a measured surface coverage of 0.22 Pt atoms/nm^2 which corresponds to a dispersion of 0.37 (relative to the Pt loading during dry impregnation). A baseline experiment with the TiO$_2$ support shows that CO uptake was nonexistent and therefore the CO adsorption on the fresh Pt/TiO$_2$ was entirely from surface Pt. The measured surface Pt significantly decreases after the flow experiments in the NH$_3$ and HCOOH solutions, however the XRD data in Figure 5.5 confirmed that Pt was still present in the material.

One possible explanation for the decreased CO uptake on the catalysts after the flow stability experiments in the NH$_3$ and HCOOH solutions is deposition of Fe atoms from the corrosion of the reactor tubing onto the surface Pt, thereby blocking access to the Pt site. The XRD pattern of the Pt/TiO$_2$ after exposure to 0.4 m HCOOH and 0.06 m NH$_3$ at 380 $^{\circ}$C (sample D) revealed new peaks consistent with α-Fe$_2$O$_3$. TGA data in Figure 5.6 of the Pt/TiO$_2$ samples after exposure to the HCOOH solution (samples D and E) show an increase in mass with increasing temperature, contrary to the behavior of the fresh Pt/TiO$_2$ (sample A). The mass increase is due to addition of O$_2$ to the sample from the air flowing through the TGA furnace. Figure 5.7 shows XRD patterns of fresh Pt/TiO$_2$ (sample A) and sample D before and after TGA.
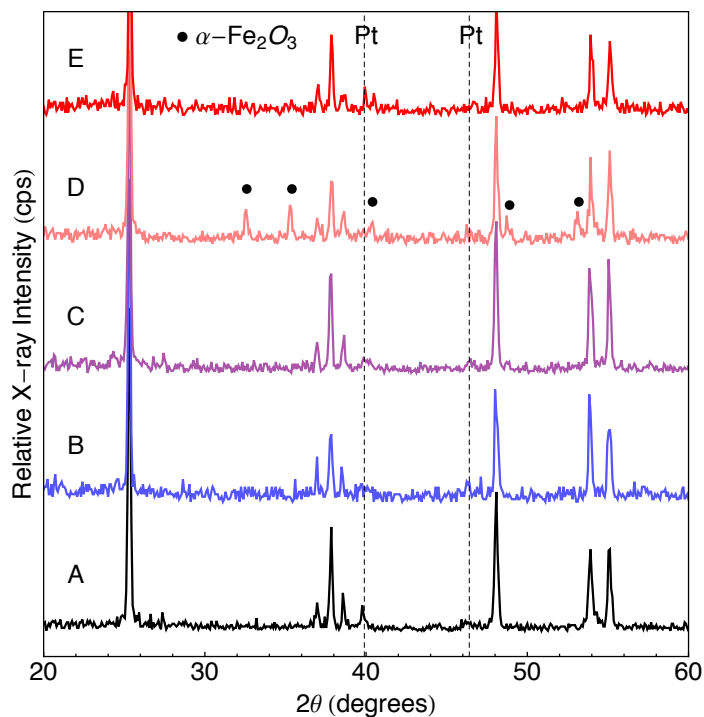
Figure 5.5: XRD patterns of TiO_2, fresh Pt/TiO_2 (A), and Pt/TiO_2 samples after SCW flow experiments in NH_3 and HCOOH solutions (B-E). Unlabeled peaks correspond to anatase TiO_2. Experimental conditions for the labeled sample profiles are defined in Table 5.2.

Comparison of the diffraction patterns before and after TGA shows a loss of α-Fe_2O_3 peaks, growth of Pt peaks, addition of rutile TiO_2 peaks (marked with blue dashed lines), and a new phase identified as $TiFe_2O_5$. The O_2 uptake observed during TGA of samples D and E possibly occurred during the phase change from α-Fe_2O_3 to $TiFe_2O_5$ as vacancies between the Ti and Fe oxides were filled with oxygen. It is unlikely that the O_2 uptake was from the phase change from anatase to rutile TiO_2, as this phase change also occurs with the fresh TiO_2 and Pt/TiO_2 samples.

TGA of the Pt/TiO_2 samples collected after flow experiments in 0.4 m NH_3 (samples B and C), however, show a decrease in mass with increasing temperature. The percent of mass decrease is also greater than that of the fresh TiO_2 support and the fresh Pt/TiO_2 (sample A). This suggests that surface species were present on the samples and were removed as the sample was heated to 1,000 °C in air. These surface
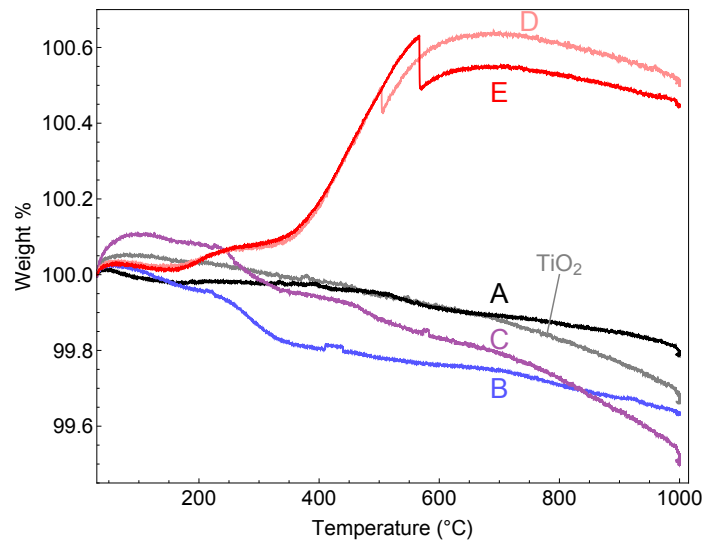
Figure 5.6: TGA profiles for TiO_2, fresh Pt/TiO_2 (A), and Pt/TiO_2 samples after SCW flow experiments in NH_3 and $HCOOH$ solutions (B-E). During TGA, temperature was ramped at 10 °C/min in flowing air (90 mL/min). Experimental conditions for the labeled sample profiles are defined in Table 5.2.
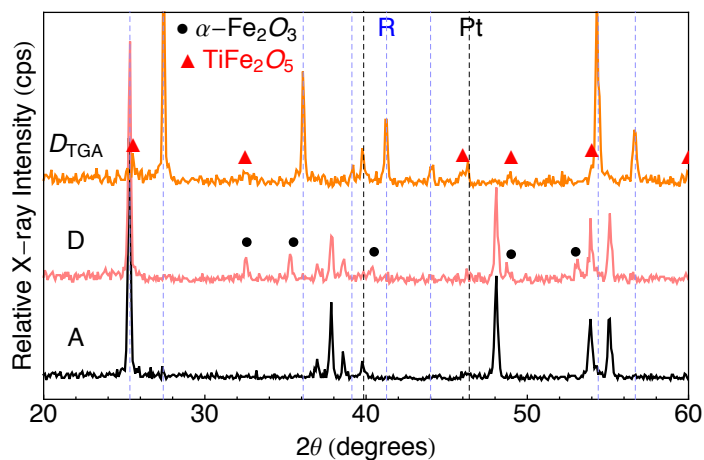
Figure 5.7: XRD patterns of fresh Pt/TiO_2 (sample A) and used Pt/TiO_2 (sample D from Table 5.2) before and after TGA. Dashed black and blue lines indicate Pt and rutile diffraction angles, respectively. Unlabeled peaks correspond to anatase TiO_2.

Reagent	mmol/ min	HCOOH: Reagent[a]	Catalyst	W/F [b] (min)	τ [c] (min)	χ (%)[d]	Product	% MS Signal
Pyridine	0.12	5:1	Pt/TiO_2	0.34	0.08	0	n.d.	-
Pyridine	0.02	5:1	Pt/TiO_2	7.91	0.48	0	n.d.	-
Propylamine	0.6	1:1	Pt/TiO_2	0.07	0.08	100	1-propanol	71 ± 1
							propanal	18 ± 2
							propanoic acid	11 ± 1
Propylamine	0.6	1:1	TiO_2	-	0.08	9 ± 1	propanal	1 ± 0.1

[a] mol:mol   [b] mol Pt/(mol reagent/min)   [c] Open reactor residence time   [d] Conversion

Table 5.3: Reaction conditions, conversion, and products for HDN of pyridine and propylamine with a Pt/TiO_2 catalyst in SCW. For all reactions, the temperature of the catalyst bed was 420 °C and the SCW pressure was 30 MPa. Time on stream for each catalyst was 5 hours except for the experiment with W/F = 7.91, which was 15 hours.

species could have blocked the Pt sites during the CO chemisorption experiment, therefore reducing the measured Pt surface coverage.

5.3.3 Pt/TiO_2 Activity for HDN of Pyridine and Propylamine

Table 5.3 summarizes the flow reaction results for the HDN of pyridine and propylamine in SCW. For these reactions, the concentration of HCOOH in the feed to the flow reactor was reduced from 0.4 mol/kg H_2O (used for experiments in Section 5.3.2) to 0.2 mol/kg H_2O. This was an attempt to reduce the corrosion of the stainless steel tubing in the preheating section of the reactor, which was observed during the experiments described in Section 5.3.2. We did not reduce the HCOOH concentration further so as to ensure that the HDN products could be detected when pyridine and propylamine concentrations were proportionally reduced.

The results for HDN of pyridine in Table 5.3 show negligible conversion, even after the W/F was increased from 0.34 to 7.91. These results are contrary to the high pyridine conversions observed with Pt catalysts in batch experiments, which had W/F values of 1.2-4.9 [39]. Several key differences between the batch reactions and the flow reaction may explain why zero conversion was observed in the flow system. In the batch reactions, the density of the water at 400 °C was 0.10 g/cm^3, corresponding to
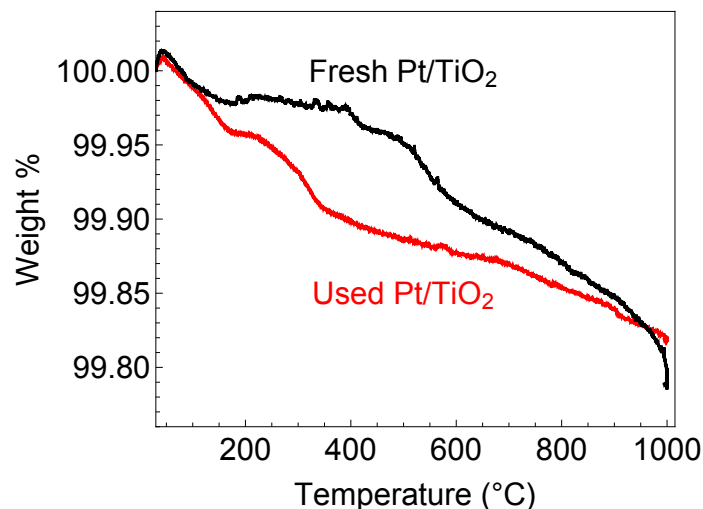
Figure 5.8: TGA profiles for Pt/TiO$_2$ before and after the SCW flow experiment with HCOOH and pyridine at 420 °C and 30 MPa (W/F = 7.91, 15 h time on stream). During TGA, temperature was ramped at 10 °C/min in flowing air (90 mL/min).

a pressure of 20 MPa. At 20 MPa, the water is just below the critical pressure (22 MPa) and is superheated steam, which can behave very differently compared to the SCW at 30 MPa which was used in the flow experiments.

Pt can strongly adsorb cyclic hydrocarbons and aromatic compounds [82, 83] and prior studies have observed Pt poisoning by aromatic compounds in SCW [84]. To test whether coke or surface pyridine species had deactivated the Pt, We performed TGA on the Pt/TiO$_2$ catalyst after the flow experiment with pyridine (W/F = 7.91, 15 h time on stream). Figure 5.8 compares the results of the TGA profiles of the fresh and used Pt/TiO$_2$ after the reaction with pyridine. The mass loss of the used Pt/TiO$_2$ occurs at a much lower temperature than that of the fresh Pt/TiO$_2$, however the total change in weight % after the analysis for the two samples was the same. While it is possible that the low-temperature mass loss of the used catalyst is from the removal of surface species adsorbed during reaction, the evidence for surface poisoning from.TGA is inconclusive and additional surface characterization is needed to further understand the differences in the TGA profiles of the fresh and used Pt/TiO$_2$.

Figure 5.9 shows XRD patterns of fresh Pt/TiO$_2$ (sample A) and used Pt/TiO$_2$
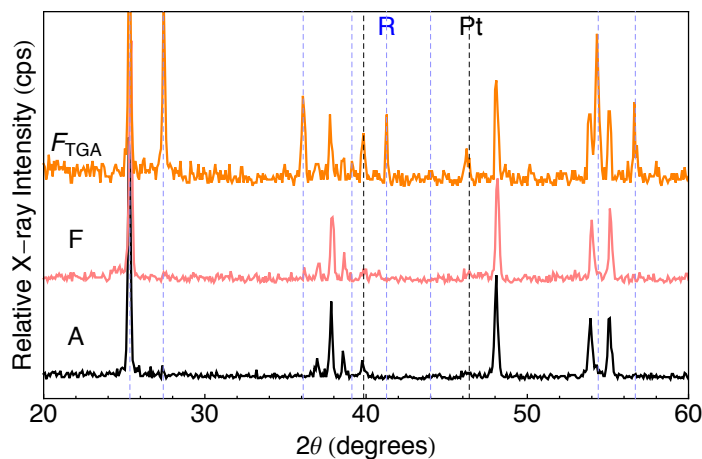
Figure 5.9: XRD patterns of fresh Pt/TiO_2 (sample A) and Pt/TiO_2 after reaction with HCOOH and pyridine in SCW before (sample F) and after (sample F_{TGA}) TGA. Sample F was recovered after 15 h on stream with W/F = 7.91. Dashed black and blue lines indicate Pt and rutile diffraction angles, respectively. Unlabeled peaks correspond to anatase TiO_2.

after the reaction with pyridine before and after TGA (samples F and F_{TGA}, respectively). Comparison of the diffraction patterns before and after TGA shows growth of Pt peaks (black dashed lines) and addition of rutile TiO_2 peaks (blue dashed lines). As no additional phases were identified and the Pt peak was present in the recovered samples, we conclude that a complete loss of Pt or Pt poisoning by Fe (or other reactor corrosion species) did not occur.

The H_2 concentration and H_2 source during the reaction may also explain the discrepancy between Pt activities observed in batch and flow. In the batch reactions, a 6.5:1 molar ratio of pure H_2/pyridine was loaded into the reactor head space. In the flow reactor, we used a 5:1 molar ratio of HCOOH/pyridine and it was assumed that the HCOOH would undergo 100% conversion and form equal moles H_2 and CO_2 per mole HCOOH. From the results in Table 5.1 for the NH_3 and HCOOH solutions, however, approximately only 25% of the expected H_2 and CO_2 from HCOOH were measured in the gas products. As a result, there may not have been sufficient H_2 in the solution to drive HDN of pyridine. The presence of CO_2 from the HCOOH in the flow experiments may have also affected the number of available Pt active sites for

pyridine reaction, compared with the absence of CO_2 in the batch experiments.

The role of the support could have also influenced the activity of the Pt for HDN of pyridine in the flow experiments compared to previously reported batch reactions [39]. In the batch reactions, Pt was supported on either activated carbon or γ-Al_2O_3. The TiO_2 support used in this work may have changed the activity of the Pt for HDN of pyridine, however Pt/TiO_2 was very active (100% conversion) for HDN of propylamine (Table 5.3). The propylamine reaction products in Table 5.3 indicate that water or possibly CO_2 participated in the reaction and exchanged the amine group for oxygenated functional groups. To differentiate the activity of the Pt from the activity of the support and the aqueous solution, a control experiment was performed with propylamine and TiO_2. Without Pt in the reactor, propylamine conversion was only 9%. This result confirms that Pt was active during the propylamine reaction in SCW. From the propylamine reaction products, however, it was likely that oxygen-containing reactive intermediates were more abundant than hydrogen on the Pt surface. The distribution of oxygen-containing surface species relative to surface hydrogen may have been the rate limiting step for HDN of pyridine as hydrogenation of the aromatic ring is the first step in the reaction pathway.

5.4 Conclusions

The construction of f_{O_2}-pH diagrams successfully identified a hydrothermally stable catalyst, Pt/TiO_2, for HDN in SCW at 380-500 °C and 22-38 MPa. The synthesized Pt/TiO_2 catalyst experienced little or no dissolution or changes in oxidation state during flow experiments in SCW solutions of HCOOH and NH_3 (38MPa and 380 and 500 °C) and during HDN of pyridine and propylamine in SCW at 420 °C and 30 MPa. Although Pt/TiO_2 was hydrothermally stable during all experiments, HDN activity was only observed for propylamine and no reaction was observed for pyridine. Possible reasons for the inactivity of Pt/TiO_2 for HDN of pyridine include insufficient

H_2 (or surface hydrogen), blockage of Pt sites by CO_2 or other oxygen-containing intermediates, or metal-support interactions that decreased the hydrogenation activity of Pt. Future experiments could further explore the influence of these variables on HDN of pyridine by increasing the H_2/pyridine ratio and investigating alternative in situ H_2 generation methods, such as partial oxidation of heptane [73]. Calculating the hydrothermal stability of other oxides in HDN reaction solutions could identify alternative Pt supports that promote catalyst sites with higher HDN activity.

When designing hydrothermal reaction systems, corrosion of the reactor materials should also be considered in addition to the hydrothermal stability of the catalyst. While the SCW reaction conditions had no adverse effects on the Pt/TiO_2 with respect to changes in oxidation state or dissolution, there was significant corrosion of the stainless steel tubing between the reactor inlet and the catalyst bed and Fe deposits were detected on the catalyst. The corrosion was determined to be a result of the pH and f_{O_2} conditions caused by the 0.4 m formic acid solution at the intermediate temperatures between the pump (ambient) and the catalyst bed (380 or 500 °C). In future flow experiments with formic acid, the preheating section of tubing should be constructed using an appropriate alternative material to stainless steel or should contain an inert liner to prevent corrosion of the tubing.

CHAPTER VI

Conclusions and Recommendations for Future Research

6.1 Summary and Conclusions

This dissertation demonstrated that thermodynamic modeling is a valuable tool for predicting the hydrothermal stability of catalytic materials and designing hydrothermal systems for reactions with heterogeneous catalysts. Use of thermodynamic models to predict catalyst oxidation and dissolution provides an estimate of the "worst case scenario" for the catalyst where the kinetics for oxidation and dissolution are fast and the catalyst quickly reaches its new equilibrium state. We showed the accuracy of the R-HKF equation of state for describing the behavior of metal, oxide, carbide, and nitride catalytic materials in practical SCW reaction systems and used the model to develop property-stability relationships and methods to determine the influence of solution pH and f_{O_2} on catalyst stability. We then used these criteria to design and test a catalyst and reaction system for HDN of pyridine and propylamine in SCW.

In Chapter II, we compared results from batch experiments with transition metals, oxides, and transition metal carbides and nitrides with results from thermodynamic models to test the viability of the models for describing catalyst behavior in hy-

drothermal reaction systems. The calculated ΔG_{rxn} values for catalyst oxidation and the solubility values calculated from the R-HKF equation of state predicted the oxidation and dissolution observed after batch screening experiments. In addition, we found that SCW at 400 °C causes oxidation and dissolution of carbides, nitrides, Ni, and Co and these materials may quickly lose catalytic activity in SCW. The aqueous metal species from these materials could contaminate the reaction products or result in some homogeneous catalysis. Through the experiments and the model, we determined that Ru, CeO_2, TiO_2, and ZrO_2 do not undergo changes in oxidation state or measurable dissolution in SCW and therefore have good hydrothermal stability. The catalyst oxidation rates that were observed experimentally increased with increasing SCW density, despite similar or greater ΔG_{rxn} values for catalyst oxidation by H_2O in high-density SCW compared to low-density SCW. We speculated that the higher rates were due to the higher water concentration and its influence on the oxidation kinetics.

In Chapter III, we used the R-HKF thermodynamic model to predict metal and oxide solubility in water at practical hydrothermal reaction conditions (150-550 °C and 22-50 MPa) and developed new correlations between the hydrothermal solubilities and readily available material properties. These correlations provide rapid estimation of metal or metal oxide solubility and facilitate identification of materials with improved hydrothermal stability. From these correlations, metal alloy catalysts should have large average electronegativities and oxides should have relatively large ionic-covalent parameters and small polarizing power values to minimize dissolution.

In Chapter IV, we described methods for predicting the influence of pH and oxygen fugacity, which vary with the concentrations of different reaction solutes, on the catalyst stability. Through the construction of f_{O_2}-pH diagrams, phase changes and dissolution of catalytic materials can be predicted with changes in the composition of hydrothermal reaction solutions. Together with f_{O_2} and pH calculations for dif-

ferent solutes in aqueous solution, these diagrams provide the information needed to select appropriate temperatures, pressures, and solute concentrations that improve the catalyst stability.

In Chapter V, we used f_{O_2}-pH diagrams to select Pt/TiO$_2$ as a stable catalyst for HDN reactions of pyridine and propylamine in SCW. This study also served as a "proof of concept" for the stability modeling work described in the earlier chapters. Pt/TiO$_2$ experienced < 2 wt% dissolution of Pt and no changes in oxidation state during flow experiments in SCW solutions of HCOOH and NH$_3$ (38MPa and 380 and 500 °C) and during HDN of pyridine and propylamine in SCW at 420 °C and 30 MPa. The denitrogenation activity of Pt/TiO$_2$, however, was evident only for propylamine. Several possible reasons for the inactivity of Pt/TiO$_2$ for HDN of pyridine were presented. In addition, corrosion of the stainless steel reactor tubing during flow experiments with solutions containing formic acid was explained using f_{O_2}-pH diagrams for Fe.

6.2   Recommendations for Future Work

The work described in this dissertation contributes to the hydrothermal catalysis literature. However, there is still much to be learned about designing catalysts for hydrothermal reactions. The correlation for solubility of oxides, presented in Chapter III, could be further improved through the identification of better material descriptors and additional thermodynamic and solubility data for mixed metal oxides. In this work, we used bulk material properties to describe hydrothermal catalyst stability, however for real catalysts the active components are typically synthesized at nanometer length-scales and thus do not always behave according to the thermodynamics of their bulk material counterparts. In addition, these nano materials are frequently deposited on other support materials which can alter the electronic structure of the active nano materials through strong metal-support interactions. Future

work should investigate the effects of reduced particle size on hydrothermal stability and determine how support-metal interactions affect the hydrothermal stabilities of both the active material and the support. The relationships between particle size, support-metal interactions, and hydrothermal stability would be valuable additions to thermodynamic stability model used in this dissertation and to the overall design of hydrothermally stable catalytic materials.

Work should also be undertaken to understand the influence of the hydrothermal solution on the activity of the heterogeneous catalyst. Other studies have shown how the ion product and dielectric constant of hydrothermal solutions influence homogeneous reactions, however the importance of these properties on catalytic surface reactions is poorly understood. Once an active and stable catalyst is identified for a hydrothermal reaction, the influence of these hydrothermal solvent properties on activity and selectivity should be investigated.

In Chapter II, we observed the formation of unique surface structures from the dissolution and subsequent precipitation of carbide and nitride catalysts in SCW. Additional work is needed to determine whether and how these altered morphologies could lead to functional materials. Future work should also test whether the unusual oxide morphologies produced from the Mo and W carbides and nitrides are retained after recarburization or renitridation of the materials.

Finally, hydrothermal reaction systems will only be practical if corrosion of the reactor components can be controlled. While reducing conditions are favorable for maintaining active catalyst phases and promoting hydrothermal hydrogenation reactions, reducing solutions can also remove the protective surface oxide of steel tubing and result in corrosion. In this dissertation and other studies [80, 81], formic acid was found to induce corrosion of the stainless steel reactor. The development of less corrosive methods for in situ H_2 generation or the use of more appropriate reactor materials would greatly improve the practicality of hydrothermal hydrogenation reactions.

APPENDICES

APPENDIX A

Experimental Batch Stability Results

This appendix contains x-ray diffraction (XRD) data and the scanning electron microscopy (SEM) images obtained before and after each batch experiment. In total, we tested the hydrothermal stability of 11 pure materials (Pd, Ru, Ni, Co, CeO_2, TiO_2, ZrO_2, Mo_2C, MoN, W_2C, and WN) in He, low-density SCW ($\rho = 0.15$ g/mL), and high-density SCW ($\rho = 0.52$ g/mL) at 400 °C for 60 minutes. The XRD data were collected using a Rigaku 600 Miniflex set at 40 kV and 15 mA ($K_\alpha = 1.5406$Å). The SEM images were collected using a Philips XL30FEG. Powder samples were adhered to the SEM posts using carbon tape and nonconducting samples were sputter coated with gold for 60 seconds. The results are organized into subsections for each catalyst.

Palladium

The Pd particles (Aldrich) were used as received with approximately 50 mg loaded in each batch reactor. The fresh Pd XRD peaks in Figure A.1 are consistent with FCC Pd. The peak width of the fresh Pd is indicative of small crystallites ($\leq$100nm), however the peaks are significantly narrower after 60 minutes in He at 400 °C. This reduction in the peak broadness means that the Pd particles sintered with thermal treatment. After exposure to He and SCW, XRD peaks consistent with PdO are present. The peaks were fit using JADE XRD analysis software and the PdO com-

position is estimated to be 5 wt% after exposure to He and 10.1 wt% and 22.8 wt% after exposure to low- and high-density SCW, respectively. In all, increasing the SCW density resulted in increased PdO formation. The SEM images in Figure A.2 of the Pd before and after exposure to SCW show that the material did not undergo any noticeable morphological changes during the 60 minute experiments.

Ruthenium

The Ru particles (Alfa Aesar) were used as received with approximately 10-12 mg loaded in each batch reactor. The XRD peaks in Figure A.3 of the fresh Ru and the Ru recovered after the batch experiments are consistent with HCP Ru and therefore oxidation did not occur. The SEM images in Figure A.4 of the Ru before and after exposure to SCW show that the material did not undergo any noticeable morphological changes during the 60 minute experiments.

Nickel

The Ni particles (Acros Organics) were used as received with approximately 50 mg loaded in each batch reactor. The XRD peaks in Figure A.5 of the fresh Ni catalyst and the Ni recovered after the batch experiments in He and low-density SCW are consistent with FCC Ni. After exposure to high-density SCW, the Ni catalyst produced new XRD peaks consistent with NiO. The peaks were fit using JADE XRD analysis software and the NiO composition is estimated to be 6.1 wt%. Increasing the SCW density resulted in increased NiO formation. The SEM images in Figure A.6 of the Ni before and after exposure to SCW show that the material experienced significant morphological changes from exposure to high-density SCW. The surface of the Ni particles after 60 minutes in high-density SCW is coated in small ($< 1\mu$m) cubic particles. These surface particles likely formed from dissolution

of Ni in high-density SCW followed by precipitation when the reactors were quenched.

Cobalt

The Co particles (QSI-Nano) were used as received with approximately 50 mg loaded in each batch reactor. The XRD peaks in Figure A.7 of the fresh Co catalyst and the Co recovered after the batch experiments in He are consistent with pure Co. After exposure to low- and high-density SCW, the Co catalyst produced new XRD peaks consistent with CoO. The peaks were fit using JADE XRD analysis software and the CoO composition is estimated to be 42.7 and 39.0 wt% after low- and high-density SCW, respectively. The SEM images in Figure A.8 of the Co before and after exposure to SCW show that the material experienced significant morphological changes from exposure to both low- and high-density SCW. Similar to Ni, the surface of the Co particles after 60 minutes in SCW is coated in many small ($< 1\mu$m), cubic particles. These surface particles likely formed from the dissolution of Co in high-density SCW and then precipitation of the dissolved aqueous ions when the reactors were quenched.
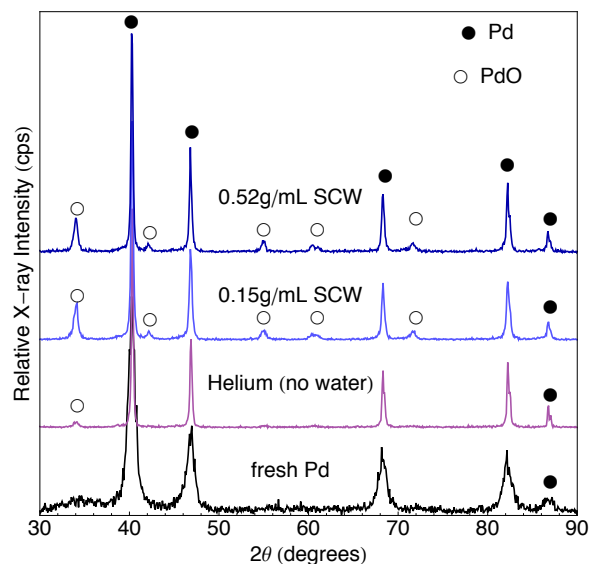
Figure A.1: X-ray diffraction of fresh Pd particles and Pd after 60 minute batch experiments at 400 °C in He, low-density (0.15g/mL) SCW, and high-density (0.52g/mL) SCW.

(a) Fresh Pd   (b) 0.15g/mL SCW   (c) 0.52 g/mL SCW
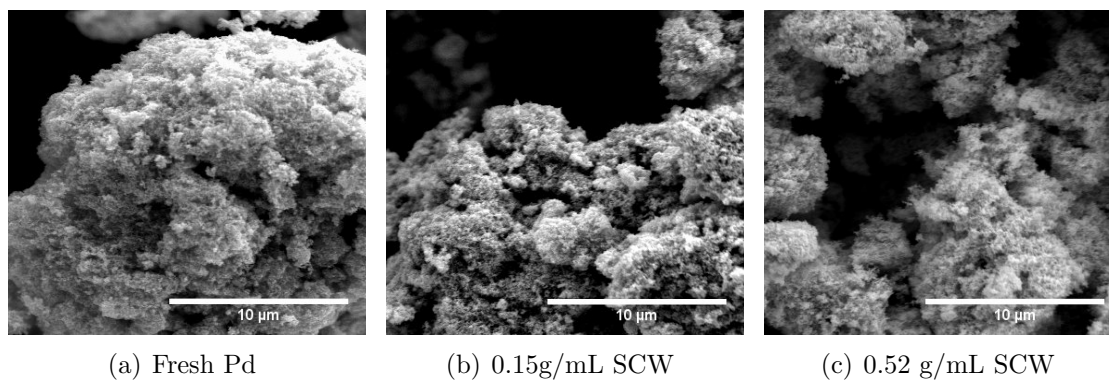
Figure A.2: SEM images of fresh Pd (a) and Pd after batch experiments at 400 °C for 60 min. in low density SCW (b), and high density SCW (c). The images were collected with 15 kV accelerating voltage and spot size 3.
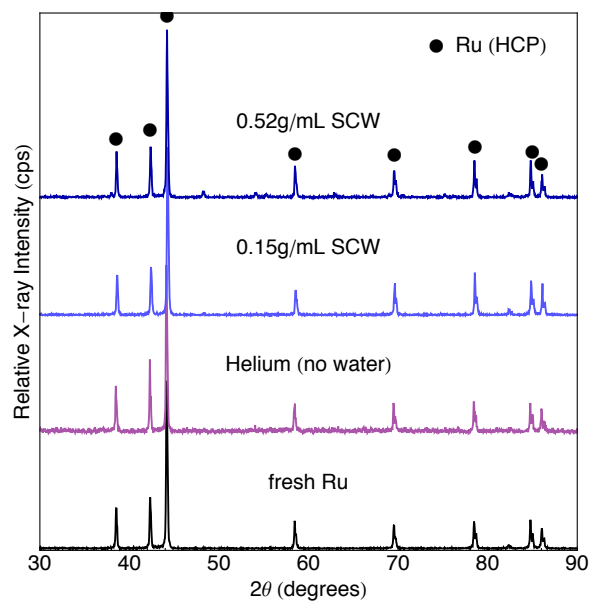
Figure A.3: X-ray diffraction of fresh Ru particles and Ru after 60 minute batch experiments at 400 °C in He, low-density (0.15 g/mL) SCW, and high-density (0.52 g/mL) SCW.

(a) Fresh Ru

(b) He (no water)

(c) 0.15g/mL SCW

(d) 0.52g/mL SCW
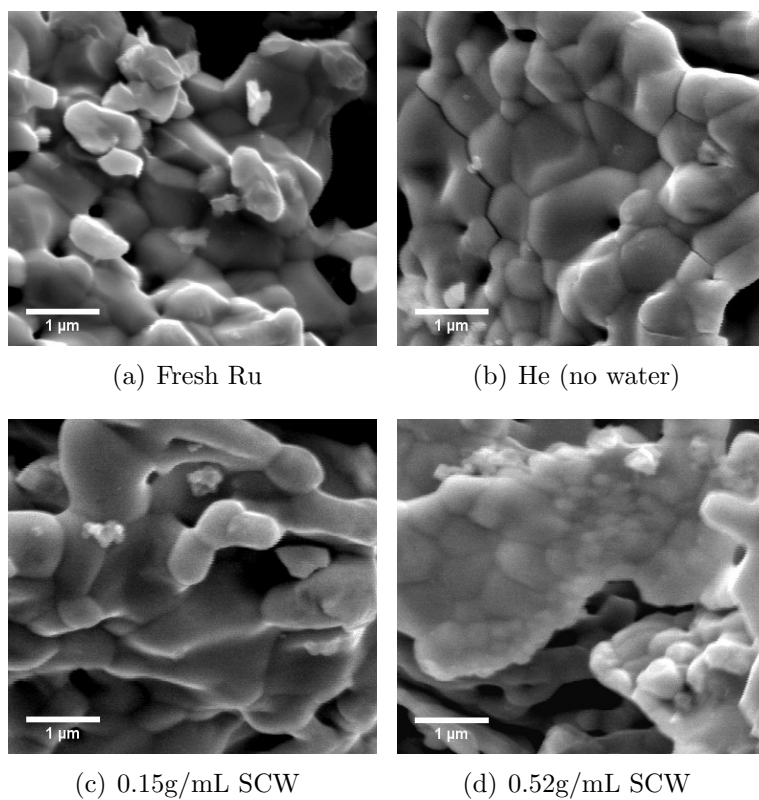
Figure A.4: SEM images of fresh Ru (a) and Ru after batch experiments at 400 °C for 60 min. in He (b), low ρ SCW (c), and high ρ SCW (d). The images were collected with 15 kV accelerating voltage and spot size 3.

95
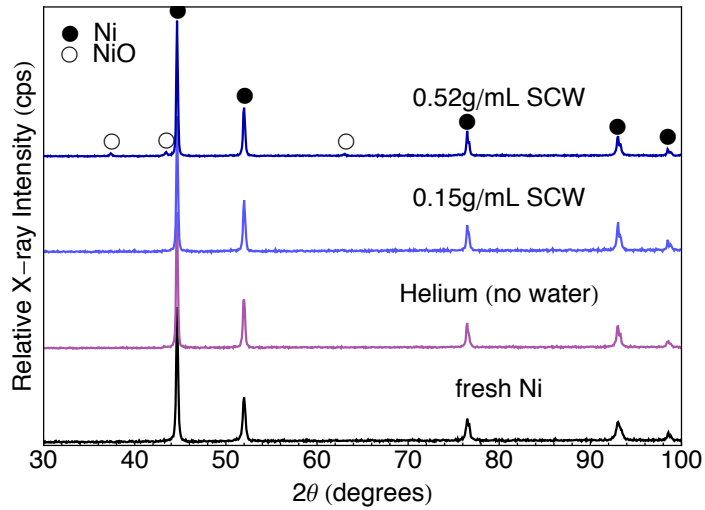
Figure A.5: X-ray diffraction of fresh Ni particles and Ni after 60 minute batch experiments at 400 °C in He, low-density (0.15g/mL) SCW, and high-density (0.52g/mL) SCW.

(a) Fresh Ni

(b) He (no water)

(c) 0.15g/mL SCW

(d) 0.52g/mL SCW
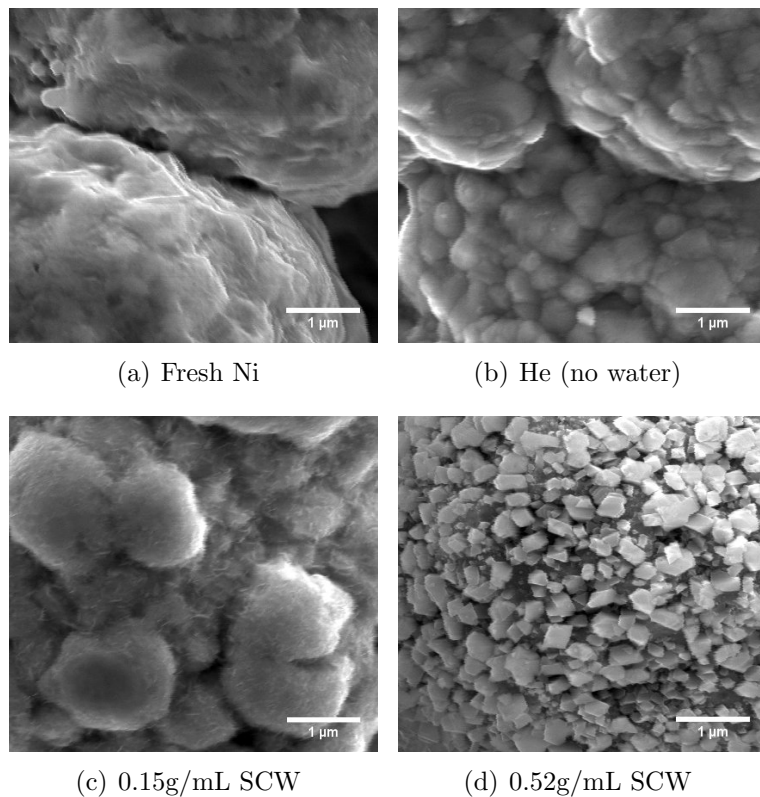
Figure A.6: SEM images of fresh Ni (a) and Ni after batch experiments at 400 °C for 60 min. in He (b), low ρ SCW (c), and high ρ SCW (d). The images were collected with 15kV accelerating voltage and spot size 3.

96
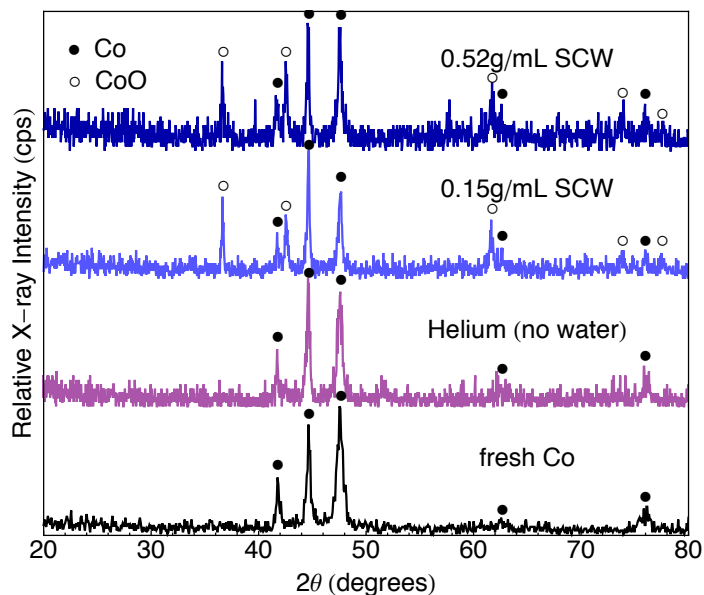
Figure A.7: X-ray diffraction of fresh Co particles and Co after 60 minute batch experiments at 400 °C in He, low-density (0.15g/mL) SCW, and high-density (0.52g/mL) SCW.

(a) Fresh Co   (b) 0.15g/mL SCW   (c) 0.52g/mL SCW
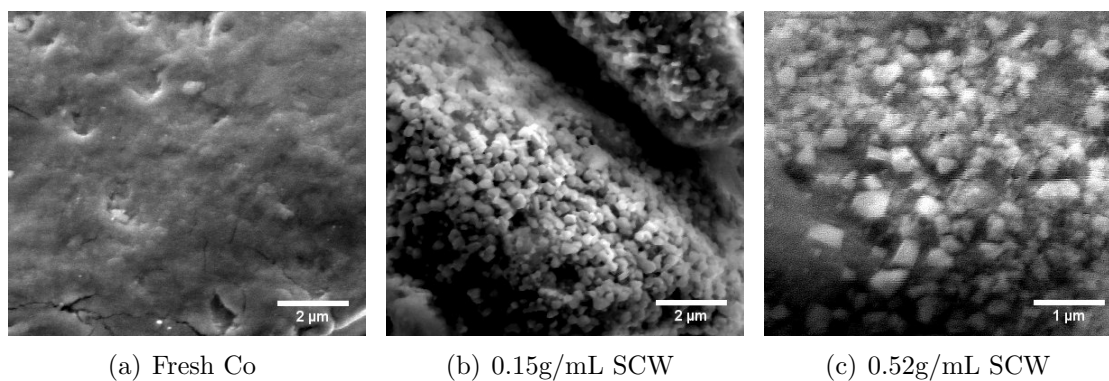
Figure A.8: SEM images of fresh Co (a) and Co after batch experiments at 400 °C for 60 min. in low ρ SCW (b) and high ρ SCW (c). The images were collected with 15kV accelerating voltage and spot size 3.

Ceria

The CeO_2 (Alfa Aesar) was used as received with approximately 50 mg loaded in each batch reactor. The XRD peaks in Figure A.9 of the fresh CeO_2 and the CeO_2 recovered after the batch experiments are consistent with cubic CeO_2, so we conclude that exposure to SCW does not change the oxidation state or crystal phase of CeO_2. The SEM images in Figure A.10 of the CeO_2 before and after exposure to SCW show that the material did not undergo any noticeable morphological changes during the 60 minute experiments.

Titania

The TiO_2 (Alfa Aesar) was used as received with approximately 50 mg loaded in each batch reactor. The XRD peaks in Figure A.11 of the fresh TiO_2 and the TiO_2 recovered after the batch experiments are consistent with anatase TiO_2, so we conclude that exposure to SCW for 60 minutes does not change the oxidation state or crystal phase of TiO_2, however longer exposure times (6 hours) result in the transformation of anatase TiO_2 to rutile [54]. The SEM images in Figure A.12 of the TiO_2 before and after exposure to SCW show that the material did not undergo any noticeable morphological changes during the 60 minute experiments.

Zirconia

The ZrO_2 (Alfa Aesar) was used as received with approximately 50 mg loaded in each batch reactor. The XRD spectra of the fresh ZrO_2 in Figure A.13 show that the initial structure is either amorphous or has crystal domains too small for effective x-ray scattering. The ZrO_2 recovered after the batch experiments have XRD peaks consistent with both tetragonal and monoclinic ZrO_2. JADE XRD analysis software was used to determine the relative amounts of each phase. The amount of

monoclinic phase after 60 minutes exposure to He, low-density SCW and high-density SCW at 400 °C was 54.9, 75.8, and 76.5 wt%, respectively, and the wt% of tetragonal phase is the difference. From XRD analysis, we conclude that exposing the fresh catalyst to high temperatures (400 °C) for 60 minutes, regardless of the presence of water, significantly increases the crystallinity and crystal domain size of the ZrO_2. In addition, increasing the SCW density increases the wt% of monoclinic ZrO_2 and decreases the wt% of the tetragonal phase. The SEM images in Figure A.14 of the ZrO_2 before and after exposure to SCW show that the material did not undergo any noticeable morphological changes during the 60 minute experiments.
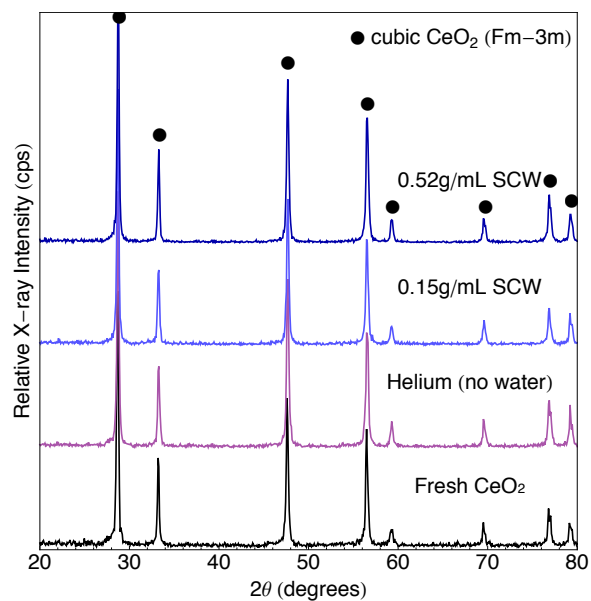
Figure A.9: X-ray diffraction of fresh CeO_2 and CeO_2 after 60 minute batch experiments at 400 °C in He, low-density (0.15g/mL) SCW, and high-density (0.52g/mL) SCW.

(a) Fresh CeO_2

(b) He (no water)

(c) 0.15g/mL SCW

(d) 0.52g/mL SCW
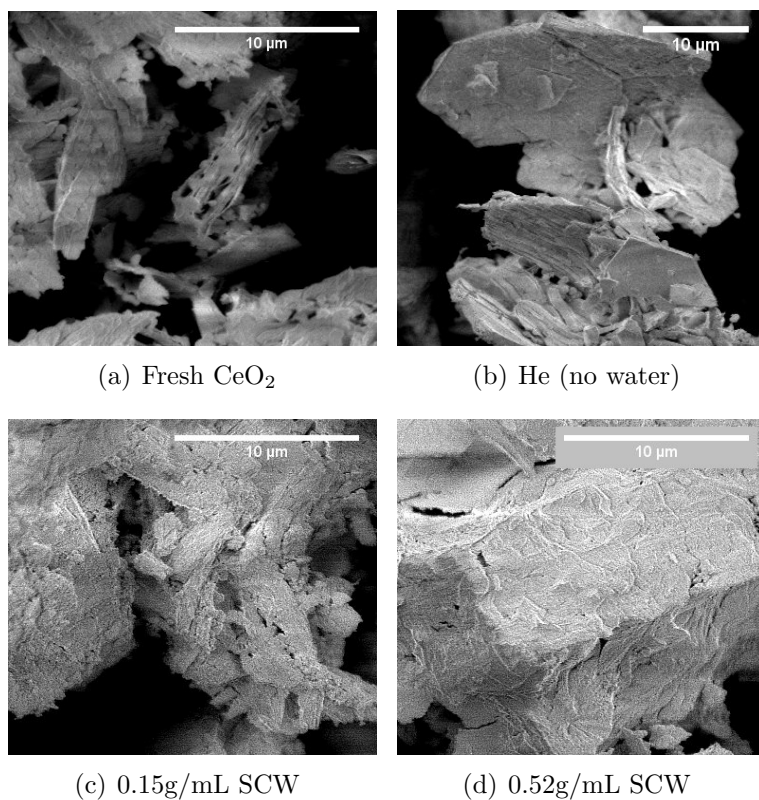
Figure A.10: SEM images of fresh CeO_2 (a) and CeO_2 after batch experiments at 400 °C for 60 min. in He (b), low ρ SCW (c), and high ρ SCW (d). The images were collected with 2 kV accelerating voltage and spot size 3.
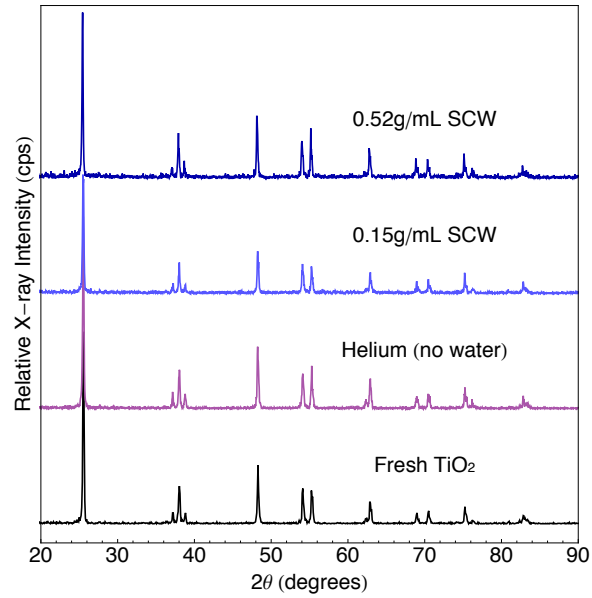
Figure A.11: X-ray diffraction of fresh TiO_2 and TiO_2 after 60 minute batch experiments at 400 °C in He, low-density (0.15g/mL) SCW, and high-density (0.52g/mL) SCW.

(a) Fresh TiO_2

(b) He (no water)

(c) 0.15g/mL SCW

(d) 0.52g/mL SCW
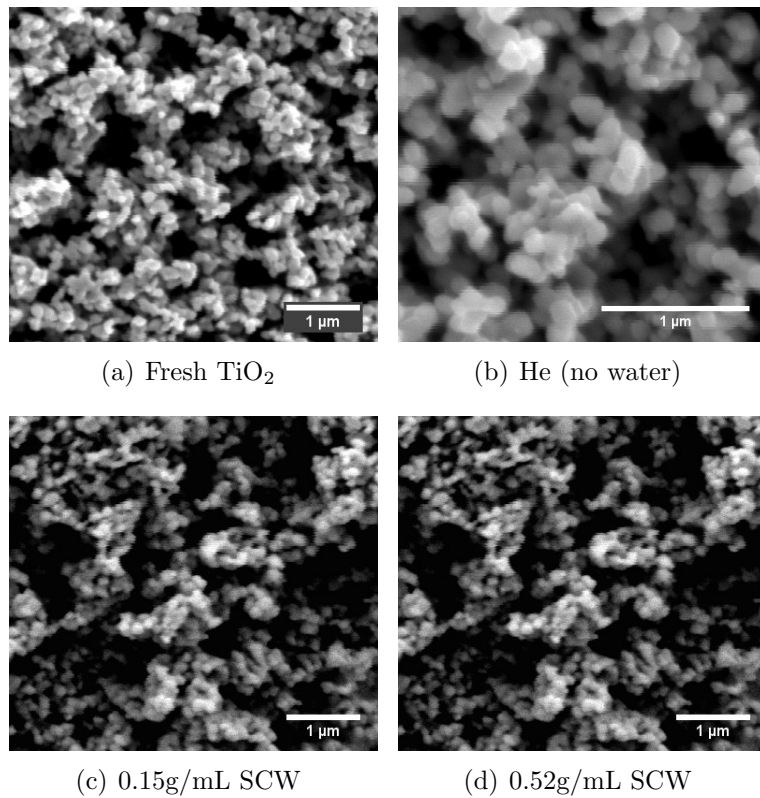
Figure A.12: SEM images of fresh TiO_2 (a) and TiO_2 after batch experiments at 400 °C for 60 min. in He (b), low ρ SCW (c), and high ρ SCW (d). The images were collected with 5 kV accelerating voltage and spot size 3.
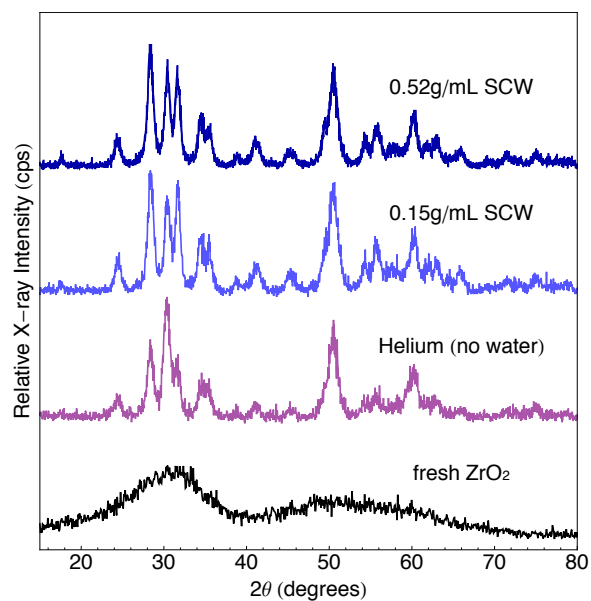
Figure A.13: X-ray diffraction of fresh ZrO_2 and ZrO_2 after 60 minute batch experiments at 400 °C in He, low-density (0.15g/mL) SCW, and high-density (0.52g/mL) SCW.

(a) Fresh ZrO_2

(b) He (no water)

(c) 0.15g/mL SCW

(d) 0.52g/mL SCW
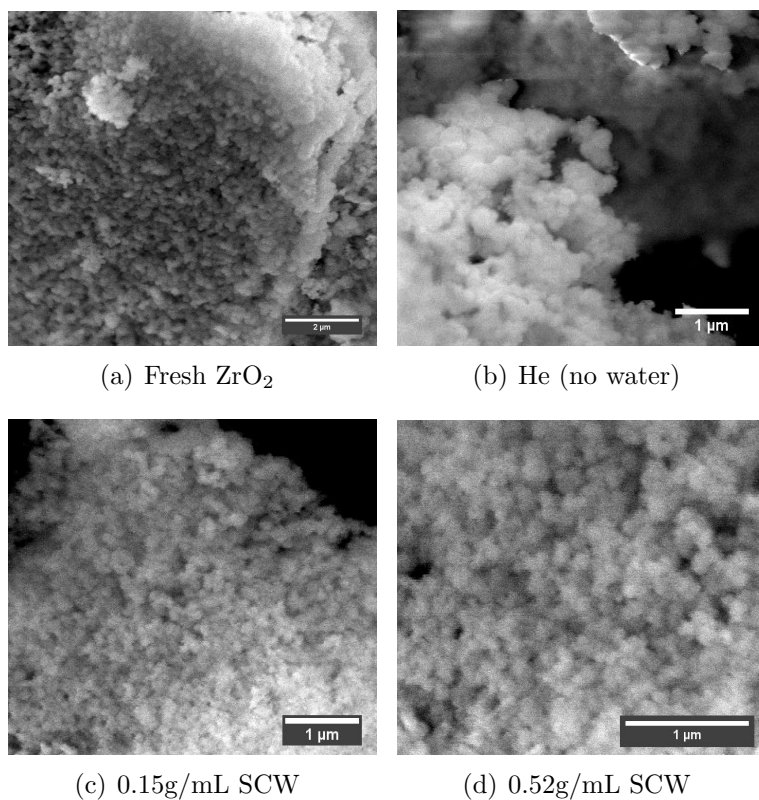
Figure A.14: SEM images of fresh ZrO_2 (a) and ZrO_2 after batch experiments at 400 °C for 60 min. in He (b), low ρ SCW (c), and high ρ SCW (d). The images were collected with 10 kV accelerating voltage and spot size 2.

Molybdenum carbide

The Mo_2C was synthesized using a temperature-programmed reaction and approximately 50 mg was loaded in each batch reactor. The XRD spectra in Figure A.15 of the fresh Mo_2C and the Mo_2C recovered after the batch experiments in He (no water) have XRD peaks consistent with α-Mo_2C. After 60 minutes exposure to both low- and high-density SCW, the recovered catalyst loses all peaks associated with Mo_2C and instead produces spectra consistent with MoO_2. From XRD analysis, we conclude SCW quickly oxidizes Mo_2C to form MoO_2.

The SEM image in Figure A.16(a) of the fresh Mo_2C shows that the material surface is initially covered with long thin cracks (macropores) 0.5-3 μm long and $\leq$ 300 nm wide. Figure A.16(b) of the SEM image of Mo_2C after 60 minutes in He at 400 °C shows very little change compared to the fresh material. The SEM image in Figure A.16(c) of Mo_2C after exposure to low-density (0.15 g/mL) SCW shows that the surface becomes rougher than the fresh material and develops spherical surface morphologies 1-2μm in diameter. After exposure to high-density (0.52 g/mL) SCW, the SEM image in Figure A.16(d) shows the surface is covered in disc-shaped particles with dendrites growing from the edges. In addition, other surface morphologies were observed after Mo_2C was exposed to high-density SCW including the $\leq$ 300 nm-diameter cube-like particles in Figure A.16(e) and the $\leq$ 400 nm-diameter rod-like particles in Figure A.16(f).
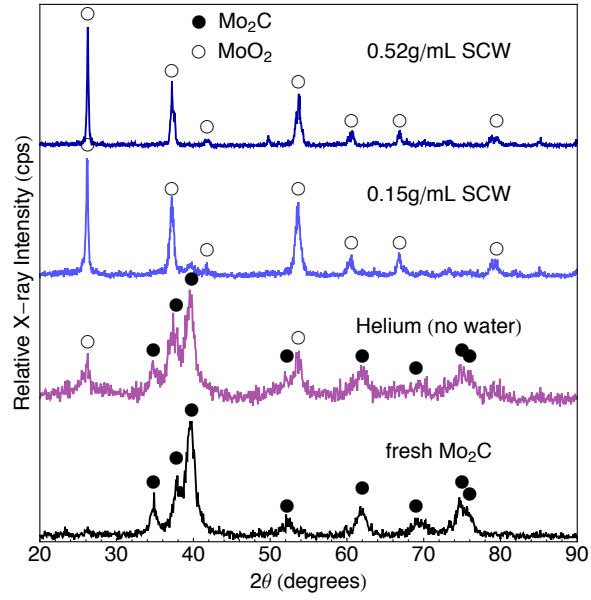
Figure A.15: X-ray diffraction of fresh Mo$_2$C and Mo$_2$C after 60 minute batch experiments at 400 °C in He, low-density (0.15g/mL) SCW, and high-density (0.52g/mL) SCW.

(a) Fresh Mo$_2$C

(b) He (no water)

(c) 0.15g/mL SCW

(d) 0.52g/mL SCW

(e) 0.52g/mL SCW

(f) 0.52g/mL SCW
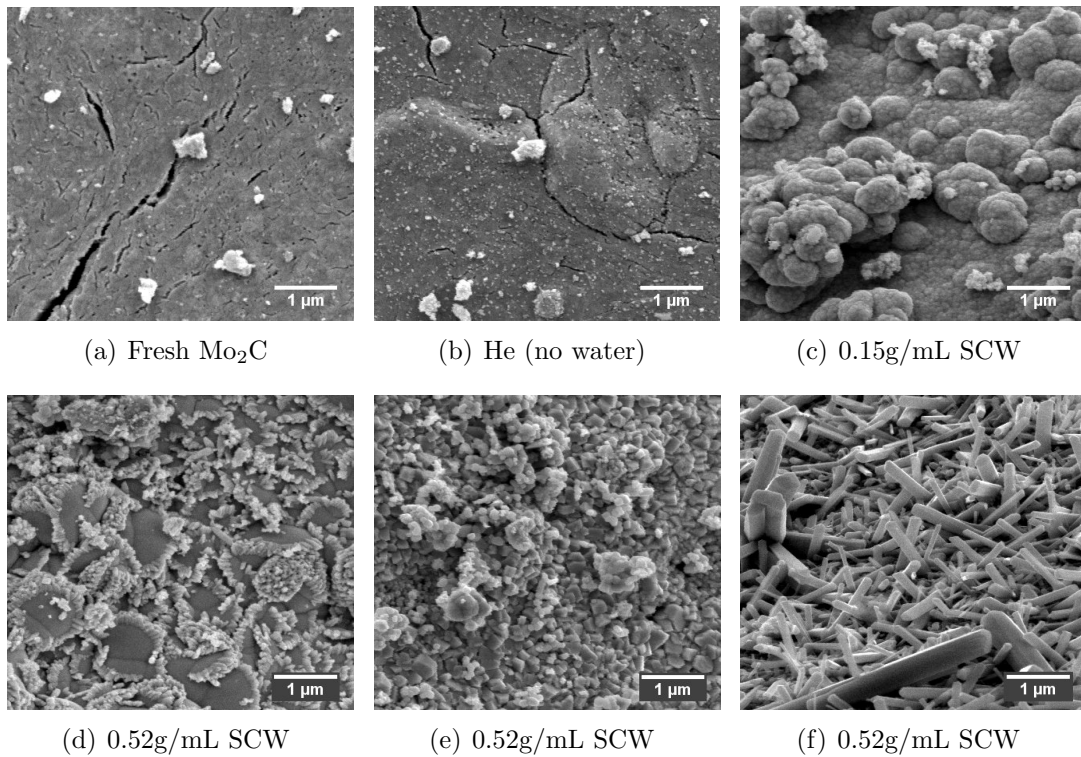
Figure A.16: SEM images of fresh Mo$_2$C (a) and Mo$_2$C after batch experiments at 400 °C for 60 min. in He (b), low ρ SCW (c), and high ρ SCW (d-f). The images were collected with 5 kV accelerating voltage and spot size 3.

Tungsten carbide

The W_2C was synthesized using a temperature-programmed reaction and approximately 50 mg was loaded in each batch reactor. The XRD spectra in Figure A.17 of the fresh W_2C and the W_2C recovered after the batch experiments in He (no water) have XRD peaks consistent with ϵ-W_2C. After 60 minutes exposure to both low- and high-density SCW, the recovered catalyst loses all peaks associated with W_2C and instead produces spectra consistent with WO_3. From XRD analysis, we conclude SCW quickly oxidizes W_2C to form WO_3.

The SEM image in Figure A.18(a) of the fresh W_2C shows that the material surface is initially rough and porous with the largest pores ≈ 900 nm in diameter and the smallest visible pores ≤ 100 nm. Figure A.18(b) of the SEM image of W_2C after 60 minutes in He at 400 °C shows very little change in the surface morphology with the exception of a few new, sparsely dispersed needle-like particles on the surface. The SEM images in Figure A.18(c) and Figure A.18(d) of W_2C after exposure to SCW show that the surface becomes coated in a thick network of whisker-like particles with diameters ≤ 100 nm.
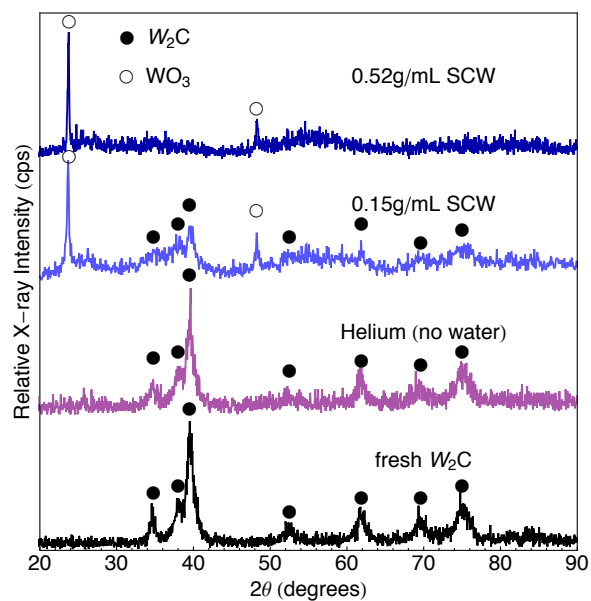
Figure A.17: X-ray diffraction of fresh W_2C and W_2C after 60 minute batch experiments at 400 °C in He, low-density (0.15g/mL) SCW, and high-density (0.52g/mL) SCW.

(a) Fresh W_2C

(b) He (no water)

(c) 0.15g/mL SCW

(d) 0.52g/mL SCW
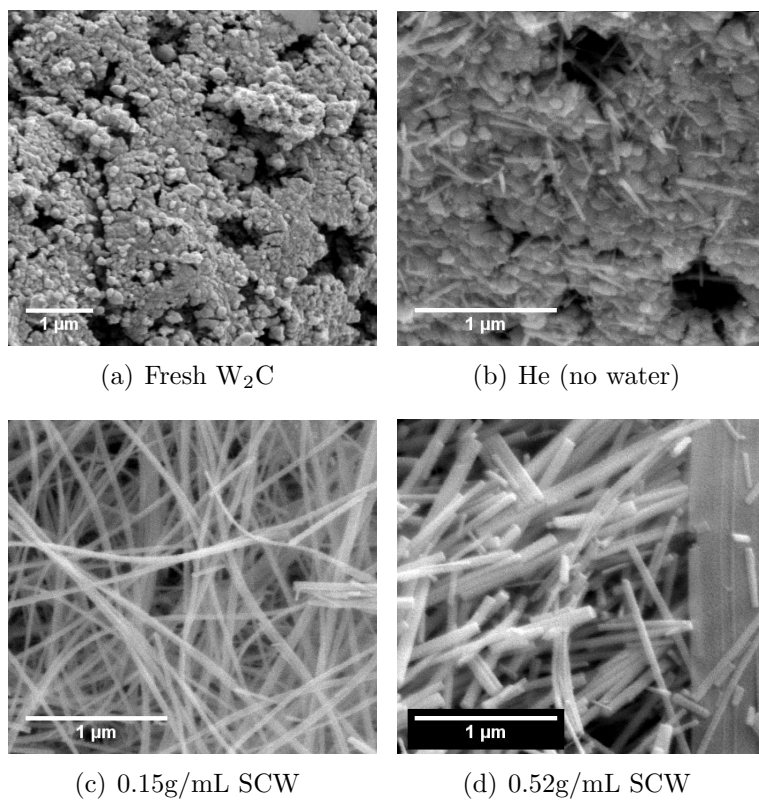
Figure A.18: SEM images of fresh W_2C (a) and W_2C after batch experiments at 400 °C for 60 min. in He (b), low ρ SCW (c), and high ρ SCW (d). The images were collected with 10 kV accelerating voltage and spot size 3.

Molybdenum nitride

The Mo_2N was synthesized using a temperature-programmed reaction and approximately 50 mg was loaded in each batch reactor. The XRD spectra in Figure A.19 of the fresh Mo_2N has XRD peaks consistent with Mo_2N (93.3wt%) and MoO_2 (6.7wt%). JADE XRD analysis software was used to determine the relative amounts of each phase. The Mo_2N recovered after the batch experiments in He (no water) contains a higher fraction of MoO_2, however the sample still retained approximately 69wt% Mo_2N. After 60 minutes exposure to both low- and high-density SCW, the recovered catalysts are predominately MoO_2. From XRD analysis, we conclude SCW quickly oxidizes Mo_2N to form MoO_2.

The SEM image in Figure A.20(a) of the fresh Mo_2N shows that the material surface is initially covered with long thin cracks (macropores) $\approx 1\mu$m long and ≤ 200 nm wide. Figure A.20(b) of the SEM image of Mo_2N after 60 minutes in He at 400 °C shows very little change. The SEM images in Figure A.20(c) and Figure A.20(d) of Mo_2N after exposure to SCW show that the surface becomes densely coated in a randomly-oriented network of needle-like particles. The particles are rougher in appearance after exposure to low-density (0.15g/mL) SCW with diameters of ≈ 200 nm. After exposure to high-density (0.52 g/mL) SCW, the needle-like particles are much smoother and larger in diameter than the particles formed after low-density SCW.
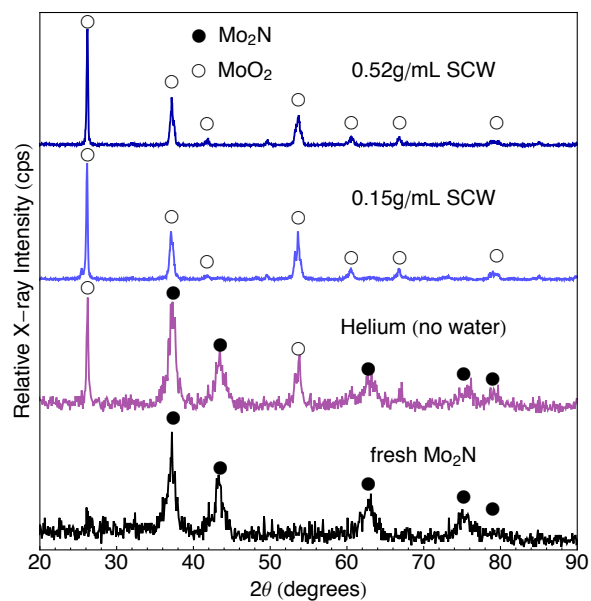
Figure A.19: X-ray diffraction of fresh Mo_2N and Mo_2N after 60 minute batch experiments at 400 °C in He, low-density (0.15g/mL) SCW, and high-density (0.52g/mL) SCW.

(a) Fresh Mo_2N

(b) He (no water)

(c) 0.15g/mL SCW

(d) 0.52g/mL SCW
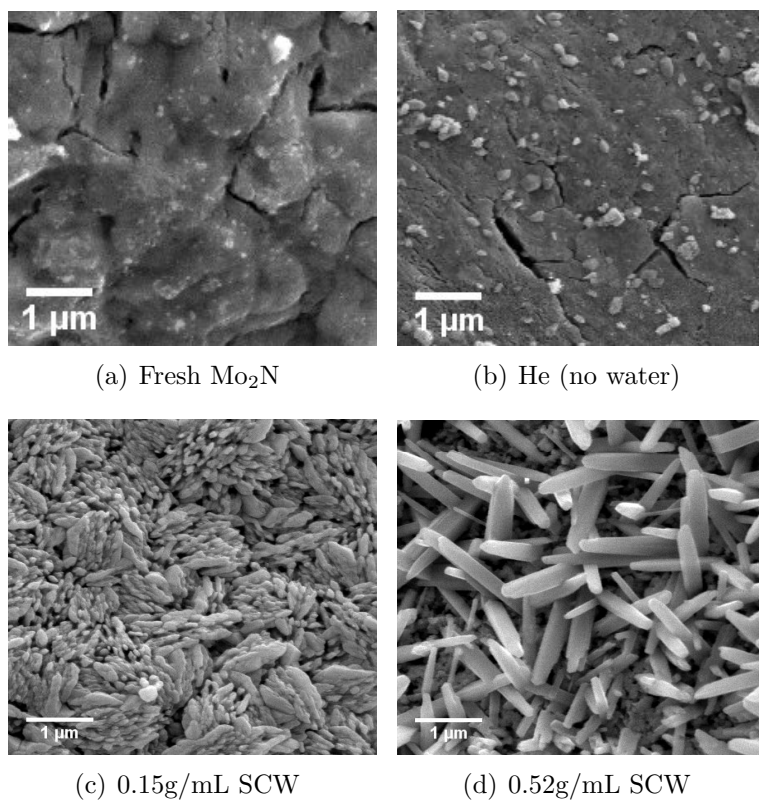
Figure A.20: SEM images of fresh Mo_2N (a) and Mo_2N after batch experiments at 400 °C for 60 min. in He (b), low ρ SCW (c), and high ρ SCW (d). The images were collected with 10 kV accelerating voltage and spot size 3.

Tungsten nitride

The WN was synthesized using a temperature-programmed reaction and approximately 50 mg was loaded in each batch reactor. The XRD spectra in Figure A.21 of the fresh WN has XRD peaks consistent with WN (85.2wt%) and WO_3 (14.8wt%). JADE XRD analysis software was used to determine the relative amounts of each phase. The WN recovered after the batch experiments in He (no water) contains a higher fraction of WO_3, however the sample still retained approximately 43wt% MoN. After 60 minutes exposure to both low- and high-density SCW, the recovered catalysts are predominately WO_3. From XRD analysis, we conclude SCW quickly oxidizes WN to form WO_3.

The SEM image in Figure A.22(a) of the fresh WN shows that the material surface is initially rough and porous, like the W_2C surface. The SEM images in Figure A.22(c) and Figure A.22(d) of WN after exposure to SCW show that the surface becomes densely coated in a randomly-oriented network of needle-like and rod-like particles. The particles are thinner and rougher in appearance after exposure to low-density (0.15g/mL) SCW (more needle-like). After exposure to high-density (0.52 g/mL) SCW, the particles are significantly thicker in diameter than the particles formed after low-density SCW. In addition, the surface of the rod-like particles formed after exposure to high-density SCW appears to have facets.
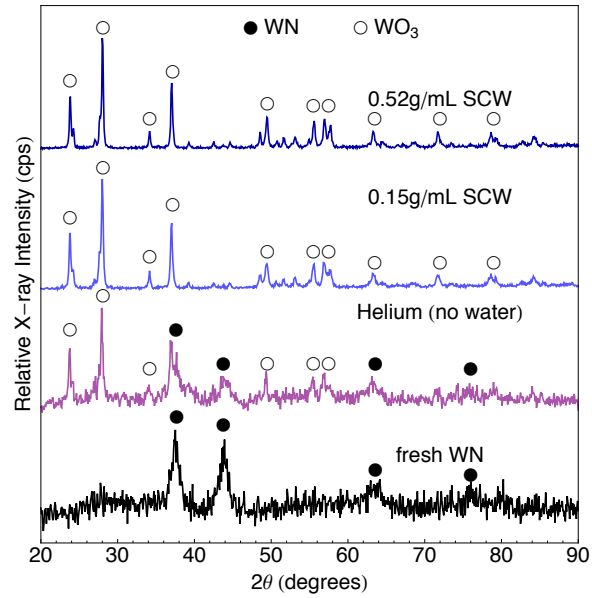
Figure A.21: X-ray diffraction of fresh WN and WN after 60 minute batch experiments at 400 °C in He, low-density (0.15g/mL) SCW, and high-density (0.52g/mL) SCW.

(a) Fresh WN

(b) He (no water)

(c) 0.15g/mL SCW

(d) 0.52g/mL SCW
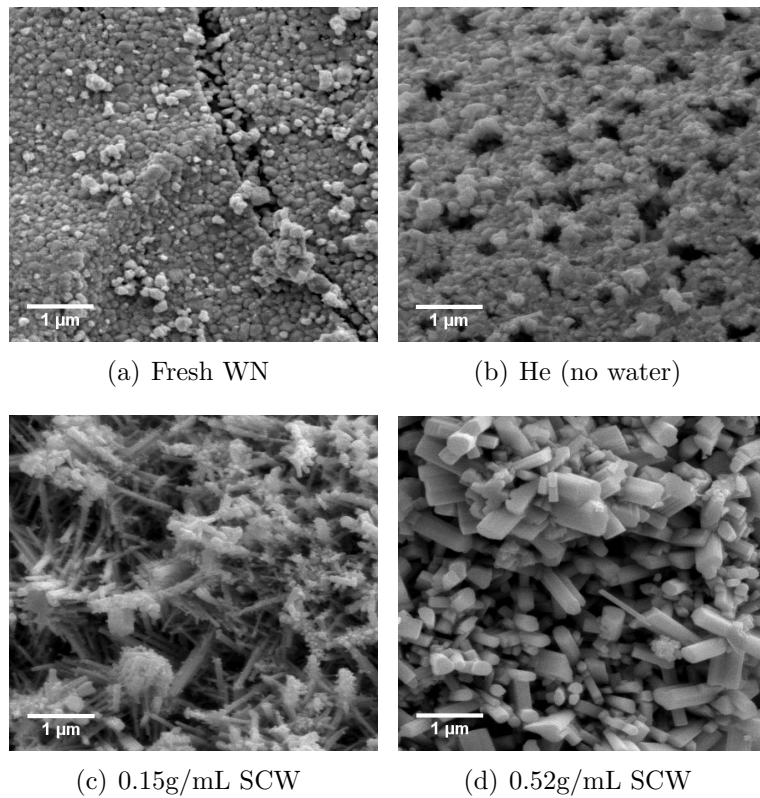
Figure A.22: SEM images of fresh WN (a) and WN after batch experiments at 400 °C for 60 min. in He (b), low ρ SCW (c), and high ρ SCW (d). The images were collected with 10 kV accelerating voltage and spot size 3.

APPENDIX B

Thermodynamic Model Parameters

The following tables contain the thermodynamic data and parameters used for calculating $\Delta G_f(T, P)$ values for the solid, aqueous, and gaseous species studied in this dissertation.

Table B.1 contains the ΔG_f^o, ΔH_f^o, S^o, V^o, and the $C_P(T)$ coefficients for 56 metals and oxides. The $C_P(T)$ coefficients correspond to the fitted polynomial in Equation (B.1) where $t = T/1000$ and T is in Kelvin.

$$C_P(T) = A + Bt + Ct^2 + Dt^3 + E/t^2 \tag{B.1}$$

Table B.2 contains values of ΔG_f^o, ΔH_f^o, S^o, C_P^o, V^o, a_1, a_2, a_3, a_4, c_1, c_2, ω_{T_r, P_r}, and r_e (with references) for all the aqueous inorganic species used to model catalyst dissolution.

$\Delta G_f(T, P)_j$ values for gaseous H_2 and O_2 were calculated using Equations (B.1), (2.5) and (2.6). ΔG_f^o, ΔH_f^o, S^o, and the $C_P(T)$ coefficients for gaseous H_2 and O_2 are tabulated in Table B.3. The ideal gas equation of state (IG-EOS) was used to solve the pressure integral ($V = RT/P$ where R is the ideal gas constant) because it can

be solved analytically as shown in eq. (B.2):

$$\Delta G_f(T, P) - \Delta G_f^o = - \int\limits_{298.15K}^{T} S(T)dT + RT \int\limits_{1bar}^{P} \frac{dP}{P} \tag{B.2}$$

While the Van der Waals equation of state (VDW-EOS) or another non-ideal EOS is preferred for modeling gases at high pressure, an analytical solution for molar volume from the VDW-EOS does not exist. To test the accuracy of the ideal gas assumption, $\Delta G_f(T, P)_j$ values calculated from the VDW-EOS were compared with values calculated from the IG-EOS at the extreme conditions of this study (22 MPa and 150 °C, 22 MPa and 550 °C, 50 MPa and 150 °C, 50 MPa and 550 °C). A root-solver program (NSolve) and a numerical integrator program (NIntegrate) in Wolfram Mathematica were used to evaluate the pressure integral in eq. (B.2) for H_2 and O_2 using the VDW-EOS. The difference between these values and those generated from the IG-EOS are < 1.2 kJ/mol, which is small compared to the overall values of ΔG_f for H_2 and O_2 (ranges from -5 to -80 kJ/mol) and for the solids (ranges from -5 to -10^7 kJ/mol). Therefore, any error arising from the ideal gas approximation is considered negligible.

Lastly, Table B.4 contains the HKF parameters for calculating $\Delta G_f(T, P)_j$ values for aqueous species in hydrothermal reaction solutions.

					Cp° coefficients for Equation (B.1) [d]					
Solid	ΔG_f^{o} [a]	ΔH_f^{o} [a]	S^{o} [b]	V^{o} [c]	A	B	C	D	E	Source [j,k]
Ag	0	0	42.68	10.28	20.694	14.708	-11.4188	5.76812	0.105816	[52]
Ag$_2$O	-11,184	-31,049	121.30	32.46	56.1185	55.8365	-34.8863	27.3917	-0.402769	[52]
Au	0	0	47.50	10.21	21.5201	14.2358	-13.9581	6.70133	0.054865	[52]
α-Al$_2$O$_3$	-1,582,300	-1,675,690	50.9	25.49	102.429	38.7498	-15.9109	2.628181	-3.007551	NIST
γ-Al$_2$O$_3$	-1,582,300	-1,675,690	50.9	25.49	108.683	37.2263	-14.2065	2.193601	-3.209881	NIST
Ce	0	0	69.45	20.77	28.5022	-7.95109	28.4669	-11.1651	-0.130962	[52]
Ce$_2$O$_3$	-1,707,925	-1,796,191	150.58	52.9	131.197	19.5318	-0.02435	0.01139	-1.73289	[52]
CeO$_2$	-1,025,379	-1,088,677	62.3	23.86	70.1418	9.22644	0.054113	-0.02222	-1.00123	[52]
Co	0	0	30.07	6.62	10.9943	54.375	-55.5132	25.817	0.164533	NIST
CoO	-214,200	-237,740	52.85	11.64	43.65	22.38373	-16.89386	6.556161	0.532263	NIST
Co(OH)$_2$	-454,168	-539,700	79.0	25.84	96.914	14.073	0.001	0	-0.9877	[85]
Co$_3$O$_4$	-794,901	-910,020	114.31	39.41	246.969	-343.788	481.918	-169.568	-5.31501	[52]
Cu	0	0	33.17	7.09	22.7489	9.95864	-8.56756	4.58639	-0.0562466	[52]
Cu$_2$O	-147,880	-170,707	92.34	23.85	63.2109	23.6737	-7.68232	2.69846	-0.632487	[52]
CuO	-128,292	-156,063	42.59	12.60	48.6344	7.2892	0.17937	-0.08048	-0.76249	[52]
Cu(OH)$_2$	-359,018	-443,086	87.03	28.97	53.54851	131.8144	-84.7009	18.07664	0.838997	[52]
Fe[f]	0	0	27.32	7.09	18.42868	24.64301	-8.91372	9.664706	-0.012643	NIST
Fe[g]					-57767.65	137919.7	-122773.2	38682.42	3993.08	NIST
Fe(OH)$_2$	-491,981[e]	-574,040	87.93	26.43	56.70701	132.1357	-83.59967	17.25465	0.711267	NIST
Fe$_3$O$_4$	-1,017,427[e]	-1,120,890	145.25	46.31	104.2096	178.5108	10.6151	1.132534	-0.994202	NIST
Fe$_2$O$_3$	-743,498[e]	-825,500	87.33	30.46	93.43834	108.3577	-50.86447	25.58683	-1.61133	NIST
Fe(OH)$_3$	-705,454[e]	-832,620	104.56	25.14	65.09091	182.2609	-100.7172	19.04084	-0.82534	NIST
Mo	0	0	28.6	9.33	24.72736	3.960425	-1.270706	1.153065	-0.170246	NIST
MoO$_2$	-533,042	-588,940	46.45	19.77	65.66788	11.56089	5.427778	0.000256	-1.217687	NIST
MoO$_3$	-668,017	-745,087	77.78	30.69	93.31366	-22.81113	52.63054	-12.74279	-1.416934	NIST
H$_2$MoO$_4$	-912,112	-1,046,000	121.34	52.24	N/A					[86]
Ni	0	0	29.87	6.59	13.6916	82.49509	-174.9548	161.6011	-0.092417	NIST
NiO	-211,539	-239,701	37.99	11.20	80.9833	-46.9115	13.0271	9.52576	-2.14491	[52]
Ni(OH)$_2$	-447,200	-529,700	88	22.62	92.949	13.372	0.006	0	-1.3278	[85]
Pd	0	0	37.82	8.86	23.97432	5.932912	0	0	-0.035564	[26]
PdO	-59,957	-85,354	55.23	14.68	44.990552	7.715296	0	0	-0.1142232	[26]
Pd(OH)$_2$	-301,248	-385,346	90.79	28.38	74.266	42.17472	0	0	-0.1142232	[26]
Pt	0	0	41.63	9.09	24.39272	5.25092	0	0	-0.0079496	[26]
Rh	0	0	31.51	8.28	23.97432	7.92868	0	0	-0.1393272	[26]
Rh$_2$O$_3$	-202,087	-285,767	90.08	31.37	86.77616	57.77392	0	0	0.00046024	[26]
Ru	0	0	28.53	8.175	20.92	7.096064	0	0	0.0933032	[26]
RuO$_2$	-253,090	-307,189	52.3	19.05	69.8729	10.46	0	0	-1.48532	[26]
Si	0	0	18.82	12.06	22.81719	3.89951	-0.082885	0.042111	-0.354063	NIST
SiO$_2$ (quartz)	-856,400	-910,860	41.46	22.69	-6.076591	251.6755	-324.7964	168.5604	0.002548	NIST
Ti	0	0	30.72	10.62	22.61942	18.98795	-18.18735	7.0080792	-0.143457	NIST
TiO	-536,302[e]	-542,660	34.76	12.90	41.78808	18.24542	-0.372713	0.065211	-0.644729	NIST
Ti$_2$O$_3$[h]	-1,433,846[e]	-1,520,880	77.25	32.02	280.3862	-665.2058	511.0882	792.4454	-4.682607	NIST
Ti$_2$O$_3$[i]					147.5509	3.649536	-0.081337	0.011812	-4.774029	NIST
TiO$_2$ (anatase)	-883,401[e]	-938,720	50.33	21.13	67.49796	18.27015	-11.25467	2.371717	-1.492815	NIST
TiO$_2$ (rutile)	-883,488[e]	-938,720	50.62	18.88	67.2983	18.7094	-11.579	2.449561	-1.485471	NIST
W	0	0	32.66	9.55	23.9593	2.63968	1.25775	-0.254642	-0.048407	NIST
WO$_2$	-533,878	-589,693	50.5	19.99	53.40876	53.53219	-39.0117	11.12019	-0.931241	NIST
WO$_3$	-764082	-842,867	75.91	32.38	30.5396	200.867	-206.248	76.5193	-0.088904	NIST
H$_2$WO$_4$	-999,976	-1,129,680	144.87	44.70	-76.71155	697.0628	-664.0259	227.2293	3.073428	NIST
Zn	0	0	41.63	9.16	25.60123	-4.405292	20.42206	-7.3997	-0.0458	NIST
ZnO	-320,500	-350,500	43.7	14.34	40.62					[87]
Zr	0	0	38.87	13.99	29.01663	-12.55597	20.74954	-5.914	-0.157249	NIST
ZrO$_2$	-1,039,715[e]	-1,097,460	50.34	21.69	69.20001	8.54829	-0.862921	0.246374	-1.382767	NIST

[a] J/mol   [b] J/mol-K   [c] cm^3/mol   [d] Cp° in units of J/mol-K   [e] Calculated from ΔH_{rxn}^{o} and ΔS_{rxn}^{o} of the elemental metal with O$_2$ (or H$_2$O)   [f] Cp° coefficients for 298-700K temperature range   [g] Cp° coefficients for 700-1042K temperature range   [h] Cp° coefficients for 298-470K temperature range   [i] Cp° coefficients for 470-2115K temperature range
[j] NIST: Thermochemistry data was accessed on the NIST Chemistry WebBook (http://webbook.nist.gov/chemistry/)
[k] C$_P$ coefficients from [52] were obtained by fitting C$_P$(T) data from $298.15 - 1000$ Kelvin to eq. (B.1)

Table B.1: Thermodynamic properties of solid catalysts at various oxidation states.

Species	ΔG_f^{o} [a]	ΔH_f^{o} [a]	S^{o} [b]	Cp^{o} [b]	V^{o} [c]	r_e [d]	a_1 [e]	a_2 [a]	a_3 [f]	a_4 [g]	c_1 [b]	c_2 [g]	$\Delta\omega$ [a]
Ag^+	77,099	105,751	73.4	33.05	-0.8	2.20	0.7232	-1,489.84	29.914	-110,115	53.50	-59,639	90,374
$AgOH$	-91,630	-133,051	72.0	-44.35	3.9	N/A	0.9575	-916.80	27.641	-112,478	-1.35	-217,304	-12,552
AgO^-	-23,012	-68,199	58.2	-135.14	-5.7	1.89	0.6125	-1,757.03	30.894	-109,006	3.68	-393,727	592,915
Au^{3+}	433,462	409,195	-229.3	-34.31	-31.4	3.71	-0.7183	-5,006.32	43.661	-95,575	98.65	-196,849	1,008,972
Au^+	163,176	200,414	107.1	-1.26	12.5	2.36	1.4775	352.63	22.652	-117,725	31.42	-129,520	68,952
Al^{3+}	-483,708	-530,673	-325.1	-135.98	-44.4	3.42	-1.4143	-7,115.77	-8.685	-84,747	44.77	-337,230	1,151,855
$AlOH^{2+}$	692,347	-766,927	-184.9	55.23	-2.2	2.37	0.8564	-1,163.70	28.609	-111,458	124.65	-14,464,	721,614
AlO^+	-661,859	-715,046	-113.0	-125.52	0.6	1.11	0.9081	-1,038.09	28.134	-111,976	-10.87	-382,648	400,409
$HAlO_2$	-869,017	-951,860	20.9	-209.20	13	N/A	1.4785	355.01	22.649	-117,738	-97.96	-553,104	-12,552
AlO_2^-	-831,332	-929,371	-32.9	-49.79	10	1.38	1.5573	1,671.68	-6.644	-123,181	63.76	-228,384	728,769
Ce^{4+}	-507,519	-576,137	-418.8	0.42	-53.3	4.78	-1.7904	-7,625.21	53.972	-84,747	168.53	-126,110	1,546,574
$Ce(OH)^{3+}$	-749,350[h]	-835,147[i]	-243.2[j]	121.63[j]	-4.4[j]	3.62[k]	0.8837[m]	-1,098.08[m]	28.374[m]	-111,734[m]	193[n]	120,794[n]	1,051,074[p]
$Ce(OH)_2^{2+}$	-1,012,500[h]	-1,137,903[i]	-142.9[j]	-91.54[j]	-0.56[j]	2.48[k]	0.9600[m]	-911.7[m]	27.642[m]	-112,504[m]	33.42[n]	-313,431[n]	671,493[p]
Ce^{3+}	-676,134	-700,402	-205	-199.58	-44.1	3.79	-1.4574	-6,811.10	50.753	-88,111	-1.49	-533,502	973,408
$CeOH^{2+}$ [q]	-865,251	-912,949	-11.3	-142.67	4.5	3.01	1.1516	-443.76	25.804	-114,437	-15.41	-416,756	460,240
CeO^+ [q]	-819,646	-874,038	56.1	-318.40	7.0	1.89	1.1886	-352.71	25.427	-114,813	-147.34	-775,550	146,063
$HCeO_{2(aq)}$ [q]	-1,001,231	-1,043,908	203.0	-563.27	23.8	N/A	2.0969	1,864.02	16.732	-123,979	-305.76	-1,274,356	-15,899
CeO_2^- [q]	-929,266	-963,575	161.5	-477.39	21.4	3.33	2.1115	1,900.21	16.580	-124,127	-213.71	-1,099,417	437,186
Ce^{2+}	-313,382	-294,135	5.9	-51.04	-14.5	3.14	0.055	-3,118.70	36.256	-103,378	35.88	-230,940	434,132
Co^{2+}	-54,392	-58,158	-113	-32.64	-25.5	2.6	-0.5126	-3,738.70	22.255	-100,813	63.6	-193,443	617,935
Co^{3+}	133,888	92,048	-305.4	-103.34	-40.5	3.45	-1.1999	-6,183.00	48.3	-90,709	68.93	-337,477	1,125,538
$Co(OH)_{2\ (aq)}$	-410,760[r]	-520,190[r]	-3.6[r]	124[r]	-12.4[j]	N/A	-0.0245[m]	-3,195.83[m]	36.619[m]	-103,062[m]	97.33[n]	125,620[n]	-12,552
$CoOH^+$	-234,409	-286,395	-41.8	100.42	-16.5	1.35	-0.1072	-3,516.20	37.847	-101,734	111.65	77,580	293,006
$HCoO_2^-$	-348,946	-489,946	-106.7	142.67	-18.6	1.13	-0.0406	-3,353.70	37.207	-102,403	187.32	163,661	845,628
$CoO_{(aq)}$	-184,096	-246,019	-74.5	20.08	-24.2	N/A	-0.6513	-4,842.40	43.008	-96,249	36.41	-86,052	-12,552
CoO_2^{2-}	-264,429	-414,216	-136.8	-132.21	-22.5	2.5	-0.0247	-3,314.50	37.045	-102,567	91.43	-396,283	1,553,394
$CoOH^{2+}$	-96,232	-151,042	-27.8	-23.01	-24.5	2.6	-0.4554	-4,366.10	41.181	-98,219	69.24	-173,841	617,935
Cu^+	49,999	71,680	30.9	65.71	-11.0	1.71	0.1782	-2,820.66	35.145	-10,4613	80.81	6,888	180,838
Cu^{2+}	65,040[r]	64,900[r]	-97[r]	-20[r]	-21.3[j]	2.6[k]	-0.2552[m]	-3,878.75[m]	39.304[m]	-100,239[m]	69.01[n]	-167,708[n]	602,066[p]
$CuOH^+$	-116,000[r]	-115,870[r]	136.1[r]	-11.1[r]	2.6[j]	2.8[k]	0.8976[m]	-1,063.99[m]	28.240[m]	-111,875[m]	21.26[n]	-149,578[n]	21,509[p]
$Cu(OH)_{2\ (aq)}$	-315,980[r]	-408,320[r]	59.3[r]	-132.45[j]	-5.6[j]	N/A	0.4364[m]	-2,190.14[m]	32.667[m]	-107,219[m]	-47.04[n]	-396,777[n]	52,452[y]
$Cu(OH)_3^-$	-498,980[r]	-659,280[r]	63.9[r]	142[r]	3.45[j]	2.0[k]	1.1556[m]	-434.08[m]	25.764[m]	-114,479[m]	162.09[n]	162,286[n]	581,620[p]
$Cu(OH)_4^{2-}$	-658,350[r]	-917,960[r]	-52.9[r]	-323.73[j]	-11.6[j]	2.8[k]	0.6157[m]	-1,752.34[m]	30.946[m]	-109,029[m]	-32.83[n]	-786,403[n]	1,436,859[p]
Fe^{2+}	-91,504	-92,257	-105.9	-33.05	-22.2	2.64	-0.3292	-4,057.18	39.948	-99,496	61.86	-194,292	601,743
$FeOH^+$	-275,516	-326,687	-41.8	62.76	-16.5	1.34	-0.1072	-3,516.19	37.847	-101,734	89.58	874.5	293,006

Table B.2: Thermodynamic properties and R-HKF parameters of aqueous metal-containing species used to model catalyst dissolution. Values were obtained from Shock et al (1997) [25] unless otherwise specified.

Species	$\Delta G_f^{o\ a}$	$\Delta H_f^{o\ a}$	$S^{o\ b}$	$Cp^{o\ b}$	$V^{o\ c}$	$r_e^{\ d}$	$a_1^{\ e}$	$a_2^{\ a}$	$a_3^{\ f}$	$a_4^{\ g}$	$c_1^{\ b}$	$c_2^{\ g}$	$\Delta\omega^{\ a}$
$FeO_{(aq)}$	-212,212	-263,383	41.8	0	-16.5	N/A	-0.2104	-3,767.78	38.824	-100,692	24.64	-126,963	-12,552
$HFeO_2^-$	-399,154	-525,929	-62.8	92.05	-12.9	1.26	0.2624	-2,612.49	34.269	-105,470	151.30	60,534	776,718
Fe^{3+}	-17,238	-49,580	-277.4	-77.82	-37	3.56	-1.0149	-5,730.45	46.501	-92,579	79.69	-285,487	1,079,974
$FeOH^{2+}$	-241,835	-292,880	-106.3	-34.32	-24.9	2.64	-0.4838	-4,435.42	41.454	-97,935	61.13	-196,849	601,743
FeO^+	-222,170	-255,224	-46.4	-201.25	-41.8	1.32	-1.5530	-7,046.19	51.712	-87,140	-64.43	-536,912	300,871
$HFeO_{2\ (aq)}$	-423,002	-503,335	92.9	-312.13	7.2	N/A	1.1465	-456.27	25.847	-114,382	-158.28	-762,764	-12,552
FeO_2^-	-368,192	-463,169	44.4	-235.56	0.9	1.79	0.9973	-820.15	27.272	-112,880	-55.73	-606,797	613,458
MoO_4^{2-}	-838,474	-997,047	37.7	-198.74	30.4	3.26	2.9142	1,133.70	78.081	-120,955	27.96	-531,795	1,287,710
$HMoO_4^-$	-863,996	-997,884	136	119.66	40.8	2.81	3.2351	4,642.80	5.819	-135,461	139.72	116,784	475,261
$H_2MoO_{4\ (aq)}$	-877,573^s	-1,027,986^i	82.0^t	111.4^t	52.2^t	N/A	3.7193^m	5,825.59^m	1.160^m	-140,356^m	209.96^n	519,679^n	-9,990^t
Ni^{2+}	-45,606	-53,974	-128.9	-48.12	-29	2.57	-0.7089	-4,986.50	43.658	-95,659	55.19	-226,685	630,400
$NiOH^+$	-221,124	-283,048	-75.3	130.12	-20.1	1.22	-0.296	-3,976.90	39.648	-99,830	133.51	137,239	344,010
$NiO_{(aq)}$	-164,599	-235,266	-104.6	41.84	-23.3	N/A	-0.5974	-4,714.38	42.588	-96,784	49.18	-41,740	-12,552
$HNiO_2^-$	-343,004	-496,892	-237.7	201.67	-24.2	1.02	-0.3407	-4,084.40	40.036	-99,383	227.01	282,127	906,420
NiO_2^{2-}	-268,613	-425,931	-162.8	-17.5	-25.8	2.44	-0.2014	-3,744.40	38.7	-100,788	129.33	-276,115	1,589,585
$Ni(OH)_2$	-410,360^r	-542,370^r	-77.1^r	23.04^r	-20.3^j	N/A	-0.4281^m	-4,300.91^m	40.963^m	-98,493^m	38.16^n	-80,031^n	-12,552
$Pd^{2+\ u}$	176,565	177,987	-88.3	-23.85	-19.4	2.52	-0.1519	-3,623.40	38.225	-101,290	71.93	-175,372	609,776
$PdOH^{+\ u}$	-54,936	-101,002	-14.2	53.56	-13.5	1.46	0.0513	3,127.20	36.274	-103,341	80.56	-17,870	253,676
$PdO_{(aq)}^{\ u}$	-48,116	-101,755	-39.7	-19.66	-16.3	N/A	-0.1989	-3,740.40	38.727	-100,805	13.12	-167,021	-12,552
$Pd(OH)_{2\ (aq)}$	-284,512	-422,777	-88.7	-22.73	-21.54	N/A	-0.4995	-4,475.30	41.649	-97,772	11.34	-173,264	-12,552
$Pt^{2+\ u}$	257,734	254,806	-98.7	-29.29	-21.7	2.68	-0.2782	-3,932.30	39.452	-100,014	70.3	-186,707	669,649
$PtOH^{+\ u}$	6,527	-44,769	-28	69.45	-15	1.4	-0.0276	-3,320.00	37.036	-102,546	91.78	14,510	274,345
$PtO_{(aq)}^{\ u}$	-4,728	-64,015	-54.4	-2.93	-17.9	N/A	-0.2906	-3,962.50	39.567	-99,889	22.93	-132,930	-12,552
$Rh^{2+\ u}$	115,897	110,458	-117.6	-39.33	-25.9	2.6	-0.5355	-4,560.90	41.925	-97,416	59.7	-206,991	617,935
$RhOH^{+\ u}$	-76,525	-132,214	-52.7	97.91	-17.7	1.3	-0.1705	-3,668.90	38.405	-101,102	111.64	72,467	308,947
$RhO_{(aq)}^{\ u}$	-30,208	-94,307	-81.2	27.61	-20.7	N/A	-0.4509	-4,354.50	41.119	-98,270	40.83	-70,714	-12,552
$Rh^{3+\ u}$	219,451	179,201	-299.6	-126.36	-43.5	3.49	-1.3751	-6,611.60	49.995	-88,935	54.49	-384,351	1,115,203
$RhOH^{2+\ u}$	-3,431	-64,475	-136	-0.42	-0.3	2.53	0.9401	-960.1	27.825	-112,299	85.21	-127,817	647,474
$RhO^{+\ u}$	13,138	-41,882	-78.2	-165.27	1.9	1.21	0.9651	-900.2	27.615	-112,550	-38.93	-463,612	348,695
$RuO_{4\ (aq)}$	-146,440	-238,488	129.7	132.38	19.45	3.38	1.8473	1,254.80	19.126	-121,461	102.24	142,694	-12,552
RuO_4^{2-}	-299,574	-461,077	27.6	-201.25	30.2	3.21	2.908	3,844.60	8.948	-132,164	27.91	-536,912	1,303,107
$Ru^{2+\ u}$	150,206	147,486	-111.3	-35.98	-24.5	2.62	-0.4564	-4,368.70	41.189	-98,207	60.89	-200,259	609,776
$RuOH^{+\ u}$	-43,806	-96,106	-44.4	88.28	-16.8	1.34	-0.123	-3,553.00	37.949	-101,579	104.89	52,865	296,897
$RuO_{(aq)}^{\ u}$	962	-59,664	-72.4	17.57	-19.8	N/A	-0.3994	-4,228.30	40.617	-98,788	34.94	-91,169	-12,552

Table B.2: Thermodynamic properties and R-HKF parameters of aqueous metal-containing species used to model catalyst dissolution. Values were obtained from Shock et al (1997) [25] unless otherwise specified.

Species	ΔG_f^{o} [a]	ΔH_f^{o} [a]	S^{o} [b]	Cp^{o} [b]	V^{o} [c]	r_e [d]	a_1 [e]	a_2 [a]	a_3 [f]	a_4 [g]	c_1 [b]	c_2 [g]	$\Delta\omega$ [a]
Ru^{3+} [u]	173,385	135,018	-296.2	-94.98	-39.4	3.5	-1.1421	-6,041.90	47.743	-91,291	72.33	-320,687	1,110,099
$RuOH^{2+}$ [u]	-51,003	-109,914	-131.8	-5.44	0.1	2.51	0.9501	-936.5	27.755	-112,399	81.87	-138,043	643,164
RuO^{+} [u]	-43,723	-96,441	-73.2	-171.13	2.1	1.23	0.975	-876.3	27.527	-112,646	-42.8	-475,545	344,008
$HSiO_3^{-}$ [v]	-1,015,879	-1,145,880	20.92	-87.86	5	1.64	1.2441	-216.77	24.881	-115,374	34.09	-305,947	648,980
$SiO_{2\ (aq)}$ [w]	-833,411	-877,699	75.3	-318.40	16.1	N/A	0.7950	711.28	83.680	-112,968	121.75	-2,142,208	54,015
Ti^{4+}	-354,180[x]	-457,000[x]	-575.3[x]	-48.22 [j]	-57.1 [j]	4.14[k]	-1.9547[m]	-7,784.15[m]	54.654[m]	-84,094[m]	160.07[n]	-225,193[n]	1,781,501[p]
$TiOH^{3+}$	-614,000[x]	-757,399[i]	-449.8 [j]	357.10 [j]	-12.3 [j]	3.06[k]	0.5496[m]	-1,913.72[m]	31.580[m]	-108,362[m]	359.52[n]	600,454[n]	1,363,844[p]
$Ti(OH)_2^{2+}$	-862,160[x]	-976,020[x]	-146.1[x]	-87.83 [j]	-0.69 [j]	2.47[k]	0.9547[m]	-924.55[m]	27.692[m]	-112,451[m]	36.04[n]	-305,884[n]	676,413[p]
$Ti(OH)_3^{+}$	-1,086,210[x]	-1,239,010[i]	-87.9[j]	100[j]	6.45[j]	1.19[k]	1.244[m]	-218.4[m]	24.916[m]	-115,371[m]	117.32[n]	76,724[n]	360,782[p]
$Ti(OH)_4^{0}$	-1,312,480[x]	-1,511,809[x]	21.9[x]	202.9[j]	13.01[j]	N/A	1.4786[m]	354.5[m]	22.665[m]	-117,739[m]	143.57[n]	286,340[n]	-12,552
$Ti(OH)_5^{-}$	-1,479,200[x]	-1,733,860[x]	80.8[x]	-284.64[j]	26.06[j]	2.10[k]	2.4406[m]	2,703.31[m]	13.433[m]	-125,449[m]	-90.29[n]	-706,779[n]	556,030[p]
WO_4^{2-}	-914,204	-989,516	40.6	-186.19	32.2	3.34	3.0156	3,679.10	18.782	-131,478	34.86	-506,226	1,282,689
HWO_4^{-}	-934,706	-1,066,920	130.5	128.03	41	2.69	3.2493	4,678.50	5.662	-135,612	145.39	133,829	483,629
$H_2WO_{4\ (aq)}$	947,652[s]	-1,071,004[y]	160.3[y]	-242.48[z]	45[z]	N/A	3.3285[m]	4,871.42[m]	4.911[m]	-136,412[m]	-113.16[m]	-621,390	36,094[z]
Zn^{2+}	-147,277	-153,385	-109.6	-22.3	-24.3	2.59	-0.4467	-3,735.90	25.64	-100,826	78.41	-224,681	609,776
$ZnOH^{+}$	-339,699	-363,966	62.8	41.84	-5.3	1.94	0.4811	-2,078.50	32.173	-107,675	62.89	-41,735	136,398
$ZnO_{(aq)}$	-282,085	-327,565	-8.4	-41.84	-21.9	N/A	-0.5196	-4,521.70	41.764	-97,575	0.12	-212,192	-12,552
$HZnO_2^{-}$	-463,252	-595,676	-66.9	83.68	-13.4	1.25	0.2353	-2,679.70	34.555	-105,190	146.81	43,488	781,111
ZnO_2^{2-}	-390,325	-552,706	-167.4	-62.76	-26.4	2.4	-0.2326	-3,822.00	39.037	-100,470	136.33	-254,806	1,598,957
Zr^{4+}	-557,602	-628,981	-461.5	-12.97	-54.3	4.55	-1.8272	-7,714.30	54.313	-84,379	166.28	-153,385	1,607,367
$ZrOH^{3+}$	-796,634	-889,100	-299.6	185.77	-12.7	3.45	0.3882	-2,305.10	33.06	-106,738	237.42	251,446	1,115,203
ZrO^{2+}	-784,918	-854,791	-223.4	0.42	-3.6	2.23	0.7955	-1,312.30	29.191	-110,843	97.79	-126,110	778,684
$HZrO_2^{+}$	-1,002,905	-1,110,015	-207.9	373.7	-0.7	1.22	0.8831	-1,100.40	28.4	-111,721	295.12	634,119	546,430
$ZrO_{2\ (aq)}$	-976,546	-1,103,739	-182.8	232.21	0.8	N/A	0.78	-1,349.90	29.338	-110,688	160.74	346,050	-12,552
$HZrO_3^{-}$	-1,177,796	-1,394,527	-136.8	211.71	7.9	1.05	1.4906	383.6	22.552	-117,855	231.59	304,286	886,966

[a] J/mol   [b] J/mol-K   [c] cm^3/mol   [d] effective radius, Å   [e] J/mol-bar   [f] J-K/mol-bar   [g] J-K/mol   [h] Hayes et al (2002) [88]
[i] Calculated from ΔG_{rxn}^{o} and ΔS_{rxn}^{o} of the species with another aqueous species and OH⁻ (and/or H_2O)   [j] Estimated from correlations in Shock et al (1997) [25]
[k] r_e calculated from S^{o} using eq. (57) in Shock and Helgeson (1988) [21]   [m] a_i values calculated from V^{o} and $\Delta\omega$ using equations in Shock and Helgeson (1988) [21]
[n] c_i values calculated from Cp^{o} and $\Delta\omega$ using eq. (31) and eq. (89) in Shock and Helgeson (1988) [21]   [p] $\Delta\omega$ calculated from r_e using eq. (2.8) (this text).
[q] Thermodynamic properties and HKF parameters obtained from Haas et al (1995) [24]   [r] Ziemniak (2000) [89]   [s] Ryzhenko et al (2010) [63]   [t] Cp^{o} from Hurtig and Williams-Jones (2014) [65] and $\Delta\omega$ fitted from experimental data from Minubayeva and Seward (2010) [64]   [u] Thermodynamic properties and HKF parameters obtained from Sassani and Shock (1998) [26]   [v] Thermodynamic properties and HKF parameters obtained from Sverjenski et al (1997) [90]   [w] Thermodynamic properties and HKF parameters obtained from Shock et al (1989) [22]   [x] Ziemniak et al (1993) [91]   [y] ΔH_f^{o} and S^{o} calculated from experimental $\Delta G_f(T, P)$ values using $\Delta H = (\frac{\partial(\Delta G/T)}{\partial(1/T)})_P$ and $S = -(\frac{\partial G}{\partial T})_P$ [92]
[z] Parameter fitted from experimental data obtained from Ivanova and Khodakovskii (1968) , Bryzgalin (1983), and Wood (1992) [92, 93]

Table B.2: Thermodynamic properties and R-HKF parameters of aqueous metal-containing species used to model catalyst dissolution. Values were obtained from Shock et al (1997) [25] unless otherwise specified.

Gas	$\Delta G_f^{o\ a}$	$\Delta H_f^{o\ a}$	$S^{o\ b}$	Cp^o coefficients [c]					Source[d]
				A	B	C	D	E	
H_2	0	0	130.68	33.066178	-11.363417	11.432816	-2.772874	-0.158558	NIST
O_2	0	0	205.15	31.32234	-20.23531	57.86644	-36.50624	-0.007374	NIST

[a] J/mol   [b] J/mol-K   [c] Cp^o in units of J/mol-K   [d] NIST: Thermochemistry data was accessed on the NIST Chemistry WebBook (http://webbook.nist.gov/chemistry/)

Table B.3: Thermodynamic properties of gaseous H_2 and O_2.

Species	$\Delta G_f^{o\ a}$	$\Delta H_f^{o\ a}$	$S^{o\ b}$	Cp$^{o\ b}$	$V^{o\ c}$	$r_e{}^d$	$a_1{}^e$	$a_2{}^a$	$a_3{}^f$	$a_4{}^g$	$c_1{}^b$	$c_2{}^g$	$\Delta\omega{}^a$
$H_{2\ (aq)}$	17,723	-4,184	57.7	166.94	25.2	-	2.1517	1,998.20	16.204	-124,533	115.58	213,091	-87,446
$O_{2\ (aq)}$	16,544	-12,134	109.0	234.30	30.38	-	2.4221	2,658.35	13.610	-127,265	147.92	350,310	-164,975
$N_{2\ (aq)}$	18,188	-10,439	95.8	234.30	33.3	-	2.5960	3,082.98	11.941	-129,018	149.75	350,310	-145,101
$CH_{4\ (aq)}$	-34,451	-87,906	87.8	277.40	37.3	-	2.8291	3,651.75	9.712	-131,365	176.12	438,094	-133,009
$CO_{2\ (aq)}$	-385,974	-413,798	117.6	243.09	32.8	-	2.6136	3,125.91	11.772	-129,198	167.50	368,209	-8,368
HCO_3^-	-586,940	-689,933	98.4	-35.40	24.6	2.26	3.1640	481.37	5.166	-118,265	54.14	-199,071	532,749
CO_3^{2-}	-527,983	-675,235	-50.0	-290.79	-5.02	2.87	1.1934	-1,667.07	26.837	-109,382	-13.89	-719,301	1,418,962
$NH_{3\ (aq)}$	-26,706	-81,337	107.8	74.89	24.43	-	2.1301	1,170.26	36.086	-121,110	84.94	-48,953	-20,920
NH_4^+	-79,454	-133,260	111.2	65.86	18.13	2.41	1.6218	981.06	35.817	-120,328	73.01	-879	62,844
HCOOH	-372,301	-425,429	162.8	79.50	34.69	-	2.6760	1,951.00	44.856	-124,336	92.85	-130,524	-144,013
$HCOO^-$	-350,879	-425,429	90.8	-92.05	26.16	2.18	2.4201	2,652.87	13.642	-127,235	71.13	-518,816	544,046

[a] J/mol   [b] J/mol-K   [c] cm^3/mol   [d] effective radius, Å   [e] J/mol-bar   [f] J-K/mol-bar   [g] J-K/mol

Table B.4: HKF parameters for aqueous species in reaction solutions. Values were obtained from Shock et al [22, 25, 94].

APPENDIX C

Reaction Equations for Calculating Catalyst Oxidation, Dissolution, and Oxygen Fugacity-pH Diagrams

Tables C.1 to C.10 contain all the reactions considered in the oxidation and dissolution modeling of each catalyst and the material-specific equations used to calculate total solubility and $f_{O_2} - pH$ boundaries. Table C.11 contains dissolution reactions for additional elements that were used to correlate solubility with material properties. Table C.12 contains all the reactions used to calculate f_{O_2} and pH of different solutes in H_2O.

Reactant/Product [a]	Reaction	K_{eq} expression [b,c,d]	f_{O_2}-pH equation [b,c,d,e]
$Ce_{(s)}/Ce_2O_{3(s)}$	$Ce + \frac{3}{4}O_2 \rightleftharpoons \frac{1}{2}Ce_2O_3$	$K_{eq} = \frac{1}{(f_{O_2})^{\frac{3}{4}}}$	$logf_{O_2} = \frac{4}{3}log(\frac{1}{K_{eq}})$
$Ce_2O_{3(s)}/CeO_{2(s)}$	$\frac{1}{2}Ce_2O_3 + \frac{1}{4}O_2 \rightleftharpoons CeO_2$	$K_{eq} = \frac{1}{(f_{O_2})^{\frac{1}{4}}}$	$logf_{O_2} = 4log(\frac{1}{K_{eq}})$
$Ce_{(s)}/Ce^{2+}_{(aq)}$	$Ce + \frac{1}{2}O_2 + 2H^+ \rightleftharpoons Ce^{2+} + H_2O$	$K_{eq} = \frac{(a_{Ce2+})}{(a_{H+})^2(f_{O_2})^{\frac{1}{2}}}$	$logf_{O_2} = 4pH + 2log(\frac{a_{Ce2+}}{K_{eq}})$
$Ce_{(s)}/Ce^{3+}_{(aq)}$	$Ce + \frac{3}{4}O_2 + 3H^+ \rightleftharpoons Ce^{3+} + \frac{3}{2}H_2O$	$K_{eq} = \frac{(a_{Ce3+})}{(a_{H+})^3(f_{O_2})^{\frac{3}{4}}}$	$logf_{O_2} = 4pH + \frac{4}{3}log(\frac{a_{Ce3+}}{K_{eq}})$
$Ce_{(s)}/CeOH^{2+}_{(aq)}$	$Ce + \frac{3}{4}O_2 + 2H^+ \rightleftharpoons CeOH^{2+} + \frac{1}{2}H_2O$	$K_{eq} = \frac{(a_{CeOH2+})}{(a_{H+})^2(f_{O_2})^{\frac{3}{4}}}$	$logf_{O_2} = \frac{8}{3}pH + \frac{4}{3}log(\frac{a_{CeOH2+}}{K_{eq}})$
$Ce_{(s)}/CeO^{+}_{(aq)}$	$Ce + \frac{3}{4}O_2 + H^+ \rightleftharpoons CeO^+ + \frac{1}{2}H_2O$	$K_{eq} = \frac{(a_{CeO+})}{(a_{H+})(f_{O_2})^{\frac{3}{4}}}$	$logf_{O_2} = \frac{4}{3}pH + \frac{4}{3}log(\frac{a_{CeO+}}{K_{eq}})$
$Ce_{(s)}/HCeO_{2(aq)}$	$Ce + \frac{3}{4}O_2 + \frac{1}{2}H_2O \rightleftharpoons HCeO_{2(aq)}$	$K_{eq} = \frac{(a_{HCeO_2})}{(f_{O_2})^{\frac{3}{4}}}$	$logf_{O_2} = \frac{4}{3}log(\frac{a_{HCeO_2}}{K_{eq}})$
$Ce_{(s)}/CeO_{2(aq)}^{-}$	$Ce + \frac{3}{4}O_2 + OH^- \rightleftharpoons CeO_2^- + \frac{1}{2}H_2O$	$K_{eq} = \frac{(a_{CeO_2^-})}{(a_{OH-})(f_{O_2})^{\frac{3}{4}}}$	$logf_{O_2} = -\frac{4}{3}pH + \frac{4}{3}log\frac{a_{CeO_2^-}}{K_{eq}K_W}$
$Ce_{(s)}/Ce^{4+}_{(aq)}$	$Ce + O_2 + 4H^+ \rightleftharpoons Ce^{4+} + 2H_2O$	$K_{eq} = \frac{(a_{Ce4+})}{(a_{H+})^4(f_{O_2})}$	$logf_{O_2} = 4pH + log(\frac{a_{Ce4+}}{K_{eq}})$
$Ce_{(s)}/CeOH^{3+}_{(aq)}$	$Ce + O_2 + 3H^+ \rightleftharpoons CeOH^{3+} + H_2O$	$K_{eq} = \frac{(a_{CeOH3+})}{(a_{H+})^3(f_{O_2})}$	$logf_{O_2} = 3pH + log(\frac{a_{CeOH3+}}{K_{eq}})$
$Ce_{(s)}/Ce(OH)_2{}^{2+}_{(aq)}$	$Ce + O_2 + 2H^+ \rightleftharpoons Ce(OH)_2{}^{2+}$	$K_{eq} = \frac{(a_{Ce(OH)_2^{2+}})}{(a_{H+})^2(f_{O_2})}$	$logf_{O_2} = 2pH + log(\frac{a_{Ce(OH)_2^{2+}}}{K_{eq}})$
$Ce_2O_{3(s)}/Ce^{2+}_{(aq)}$	$\frac{1}{2}Ce_2O_3 + 2H^+ \rightleftharpoons Ce^{2+} + H_2O + \frac{1}{4}O_2$	$K_{eq} = \frac{(a_{Ce2+})(f_{O_2})^{\frac{1}{4}}}{(a_{H+})^2}$	$logf_{O_2} = -8pH - 4log(\frac{a_{Ce2+}}{K_{eq}})$
$Ce_2O_{3(s)}/Ce^{3+}_{(aq)}$	$\frac{1}{2}Ce_2O_3 + 3H^+ \rightleftharpoons Ce^{3+} + \frac{3}{2}H_2O$	$K_{eq} = \frac{(a_{Ce3+})}{(a_{H+})^3}$	$pH = -\frac{1}{3}log(\frac{a_{Ce3+}}{K_{eq}})$
$Ce_2O_{3\ (s)}/CeOH^{2+}_{(aq)}$	$\frac{1}{2}Ce_2O_3 + 2H^+ \rightleftharpoons CeOH^{2+} + \frac{1}{2}H_2O$	$K_{eq} = \frac{(a_{CeOH2+})}{(a_{H+})^2}$	$pH = -\frac{1}{2}log(\frac{a_{CeOH2+}}{K_{eq}})$
$Ce_2O_{3(s)}/CeO^{+}_{(aq)}$	$\frac{1}{2}Ce_2O_3 + H^+ \rightleftharpoons CeO^+ + \frac{1}{2}H_2O$	$K_{eq} = \frac{(a_{CeO+})}{(a_{H+})}$	$pH = -log(\frac{a_{CeO+}}{K_{eq}})$
$Ce_2O_{3(s)}/HCeO_{2(aq)}$	$\frac{1}{2}Ce_2O_3 + \frac{1}{2}H_2O \rightleftharpoons HCeO_{2(aq)}$	$K_{eq} = a_{HCeO_2}$	-
$Ce_2O_{3(s)}/CeO_{2(aq)}^{-}$	$\frac{1}{2}Ce_2O_3 + OH^- \rightleftharpoons CeO_2^- + \frac{1}{2}H_2O$	$K_{eq} = \frac{(a_{CeO_2^-})}{(a_{OH-})}$	$pH = log(\frac{a_{CeO_2^-}}{K_{eq}K_W})$
$Ce_2O_{3(s)}/Ce^{4+}_{(aq)}$	$\frac{1}{2}Ce_2O_3 + \frac{1}{4}O_2 + 4H^+ \rightleftharpoons Ce^{4+} + 2H_2O$	$K_{eq} = \frac{(a_{Ce4+})}{(a_{H+})^4(f_{O_2})^{\frac{1}{4}}}$	$logf_{O_2} = 16pH + 4log(\frac{a_{Ce4+}}{K_{eq}})$
$Ce_2O_{3(s)}/CeOH^{3+}_{(aq)}$	$\frac{1}{2}Ce_2O_3 + \frac{1}{4}O_2 + 3H^+ \rightleftharpoons CeOH^{3+} + H_2O$	$K_{eq} = \frac{(a_{CeOH3+})}{(a_{H+})^3(f_{O_2})^{\frac{1}{4}}}$	$logf_{O_2} = 12pH + 4log(\frac{a_{CeOH3+}}{K_{eq}})$
$Ce_2O_{3(s)}/Ce(OH)_2{}^{2+}_{(aq)}$	$\frac{1}{2}Ce_2O_3 + \frac{1}{4}O_2 + 2H^+ \rightleftharpoons Ce(OH)_2{}^{2+}$	$K_{eq} = \frac{(a_{Ce(OH)_2^{2+}})}{(a_{H+})^2(f_{O_2})^{\frac{1}{4}}}$	$logf_{O_2} = 8pH + 4log(\frac{a_{Ce(OH)_2^{2+}}}{K_{eq}})$
$CeO_{2(s)}/Ce^{2+}_{(aq)}$	$CeO_2 + 2H^+ \rightleftharpoons Ce^{2+} + H_2O + \frac{1}{2}O_2$	$K_{eq} = \frac{(a_{Ce2+})(f_{O_2})^{\frac{1}{2}}}{(a_{H+})^2}$	$logf_{O_2} = -4pH - 2log(\frac{a_{Ce2+}}{K_{eq}})$
$CeO_{2(s)}/Ce^{3+}_{(aq)}$	$CeO_2 + 3H^+ \rightleftharpoons Ce^{3+} + \frac{3}{2}H_2O + \frac{1}{4}O_2$	$K_{eq} = \frac{(a_{Ce3+})(f_{O_2})^{\frac{1}{4}}}{(a_{H+})^3}$	$logf_{O_2} = -12pH - 4log(\frac{a_{Ce3+}}{K_{eq}})$
$CeO_{2(s)}/CeOH^{2+}_{(aq)}$	$CeO_2 + 2H^+ \rightleftharpoons CeOH^{2+} + \frac{1}{2}H_2O + \frac{1}{4}O_2$	$K_{eq} = \frac{(a_{CeOH-})(f_{O_2})^{\frac{1}{4}}}{(a_{H+})^2}$	$logf_{O_2} = -8pH - 4log(\frac{a_{CeOH2+}}{K_{eq}})$
$CeO_{2(s)}/CeO^{+}_{(aq)}$	$CeO_2 + H^+ \rightleftharpoons CeO^+ + \frac{1}{2}H_2O + \frac{1}{4}O_2$	$K_{eq} = \frac{(a_{CeO+})(f_{O_2})^{\frac{1}{4}}}{(a_{H+})}$	$logf_{O_2} = -4pH - 4log(\frac{a_{CeO+}}{K_{eq}})$
$CeO_{2(s)}/HCeO_{2(aq)}$	$CeO_2 + \frac{1}{2}H_2O \rightleftharpoons HCeO_{2(aq)} + \frac{1}{4}O_2$	$K_{eq} = a_{HCeO_2}(f_{O_2})^{\frac{1}{4}}$	$logf_{O_2} = -4log(\frac{a_{HCeO_2}}{K_{eq}})$
$CeO_{2(s)}/CeO_{2(aq)}^{-}$	$CeO_2 + OH^- \rightleftharpoons CeO_2^- + \frac{1}{2}H_2O + \frac{1}{4}O_2$	$K_{eq} = \frac{(a_{CeO_2^-})(f_{O_2})^{\frac{1}{4}}}{(a_{OH-})}$	$logf_{O_2} = 4pH - 4log(\frac{a_{CeO_2^-}}{K_{eq}K_@})$
$CeO_{2(s)}/Ce^{4+}_{(aq)}$	$CeO_2 + 4H^+ \rightleftharpoons Ce^{4+} + 2H_2O$	$K_{eq} = \frac{(a_{Ce4+})}{(a_{H+})^4}$	$pH = -\frac{1}{4}log(\frac{a_{Ce4+}}{K_{eq}})$
$CeO_{2(s)}/CeOH^{3+}_{(aq)}$	$CeO_2 + 3H^+ \rightleftharpoons CeOH^{3+} + H_2O$	$K_{eq} = \frac{(a_{CeOH3+})}{(a_{H+})^3}$	$pH = -\frac{1}{3}log(\frac{a_{CeOH3+}}{K_{eq}})$
$CeO_{2(s)}/Ce(OH)_2{}^{2+}_{(aq)}$	$CeO_2 + 2H^+ \rightleftharpoons Ce(OH)_2{}^{2+}$	$K_{eq} = \frac{(a_{Ce(OH)_2^{2+}})}{(a_{H+})^2}$	$pH = -\frac{1}{2}log(\frac{a_{Ce(OH)_2^{2+}}}{K_{eq}})$

[a] s - solid, aq - aqueous   [b] log refers to log_{10} [c] the activity of aqueous species $a_j = \gamma_j m_j/m_\Theta$, where γ_j is the dimensionless activity coefficient, m_j is molal concentration (mol/kg H_2O), and $m_\Theta = 1$ mol/kg H_2O [d] fugacity f is in units of bar
[e] K_W is the dissociation constant of water in units of (mol/kg H_2O)^2

Table C.1: Equilibrium reaction equations used to model CeO_2 reduction and dissolution.

Reactant/Product [a]	Reaction	K_{eq} expression [b,c,d]	f_{O_2}-pH equation [b,c,d,e]
$Co_{(s)}/CoO_{(s)}$	$Co + \frac{1}{2}O_2 \rightleftharpoons CoO$	$K_{eq} = \frac{1}{(f_{O_2})^{\frac{1}{2}}}$	$log f_{O_2} = 2log(\frac{1}{K_{eq}})$
$Co_{(s)}/Co(OH)_{2(s)}$	$Co + \frac{1}{2}O_2 + H_2O \rightleftharpoons Co(OH)_2$	$K_{eq} = \frac{1}{(f_{O_2})^{\frac{1}{2}}}$	$log f_{O_2} = 2log(\frac{1}{K_{eq}})$
$CoO_{(s)}/Co(OH)_{2(s)}$	$CoO + H_2O \rightleftharpoons Co(OH)_2$	-	-
$CoO_{(s)}/Co_3O_{4(s)}$	$3CoO + \frac{1}{2}O_2 \rightleftharpoons Co_3O_4$	$K_{eq} = \frac{1}{(f_{O_2})^{\frac{1}{2}}}$	$log f_{O_2} = 2log(\frac{1}{K_{eq}})$
$Co(OH)_{2(s)}/Co_3O_{4(s)}$	$3Co(OH)_2 + \frac{1}{2}O_2 \rightleftharpoons Co_3O_4 + 3H_2O$	$K_{eq} = \frac{1}{(f_{O_2})^{\frac{1}{2}}}$	$log f_{O_2} = 2log(\frac{1}{K_{eq}})$
$Co_{(s)}/Co^{2+}_{(aq)}$	$Co + \frac{1}{2}O_2 + 2H^+ \rightleftharpoons Co^{2+} + H_2O$	$K_{eq} = \frac{(a_{Co2+})}{(a_{H+})^2(f_{O_2})^{\frac{1}{2}}}$	$log f_{O_2} = 4pH + 2log(\frac{a_{Co2+}}{K_{eq}})$
$Co_{(s)}/CoOH^+_{(aq)}$	$Co + \frac{1}{2}O_2 + H^+ \rightleftharpoons CoOH^+$	$K_{eq} = \frac{(a_{CoOH+})}{(a_{H+})(f_{O_2})^{\frac{1}{2}}}$	$log f_{O_2} = 2pH + 2log(\frac{a_{CoOH+}}{K_{eq}})$
$Co_{(s)}/CoO_{(aq)}$	$Co + \frac{1}{2}O_2 \rightleftharpoons CoO_{aq}$	$K_{eq} = \frac{(a_{CoOaq})}{(f_{O_2})^{\frac{1}{2}}}$	$log f_{O_2} = 2log(\frac{a_{CoOaq}}{K_{eq}})$
$Co_{(s)}/Co(OH)_{2(aq)}$	$Co + \frac{1}{2}O_2 + H_2O \rightleftharpoons Co(OH)_{2(aq)}$	$K_{eq} = \frac{a_{Co(OH)2(aq)}}{(f_{O_2})^{\frac{1}{2}}}$	$log f_{O_2} = 2log(\frac{a_{Co(OH)2(aq)}}{K_{eq}})$
$Co_{(s)}/HCoO^-_{2(aq)}$	$Co + \frac{1}{2}O_2 + OH^- \rightleftharpoons HCoO_2^-$	$K_{eq} = \frac{(a_{HCoO_2^-})}{(a_{OH-})(f_{O_2})^{\frac{1}{2}}}$	$log f_{O_2} = -2pH + 2log(\frac{a_{HCoO_2^-}}{K_{eq}K_W})$
$Co_{(s)}/CoO^{2-}_{2(aq)}$	$Co + \frac{1}{2}O_2 + 2OH^- \rightleftharpoons CoO_2^{2-} + H_2O$	$K_{eq} = \frac{(a_{CoO_2^{2-}})}{(a_{OH-})^2(f_{O_2})^{\frac{1}{2}}}$	$log f_{O_2} = -4pH + 2log(\frac{a_{CoO_2^{2-}}}{K_{eq}K_W^2})$
$Co_{(s)}/Co^{3+}_{(aq)}$	$Co + \frac{3}{4}O_2 + 3H^+ \rightleftharpoons Co^{3+} + \frac{3}{2}H_2O$	$K_{eq} = \frac{(a_{Co3+})}{(a_{H+})^3(f_{O_2})^{\frac{3}{4}}}$	$log f_{O_2} = 4pH + \frac{4}{3}log(\frac{a_{Co3+}}{K_{eq}})$
$Co_{(s)}/CoOH^{2+}_{(aq)}$	$Co + \frac{3}{4}O_2 + 2H^+ \rightleftharpoons CoOH^{2+} + \frac{1}{2}H_2O$	$K_{eq} = \frac{(a_{CoOH2+})}{(a_{H+})^2(f_{O_2})^{\frac{3}{4}}}$	$log f_{O_2} = \frac{8}{3}pH + \frac{4}{3}log(\frac{a_{CoOH2+}}{K_{eq}})$
$CoO_{(s)}/Co^{2+}_{(aq)}$	$CoO + 2H^+ \rightleftharpoons Co^{2+} + H_2O$	$K_{eq} = \frac{(a_{Co2+})}{(a_{H+})^2}$	$pH = -\frac{1}{2}log(\frac{a_{Co2+}}{K_{eq}})$
$CoO_{(s)}/CoOH^+_{(aq)}$	$CoO + H^+ \rightleftharpoons CoOH^+$	$K_{eq} = \frac{(a_{CoOH+})}{(a_{H+})}$	$pH = -log(\frac{a_{CoOH+}}{K_{eq}})$
$CoO_{(s)}/CoO_{(aq)}$	$CoO \rightleftharpoons CoO_{aq}$	$K_{eq} = a_{CoOaq}$	-
$CoO_{(s)}/Co(OH)_{2(aq)}$	$CoO + H_2O \rightleftharpoons Co(OH)_{2(aq)}$	$K_{eq} = a_{Co(OH)2(aq)}$	-
$CoO_{(s)}/HCoO^-_{2(aq)}$	$CoO + OH^- \rightleftharpoons HCoO_2^-$	$K_{eq} = \frac{(a_{HCoO_2^-})}{(a_{OH-})}$	$pH = log(\frac{a_{HCoO_2^-}}{K_{eq}K_W})$
$CoO_{(s)}/CoO^{2-}_{2(aq)}$	$CoO + 2OH^- \rightleftharpoons CoO_2^{2-} + H_2O$	$K_{eq} = \frac{(a_{CoO_2^{2-}})}{(a_{OH-})^2}$	$pH = \frac{1}{2}log(\frac{a_{CoO_2^{2-}}}{K_{eq}K_W^2})$
$CoO_{(s)}/Co^{3+}_{(aq)}$	$CoO + \frac{1}{4}O_2 + 3H^+ \rightleftharpoons Co^{3+} + \frac{3}{2}H_2O$	$K_{eq} = \frac{(a_{Co3+})}{(a_{H+})^3(f_{O_2})^{\frac{1}{4}}}$	$log f_{O_2} = 12pH + 4log(\frac{a_{Co3+}}{K_{eq}})$
$CoO_{(s)}/CoOH^{2+}_{(aq)}$	$CoO + \frac{1}{4}O_2 + 2H^+ \rightleftharpoons CoOH^{2+} + \frac{1}{2}H_2O$	$K_{eq} = \frac{(a_{CoOH2+})}{(a_{H+})^2(f_{O_2})^{\frac{1}{4}}}$	$log f_{O_2} = 8pH + 4log(\frac{a_{CoOH2+}}{K_{eq}})$
$Co(OH)_{2(s)}/Co^{2+}_{(aq)}$	$Co(OH)_2 + 2H^+ \rightleftharpoons Co^{2+} + 2H_2O$	$K_{eq} = \frac{(a_{Co2+})}{(a_{H+})^2}$	$pH = -\frac{1}{2}log(\frac{a_{Co2+}}{K_{eq}})$
$Co(OH)_{2(s)}/CoOH^+_{(aq)}$	$Co(OH)_2 + H^+ \rightleftharpoons CoOH^+ + H_2O$	$K_{eq} = \frac{(a_{CoOH+})}{(a_{H+})}$	$pH = -log(\frac{a_{CoOH+}}{K_{eq}})$
$Co(OH)_{2(s)}/CoO_{(aq)}$	$Co(OH)_2 \rightleftharpoons CoO_{aq} + H_2O$	$K_{eq} = a_{CoOaq}$	-
$Co(OH)_{2(s)}/Co(OH)_{2(aq)}$	$Co(OH)_2 \rightleftharpoons Co(OH)_{2(aq)}$	$K_{eq} = a_{Co(OH)2(aq)}$	-
$Co(OH)_{2(s)}/HCoO^-_{2(aq)}$	$Co(OH)_2 + OH^- \rightleftharpoons HCoO_2^- + H_2O$	$K_{eq} = \frac{(a_{HCoO_2^-})}{(a_{OH-})}$	$pH = log(\frac{a_{HCoO_2^-}}{K_{eq}K_W})$
$Co(OH)_{2(s)}/CoO^{2-}_{2(aq)}$	$Co(OH)_2 + 2OH^- \rightleftharpoons CoO_2^{2-} + 2H_2O$	$K_{eq} = \frac{(a_{CoO_2^{2-}})}{(a_{OH-})^2}$	$pH = \frac{1}{2}log(\frac{a_{CoO_2^{2-}}}{K_{eq}K_W^2})$
$Co(OH)_{2(s)}/Co^{3+}_{(aq)}$	$Co(OH)_2 + \frac{1}{4}O_2 + 3H^+ \rightleftharpoons Co^{3+} + \frac{5}{2}H_2O$	$K_{eq} = \frac{(a_{Co3+})}{(a_{H+})^3(f_{O_2})^{\frac{1}{4}}}$	$log f_{O_2} = 12pH + 4log(\frac{a_{Co3+}}{K_{eq}})$

. . . table continued on next page

Table C.2: Equilibrium reaction equations used to model Co oxidation and dissolution.

Reactant/Product [a]	Reaction	K_{eq} expression [b,c,d]	f_{O_2}-pH equation [b,c,d,e]
$Co(OH)_{2(s)}/CoOH^{2+}_{(aq)}$	$Co(OH)_2 + \frac{1}{4}O_2 + 2H^+ \rightleftharpoons CoOH^{2+} + \frac{3}{2}H_2O$	$K_{eq} = \frac{(a_{CoOH2+})}{(a_{H+})^2(f_{O_2})^{\frac{1}{4}}}$	$logf_{O_2} = 8pH + 4log(\frac{a_{CoOH2+}}{K_{eq}})$
$Co_3O_{4(s)}/Co^{2+}_{(aq)}$	$\frac{1}{3}Co_3O_4 + 2H^+ \rightleftharpoons Co^{2+} + H_2O + \frac{1}{6}O_2$	$K_{eq} = \frac{(a_{Co2+})(f_{O_2})^{\frac{1}{6}}}{(a_{H+})^2}$	$logf_{O_2} = -12pH - 6log(\frac{a_{Co2+}}{K_{eq}})$
$Co_3O_{4(s)}/CoOH^+_{(aq)}$	$\frac{1}{3}Co_3O_4 + H^+ \rightleftharpoons CoOH^+ + \frac{1}{6}O_2$	$K_{eq} = \frac{(a_{CoOH+})(f_{O_2})^{\frac{1}{6}}}{(a_{H+})}$	$logf_{O_2} = -6pH - 6log(\frac{a_{Co2+}}{K_{eq}})$
$Co_3O_{4(s)}/CoO_{(aq)}$	$\frac{1}{3}Co_3O_4 \rightleftharpoons CoO_{aq} + \frac{1}{6}O_2$	$K_{eq} = a_{CoOaq}(f_{O_2})^{\frac{1}{6}}$	$logf_{O_2} = -6log(\frac{a_{CoOaq}}{K_{eq}})$
$Co_3O_{4(s)}/Co(OH)_{2(aq)}$	$\frac{1}{3}Co_3O_4 + H_2O \rightleftharpoons Co(OH)_{2(aq)} + \frac{1}{6}O_2$	$K_{eq} = a_{Co(OH)2}f_{O_2}^{\frac{1}{6}}$	$logf_{O_2} = -6log(\frac{a_{Co(OH)2}}{K_{eq}})$
$Co_3O_{4(s)}/HCoO_2^-_{(aq)}$	$\frac{1}{3}Co_3O_4 + OH^- \rightleftharpoons HCoO_2^- + \frac{1}{6}O_2$	$K_{eq} = \frac{(a_{HCoO_2^-})(f_{O_2})^{\frac{1}{6}}}{(a_{OH-})}$	$logf_{O_2} = 6pH - 6log(\frac{a_{HCoO_2^-}}{K_{eq}K_W})$
$Co_3O_{4(s)}/CoO_2^{2-}_{(aq)}$	$\frac{1}{3}Co_3O_4 + 2OH^- \rightleftharpoons CoO_2^{2-} + H_2O + \frac{1}{6}O_2$	$K_{eq} = \frac{(a_{CoO_2^{2-}})(f_{O_2})^{\frac{1}{6}}}{(a_{OH-})^2}$	$logf_{O_2} = 12pH - 6log(\frac{a_{CoO_2^{2-}}}{K_{eq}K_W^2})$
$Co_3O_{4(s)}/Co^{3+}_{(aq)}$	$\frac{1}{3}Co_3O_4 + \frac{1}{12}O_2 + 3H^+ \rightleftharpoons Co^{3+} + \frac{3}{2}H_2O$	$K_{eq} = \frac{(a_{Co3+})}{(a_{H+})^3(f_{O_2})^{\frac{1}{12}}}$	$logf_{O_2} = 36pH + 12log(\frac{a_{Co3+}}{K_{eq}})$
$Co_3O_{4(s)}/CoOH^{2+}_{(aq)}$	$\frac{1}{3}Co_3O_4 + \frac{1}{12}O_2 + 2H^+ \rightleftharpoons CoOH^{2+} + \frac{1}{2}H_2O$	$K_{eq} = \frac{(a_{CoOH2+})}{(a_{H+})^2(f_{O_2})^{\frac{1}{12}}}$	$logf_{O_2} = 24pH + 12log(\frac{a_{CoOH2+}}{K_{eq}})$

[a] s - solid, aq - aqueous   [b] log refers to log_{10} [c] the activity of aqueous species $a_j = \gamma_j m_j/m_\Theta$, where γ_j is the dimensionless activity coefficient, m_j is molal concentration (mol/kg H_2O), and $m_\Theta = 1$ mol/kg H_2O [d] fugacity f is in units of bar
[e] K_W is the dissociation constant of water in units of (mol/kg H_2O)^2

Table C.2: Equilibrium reaction equations used to model Co oxidation and dissolution.

Reactant/Product [a]	Reaction	K_{eq} expression [b,c,d]	f_{O_2}-pH equation [b,c,d,e]
$Mo_{(s)}/MoO_{2(s)}$	$Mo + O_2 \rightleftharpoons MoO_2$	$K_{eq} = \frac{1}{f_{O_2}}$	$logf_{O_2} = log(\frac{1}{K_{eq}})$
$MoO_{2(s)}/MoO_{3(s)}$	$MoO_2 + \frac{1}{2}O_2 \rightleftharpoons MoO_3$	$K_{eq} = \frac{1}{(f_{O_2})^{\frac{1}{2}}}$	$logf_{O_2} = 2log(\frac{1}{K_{eq}})$
$Mo_{(s)}/MoO_4^{2-}_{(aq)}$	$Mo + \frac{3}{2}O_2 + 2OH^- \rightleftharpoons MoO_4^{2-} + H_2O$	$K_{eq} = \frac{(a_{MoO_4^{2-}})}{(a_{OH-})^2(f_{O_2})^{\frac{3}{2}}}$	$logf_{O_2} = -\frac{4}{3}pH + \frac{2}{3}log(\frac{a_{MoO_4^{2-}}}{K_{eq}K_W^2})$
$Mo_{(s)}/HMoO_4^-_{(aq)}$	$Mo + \frac{3}{2}O_2 + OH^- \rightleftharpoons HMoO_4^-$	$K_{eq} = \frac{(a_{HMoO_4^-})}{(a_{OH-})(f_{O_2})^{\frac{3}{2}}}$	$logf_{O_2} = -\frac{2}{3}pH + \frac{2}{3}log(\frac{a_{HMoO_4^-}}{K_{eq}K_W})$
$Mo_{(s)}/H_2MoO_4^0_{(aq)}$	$Mo + \frac{3}{2}O_2 + H_2O \rightleftharpoons H_2MoO_{4(aq)}$	$K_{eq} = \frac{(a_{H_2MoO_4})}{(f_{O_2})^{\frac{3}{2}}}$	$logf_{O_2} = \frac{2}{3}log(\frac{a_{H_2MoO_4}}{K_{eq}})$
$MoO_{2(s)}/MoO_4^{2-}_{(aq)}$	$MoO_2 + \frac{1}{2}O_2 + 2OH^- \rightleftharpoons MoO_4^{2-} + H_2O$	$K_{eq} = \frac{(a_{MoO_4^{2-}})}{(a_{OH-})^2(f_{O_2})^{\frac{1}{2}}}$	$logf_{O_2} = -4pH + 2log(\frac{a_{MoO_4^{2-}}}{K_{eq}K_W^2})$
$MoO_{2(s)}/HMoO_4^-_{(aq)}$	$MoO_2 + \frac{1}{2}O_2 + OH^- \rightleftharpoons HMoO_4^-$	$K_{eq} = \frac{(a_{HMoO_4^-})}{(a_{OH-})(f_{O_2})^{\frac{1}{2}}}$	$logf_{O_2} = -2pH + 2log(\frac{a_{HMoO_4^-}}{K_{eq}K_W})$
$MoO_{2(s)}/H_2MoO_4^0_{(aq)}$	$MoO_2 + \frac{1}{2}O_2 + H_2O \rightleftharpoons H_2MoO_{4(aq)}$	$K_{eq} = \frac{(a_{H_2MoO_4})}{(f_{O_2})^{\frac{1}{2}}}$	$logf_{O_2} = 2log(\frac{a_{H_2MoO_4}}{K_{eq}})$
$MoO_{3(s)}/MoO_4^{2-}_{(aq)}$	$MoO_3 + 2OH^- \rightleftharpoons MoO_4^{2-} + H_2O$	$K_{eq} = \frac{(a_{MoO_4^{2-}})}{(a_{OH-})^2}$	$pH = \frac{1}{2}log(\frac{a_{MoO_4^{2-}}}{K_{eq}K_W^2})$
$MoO_{3\ (s)}/HMoO_4^-_{(aq)}$	$MoO_3 + OH^- \rightleftharpoons HMoO_4^-$	$K_{eq} = \frac{(a_{HMoO_4^-})}{(a_{OH-})}$	$pH = log(\frac{a_{HMoO_4^-}}{K_{eq}K_W})$
$MoO_{3\ (s)}/H_2MoO_4^0_{(aq)}$	$MoO_3 + H_2O \rightleftharpoons H_2MoO_{4(aq)}$	$K_{eq} = a_{H_2MoO_4}$	-

[a] s - solid, aq - aqueous   [b] log refers to log_{10} [c] the activity of aqueous species $a_j = \gamma_j m_j/m_\Theta$, where γ_j is the dimensionless activity coefficient, m_j is molal concentration (mol/kg H_2O), and $m_\Theta = 1$ mol/kg H_2O [d] fugacity f is in units of bar
[e] K_W is the dissociation constant of water in units of (mol/kg H_2O)^2

Table C.3: Equilibrium reaction equations used to model Mo oxidation and dissolution.

Reactant/Product [a]	Reaction	K_{eq} expression [b,c,d]	f_{O_2}-pH equation [b,c,d,e]
$Ni_{(s)}/NiO_{(s)}$	$Ni + \frac{1}{2}O_2 \rightleftharpoons NiO$	$K_{eq} = \frac{1}{(f_{O_2})^{\frac{1}{2}}}$	$log f_{O_2} = 2log(\frac{1}{K_{eq}})$
$Ni_{(s)}/Ni(OH)_{2(s)}$	$Ni + \frac{1}{2}O_2 + H_2O \rightleftharpoons Ni(OH)_2$	$K_{eq} = \frac{1}{(f_{O_2})^{\frac{1}{2}}}$	$log f_{O_2} = 2log(\frac{1}{K_{eq}})$
$NiO_{(s)}/Ni(OH)_{2(s)}$	$NiO + H_2O \rightleftharpoons Ni(OH)_2$	-	-
$Ni_{(s)}/Ni^{2+}_{(aq)}$	$Ni + \frac{1}{2}O_2 + 2H^+ \rightleftharpoons Ni^{2+} + H_2O$	$K_{eq} = \frac{(a_{Ni2+})}{(a_{H+})^2(f_{O_2})^{\frac{1}{2}}}$	$log f_{O_2} = 4pH + 2log(\frac{a_{Ni2+}}{K_{eq}})$
$Ni_{(s)}/NiOH^+_{(aq)}$	$Ni + \frac{1}{2}O_2 + H^+ \rightleftharpoons NiOH^+$	$K_{eq} = \frac{(a_{NiOH+})}{(a_{H+})(f_{O_2})^{\frac{1}{2}}}$	$log f_{O_2} = 2pH + 2log(\frac{a_{NiOH+}}{K_{eq}})$
$Ni_{(s)}/NiO_{(aq)}$	$Ni + \frac{1}{2}O_2 \rightleftharpoons NiO_{aq}$	$K_{eq} = \frac{(a_{NiO_{aq}})}{(f_{O_2})^{\frac{1}{2}}}$	$log f_{O_2} = 2log(\frac{a_{NiO_{aq}}}{K_{eq}})$
$Ni_{(s)}/Ni(OH)_{2(aq)}$	$Ni + \frac{1}{2}O_2 + H_2O \rightleftharpoons Ni(OH)_{2(aq)}$	$K_{eq} = \frac{a_{Ni(OH)_{2(aq)}}}{(f_{O_2})^{\frac{1}{2}}}$	$log f_{O_2} = 2log(\frac{a_{Ni(OH)_{2(aq)}}}{K_{eq}})$
$Ni_{(s)}/HNiO^-_{2(aq)}$	$Ni + \frac{1}{2}O_2 + OH^- \rightleftharpoons HNiO_2^-$	$K_{eq} = \frac{(a_{HNiO_2^-})}{(a_{OH-})(f_{O_2})^{\frac{1}{2}}}$	$log f_{O_2} = -2pH + 2log(\frac{a_{HNiO_2^-}}{K_{eq}K_W})$
$Ni_{(s)}/NiO^{2-}_{2(aq)}$	$Ni + \frac{1}{2}O_2 + 2OH^- \rightleftharpoons NiO_2^{2-} + H_2O$	$K_{eq} = \frac{(a_{NiO_2^{2-}})}{(a_{OH-})^2(f_{O_2})^{\frac{1}{2}}}$	$log f_{O_2} = -4pH + 2log(\frac{a_{NiO_2^{2-}}}{K_{eq}K_W^2})$
$NiO_{(s)}/Ni^{2+}_{(aq)}$	$NiO + 2H^+ \rightleftharpoons Ni^{2+} + H_2O$	$K_{eq} = \frac{(a_{Ni2+})}{(a_{H+})^2}$	$pH = -\frac{1}{2}log(\frac{a_{Ni2+}}{K_{eq}})$
$NiO_{(s)}/NiOH^+_{(aq)}$	$NiO + H^+ \rightleftharpoons NiOH^+$	$K_{eq} = \frac{(a_{NiOH+})}{(a_{H+})}$	$pH = -log(\frac{a_{NiOH+}}{K_{eq}})$
$NiO_{(s)}/NiO_{(aq)}$	$NiO \rightleftharpoons NiO_{aq}$	$K_{eq} = a_{NiO_{aq}}$	-
$NiO_{(s)}/Ni(OH)_{2(aq)}$	$NiO + H_2O \rightleftharpoons Ni(OH)_{2(aq)}$	$K_{eq} = a_{Ni(OH)_{2(aq)}}$	-
$NiO_{(s)}/HNiO^-_{2(aq)}$	$NiO + OH^- \rightleftharpoons HNiO_2^-$	$K_{eq} = \frac{(a_{HNiO_2^-})}{(a_{OH-})}$	$pH = log(\frac{a_{HNiO_2^-}}{K_{eq}K_W})$
$NiO_{(s)}/NiO^{2-}_{2(aq)}$	$NiO + 2OH^- \rightleftharpoons NiO_2^{2-} + H_2O$	$K_{eq} = \frac{(a_{NiO_2^{2-}})}{(a_{OH-})^2}$	$pH = \frac{1}{2}log(\frac{a_{NiO_2^{2-}}}{K_{eq}K_W^2})$
$Ni(OH)_{2(s)}/Ni^{2+}_{(aq)}$	$Ni(OH)_2 + 2H^+ \rightleftharpoons Ni^{2+} + 2H_2O$	$K_{eq} = \frac{(a_{Ni2+})}{(a_{H+})^2}$	$pH = -\frac{1}{2}log(\frac{a_{Ni2+}}{K_{eq}})$
$Ni(OH)_{2(s)}/NiOH^+_{(aq)}$	$Ni(OH)_2 + H^+ \rightleftharpoons NiOH^+ + H_2O$	$K_{eq} = \frac{(a_{NiOH+})}{(a_{H+})}$	$pH = -log(\frac{a_{NiOH+}}{K_{eq}})$
$Ni(OH)_{2(s)}/NiO_{(aq)}$	$Ni(OH)_2 \rightleftharpoons NiO_{aq} + H_2O$	$K_{eq} = a_{NiO_{aq}}$	-
$Ni(OH)_{2(s)}/Ni(OH)_{2(aq)}$	$Ni(OH)_2 \rightleftharpoons Ni(OH)_{2(aq)}$	$K_{eq} = a_{Ni(OH)_{2(aq)}}$	-
$Ni(OH)_{2(s)}/HNiO^-_{2(aq)}$	$Ni(OH)_2 + OH^- \rightleftharpoons HNiO_2^- + H_2O$	$K_{eq} = \frac{(a_{HNiO_2^-})}{(a_{OH-})}$	$pH = log(\frac{a_{HNiO_2^-}}{K_{eq}K_W})$
$Ni(OH)_{2(s)}/NiO^{2-}_{2(aq)}$	$Ni(OH)_2 + 2OH^- \rightleftharpoons NiO_2^{2-} + 2H_2O$	$K_{eq} = \frac{(a_{NiO_2^{2-}})}{(a_{OH-})^2}$	$pH = \frac{1}{2}log(\frac{a_{NiO_2^{2-}}}{K_{eq}K_W^2})$

[a] s - solid, aq - aqueous   [b] log refers to log_{10} [c] the activity of aqueous species $a_j = \gamma_j m_j/m_\Theta$, where γ_j is the dimensionless activity coefficient, m_j is molal concentration (mol/kg H_2O), and $m_\Theta = 1$ mol/kg H_2O [d] fugacity f is in units of bar
[e] K_W is the dissociation constant of water in units of (mol/kg H_2O)^2

Table C.4: Equilibrium reaction equations used to model Ni oxidation and dissolution.

Reactant/Product [a]	Reaction	K_{eq} expression [b,c,d]	f_{O_2}-pH equation [b,c,d]
$Pd_{(s)}/PdO_{(s)}$	$Pd + \frac{1}{2}O_2 \rightleftharpoons PdO$	$K_{eq} = \frac{1}{(f_{O_2})^{\frac{1}{2}}}$	$\log f_{O_2} = 2\log(\frac{1}{K_{eq}})$
$Pd_{(s)}/Pd(OH)_{2(s)}$	$Pd + \frac{1}{2}O_2 + H_2O \rightleftharpoons Pd(OH)_2$	$K_{eq} = \frac{1}{(f_{O_2})^{\frac{1}{2}}}$	$\log f_{O_2} = 2\log(\frac{1}{K_{eq}})$
$PdO_{(s)}/Pd(OH)_{2(s)}$	$PdO + H_2O \rightleftharpoons Pd(OH)_2$	-	-
$Pd_{(s)}/Pd^{2+}_{(aq)}$	$Pd + \frac{1}{2}O_2 + 2H^+ \rightleftharpoons Pd^{2+} + H_2O$	$K_{eq} = \frac{(a_{Pd2+})}{(a_{H+})^2(f_{O_2})^{\frac{1}{2}}}$	$\log f_{O_2} = 4pH + 2\log(\frac{a_{Pt2+}}{K_{eq}})$
$Pd_{(s)}/PdOH^+_{(aq)}$	$Pd + \frac{1}{2}O_2 + H^+ \rightleftharpoons PdOH^+$	$K_{eq} = \frac{(a_{PdOH+})}{(a_{H+})(f_{O_2})^{\frac{1}{2}}}$	$\log f_{O_2} = 2pH + 2\log(\frac{a_{PdOH+}}{K_{eq}})$
$Pd_{(s)}/PdO_{(aq)}$	$Pd + \frac{1}{2}O_2 \rightleftharpoons PdO_{aq}$	$K_{eq} = \frac{(a_{PdO_{aq}})}{(f_{O_2})^{\frac{1}{2}}}$	$\log f_{O_2} = 2\log(\frac{a_{PdO_{aq}}}{K_{eq}})$
$Pd_{(s)}/Pd(OH)_{2(aq)}$	$Pd + \frac{1}{2}O_2 + H_2O \rightleftharpoons Pd(OH)_{2(aq)}$	$K_{eq} = \frac{a_{Pd(OH)_{2(aq)}}}{(f_{O_2})^{\frac{1}{2}}}$	$\log f_{O_2} = 2\log(\frac{a_{Pd(OH)_{2(aq)}}}{K_{eq}})$
$PdO_{(s)}/Pd^{2+}_{(aq)}$	$PdO + 2H^+ \rightleftharpoons Pd^{2+} + H_2O$	$K_{eq} = \frac{(a_{Pd2+})}{(a_{H+})^2}$	$pH = -\frac{1}{2}\log(\frac{a_{Pt2+}}{K_{eq}})$
$PdO_{(s)}/PdOH^+_{(aq)}$	$PdO + H^+ \rightleftharpoons PdOH^+$	$K_{eq} = \frac{(a_{PdOH+})}{(a_{H+})}$	$pH = -\log(\frac{a_{PdOH+}}{K_{eq}})$
$PdO_{(s)}/PdO_{(aq)}$	$PdO \rightleftharpoons PdO_{aq}$	$K_{eq} = a_{PdO_{aq}}$	-
$PdO_{(s)}/Pd(OH)_{2(aq)}$	$PdO + H_2O \rightleftharpoons Pd(OH)_{2(aq)}$	$K_{eq} = a_{Pd(OH)_{2(aq)}}$	-
$Pd(OH)_{2(s)}/Pd^{2+}_{(aq)}$	$Pd(OH)_2 + 2H^+ \rightleftharpoons Pd^{2+} + 2H_2O$	$K_{eq} = \frac{(a_{Pd2+})}{(a_{H+})^2}$	$pH = -\frac{1}{2}\log(\frac{a_{Pt2+}}{K_{eq}})$
$Pd(OH)_{2(s)}/PdOH^+_{(aq)}$	$Pd(OH)_2 + H^+ \rightleftharpoons PdOH^+ + H_2O$	$K_{eq} = \frac{(a_{PdOH+})}{(a_{H+})}$	$pH = -\log(\frac{a_{PdOH+}}{K_{eq}})$
$Pd(OH)_{2(s)}/PdO_{(aq)}$	$Pd(OH)_2 \rightleftharpoons PdO_{aq} + H_2O$	$K_{eq} = a_{PdO_{aq}}$	-
$Pd(OH)_{2(s)}/Pd(OH)_{2(aq)}$	$Pd(OH)_2 \rightleftharpoons Pd(OH)_{2(aq)}$	$K_{eq} = a_{Pd(OH)_{2(aq)}}$	-

[a] s - solid, aq - aqueous   [b] log refers to $\log_{10}$ [c] the activity of aqueous species $a_j = \gamma_j m_j / m_\Theta$, where γ_j is the dimensionless activity coefficient, m_j is molal concentration (mol/kg H_2O), and $m_\Theta = 1$ mol/kg H_2O [d] fugacity f is in units of bar

Table C.5: Equilibrium reaction equations used to model Pd oxidation and dissolution.

Reactant/Product [a]	Reaction	K_{eq} expression [b,c,d]	f_{O_2}-pH equation [b,c,d]
$Pt_{(s)}/Pt^{2+}_{(aq)}$	$Pt + \frac{1}{2}O_2 + 2H^+ \rightleftharpoons Pt^{2+} + H_2O$	$K_{eq} = \frac{(a_{Pt2+})}{(a_{H+})^2(f_{O_2})^{\frac{1}{2}}}$	$\log f_{O_2} = 4pH + 2\log(\frac{a_{Pt2+}}{K_{eq}})$
$Pt_{(s)}/PtOH^+_{(aq)}$	$Pt + O_2 + H^+ \rightleftharpoons PtOH^+$	$K_{eq} = \frac{(a_{PtOH+})}{(a_{H+})(f_{O_2})^{\frac{1}{2}}}$	$\log f_{O_2} = 2pH + 2\log(\frac{a_{PtOH+}}{K_{eq}})$
$Pt_{(s)}/PtO_{(aq)}$	$Pt + \frac{1}{2}O_2 \rightleftharpoons PtO_{aq}$	$K_{eq} = \frac{(a_{PtO_{aq}})}{(f_{O_2})^{\frac{1}{2}}}$	$\log f_{O_2} = 2\log(\frac{a_{PtO_{aq}}}{K_{eq}})$

[a] s - solid, aq - aqueous   [b] log refers to $\log_{10}$ [c] the activity of aqueous species $a_j = \gamma_j m_j / m_\Theta$, where γ_j is the dimensionless activity coefficient, m_j is molal concentration (mol/kg H_2O), and $m_\Theta = 1$ mol/kg H_2O [d] fugacity f is in units of bar

Table C.6: Equilibrium reaction equations used to model Pt dissolution.

Reactant/Product [a]	Reaction	K_{eq} expression [b,c,d]	f_{O_2}-pH equation [b,c,d,e]
$Ru_{(s)}/RuO_{2(s)}$	$Ru + O_2 \rightleftharpoons RuO_2$	$K_{eq} = \frac{1}{f_{O_2}}$	$log f_{O_2} = log(\frac{1}{K_{eq}})$
$Ru_{(s)}/Ru^{2+}_{(aq)}$	$Ru + \frac{1}{2}O_2 + 2H^+ \rightleftharpoons Ru^{2+} + H_2O$	$K_{eq} = \frac{(a_{Ru2+})}{(a_{H+})^2(f_{O_2})^{\frac{1}{2}}}$	$log f_{O_2} = 4pH + 2log(\frac{a_{Ru2+}}{K_{eq}})$
$Ru_{(s)}/RuOH^+_{(aq)}$	$Ru + \frac{1}{2}O_2 + H^+ \rightleftharpoons RuOH^+$	$K_{eq} = \frac{(a_{RuOH+})}{(a_{H+})(f_{O_2})^{\frac{1}{2}}}$	$log f_{O_2} = 2pH + 2log(\frac{a_{RuOH+}}{K_{eq}})$
$Ru_{(s)}/RuO_{(aq)}$	$Ru + \frac{1}{2}O_2 \rightleftharpoons RuO_{aq}$	$K_{eq} = \frac{(a_{RuO_{aq}})}{(f_{O_2})^{\frac{1}{2}}}$	$log f_{O_2} = 2log(\frac{a_{RuO_{aq}}}{K_{eq}})$
$Ru_{(s)}/Ru^{3+}_{(aq)}$	$Ru + \frac{3}{4}O_2 + 3H^+ \rightleftharpoons Ru^{3+} + \frac{3}{2}H_2O$	$K_{eq} = \frac{(a_{Ru3+})}{(a_{H+})^3(f_{O_2})^{\frac{3}{4}}}$	$log f_{O_2} = 4pH + \frac{4}{3}log(\frac{a_{Ru3+}}{K_{eq}})$
$Ru_{(s)}/RuOH^{2+}_{(aq)}$	$Ru + \frac{3}{4}O_2 + 2H^+ \rightleftharpoons RuOH^{2+} + \frac{1}{2}H_2O$	$K_{eq} = \frac{(a_{RuOH2+})}{(a_{H+})^2(f_{O_2})^{\frac{3}{4}}}$	$log f_{O_2} = \frac{8}{3}pH + \frac{4}{3}log(\frac{a_{RuOH2+}}{K_{eq}})$
$Ru_{(s)}/RuO^+_{(aq)}$	$Ru + \frac{3}{4}O_2 + H^+ \rightleftharpoons RuO^+ + \frac{1}{2}H_2O$	$K_{eq} = \frac{(a_{RuO+})}{(a_{H+})(f_{O_2})^{\frac{3}{4}}}$	$log f_{O_2} = \frac{4}{3}pH + \frac{4}{3}log(\frac{a_{RuO+}}{K_{eq}})$
$Ru_{(s)}/RuO_4^{2-}{}_{(aq)}$	$Ru + \frac{3}{2}O_2 + 2OH^- \rightleftharpoons RuO_4{}^{2-} + H_2O$	$K_{eq} = \frac{(a_{RuO_4^{2-}})}{(a_{OH-})^2(f_{O_2})^{\frac{3}{2}}}$	$log f_{O_2} = -\frac{4}{3}pH + \frac{2}{3}log(\frac{a_{RuO_4^{2-}}}{K_{eq}K_W^2})$
$Ru_{(s)}/RuO_{4(aq)}$	$Ru + 2O_2 \rightleftharpoons RuO_{4(aq)}$	$K_{eq} = \frac{(a_{RuO4(aq)})}{(f_{O_2})^2}$	$log f_{O_2} = \frac{1}{2}log(\frac{a_{RuO4(aq)}}{K_{eq}})$
$RuO_{2(s)}/Ru^{2+}_{(aq)}$	$RuO_2 + 2H^+ \rightleftharpoons Ru^{2+} + H_2O + \frac{1}{2}O_2$	$K_{eq} = \frac{(a_{Ru2+})(f_{O_2})^{\frac{1}{2}}}{(a_{H+})^2}$	$log f_{O_2} = -4pH - 2log(\frac{a_{Ru2+}}{K_{eq}})$
$RuO_{2(s)}/RuOH^+_{(aq)}$	$RuO_2 + H^+ \rightleftharpoons RuOH^+ + \frac{1}{2}O_2$	$K_{eq} = \frac{(a_{RuOH+})(f_{O_2})^{\frac{1}{2}}}{(a_{H+})}$	$log f_{O_2} = -2pH - 2log(\frac{a_{RuOH+}}{K_{eq}})$
$RuO_{2(s)}/RuO_{(aq)}$	$RuO_2 \rightleftharpoons RuO_{aq} + \frac{1}{2}O_2$	$K_{eq} = a_{RuO_{aq}}(f_{O_2})^{\frac{1}{2}}$	$log f_{O_2} = -2log(\frac{a_{RuO_{aq}}}{K_{eq}})$
$RuO_{2(s)}/Ru^{3+}_{(aq)}$	$RuO_2 + 3H^+ \rightleftharpoons Ru^{3+} + \frac{3}{2}H_2O + \frac{1}{4}O_2$	$K_{eq} = \frac{(a_{Ru3+})(f_{O_2})^{\frac{1}{4}}}{(a_{H+})^3}$	$log f_{O_2} = -12pH - 4log(\frac{a_{Ru3+}}{K_{eq}})$
$RuO_{2(s)}/RuOH^{2+}_{(aq)}$	$RuO_2 + 2H^+ \rightleftharpoons RuOH^{2+} + \frac{1}{2}H_2O + \frac{1}{4}O_2$	$K_{eq} = \frac{a_{RuOH2+}(f_{O_2})^{\frac{1}{4}}}{(a_{H+})^2}$	$log f_{O_2} =$ $-8pH - 4log(\frac{a_{RuOH2+}}{K_{eq}})$
$RuO_{2(s)}/RuO^+_{(aq)}$	$RuO_2 + H^+ \rightleftharpoons RuO^+ + \frac{1}{2}H_2O + \frac{1}{4}O_2$	$K_{eq} = \frac{(a_{RuO+})(f_{O_2})^{\frac{1}{4}}}{(a_{H+})}$	$log f_{O_2} = -4pH - 4log(\frac{a_{RuO+}}{K_{eq}})$
$RuO_{2(s)}/RuO_4^{2-}{}_{(aq)}$	$RuO_2 + \frac{1}{4}O_2 + 2OH^- \rightleftharpoons RuO_4{}^{2-} + H_2O$	$K_{eq} = \frac{(a_{RuO_4^{2-}})}{(a_{OH-})^2(f_{O_2})^{\frac{1}{4}}}$	$log f_{O_2} = -8pH + 4log(\frac{a_{RuO_4^{2-}}}{K_{eq}K_W^2})$
$RuO_{2(s)}/RuO_{4(aq)}$	$RuO_2 + O_2 \rightleftharpoons RuO_{4(aq)}$	$K_{eq} = \frac{a_{RuO4(aq)}}{f_{O_2}}$	$log f_{O_2} = log(\frac{a_{RuO4(aq)}}{K_{eq}})$

[a] s - solid, aq - aqueous   [b] log refers to log_{10} [c] the activity of aqueous species $a_j = \gamma_j m_j/m_\Theta$, where γ_j is the dimensionless activity coefficient, m_j is molal concentration (mol/kg H_2O), and $m_\Theta = 1$ mol/kg H_2O [d] fugacity f is in units of bar
[e] K_W is the dissociation constant of water in units of (mol/kg $H_2O)^2$

Table C.7: Equilibrium reaction equations used to model Ru oxidation and dissolution.

Reactant/Product [a]	Reaction	K_{eq} expression [b,c,d]	f_{O_2}-pH equation [b,c,d,e]
$Ti_{(s)}/TiO_{(s)}$	$Ti + \frac{1}{2}O_2 \rightleftharpoons TiO$	$K_{eq} = \frac{1}{(f_{O_2})^{\frac{1}{2}}}$	$log f_{O_2} = 2log(\frac{1}{K_{eq}})$
$TiO_{(s)}/Ti_2O_{3(s)}$	$TiO + \frac{1}{4}O_2 \rightleftharpoons \frac{1}{2}Ti_2O_3$	$K_{eq} = \frac{1}{(f_{O_2})^{\frac{1}{4}}}$	$log f_{O_2} = 4log(\frac{1}{K_{eq}})$
$Ti_2O_{3(s)}/TiO_{2(s)}$	$\frac{1}{2}Ti_2O_3 + \frac{1}{4}O_2 \rightleftharpoons TiO_2$	$K_{eq} = \frac{1}{(f_{O_2})^{\frac{1}{4}}}$	$log f_{O_2} = 4log(\frac{1}{K_{eq}})$
$Ti_{(s)}/Ti^{4+}_{(aq)}$	$Ti + O_2 + 4H^+ \rightleftharpoons Ti^{4+} + 2H_2O$	$K_{eq} = \frac{(a_{Ti4+})}{(a_{H+})^4(f_{O_2})}$	$log f_{O_2} = 4pH + log(\frac{a_{Ti4+}}{K_{eq}})$
$Ti_{(s)}/TiOH^{3+}_{(aq)}$	$Ti + O_2 + 3H^+ \rightleftharpoons TiOH^{3+} + H_2O$	$K_{eq} = \frac{(a_{TiOH3+})}{(a_{H+})^3(f_{O_2})}$	$log f_{O_2} = 3pH + log(\frac{a_{TiOH3+}}{K_{eq}})$
$Ti_{(s)}/Ti(OH)^{2+}_{2(aq)}$	$Ti + O_2 + 2H^+ \rightleftharpoons Ti(OH)_2^{2+}$	$K_{eq} = \frac{(a_{Ti(OH)_2^{2+}})}{(a_{H+})^2(f_{O_2})}$	$log f_{O_2} = 2pH + log(\frac{a_{Ti(OH)_2^{2+}}}{K_{eq}})$
$Ti_{(s)}/Ti(OH)^{+}_{3(aq)}$	$Ti + O_2 + H^+ + H_2O \rightleftharpoons Ti(OH)_3^+$	$K_{eq} = \frac{(a_{Ti(OH)_3^+})}{(a_{H+})(f_{O_2})}$	$log f_{O_2} = pH + log(\frac{a_{Ti(OH)_3^+}}{K_{eq}})$
$Ti_{(s)}/Ti(OH)^{0}_{4(aq)}$	$Ti + O_2 + 2H_2O \rightleftharpoons Ti(OH)_4^0$	$K_{eq} = \frac{a_{Ti(OH)_4^0}}{f_{O_2}}$	$log f_{O_2} = log(\frac{a_{Ti(OH)_4^0}}{K_{eq}})$
$Ti_{(s)}/Ti(OH)^{-}_{5(aq)}$	$Ti + O_2 + OH^- + 2H_2O \rightleftharpoons Ti(OH)_5^-$	$K_{eq} = \frac{a_{Ti(OH)_5^-}}{(a_{OH-})(f_{O_2})}$	$log f_{O_2} = -pH + log(\frac{a_{Ti(OH)_5^-}}{K_{eq}K_W})$
$TiO_{(s)}/Ti^{4+}_{(aq)}$	$TiO + \frac{1}{2}O_2 + 4H^+ \rightleftharpoons Ti^{4+} + 2H_2O$	$K_{eq} = \frac{(a_{Ti4+})}{(a_{H+})^4(f_{O_2})^{\frac{1}{2}}}$	$log f_{O_2} = 8pH + 2log(\frac{a_{Ti4+}}{K_{eq}})$
$TiO_{(s)}/TiOH^{3+}_{(aq)}$	$TiO + \frac{1}{2}O_2 + 3H^+ \rightleftharpoons TiOH^{3+} + H_2O$	$K_{eq} = \frac{(a_{TiOH3+})}{(a_{H+})^3(f_{O_2})^{\frac{1}{2}}}$	$log f_{O_2} = 6pH + 2log(\frac{a_{TiOH3+}}{K_{eq}})$
$TiO_{(s)}/Ti(OH)^{2+}_{2(aq)}$	$TiO + \frac{1}{2}O_2 + 2H^+ \rightleftharpoons Ti(OH)_2^{2+}$	$K_{eq} = \frac{(a_{Ti(OH)_2^{2+}})}{(a_{H+})^2(f_{O_2})^{\frac{1}{2}}}$	$log f_{O_2} = 4pH + 2log(\frac{a_{Ti(OH)_2^{2+}}}{K_{eq}})$
$TiO_{(s)}/Ti(OH)^{+}_{3(aq)}$	$TiO + \frac{1}{2}O_2 + H^+ + H_2O \rightleftharpoons Ti(OH)_3^+$	$K_{eq} = \frac{(a_{Ti(OH)_3^+})}{(a_{H+})(f_{O_2})^{\frac{1}{2}}}$	$log f_{O_2} = 2pH + 2log(\frac{a_{Ti(OH)_3^+}}{K_{eq}})$
$TiO_{(s)}/Ti(OH)^{0}_{4(aq)}$	$TiO + \frac{1}{2}O_2 + 2H_2O \rightleftharpoons Ti(OH)_4^0$	$K_{eq} = \frac{a_{Ti(OH)_4^0}}{(f_{O_2})^{\frac{1}{2}}}$	$log f_{O_2} = 2log(\frac{a_{Ti(OH)_4^0}}{K_{eq}})$
$TiO_{(s)}/Ti(OH)^{-}_{5(aq)}$	$TiO + \frac{1}{2}O_2 + OH^- + 2H_2O \rightleftharpoons Ti(OH)_5^-$	$K_{eq} = \frac{(a_{Ti(OH)_5^-})}{(a_{OH-})(f_{O_2})^{\frac{1}{2}}}$	$log f_{O_2} = -2pH + 2log(\frac{a_{Ti(OH)_5^-}}{K_{eq}K_W})$
$Ti_2O_{3(s)}/Ti^{4+}_{(aq)}$	$\frac{1}{2}Ti_2O_3 + \frac{1}{4}O_2 + 4H^+ \rightleftharpoons Ti^{4+} + 2H_2O$	$K_{eq} = \frac{(a_{Ti4+})}{(a_{H+})^4(f_{O_2})^{\frac{1}{4}}}$	$log f_{O_2} = 16pH + 4log(\frac{a_{Ti4+}}{K_{eq}})$
$Ti_2O_{3(s)}/TiOH^{3+}_{(aq)}$	$\frac{1}{2}Ti_2O_3 + \frac{1}{4}O_2 + 3H^+ \rightleftharpoons TiOH^{3+} + H_2O$	$K_{eq} = \frac{(a_{TiOH3+})}{(a_{H+})^3(f_{O_2})^{\frac{1}{4}}}$	$log f_{O_2} = 12pH + 4log(\frac{a_{TiOH3+}}{K_{eq}})$
$Ti_2O_{3(s)}/Ti(OH)^{2+}_{2(aq)}$	$\frac{1}{2}Ti_2O_3 + \frac{1}{4}O_2 + 2H^+ \rightleftharpoons Ti(OH)_2^{2+}$	$K_{eq} = \frac{(a_{Ti(OH)_2^{2+}})}{(a_{H+})^2(f_{O_2})^{\frac{1}{4}}}$	$log f_{O_2} = 8pH + 4log(\frac{a_{Ti(OH)_2^{2+}}}{K_{eq}})$
$Ti_2O_{3(s)}/Ti(OH)^{+}_{3(aq)}$	$\frac{1}{2}Ti_2O_3 + \frac{1}{4}O_2 + H^+ + H_2O \rightleftharpoons Ti(OH)_3^+$	$K_{eq} = \frac{(a_{Ti(OH)_3^+})}{(a_{H+})(f_{O_2})^{\frac{1}{4}}}$	$log f_{O_2} = 4pH + 4log(\frac{a_{Ti(OH)_3^+}}{K_{eq}})$
$Ti_2O_{3(s)}/Ti(OH)^{0}_{4(aq)}$	$\frac{1}{2}Ti_2O_3 + \frac{1}{4}O_2 + 2H_2O \rightleftharpoons Ti(OH)_4^0$	$K_{eq} = \frac{a_{Ti(OH)_4^0}}{(f_{O_2})^{\frac{1}{4}}}$	$log f_{O_2} = 4log(\frac{a_{Ti(OH)_4^0}}{K_{eq}})$
$Ti_2O_{3(s)}/Ti(OH)^{-}_{5(aq)}$	$\frac{1}{2}Ti_2O_3 + \frac{1}{4}O_2 + OH^- + 2H_2O \rightleftharpoons Ti(OH)_5^-$	$K_{eq} = \frac{(a_{Ti(OH)_5^-})}{(a_{OH-})(f_{O_2})^{\frac{1}{4}}}$	$log f_{O_2} = -4pH + 4log(\frac{a_{Ti(OH)_5^-}}{K_{eq}K_W})$
$TiO_{2(s)}/Ti^{4+}_{(aq)}$	$TiO_2 + 4H^+ \rightleftharpoons Ti^{4+} + 2H_2O$	$K_{eq} = \frac{(a_{Ti4+})}{(a_{H+})^4}$	$pH = -\frac{1}{4}log(\frac{a_{Ti4+}}{K_{eq}})$
$TiO_{2(s)}/TiOH^{3+}_{(aq)}$	$TiO_2 + 3H^+ \rightleftharpoons TiOH^{3+} + H_2O$	$K_{eq} = \frac{(a_{TiOH3+})}{(a_{H+})^3}$	$pH = -\frac{1}{3}log(\frac{a_{TiOH3+}}{K_{eq}})$
$TiO_{2(s)}/Ti(OH)^{2+}_{2(aq)}$	$TiO_2 + 2H^+ \rightleftharpoons Ti(OH)_2^{2+}$	$K_{eq} = \frac{(a_{Ti(OH)_2^{2+}})}{(a_{H+})^2}$	$pH = -\frac{1}{2}log(\frac{a_{Ti(OH)_2^{2+}}}{K_{eq}})$
$TiO_{2(s)}/Ti(OH)^{+}_{3(aq)}$	$TiO_2 + H^+ + H_2O \rightleftharpoons Ti(OH)_3^+$	$K_{eq} = \frac{(a_{Ti(OH)_3^+})}{(a_{H+})}$	$pH = -log(\frac{a_{Ti(OH)_3^+}}{K_{eq}})$
$TiO_{2(s)}/Ti(OH)^{0}_{4(aq)}$	$TiO_2 + 2H_2O \rightleftharpoons Ti(OH)_4^0$	$K_{eq} = a_{Ti(OH)_4^0}$	-
$TiO_{2(s)}/Ti(OH)^{-}_{5(aq)}$	$TiO_2 + OH^- + 2H_2O \rightleftharpoons Ti(OH)_5^-$	$K_{eq} = \frac{(a_{Ti(OH)_5^-})}{(a_{OH-})}$	$pH = log(\frac{a_{Ti(OH)_5^-}}{K_{eq}K_W})$

[a] s - solid, aq - aqueous   [b] log refers to log_{10} [c] the activity of aqueous species $a_j = \gamma_j m_j/m_\Theta$, where γ_j is the dimensionless activity coefficient, m_j is molal concentration (mol/kg H_2O), and $m_\Theta = 1$ mol/kg H_2O [d] fugacity f is in units of bar
[e] K_W is the dissociation constant of water in units of (mol/kg H_2O)^2

Table C.8: Equilibrium reaction equations used to model TiO_2 reduction and dissolution.

Reactant/Product [a]	Reaction	K_{eq} expression [b,c,d]	f_{O_2}-pH equation [b,c,d,e]
$W_{(s)}/WO_{2(s)}$	$W + O_2 \rightleftharpoons WO_2$	$K_{eq} = \frac{1}{f_{O_2}}$	$\log f_{O_2} = \log(\frac{1}{K_{eq}})$
$WO_{2(s)}/WO_{3(s)}$	$WO_2 + \frac{1}{2}O_2 \rightleftharpoons WO_3$	$K_{eq} = \frac{1}{(f_{O_2})^{\frac{1}{2}}}$	$\log f_{O_2} = 2\log(\frac{1}{K_{eq}})$
$W_{(s)}/WO_{4(aq)}^{2-}$	$W + \frac{3}{2}O_2 + 2OH^- \rightleftharpoons WO_4^{2-} + H_2O$	$K_{eq} = \frac{(a_{WO_4^{2-}})}{(a_{OH^-})^2(f_{O_2})^{\frac{3}{2}}}$	$\log f_{O_2} = -\frac{4}{3}pH + \frac{2}{3}\log(\frac{a_{WO_4^{2-}}}{K_{eq}K_W^2})$
$W_{(s)}/HWO_{4(aq)}^{-}$	$W + \frac{3}{2}O_2 + OH^- \rightleftharpoons HWO_4^-$	$K_{eq} = \frac{(a_{HWO_4^-})}{(a_{OH^-})(f_{O_2})^{\frac{3}{2}}}$	$\log f_{O_2} = -\frac{2}{3}pH + \frac{2}{3}\log(\frac{a_{HWO_4^-}}{K_{eq}K_W})$
$W_{(s)}/H_2WO_{4(aq)}^{0}$	$W + \frac{3}{2}O_2 + H_2O \rightleftharpoons H_2WO_{4(aq)}$	$K_{eq} = \frac{(a_{H_2WO_4})}{(f_{O_2})^{\frac{3}{2}}}$	$\log f_{O_2} = \frac{2}{3}\log(\frac{a_{H_2WO_4}}{K_{eq}})$
$WO_{2(s)}/WO_{4(aq)}^{2-}$	$WO_2 + \frac{1}{2}O_2 + 2OH^- \rightleftharpoons WO_4^{2-} + H_2O$	$K_{eq} = \frac{(a_{WO_4^{2-}})}{(a_{OH^-})^2(f_{O_2})^{\frac{1}{2}}}$	$\log f_{O_2} = -4pH + 2\log(\frac{a_{WO_4^{2-}}}{K_{eq}K_W^2})$
$WO_{2(s)}/HWO_{4(aq)}^{-}$	$WO_2 + \frac{1}{2}O_2 + OH^- \rightleftharpoons HWO_4^-$	$K_{eq} = \frac{(a_{HWO_4^-})}{(a_{OH^-})(f_{O_2})^{\frac{1}{2}}}$	$\log f_{O_2} = -2pH + 2\log(\frac{a_{HWO_4^-}}{K_{eq}K_W})$
$WO_{2(s)}/H_2WO_{4(aq)}^{0}$	$WO_2 + \frac{1}{2}O_2 + H_2O \rightleftharpoons H_2WO_{4(aq)}$	$K_{eq} = \frac{(a_{H_2WO_4})}{(f_{O_2})^{\frac{1}{2}}}$	$\log f_{O_2} = 2\log(\frac{a_{H_2WO_4}}{K_{eq}})$
$WO_{3(s)}/WO_{4(aq)}^{2-}$	$WO_3 + 2OH^- \rightleftharpoons WO_4^{2-} + H_2O$	$K_{eq} = \frac{(a_{WO_4^{2-}})}{(a_{OH^-})^2}$	$pH = \frac{1}{2}\log(\frac{a_{WO_4^{2-}}}{K_{eq}K_W^2})$
$WO_{3(s)}/HWO_{4(aq)}^{-}$	$WO_3 + OH^- \rightleftharpoons HWO_4^-$	$K_{eq} = \frac{(a_{HWO_4^-})}{(a_{OH^-})}$	$pH = \log(\frac{a_{HWO_4^-}}{K_{eq}K_W})$
$WO_{3(s)}/H_2WO_{4(aq)}^{0}$	$WO_3 + H_2O \rightleftharpoons H_2WO_{4(aq)}$	$K_{eq} = a_{H_2WO_4}$	-

[a] s - solid, aq - aqueous   [b] log refers to $\log_{10}$ [c] the activity of aqueous species $a_j = \gamma_j m_j / m_\Theta$, where γ_j is the dimensionless activity coefficient, m_j is molal concentration (mol/kg H_2O), and $m_\Theta = 1$ mol/kg H_2O [d] fugacity f is in units of bar
[e] K_W is the dissociation constant of water in units of (mol/kg $H_2O)^2$

Table C.9: Equilibrium reaction equations used to model W oxidation and dissolution.

Reactant/Product [a]	Reaction	K_{eq} expression [b,c,d]	f_{O_2}-pH equation [b,c,d,e]
$Zr_{(s)}/ZrO_{2(s)}$	$Zr + O_2 \rightleftharpoons ZrO_2$	$K_{eq} = \frac{1}{f_{O_2}}$	$\log f_{O_2} = \log(\frac{1}{K_{eq}})$
$Zr_{(s)}/Zr_{(aq)}^{4+}$	$Zr + O_2 + 4H^+ \rightleftharpoons Zr^{4+} + 2H_2O$	$K_{eq} = \frac{(a_{Zr^{4+}})}{(a_{H^+})^4(f_{O_2})}$	$\log f_{O_2} = 4pH + \log(\frac{a_{Zr^{4+}}}{K_{eq}})$
$Zr_{(s)}/ZrOH_{(aq)}^{3+}$	$Zr + O_2 + 3H^+ \rightleftharpoons ZrOH^{3+} + H_2O$	$K_{eq} = \frac{(a_{ZrOH^{3+}})}{(a_{H^+})^3(f_{O_2})}$	$\log f_{O_2} = 3pH + \log(\frac{a_{ZrOH^{3+}}}{K_{eq}})$
$Zr_{(s)}/ZrO_{(aq)}^{2+}$	$Zr + O_2 \equiv 2H^+ \rightleftharpoons ZrO^{2+} + H_2O$	$K_{eq} = \frac{(a_{ZrO^{2+}})}{(a_{H^+})^2(f_{O_2})}$	$\log f_{O_2} = 2pH + \log(\frac{a_{ZrO^{2+}}}{K_{eq}})$
$Zr_{(s)}/HZrO_{2(aq)}^{+}$	$Zr + O_2 + H^+ \rightleftharpoons HZrO_2^+$	$K_{eq} = \frac{(a_{HZrO_2^+})}{(a_{H^+})(f_{O_2})}$	$\log f_{O_2} = pH + \log(\frac{a_{HZrO_2^+}}{K_{eq}})$
$Zr_{(s)}/ZrO_{2(aq)}$	$Zr + O_2 \rightleftharpoons ZrO_{2(aq)}$	$K_{eq} = \frac{a_{ZrO_2(aq)}}{f_{O_2}}$	$\log f_{O_2} = \log(\frac{a_{ZrO_2(aq)}}{K_{eq}})$
$Zr_{(s)}/HZrO_{3(aq)}^{-}$	$Zr + O_2 + OH^- \rightleftharpoons HZrO_3^-$	$K_{eq} = \frac{a_{HZrO_3^-}}{(a_{OH^-})(f_{O_2})}$	$\log f_{O_2} = -pH + \log(\frac{a_{HZrO_3^-}}{K_{eq}K_W})$
$ZrO_{2(s)}/Zr_{(aq)}^{4+}$	$ZrO_2 + 4H^+ \rightleftharpoons Zr^{4+} + 2H_2O$	$K_{eq} = \frac{(a_{Zr^{4+}})}{(a_{H^+})^4}$	$pH = -\frac{1}{4}\log(\frac{a_{Zr^{4+}}}{K_{eq}})$
$ZrO_{2(s)}/ZrOH_{(aq)}^{3+}$	$ZrO_2 + 3H^+ \rightleftharpoons ZrOH^{3+} + H_2O$	$K_{eq} = \frac{(a_{ZrOH^{3+}})}{(a_{H^+})^3}$	$pH = -\frac{1}{3}\log(\frac{a_{ZrOH^{3+}}}{K_{eq}})$
$ZrO_{2(s)}/ZrO_{(aq)}^{2+}$	$ZrO_2 + 2H^+ \rightleftharpoons ZrO^{2+} + H_2O$	$K_{eq} = \frac{(a_{ZrO^{2+}})}{(a_{H^+})^2}$	$pH = -\frac{1}{2}\log(\frac{a_{ZrO^{2+}}}{K_{eq}})$
$ZrO_{2(s)}/HZrO_{2(aq)}^{+}$	$ZrO_2 + H^+ \rightleftharpoons HZrO_2^+$	$K_{eq} = \frac{(a_{HZrO_2^+})}{(a_{H^+})}$	$pH = -\log(\frac{a_{HZrO_2^+}}{K_{eq}})$
$ZrO_{2(s)}/ZrO_{2(aq)}$	$ZrO_2 \rightleftharpoons ZrO_{2(aq)}$	$K_{eq} = a_{ZrO_2(aq)}$	-
$ZrO_{2(s)}/HZrO_{3(aq)}^{-}$	$ZrO_2 + OH^- \rightleftharpoons HZrO_3^-$	$K_{eq} = \frac{(a_{HZrO_3^-})}{(a_{OH^-})}$	$pH = \log(\frac{a_{HZrO_3^-}}{K_{eq}K_W})$

[a] s - solid, aq - aqueous   [b] log refers to $\log_{10}$ [c] the activity of aqueous species $a_j = \gamma_j m_j / m_\Theta$, where γ_j is the dimensionless activity coefficient, m_j is molal concentration (mol/kg H_2O), and $m_\Theta = 1$ mol/kg H_2O [d] fugacity f is in units of bar
[e] K_W is the dissociation constant of water in units of (mol/kg $H_2O)^2$

Table C.10: Equilibrium reaction equations used to model ZrO_2 reduction and dissolution.

Reactant/Product [a]	Reaction	K_{eq} expression [b,c,d]
$Ag_{(s)}/Ag^+_{(aq)}$	$Ag + H^+ + \frac{1}{4}O_2 \rightleftharpoons Ag^+ + \frac{1}{2}H_2O$	$K_{eq} = \dfrac{a_{Ag^+}}{(a_{H^+})(f_{O_2})^{\frac{1}{4}}}$
$Ag_{(s)}/AgOH_{(aq)}$	$Ag + \frac{1}{4}O_2 + \frac{1}{2}H_2O \rightleftharpoons AgOH_{aq}$	$K_{eq} = \dfrac{a_{AgOH}}{(f_{O_2})^{\frac{1}{4}}}$
$Ag_{(s)}/AgO^-_{(aq)}$	$Ag + OH^- + \frac{1}{4}O_2 \rightleftharpoons AgO^- + H_2O$	$K_{eq} = \dfrac{a_{AgO^-}}{(a_{OH^-})(f_{O_2})^{\frac{1}{4}}}$
$Au_{(s)}/Au^+_{(aq)}$	$Au + H^+ + \frac{1}{4}O_2 \rightleftharpoons Au^+ + \frac{1}{2}H_2O$	$K_{eq} = \dfrac{a_{Au^+}}{(a_{H^+})(f_{O_2})^{\frac{1}{4}}}$
$Au_{(s)}/Au^{3+}_{(aq)}$	$Au + 3H^+ + \frac{3}{4}O_2 \rightleftharpoons Au^{3+} + \frac{3}{2}H_2O$	$K_{eq} = \dfrac{a_{Au^{3+}}}{(a_{H^+})^3(f_{O_2})^{\frac{3}{4}}}$
$Al_2O_{3(s)}/Al^{3+}_{(aq)}$	$\frac{1}{2}Al_2O_3 + 3H^+ \rightleftharpoons Al^{3+} + \frac{3}{2}H_2O$	$K_{eq} = \dfrac{a_{Al^{3+}}}{(a_{H^+})^3}$
$Al_2O_{3(s)}/AlOH^{2+}_{(aq)}$	$\frac{1}{2}Al_2O_3 + 2H^+ \rightleftharpoons AlOH^{2+} + \frac{1}{2}H_2O$	$K_{eq} = \dfrac{a_{AlOH^{2+}}}{(a_{H^+})^2}$
$Al_2O_{3(s)}/AlO^+_{(aq)}$	$\frac{1}{2}Al_2O_3 + H^+ \rightleftharpoons AlO^+ + \frac{1}{2}H_2O$	$K_{eq} = \dfrac{a_{AlO^+}}{a_{H^+}}$
$Al_2O_{3(s)}/HAlO_{2(aq)}$	$\frac{1}{2}Al_2O_3 + \frac{1}{2}H_2O \rightleftharpoons HAlO_{2(aq)}$	$K_{eq} = a_{HAlO_{2(aq)}}$
$Al_2O_{3(s)}/AlO^-_{2(aq)}$	$\frac{1}{2}Al_2O_3 + OH^- \rightleftharpoons AlO^-_2 + \frac{1}{2}H_2O$	$K_{eq} = \dfrac{a_{AlO^-_2}}{a_{OH^-}}$
$Cu_{(s)}/Cu^+_{(aq)}$	$Cu + H^+ + \frac{1}{4}O_2 \rightleftharpoons Cu^+ + \frac{1}{2}H_2O$	$K_{eq} = \dfrac{a_{Cu^+}}{(a_{H^+})(f_{O_2})^{\frac{1}{4}}}$
$Cu_{(s)}/Cu^{2+}_{(aq)}$	$Cu + 2H^+ + \frac{1}{2}O_2 \rightleftharpoons Cu^{2+} + H_2O$	$K_{eq} = \dfrac{a_{Cu^{2+}}}{(a_{H^+})^2(f_{O_2})^{\frac{1}{2}}}$
$Cu_{(s)}/CuOH^+_{(aq)}$	$Cu + H^+ + \frac{1}{2}O_2 \rightleftharpoons CuOH^+$	$K_{eq} = \dfrac{a_{CuOH^+}}{(a_{H^+})(f_{O_2})^{\frac{1}{2}}}$
$Cu_{(s)}/CuO_{(aq)}$	$Cu + \frac{1}{2}O_2 \rightleftharpoons CuO_{aq}$	$K_{eq} = \dfrac{a_{CuO_{aq}}}{(f_{O_2})^{\frac{1}{2}}}$
$Cu_{(s)}/HCuO^-_{2(aq)}$	$Cu + OH^- + \frac{1}{2}O_2 \rightleftharpoons HCuO^-_2$	$K_{eq} = \dfrac{a_{HCuO^-_2}}{(a_{OH^-})(f_{O_2})^{\frac{1}{2}}}$
$Cu_{(s)}/CuO^{2-}_{2(aq)}$	$Cu + 2OH^- + \frac{1}{2}O_2 \rightleftharpoons CuO^{2-}_2 + H_2O$	$K_{eq} = \dfrac{a_{CuO^{2-}_2}}{(a_{OH^-})^2(f_{O_2})^{\frac{1}{2}}}$
$CuO_{(s)}/Cu^+_{(aq)}$	$CuO + H^+ \rightleftharpoons Cu^+ + \frac{1}{2}H_2O + \frac{1}{4}O_2$	$K_{eq} = \dfrac{(a_{Cu^+})(f_{O_2})^{\frac{1}{4}}}{(a_{H^+})}$
$CuO_{(s)}/Cu^{2+}_{(aq)}$	$CuO + 2H^+ \rightleftharpoons Cu^{2+} + H_2O$	$K_{eq} = \dfrac{a_{Cu^{2+}}}{(a_{H^+})^2}$
$CuO_{(s)}/CuOH^+_{(aq)}$	$CuO + H^+ \rightleftharpoons CuOH^+$	$K_{eq} = \dfrac{a_{CuOH^+}}{(a_{H^+})}$
$CuO_{(s)}/CuO_{(aq)}$	$CuO \rightleftharpoons CuO_{aq}$	$K_{eq} = a_{CuO_{aq}}$
$CuO_{(s)}/HCuO^-_{2(aq)}$	$CuO + OH^- \rightleftharpoons HCuO^-_2$	$K_{eq} = \dfrac{a_{HCuO^-_2}}{(a_{OH^-})}$
$CuO_{(s)}/CuO^{2-}_{2(aq)}$	$CuO + 2OH^- \rightleftharpoons CuO^{2-}_2 + H_2O$	$K_{eq} = \dfrac{a_{CuO^{2-}_2}}{(a_{OH^-})^2}$
$SiO_{2(s)}/HSiO^-_{3(aq)}$	$SiO_2 + OH^- \rightleftharpoons HSiO^-_3$	$K_{eq} = \dfrac{(a_{HSiO^-_3})}{(a_{OH^-})}$
$SiO_{2(s)}/SiO_{2(aq)}$	$SiO_2 \rightleftharpoons SiO_{2(aq)}$	$K_{eq} = a_{SiO_{2(aq)}}$

Table C.11: Equations used to model dissolution of additional elements.

Reactant/Product [a]	Reaction	K_{eq} expression [b,c,d]
$Fe_2O_{3(s)}/Fe^{2+}_{(aq)}$	$\frac{1}{2}Fe_2O_3+2H^+ \rightleftharpoons Fe^{2+}+H_2O+\frac{1}{4}O_2$	$K_{eq}=\frac{(a_{Fe2+})(f_{O_2})^{\frac{1}{4}}}{(a_{H+})^2}$
$Fe_2O_{3(s)}/FeOH^+_{(aq)}$	$\frac{1}{2}Fe_2O_3+H^+ \rightleftharpoons FeOH^+ +\frac{1}{4}O_2$	$K_{eq}=\frac{(a_{FeOH+})(f_{O_2})^{\frac{1}{4}}}{(a_{H+})}$
$Fe_2O_{3(s)}/FeO_{(aq)}$	$\frac{1}{2}Fe_2O_3 \rightleftharpoons FeO_{aq}+\frac{1}{4}O_2$	$K_{eq}=(a_{FeO_{aq}})(f_{O_2})^{\frac{1}{4}}$
$Fe_2O_{3(s)}/HFeO^-_{2(aq)}$	$\frac{1}{2}Fe_2O_3+OH^- \rightleftharpoons HFeO_2^- +\frac{1}{4}O_2$	$K_{eq}=\frac{(a_{HFeO_2^-})(f_{O_2})^{\frac{1}{4}}}{(a_{OH-})}$
$Fe_2O_{3(s)}/Fe^{3+}_{(aq)}$	$\frac{1}{2}Fe_2O_3+3H^+ \rightleftharpoons Fe^{3+}+\frac{3}{2}H_2O$	$K_{eq}=\frac{(a_{Fe3+})}{(a_{H+})^3}$
$Fe_2O_{3(s)}/FeOH^{2+}_{(aq)}$	$\frac{1}{2}Fe_2O_3+2H^+ \rightleftharpoons FeOH^{2+}+\frac{1}{2}H_2O$	$K_{eq}=\frac{(a_{FeOH2+})}{(a_{H+})^2}$
$Fe_2O_{3(s)}/FeO^+_{(aq)}$	$\frac{1}{2}Fe_2O_3+H^+ \rightleftharpoons FeO^+ +\frac{1}{2}H_2O$	$K_{eq}=\frac{(a_{FeO+})}{(a_{H+})}$
$Fe_2O_{3(s)}/HFeO_{2(aq)}$	$\frac{1}{2}Fe_2O_3+\frac{1}{2}H_2O \rightleftharpoons HFeO_{2(aq)}$	$K_{eq}=a_{HFeO_{2(aq)}}$
$Fe_2O_{3\ (s)}/FeO_2^-{}_{(aq)}$	$\frac{1}{2}Fe_2O_3+OH^- \leftrightarrow FeO_2^- +\frac{1}{2}H_2O$	$K_{eq}=\frac{(a_{FeO_2^-})}{(a_{OH-})}$
$Rh(s)/Rh^{2+}_{(aq)}$	$Rh+2H^+ +\frac{1}{2}O_2 \rightleftharpoons Rh^{2+}+H_2O$	$K_{eq}=\frac{(a_{Rh2+})}{(a_{H+})^2(f_{O_2})^{\frac{1}{2}}}$
$Rh(s)/RhOH^+_{(aq)}$	$Rh+H^+ +\frac{1}{2}O_2 \rightleftharpoons RhOH^+$	$K_{eq}=\frac{(a_{RhOH+})}{(a_{H+})(f_{O_2})^{\frac{1}{2}}}$
$Rh(s)/RhO_{(aq)}$	$Rh+\frac{1}{2}O_2 \rightleftharpoons RhO_{aq}$	$K_{eq}=\frac{(a_{RhO_{aq}})}{(f_{O_2})^{\frac{1}{2}}}$
$Rh(s)/Rh^{3+}_{(aq)}$	$Rh+3H^+ +\frac{3}{4}O_2 \rightleftharpoons Rh^{3+}+\frac{3}{2}H_2O$	$K_{eq}=\frac{(a_{Rh3+})}{(a_{H+})^3(f_{O_2})^{\frac{3}{4}}}$
$Rh(s)/RhOH^{2+}_{(aq)}$	$Rh+2H^+ +\frac{3}{4}O_2 \rightleftharpoons RhOH^{2+}+\frac{1}{2}H_2O$	$K_{eq}=\frac{(a_{RhOH2+})}{(a_{H+})^2(f_{O_2}^{\frac{3}{4}})}$
$Rh(s)/RhO^+_{(aq)}$	$Rh+H^+ +\frac{3}{4}O_2 \rightleftharpoons RhO^+ +\frac{1}{2}H_2O$	$K_{eq}=\frac{(a_{RhO+})}{(a_{H+})(f_{O_2})^{\frac{3}{4}}}$
$Rh_2O_{3(s)}/Rh^{2+}_{(aq)}$	$\frac{1}{2}Rh_2O_3+2H^+ \rightleftharpoons Rh^{2+}+H_2O+\frac{1}{4}O_2$	$K_{eq}=\frac{(a_{Rh2+})(f_{O_2})^{\frac{1}{4}}}{(a_{H+})^2}$
$Rh_2O_{3(s)}/RhOH^+_{(aq)}$	$\frac{1}{2}Rh_2O_3+H^+ \rightleftharpoons RhOH^+ +\frac{1}{4}O_2$	$K_{eq}=\frac{(a_{RhOH+})(f_{O_2})^{\frac{1}{4}}}{(a_{H+})}$
$Rh_2O_{3(s)}/RhO_{(aq)}$	$\frac{1}{2}Rh_2O_3 \rightleftharpoons RhO_{aq}+\frac{1}{4}O_2$	$K_{eq}=(a_{RhO_{aq}})(f_{O_2})^{\frac{1}{4}}$
$Rh_2O_{3(s)}/Rh^{3+}_{(aq)}$	$\frac{1}{2}Rh_2O_3+3H^+ \rightleftharpoons Rh^{3+}+\frac{3}{2}H_2O$	$K_{eq}=\frac{(a_{Rh3+})}{(a_{H+})^3}$
$Rh_2O_{3(s)}/RhOH^{2+}_{(aq)}$	$\frac{1}{2}Rh_2O_3+2H^+ \rightleftharpoons RhOH^{2+}+\frac{1}{2}H_2O$	$K_{eq}=\frac{(a_{RhOH2+})}{(a_{H+})^2}$
$Rh_2O_{3(s)}/RhO^+_{(aq)}$	$\frac{1}{2}Rh_2O_3+H^+ \rightleftharpoons RhO^+ +\frac{1}{2}H_2O$	$K_{eq}=\frac{(a_{RhO+})}{(a_{H+})}$
$ZnO_{(s)}/Zn^+_{(aq)}$	$ZnO+H^+ \rightleftharpoons Zn^+ +\frac{1}{2}H_2O+\frac{1}{4}O_2$	$K_{eq}=\frac{(a_{Zn+})(f_{O_2})^{\frac{1}{4}}}{(a_{H+})}$
$ZnO_{(s)}/Zn^{2+}_{(aq)}$	$ZnO+2H^+ \rightleftharpoons Zn^{2+}+H_2O$	$K_{eq}=\frac{a_{Zn2+}}{(a_{H+})^2}$
$ZnO_{(s)}/ZnOH^+_{(aq)}$	$ZnO+H^+ \rightleftharpoons ZnOH^+$	$K_{eq}=\frac{a_{ZnOH+}}{(a_{H+})}$
$ZnO_{(s)}/ZnO_{(aq)}$	$ZnO \rightleftharpoons ZnO_{aq}$	$K_{eq}=a_{ZnO_{aq}}$
$ZnO_{(s)}/HZnO^-_{2(aq)}$	$ZnO+OH^- \rightleftharpoons HZnO_2^-$	$K_{eq}=\frac{a_{HZnO_2^-}}{(a_{OH-})}$
$ZnO_{(s)}/ZnO^{2-}_{2(aq)}$	$ZnO+2OH^- \rightleftharpoons ZnO_2^{2-}+H_2O$	$K_{eq}=\frac{a_{ZnO_2^{2-}}}{(a_{OH-})^2}$

[a] s - solid, aq - aqueous   [b] log refers to $\log_{10}$ [c] the activity of aqueous species $a_j = \gamma_j m_j/m_\ominus$, where γ_j is the dimensionless activity coefficient, m_j is molal concentration (mol/kg H_2O), and $m_\ominus = 1$ mol/kg H_2O [d] fugacity f is in units of bar

Table C.11: Equations used to model dissolution of additional elements.

Solute	Reaction	K_{eq} expression [a]
H_2O	$H_2O \rightleftharpoons H^+ + OH^-$	$K_W = (a_{H^+})(a_{OH^-})$
	$2\,H_2O \rightleftharpoons 2\,H_2 + O_2$	$K_{WS} = (a_{H_{2(aq)}})^2(a_{O_{2(aq)}})$
CO_2	$CO_2 + H_2O \rightleftharpoons H^+ + HCO_3^-$	$K_{eq} = \frac{(a_{H^+})(a_{HCO_3^-})}{(a_{CO_2})}$
	$HCO_3^- \rightleftharpoons H^+ + CO_3^{2-}$	$K_{eq} = \frac{(a_{CO_3^{2-}})(a_{H^+})}{(a_{HCO_3^-})}$
CH_4	$CH_4 + O_2 \rightleftharpoons 2\,H_2 + CO_2$	$K_{eq} = \frac{(a_{CO_2})(a_{H_{2(aq)}})^2}{(a_{CH_4})(a_{O_{2(aq)}})}$
	$CO_2 + H_2O \rightleftharpoons H^+ + HCO_3^-$	$K_{eq} = \frac{(a_{H^+})(a_{HCO_3^-})}{(a_{CO_2})}$
	$HCO_3^- \rightleftharpoons H^+ + CO_3^{2-}$	$K_{eq} = \frac{(a_{CO_3^{2-}})(a_{H^+})}{(a_{HCO_3^-})}$
NH_3	$NH_3 + H^+ \rightleftharpoons NH_4^+$	$K_{eq} = \frac{(a_{NH_4^+})}{(a_{H^+})(a_{NH_3})}$
	$2\,NH_3 \rightleftharpoons N_2 + 3\,H_2$	$K_{eq} = \frac{(a_{N_2})(a_{H_{2(aq)}})^3}{(a_{NH_3})^2}$
Formic acid	$HCOOH \rightleftharpoons H_2 + CO_2$	$K_{eq} = \frac{(a_{CO_2})(a_{H_{2(aq)}})}{(a_{HCOOH})}$
	$HCOOH \rightleftharpoons H^+ + HCOO^-$	$K_{eq} = \frac{(a_{HCOO^-})(a_{H^+})}{(a_{HCOOH})}$
	$CO_2 + H_2O \rightleftharpoons H^+ + HCO_3^-$	$K_{eq} = \frac{(a_{H^+})(a_{HCO_3^-})}{(a_{CO_2})}$
	$HCO_3^- \rightleftharpoons H^+ + CO_3^{2-}$	$K_{eq} = \frac{(a_{CO_3^{2-}})(a_{H^+})}{(a_{HCO_3^-})}$

[a] the activity of aqueous species $a_j = \gamma_j m_j/m_\Theta$, where γ_j is the dimensionless activity coefficient, m_j is molal concentration (mol/kg H_2O), and $m_\Theta = 1$ mol/kg H_2O

Table C.12: Reactions used to model the oxygen fugacity and pH of CO_2, CH_4, NH_3, and formic acid in H_2O. These solutes are frequently present during various hydrothermal reactions.

APPENDIX D

Equilibrium Concentrations of Individual Aqueous Metal Species

Figures D.1 to D.15 show the equilibrium concentrations of aqueous species derived from each catalytic material at different temperatures and pressures. The total material solubility is therefore the sum of all the individual aqueous metal-containing species.
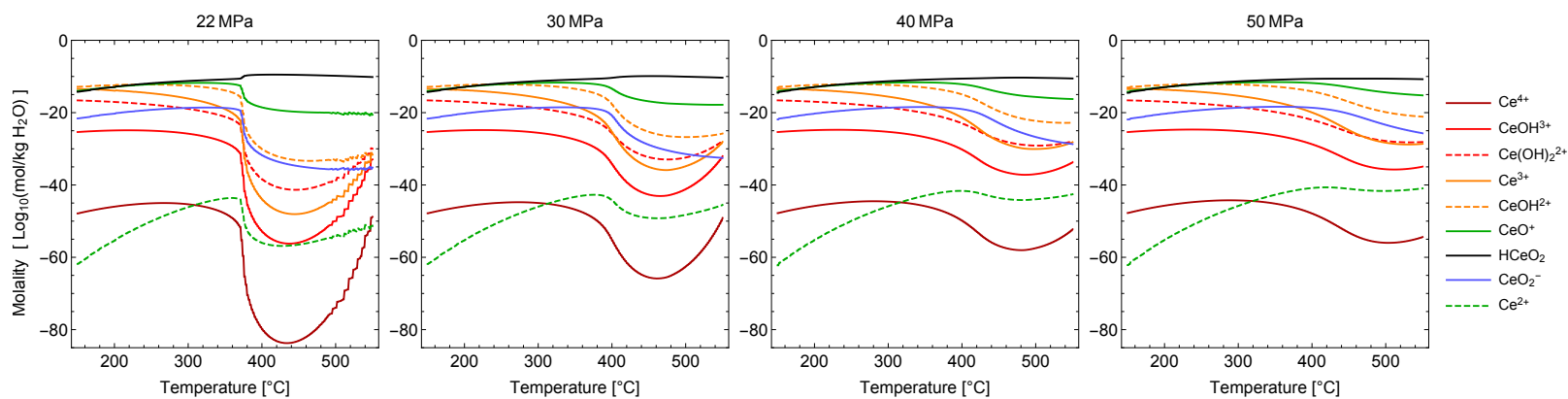
Figure D.1: Equilibrium concentrations of aqueous species from CeO_2 in H_2O as a function of temperature at 22, 30, 40, and 50 MPa.
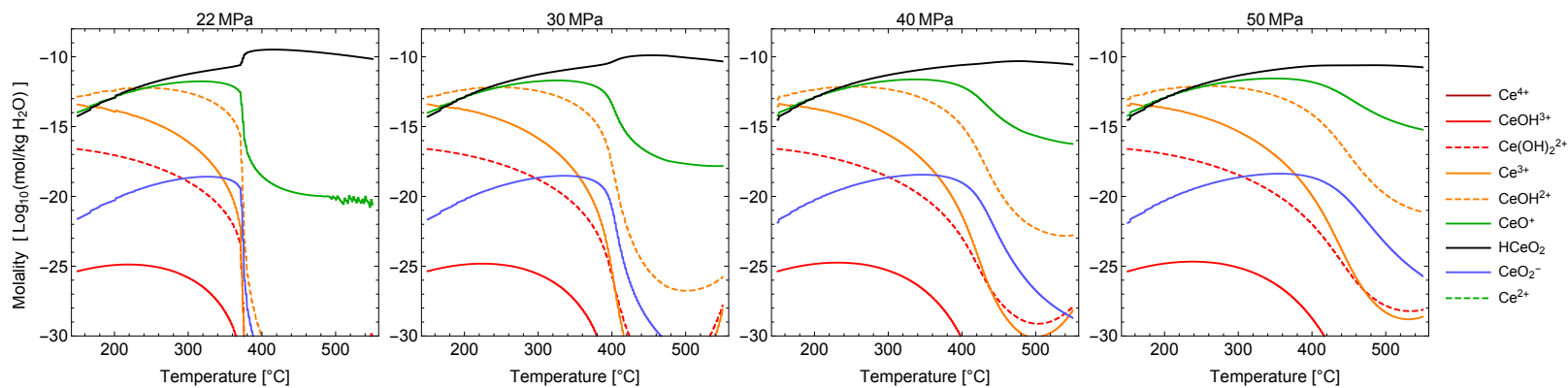
Figure D.2: Magnified view of the equilibrium concentrations of aqueous species from CeO_2 in H_2O as a function of temperature at 22, 30, 40, and 50 MPa.
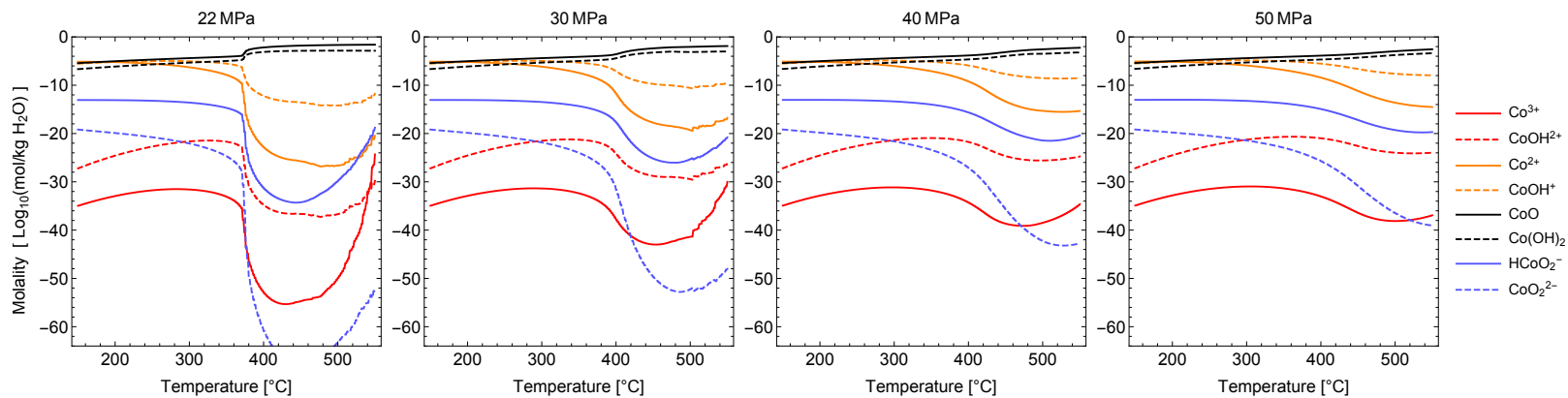
Figure D.3: Equilibrium concentrations of aqueous species from Co in H_2O as a function of temperature at 22, 30, 40, and 50 MPa.
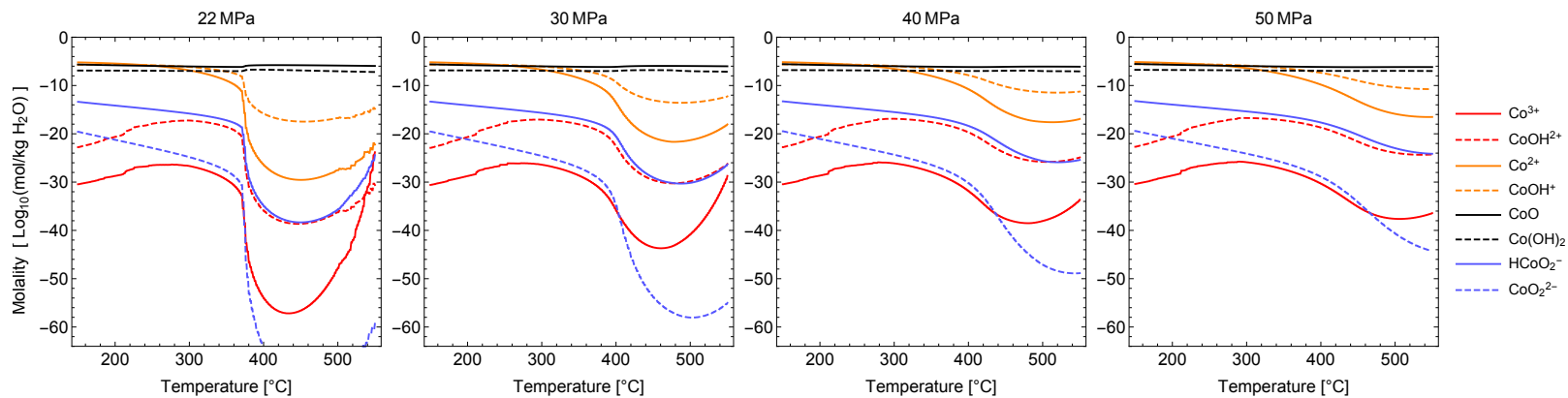
Figure D.4: Equilibrium concentrations of aqueous species from CoO in H_2O as a function of temperature at 22, 30, 40, and 50 MPa.
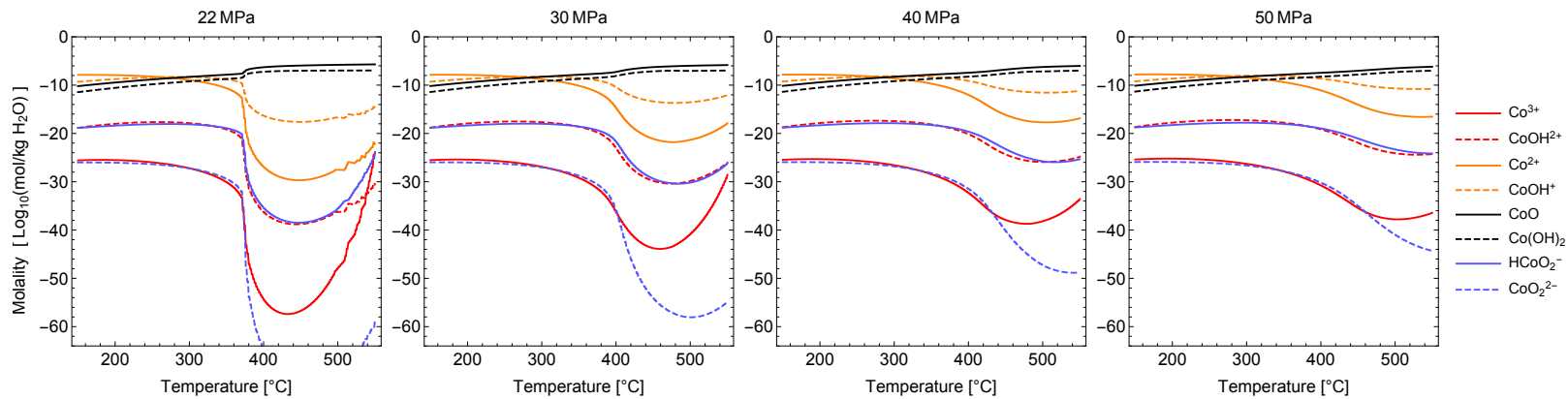
Figure D.5: Equilibrium concentrations of aqueous species from Co_3O_4 in H_2O as a function of temperature at 22, 30, 40, and 50 MPa.
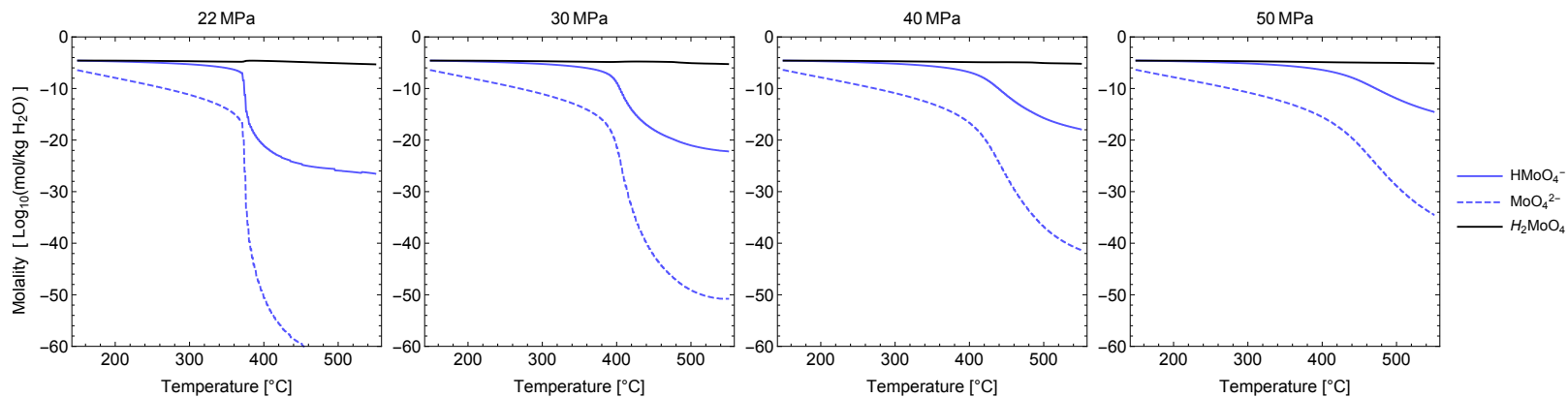
Figure D.6: Equilibrium concentrations of aqueous species from MoO_3 in H_2O as a function of temperature at 22, 30, 40, and 50 MPa.
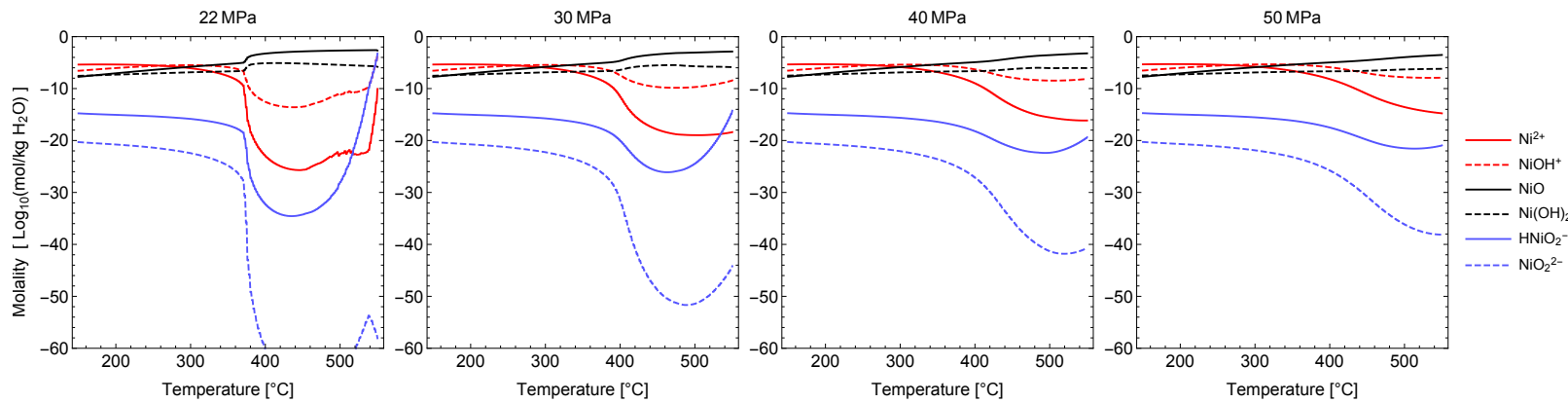
Figure D.7: Equilibrium concentrations of aqueous species from Ni in H₂O as a function of temperature at 22, 30, 40, and 50 MPa.
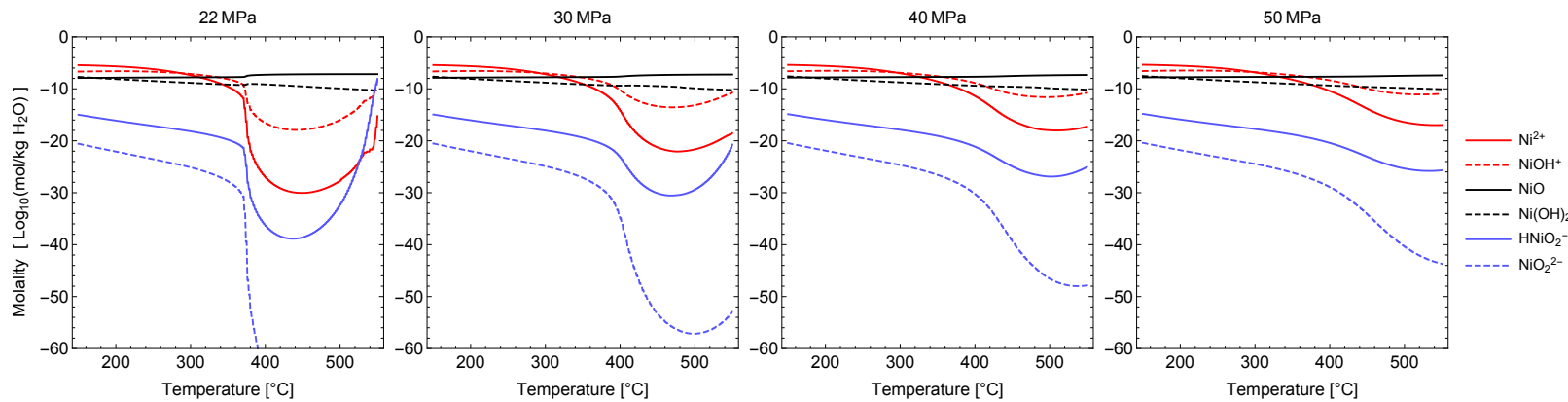
Figure D.8: Equilibrium concentrations of aqueous species from NiO in H₂O as a function of temperature at 22, 30, 40, and 50 MPa.
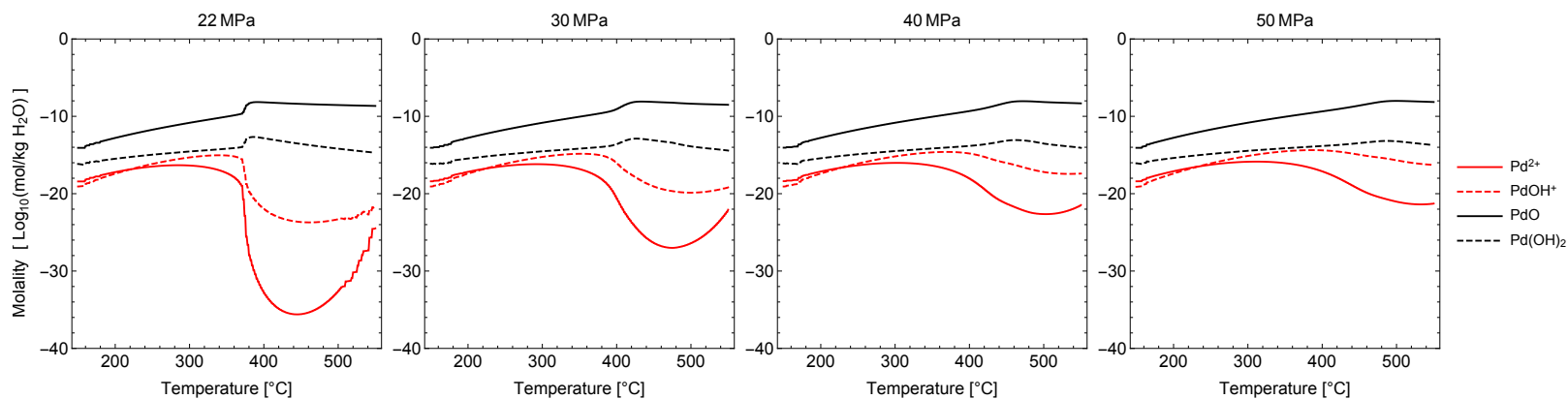
Figure D.9: Equilibrium concentrations of aqueous species from Pd in H_2O as a function of temperature at 22, 30, 40, and 50 MPa.
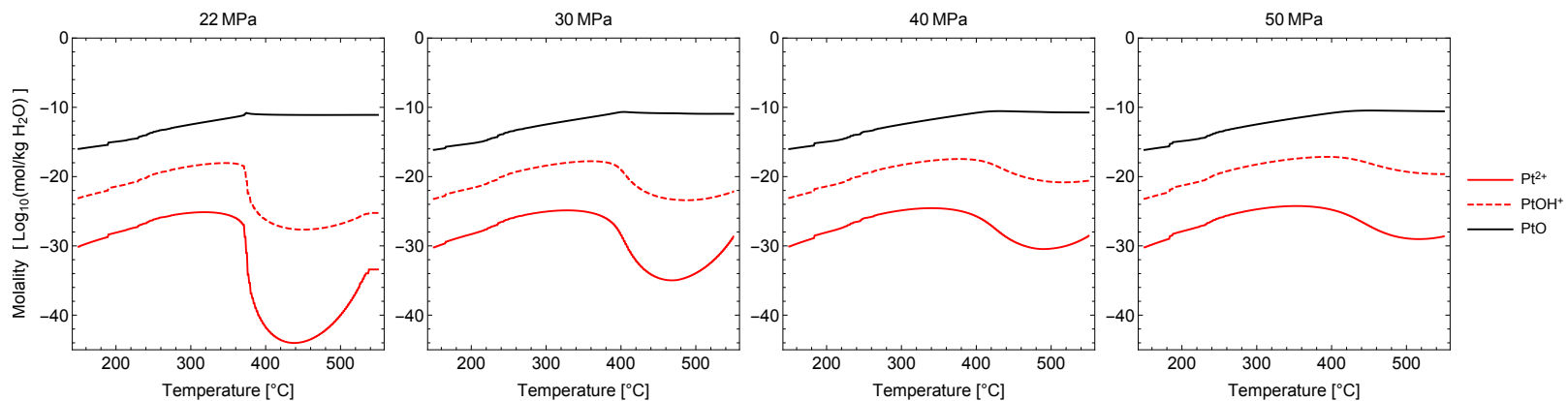
Figure D.10: Equilibrium concentrations of aqueous species from Pt in H_2O as a function of temperature at 22, 30, 40, and 50 MPa.
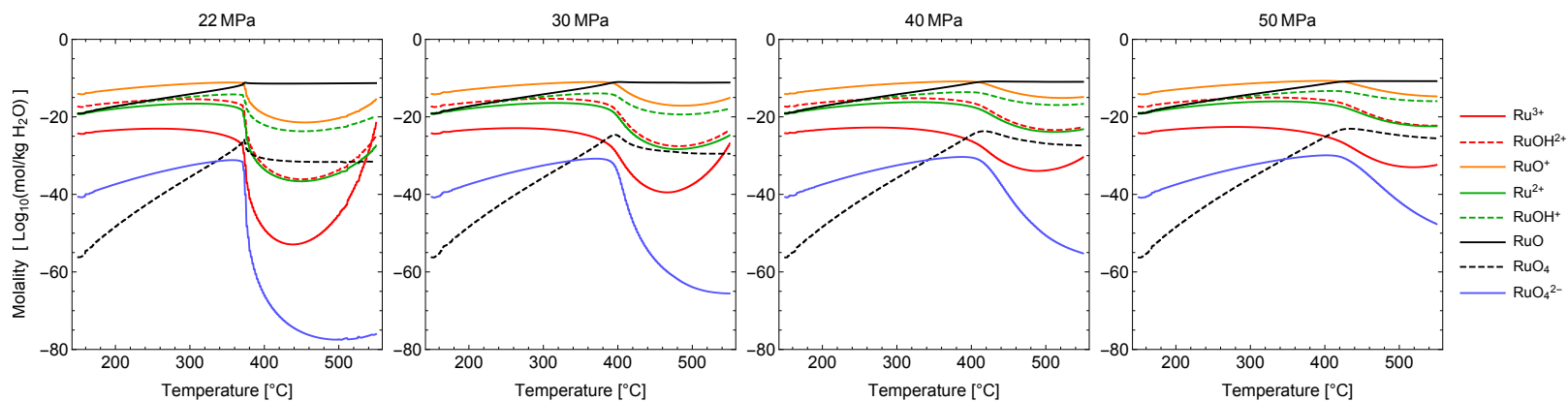
Figure D.11: Equilibrium concentrations of aqueous species from Ru in H_2O as a function of temperature at 22, 30, 40, and 50 MPa.
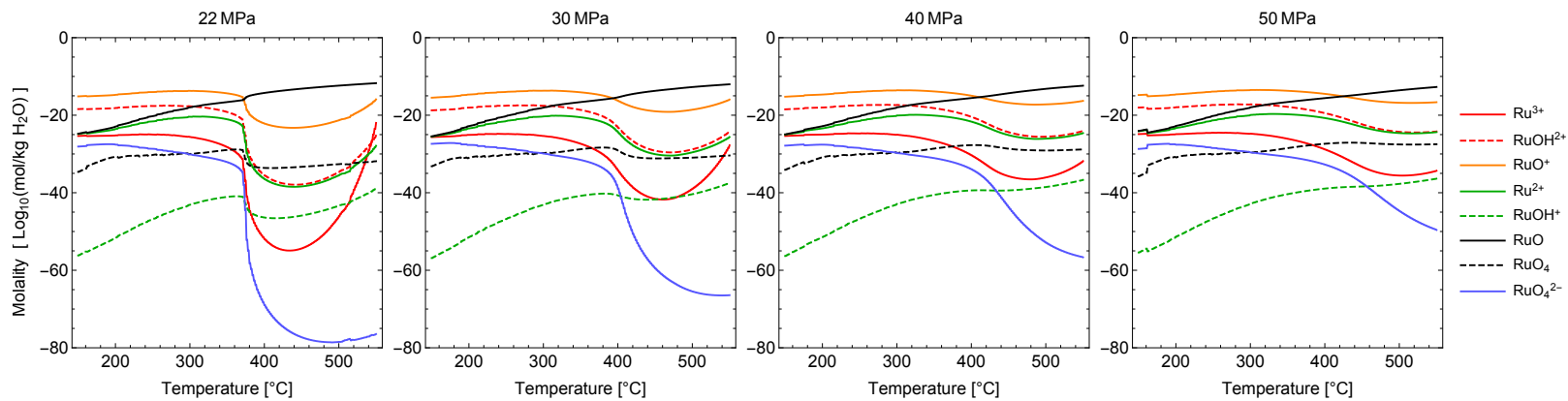
Figure D.12: Equilibrium concentrations of aqueous species from RuO_2 in H_2O as a function of temperature at 22, 30, 40, and 50 MPa.
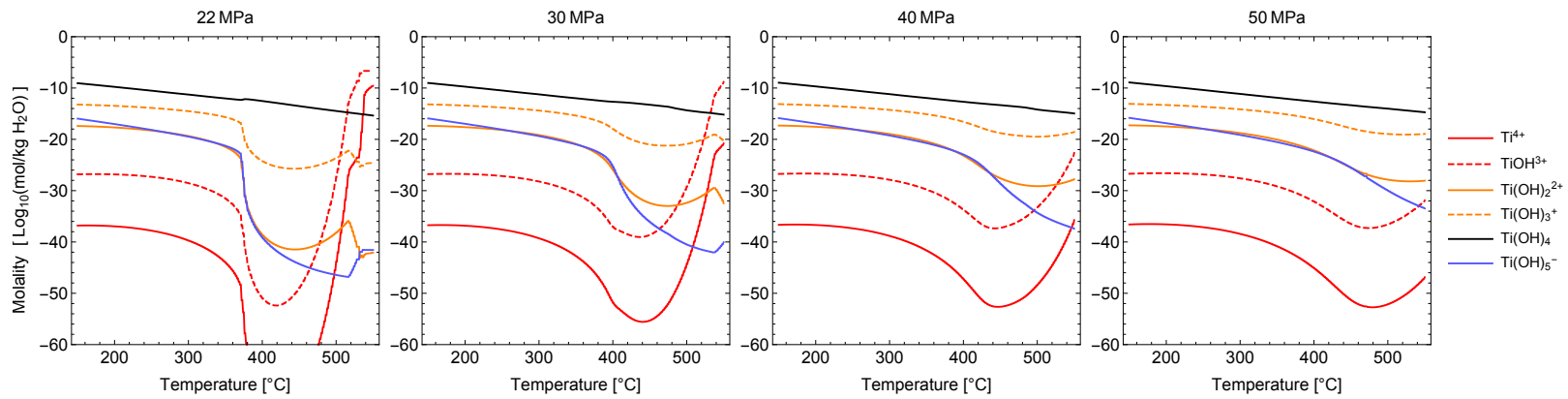
Figure D.13: Equilibrium concentrations of aqueous species from TiO_2 in H_2O as a function of temperature at 22, 30, 40, and 50 MPa.
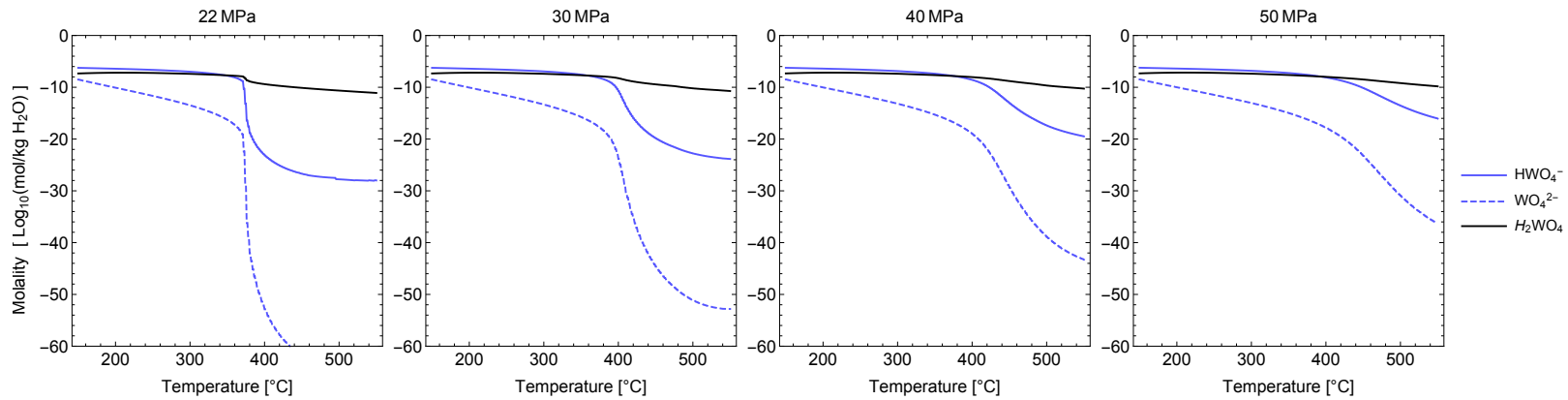
Figure D.14: Equilibrium concentrations of aqueous species from WO_3 in H_2O as a function of temperature at 22, 30, 40, and 50 MPa.
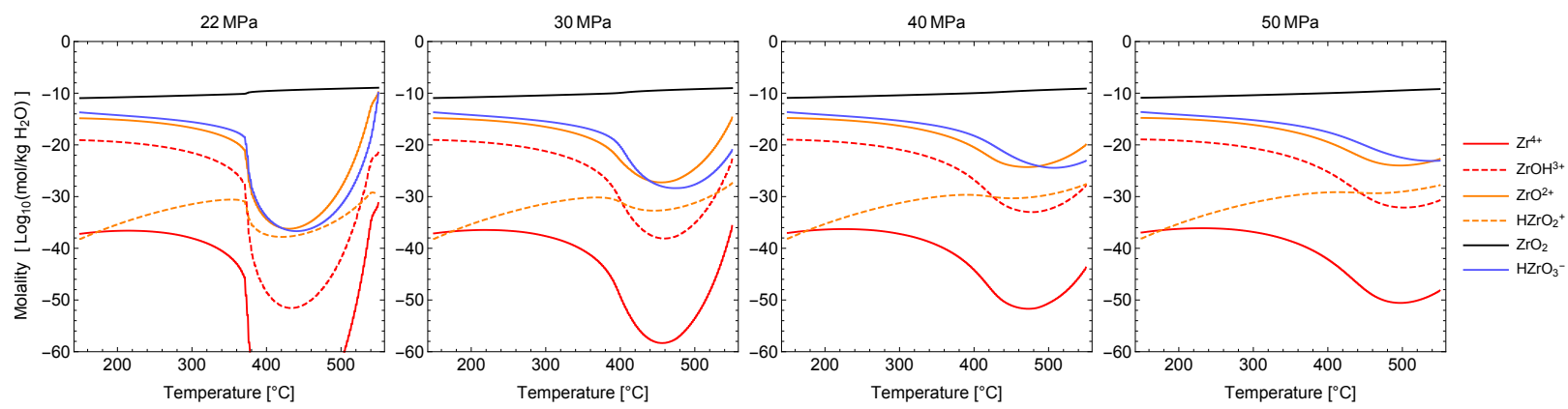
Figure D.15: Equilibrium concentrations of aqueous species from ZrO_2 in H_2O as a function of temperature at 22, 30, 40, and 50 MPa.

APPENDIX E

Additional Oxygen Fugacity-pH Diagrams

Figures E.1 to E.11 show $f_{O_2} - pH$ diagrams for additional T and P conditions and additional catalysts not shown in the main text.
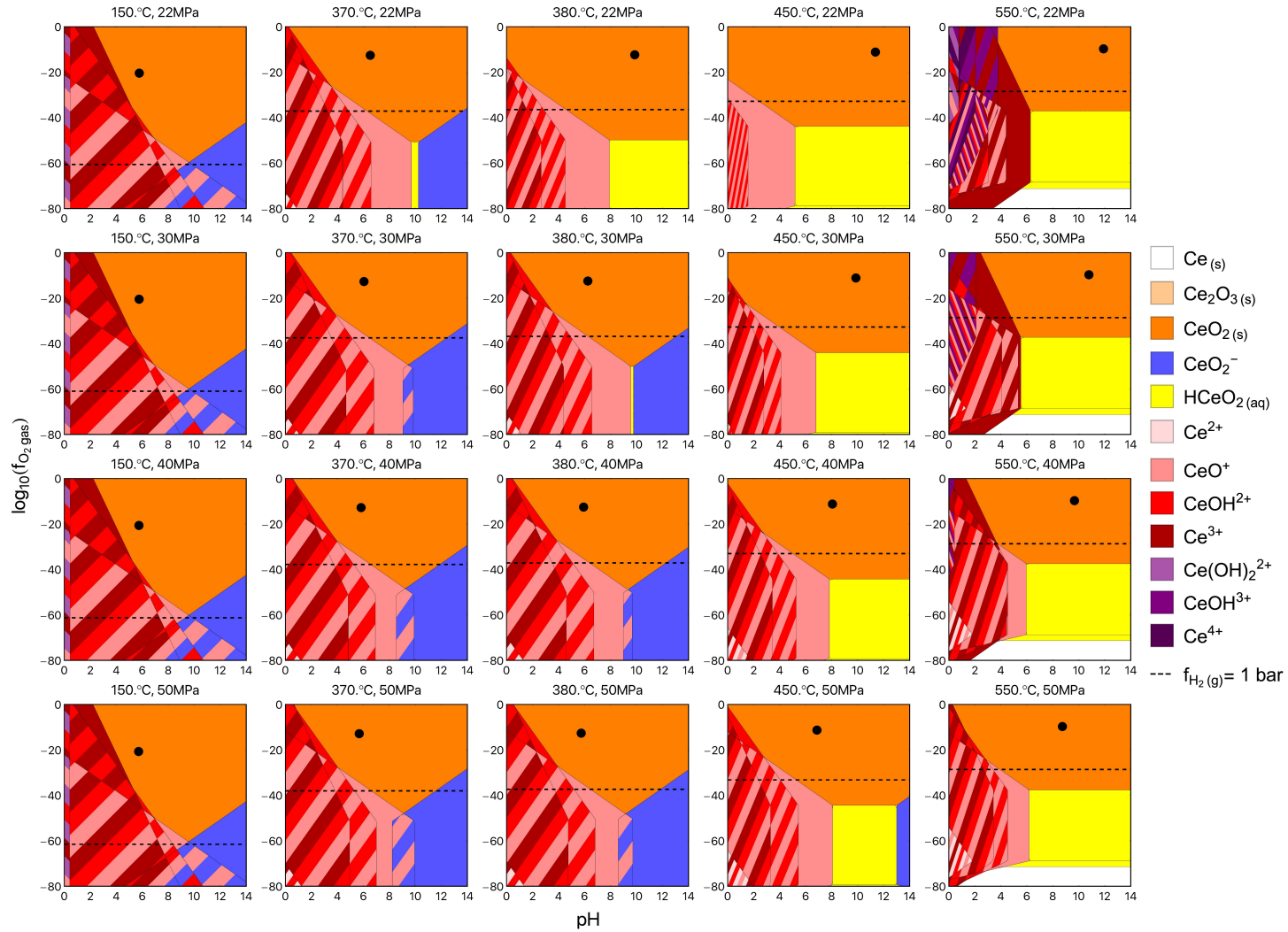
Figure E.1: f_{O_2}-pH diagrams for Ce-H_2O system. f_{O_2} is in bar, and pH is in log_{10}(mol/kg H_2O). Boundaries for aqueous metal species are defined as $a_j = 10^{-6}$ (≈ 1 μmol/kg H_2O). The f_{O_2} and pH values of pure H_2O are plotted as ●.
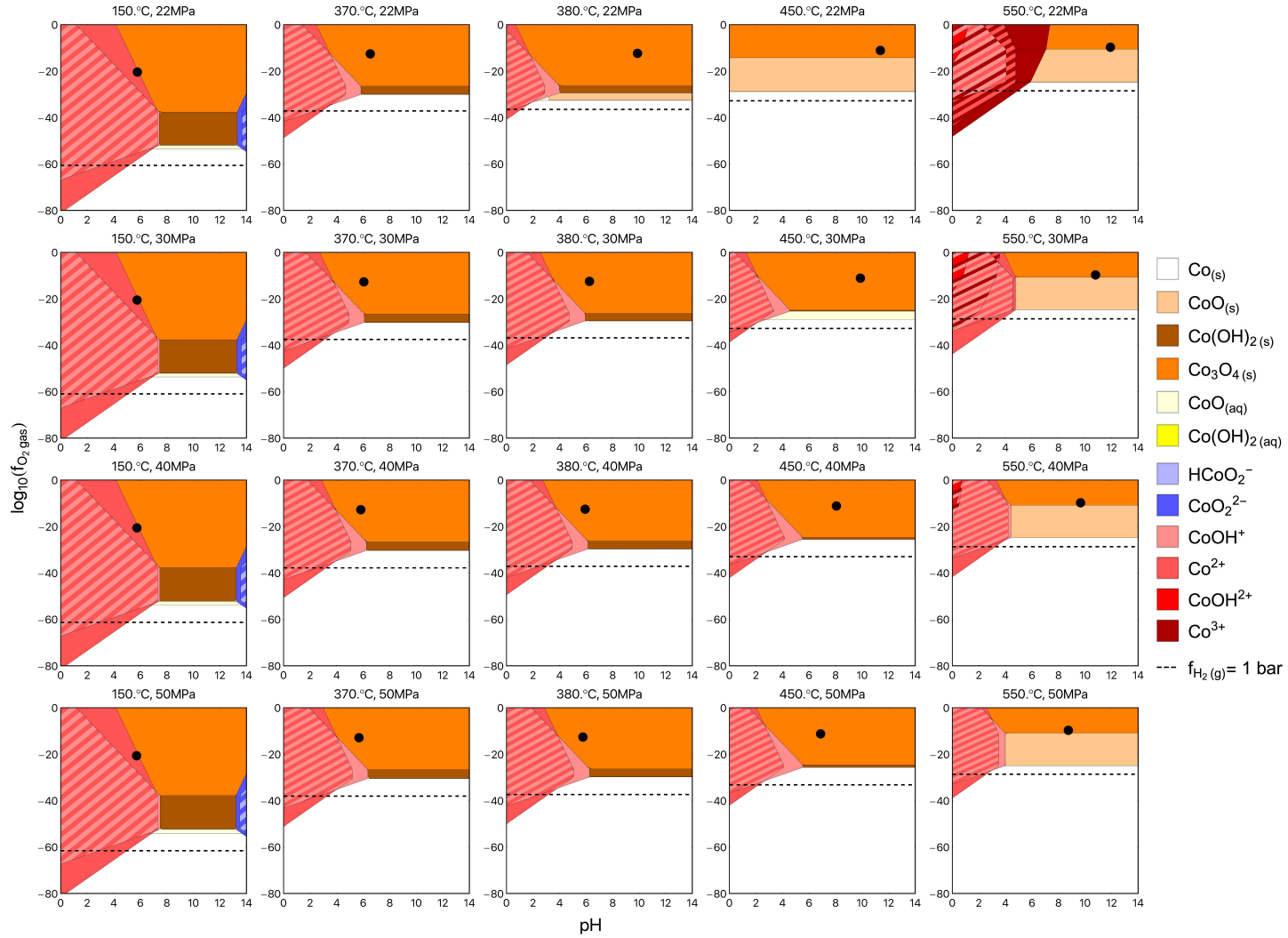
Figure E.2: f_{O_2}-pH diagrams for Co-H$_2$O system. f_{O_2} is in bar, and pH is in log_{10}(mol/kg H$_2$O). Boundaries for aqueous metal species are defined as $a_j = 10^{-6}$ (≈ 1 μmol/kg H$_2$O). The f_{O_2} and pH values of pure H$_2$O are plotted as ●.
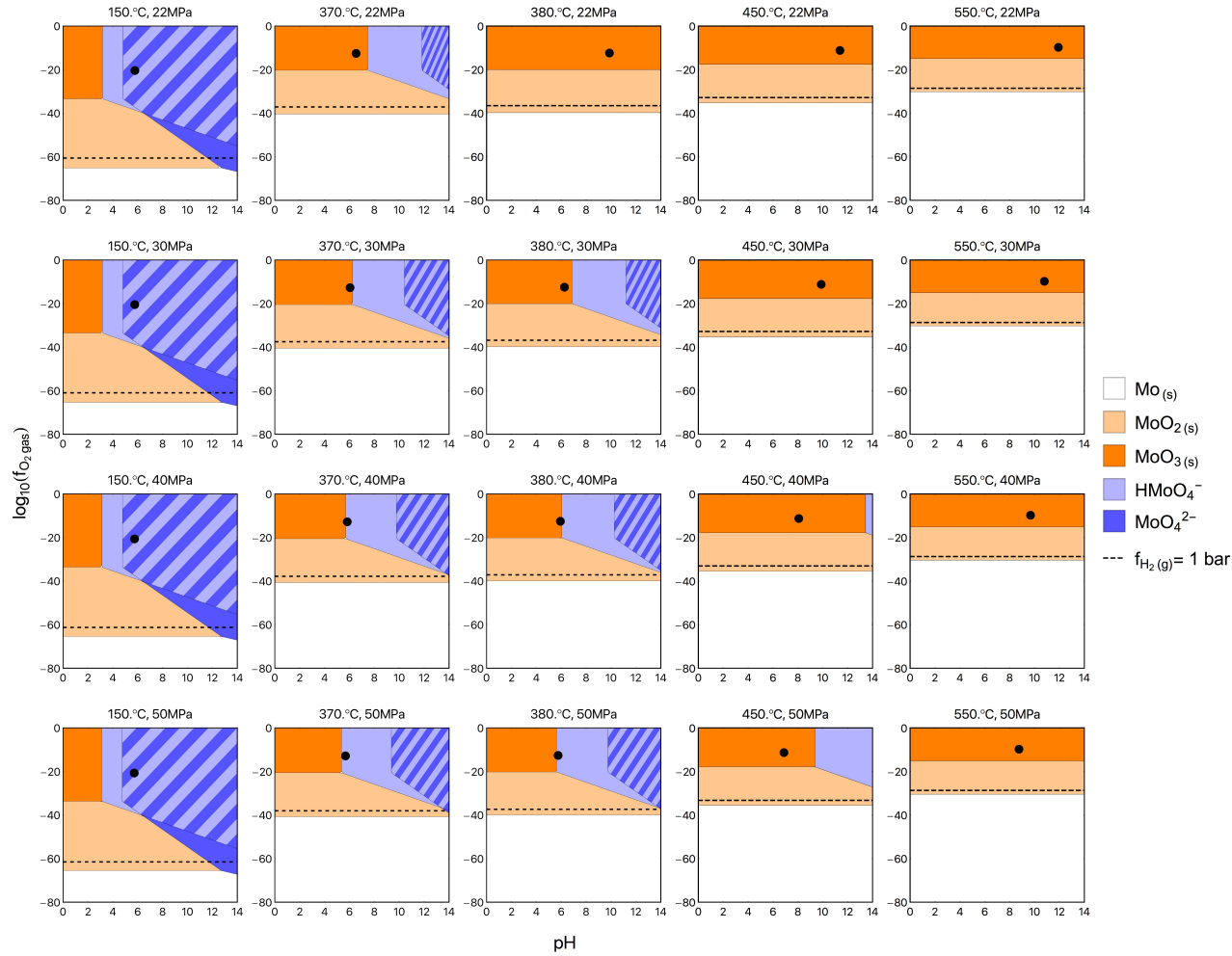
Figure E.3: f_{O_2}-pH diagrams for Mo-H$_2$O system. f_{O_2} is in bar, and pH is in log_{10}(mol/kg H$_2$O). Boundaries for aqueous metal species are defined as $a_j = 10^{-6}$ (≈ 1 μmol/kg H$_2$O). The f_{O_2} and pH values of pure H$_2$O are plotted as $\bullet$. H$_2$MoO$_{4 \text{ (aq)}}$ was omitted for visualization of other species.
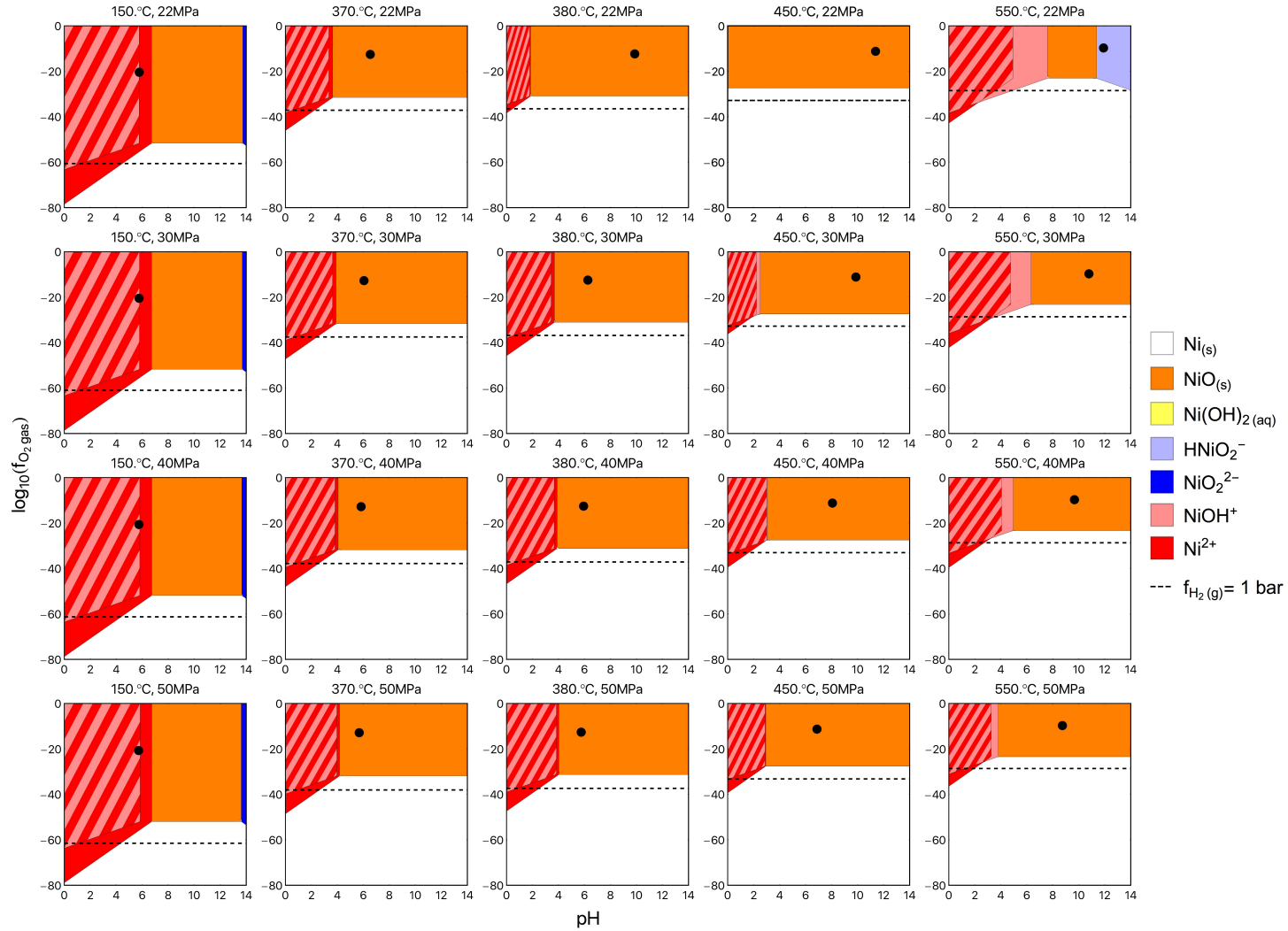
Figure E.4: f_{O_2}-pH diagrams for Ni-H$_2$O system. f_{O_2} is in bar, and pH is in log_{10}(mol/kg H$_2$O). Boundaries for aqueous metal species are defined as $a_j = 10^{-6}$ (≈ 1 μmol/kg H$_2$O). The f_{O_2} and pH values of pure H$_2$O are plotted as ●.
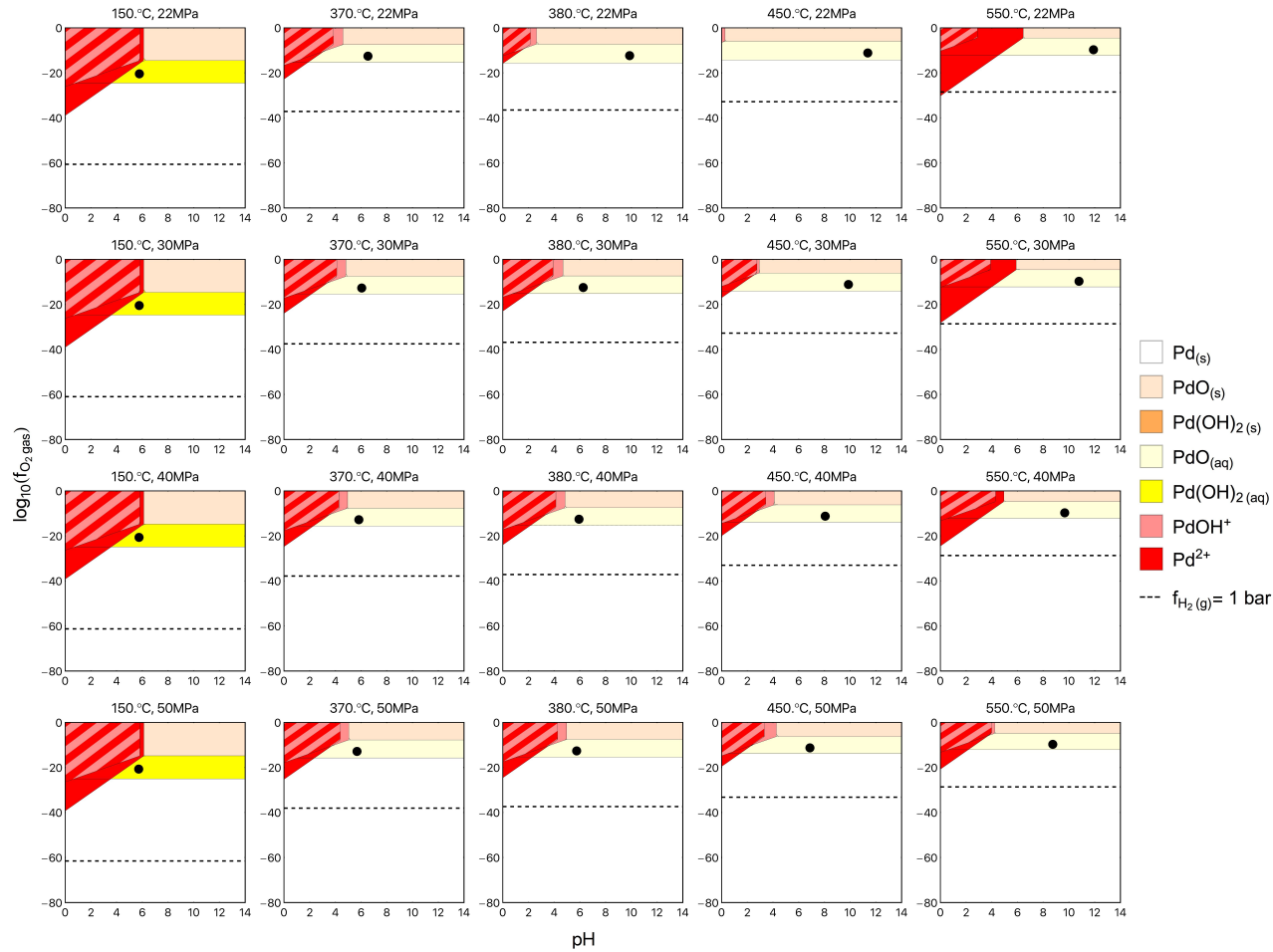
Figure E.5: f_{O_2}-pH diagrams for Pd-H$_2$O system. f_{O_2} is in bar, and pH is in log_{10}(mol/kg H$_2$O). Boundaries for aqueous metal species are defined as $a_j = 10^{-8}$ (≈ 0.01 μmol/kg H$_2$O). The f_{O_2} and pH values of pure H$_2$O are plotted as $\bullet$.
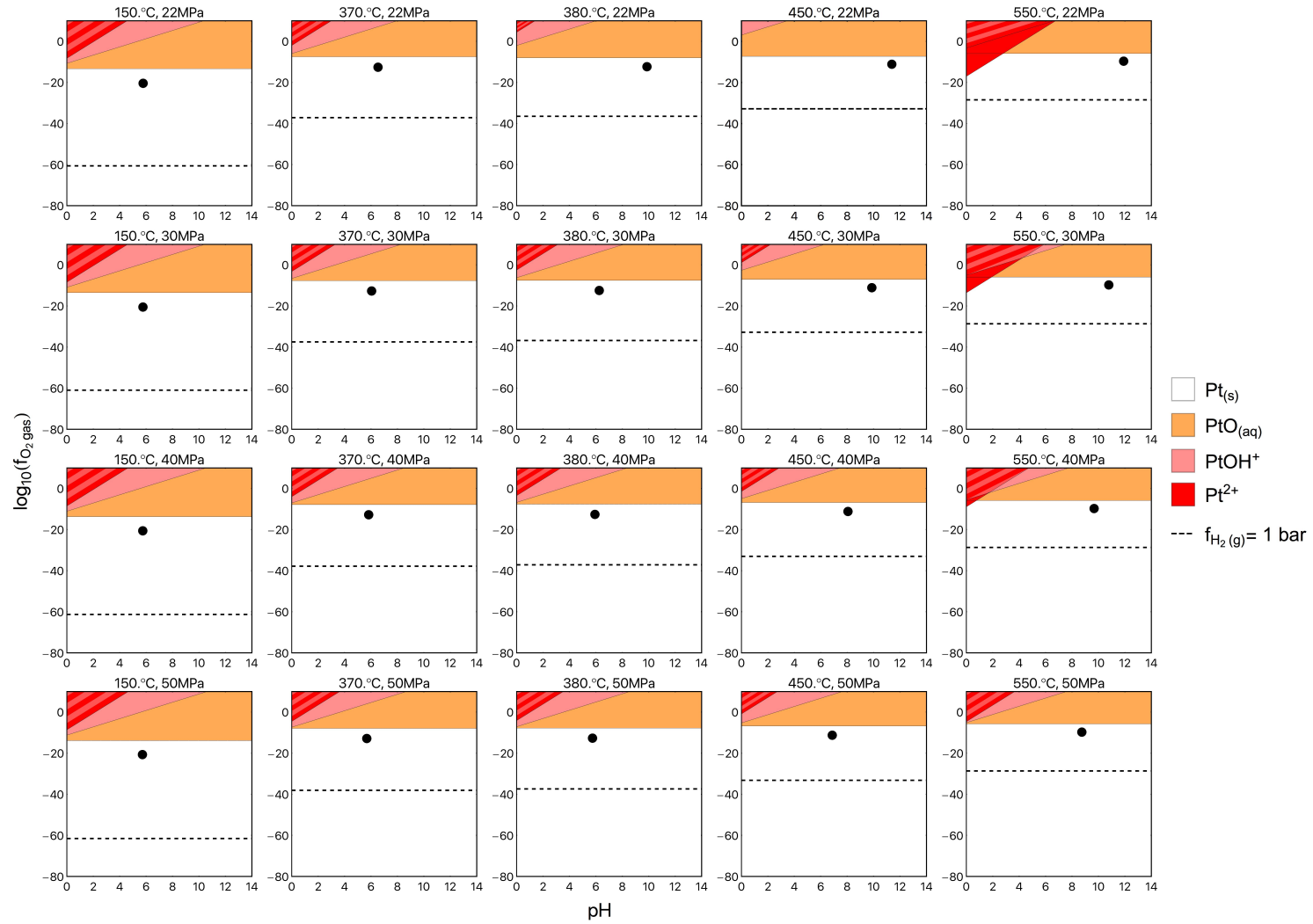
Figure E.6: f_{O_2}-pH diagrams for Pt-H$_2$O system. f_{O_2} is in bar, and pH is in log_{10}(mol/kg H$_2$O). Boundaries for aqueous metal species are defined as $a_j = 10^{-8}$ (≈ 0.01 μmol/kg H$_2$O). The f_{O_2} and pH values of pure H$_2$O are plotted as ●.

Figure E.7: f_{O_2}-pH diagrams for Ru-H_2O system. f_{O_2} is in bar, and pH is in log_{10}(mol/kg H_2O). Boundaries for aqueous metal species are defined as $a_j = 10^{-6}$ (≈ 1 μmol/kg H_2O). The f_{O_2} and pH values of pure H_2O are plotted as ●.
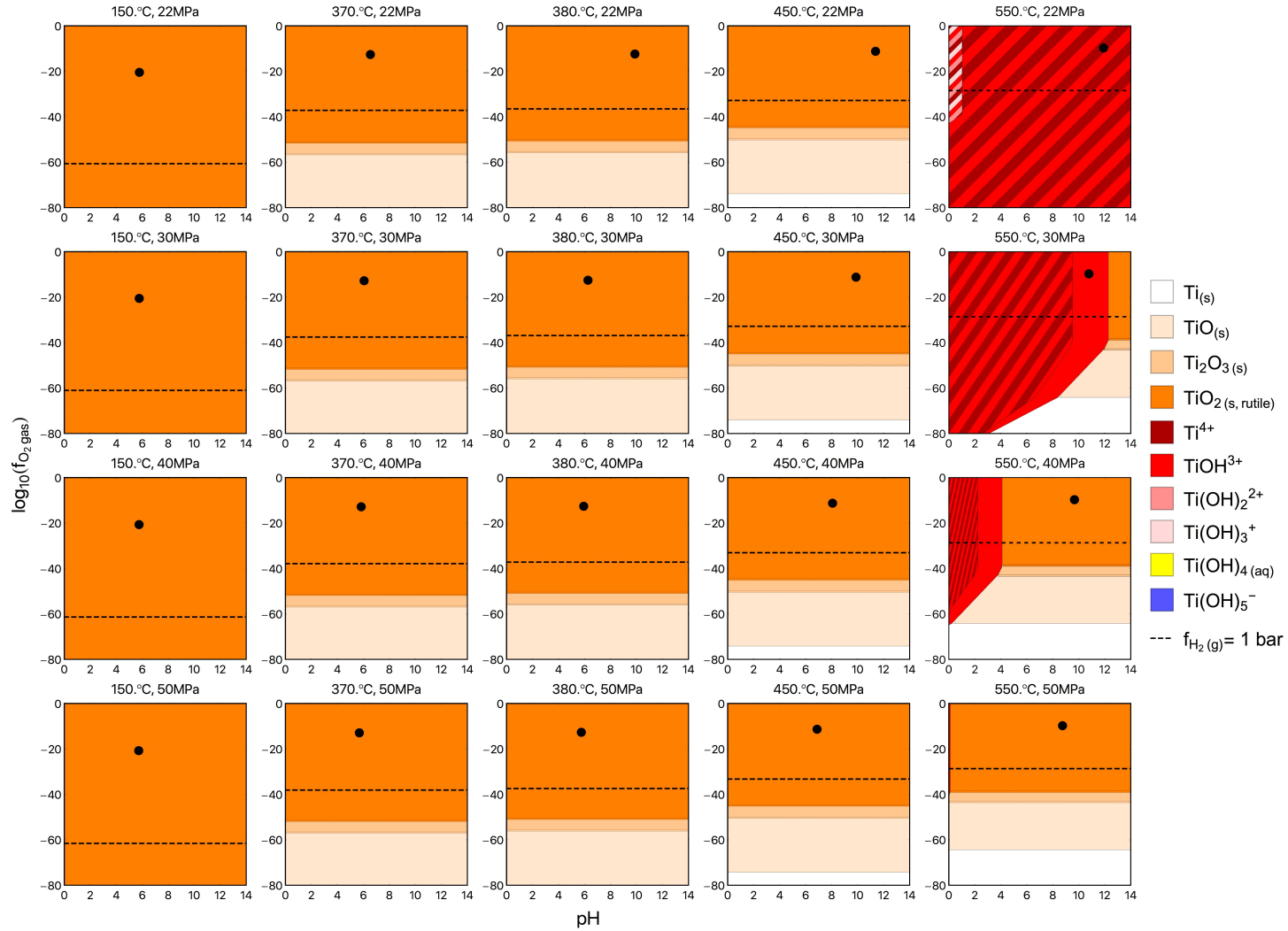
Figure E.8: f_{O_2}-pH diagrams for Ti-H_2O system. f_{O_2} is in bar, and pH is in log_{10}(mol/kg H_2O). Boundaries for aqueous metal species are defined as $a_j = 10^{-6}$ (≈ 1 μmol/kg H_2O). The f_{O_2} and pH values of pure H_2O are plotted as ●..
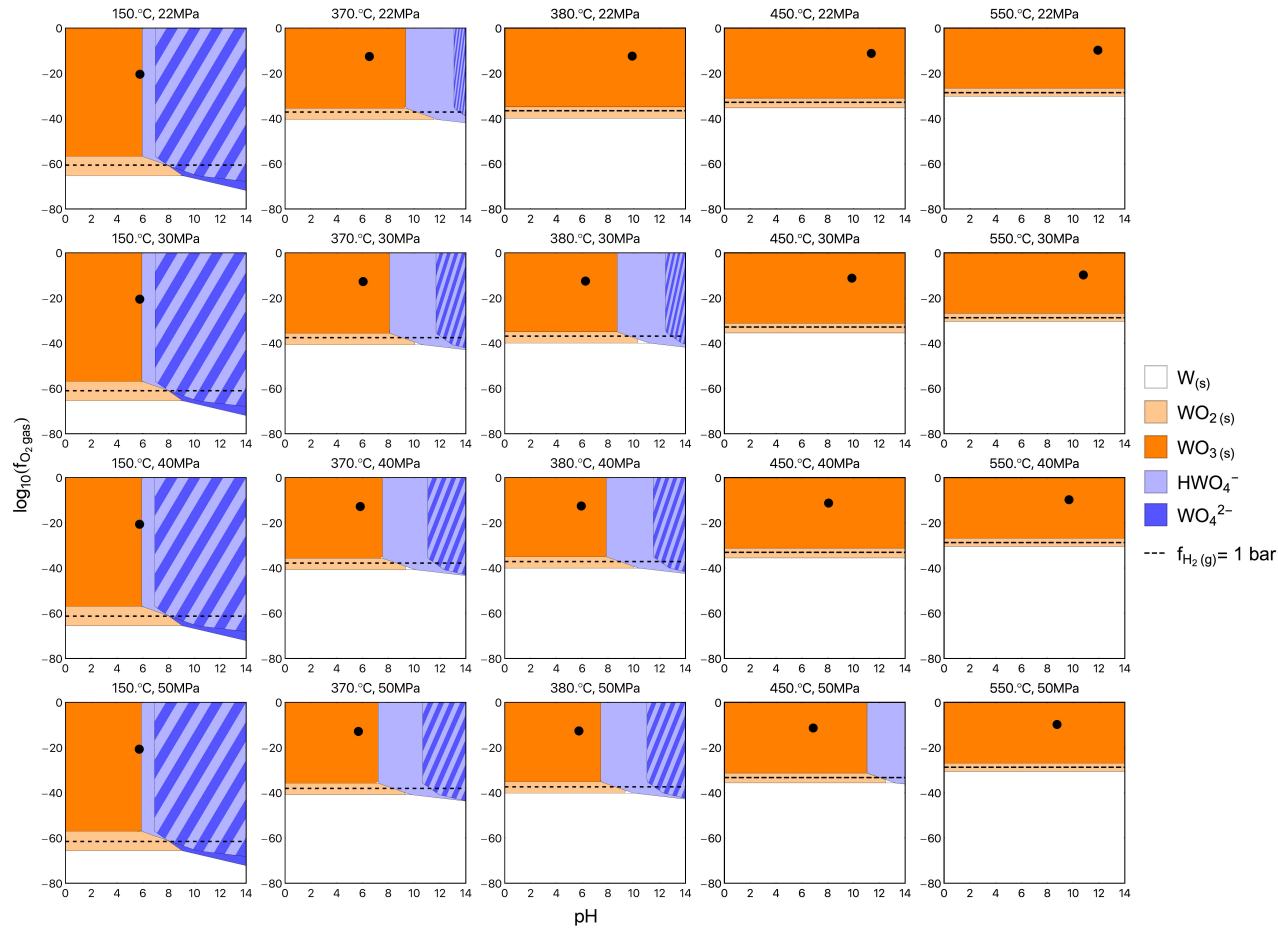
Figure E.9: f_{O_2}-pH diagrams for W-H$_2$O system. f_{O_2} is in bar, and pH is in log_{10}(mol/kg H$_2$O). Boundaries for aqueous metal species are defined as $a_j = 10^{-6}$ ($\approx$ 1 μmol/kg H$_2$O). The f_{O_2} and pH values of pure H$_2$O are plotted as $\bullet$. H$_2$WO$_{4\text{ (aq)}}$ was omitted for visualization of other species.
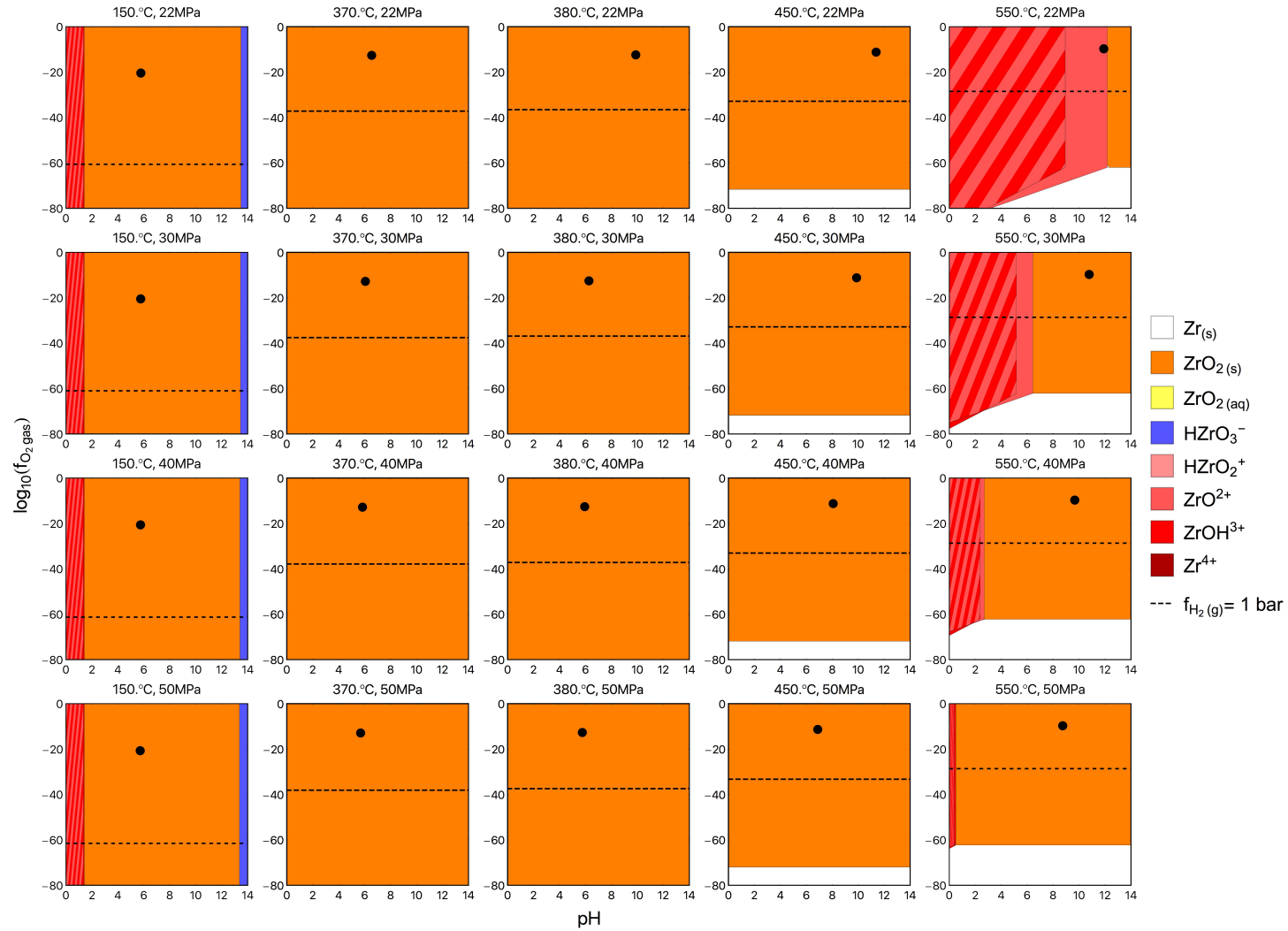
Figure E.10: f_{O_2}-pH diagrams for ZrO_2-H_2O system. f_{O_2} is in bar, and pH is in log_{10}(mol/kg H_2O). Boundaries for aqueous metal species are defined as $a_j = 10^{-6}$ (≈ 1 μmol/kg H_2O). The f_{O_2} and pH values of pure H_2O are plotted as $\bullet$.
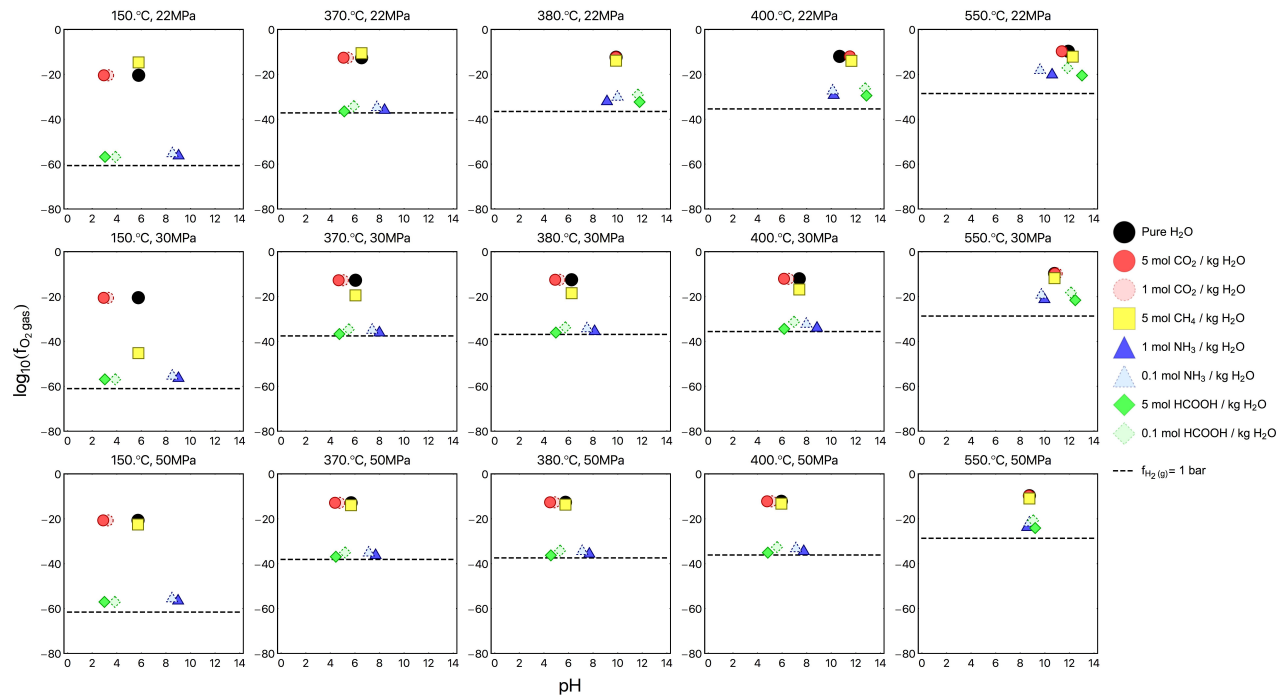
Figure E.11: f_{O_2}-pH diagrams of aqueous solutions of CO_2, CH_4, NH_3, and formic acid (HCOOH) at equilibrium. f_{O_2} is in bar, and pH is in log_{10}(mol/kg H_2O).

BIBLIOGRAPHY

BIBLIOGRAPHY

[1] S F Matar, G Campet, and M A Subramanian. Progress in Solid State Chemistry Electronic properties of oxides : Chemical and theoretical approaches. *Prog. Solid State Chem.*, 39(2):70–95, 2011.

[2] Naoko Akiya and Phillip E. Savage. Roles of Water for Chemical Reactions in High-Temperature Water. *Chem. Rev.*, 102(8):2725–2750, 8 2002.

[3] William L. Marshall and E. U. Franck. Ion Product of Water Substance, 0-1000 °C, 1-10,000 Bars. New International Formulation and Its Background. *J. Phys. Chem. Ref. Data*, 10(2):295–304, 1981.

[4] James W Johnson and Denis Norton. Critical Phenomena in Hydrothermal Systems; State, Thermodynamic, Electrostatic, and Transport Properties of H_2O in the Critical Region. *Am. J. Sci.*, 291(6):541–648, 6 1991.

[5] Thomas M. Yeh, Jacob G. Dickinson, Allison Franck, Suljo Linic, Levi T. Thompson, and Phillip E. Savage. Hydrothermal Catalytic Production of Fuels and Chemicals from Aquatic Biomass. *J. Chem. Technol. Biotechnol.*, 88(1):13–24, 1 2013.

[6] Douglas C. Elliott, Patrick Biller, Andrew B. Ross, Andrew J. Schmidt, and Susanne B. Jones. Hydrothermal liquefaction of biomass: Developments from batch to continuous process. *Bioresour. Technol.*, 178:147–156, 2015.

[7] Changyan Yang, Rui Li, Chang Cui, Shengpeng Liu, Qi Qiu, Yigang Ding, Yuanxin Wu, and Bo Zhang. Catalytic hydroprocessing of microalgae-derived biofuels: a review. *Green Chem.*, 18(13):3684–3699, 2016.

[8] Phillip E. Savage. Organic Chemical Reactions in Supercritical Water. *Chem. Rev.*, 99(2):603–621, 2 1999.

[9] Phillip E. Savage. A Perspective on Catalysis in Sub- and Supercritical Water. *J. Supercrit. Fluids*, 47(3):407–414, 1 2009.

[10] Pooya Azadi and Ramin Farnood. Review of Heterogeneous Catalysts for Sub- and Supercritical Water Gasification of Biomass and Wastes. *Int. J. Hydrogen Energy*, 36(16):9529–9541, 8 2011.

[11] Edward Furimsky. Hydroprocessing in Aqueous Phase. *Ind. Eng. Chem. Res.*, 52(50):17695–17713, 12 2013.

[12] T.V. Choudhary and C.B. Phillips. Renewable Fuels via Catalytic Hydrodeoxygenation. *Appl. Catal., A*, 397(1-2):1–12, 4 2011.

[13] Douglas C Elliott. Catalytic Hydrothermal Gasification of Biomass. *Biofuels, Bioprod. Biorefin.*, 2:254–265, 2008.

[14] P. Kritzer, N. Boukis, and E. Dinjus. Factors Controlling Corrosion in High-Temperature Aqueous Solutions: A Contribution to the Dissociation and Solubility Data Influencing Corrosion Processes. *J. Supercrit. Fluids*, 15(3):205–227, 1999.

[15] Peter Kritzer. Corrosion in High-Temperature and Supercritical Water and Aqueous Solutions: A Review. *J. Supercrit. Fluids*, 29(1-2):1–29, 4 2004.

[16] Philip A. Marrone and Glenn T. Hong. Corrosion Control Methods in Supercritical Water Oxidation and Gasification Processes. *J. Supercrit. Fluids*, 51(2):83–103, 2009.

[17] Chunwen Sun, Rob Hui, Wei Qu, and Sing Yick. Progress in Corrosion Resistant Materials for Supercritical Water Reactors. *Corros. Sci.*, 51(11):2508–2523, 2009.

[18] Z Y Ding, M a Frisch, L X Li, and E F Gloyna. Catalytic Oxidation in Supercritical Water. *Ind. Eng. Chem. Res.*, 35(10):3257–3279, 1996.

[19] Haifeng Xiong, Hien N Pham, and Abhaya K Datye. Hydrothermally Stable Heterogeneous Catalysts for Conversion of Biorenewables. *Green Chem.*, 16(11):4627–4643, 2014.

[20] J. C. Tanger and H. C. Helgeson. Calculation of the Thermodynamic and Transport Properties of Aqueous Species at High Pressures and Temperatures; Revised Equations of State for the Standard Partial Molal Properties of Ions and Electrolytes. *Am. J. Sci.*, 288(1):19–98, 1988.

[21] Everett L. Shock and Harold C. Helgeson. Calculation of the Thermodynamic and Transport Properties of Aqueous Species at High Pressures and Temperatures: Correlation Algorithms for Ionic Species and Equation of State Predictions to 5 kb and 1000 °C. *Geochim. Cosmochim. Acta*, 52(8):2009–2036, 1988.

[22] Everett L Shock, Harold C Helgeson, and Dimitri a Sverjensky. Calculation of the Thermodynamic and Transport Properties of Aqueous Species at High Pressures and Temperatures: Standard Partial Molal Properties of Inorganic Neutral Species. *Geochim. Cosmochim. Acta*, 53(9):2157–2183, 1989.

[23] Everett L. Shock, Eric H. Oelkers, James W. Johnson, Dimitri A. Sverjensky, and Harold C. Helgeson. Calculation of the Thermodynamic Properties of Aqueous Species at High Pressures and Temperatures: Effective Electrostatic Radii,

Dissociation Constants and Standard Partial Molal Properties to 1000 °C and 5 kbar. *J. Chem. Soc., Faraday Trans.*, 88(6):803–826, 1992.

[24] Johnson R Haas, Everett L Shock, and David C Sassani. Rare Earth Elements in Hydrothermal Systems : Estimates of Standard Partial Molal Thermodynamic Properties of Aqueous Complexes of the Rare Earth Elements at High Pressures and Temperatures. *Geochim. Cosmochim. Acta*, 59(21):4329–4350, 1995.

[25] Everett L Shock, David C Sassani, Marc Willis, and Dimitri A. Sverjensky. Inorganic species in geologic fluids: Correlations Among Standard Molal Thermodynamic Properties of Aqueous Ions and Hydroxide Complexes. *Geochim. Cosmochim. Acta*, 61(5):907–950, 1997.

[26] David C. Sassani and Everett L. Shock. Solubility and Transport of Platinum-Group Elements in Supercritical Fluids: Summary and Estimates of Thermodynamic Properties for Ruthenium, Rhodium, Palladium, and Platinum Solids, Aqueous Ions, and Complexes to 1000 °C and 5 kbar. *Geochim. Cosmochim. Acta*, 62(15):2643–2671, 1998.

[27] Kiwamu Sue, Tadafumi Adschiri, and Kunio Arai. Predictive Model for Equilibrium Constants of Aqueous Inorganic Species at Subcritical and Supercritical Conditions. *Ind. Eng. Chem. Res.*, 41(13):3298–3306, 2002.

[28] F. Masoodiyeh, M.R. Mozdianfard, and J. Karimi-Sabet. Solubility Estimation of Inorganic Salts in Supercritical Water. *J. Chem. Thermodyn.*, 78(3):260–268, 2014.

[29] G S Was, P Ampornrat, G Gupta, S Teysseyre, E A West, T. R. Allen, K. Sridharan, L. Tan, Y. Chen, X. Ren, and C. Pister. Corrosion and Stress Corrosion Cracking in Supercritical Water. *J. Nucl. Mater.*, 371(1-3):176–201, 2007.

[30] Norihisa Saito and Yoshie Akai. Chemical Thermodynamics Consideration on Corrosion Products in Supercritical-Water-Cooled Reactor Coolant Management and Disposal. *Nucl. Technol.*, 155(July):105–113, 2006.

[31] A. Aimable, H. Muhr, C. Gentric, F. Bernard, F. Le Cras, and D. Aymes. Continuous Hydrothermal Synthesis of Inorganic Nanopowders in Supercritical Water: Towards a Better Control of the Process. *Powder Technol.*, 190(1-2):99–106, 2009.

[32] Hiromichi Hayashi and Yukiya Hakuta. Hydrothermal Synthesis of Metal Oxide Nanoparticles in Supercritical Water. *Materials*, 3(7):3794–3817, 2010.

[33] Tadafumi Adschiri, Youn-Woo Lee, Motonobu Goto, and Seiichi Takami. Green Materials Synthesis with Supercritical Water. *Green Chem.*, 13(6):1380, 2011.

[34] Jennifer N. Jocz, Levi T. Thompson, and Phillip E. Savage. Catalyst Oxidation and Dissolution in Supercritical Water. *Chem. Mater.*, 30(4):1218–1229, 01 2018.

[35] David J. Wesolowski, Stephen E. Ziemniak, Lawrence M. Anovitz, Michael L. Machesky, and Pascale Bénézeth. Solubility and surface adsorption characteristics of metal oxides. In D.A. Palmer and R. Fernández-Prini, editors, *Aqueous Systems at Elevated Temperatures and Pressures: Physical Chemistry in Water, Steam, and Hydrothermal Solutions*, chapter 14, pages 493–595. Elsevier Ltd., 2004.

[36] Daniel A. Ruddy, Joshua A. Schaidle, Jack R. Ferrell III, Jun Wang, Luc Moens, and Jesse E. Hensley. Recent Advances in Heterogeneous Catalysts for Bio-Oil Upgrading via "*Ex Situ* Catalytic Fast Pyrolysis": Catalyst Development through the Study of Model Compounds. *Green Chem.*, 16(2):454–490, 2014.

[37] Allison M. Robinson, Jesse E. Hensley, and J. Will Medlin. Bifunctional Catalysts for Upgrading of Biomass-Derived Oxygenates: A Review. *ACS Catal.*, 6(8):5026–5043, 2016.

[38] Peigao Duan and Phillip E. Savage. Catalytic Treatment of Crude Algal Bio-Oil in Supercritical Water: Pptimization Studies. *Energy Environ. Sci.*, 4(4):1447, 2011.

[39] Peigao Duan and Phillip E. Savage. Catalytic Hydrothermal Hydrodenitrogenation of Pyridine. *Appl. Catal., B*, 108-109:54–60, 10 2011.

[40] Yuping Xu, Peigao Duan, and Bing Wang. Catalytic Upgrading of Pretreated Algal Oil with a Two-Component Catalyst Mixture in Supercritical Water. *Algal Res.*, 9:186–193, 2015.

[41] Xiujun Bai, Peigao Duan, Yuping Xu, Aiyun Zhang, and Phillip E. Savage. Hydrothermal Catalytic Processing of Pretreated Algal Oil: A Catalyst Screening Study. *Fuel*, 120:141–149, 3 2014.

[42] Na Ji, Tao Zhang, Mingyuan Zheng, Aiqin Wang, Hui Wang, Xiaodong Wang, and Jingguang G. Chen. Direct Catalytic Conversion of Cellulose into Ethylene Glycol using Nickel-Promoted Tungsten Carbide Catalysts. *Angew. Chem., Int. Ed.*, 47(44):8510–8513, 2008.

[43] Joshua A. Schaidle, Adam C. Lausche, and Levi T. Thompson. Effects of Sulfur on Mo_2C and Pt/Mo_2C Catalysts: Water Gas Shift Reaction. *J. Catal.*, 272(2):235–245, 2010.

[44] Adam C. Lausche, Joshua A. Schaidle, and Levi T. Thompson. Understanding the Effects of Sulfur on Mo_2C and Pt/Mo_2C Catalysts: Methanol Steam Reforming. *Appl. Catal., A*, 401(1-2):29–36, 2011.

[45] Joshua A. Schaidle, Neil M. Schweitzer, Olabode T. Ajenifujah, and Levi T. Thompson. On the Preparation of Molybdenum Carbide-Supported Metal Catalysts. *J. Catal.*, 289:210–217, 2012.

[46] Jeong-Gil Choi, Curl L. Rane, and Levi T. Thompson. Molybdenum Nitride Catalysts 1. Influence of the Synthesis Factors on Structural Properties. *J. Catal.*, 146:218–227, 1994.

[47] M K Neylon, S Choi, H Kwon, K E Curry, and L T Thompson. Catalytic Properties of Early Transition Metal Nitrides and Carbides: N-Butane Hydrogenolysis, Dehydrogenation and Isomerization. *Appl. Catal., A*, 183(2):253–263, 1999.

[48] Peigao Duan and Phillip E Savage. Upgrading of Crude Algal Bio-Oil in Supercritical Water. *Bioresour. Technol.*, 102(2):1899–1906, 1 2011.

[49] W J Lamb, G A Hoffman, and J Jonas. Self-Diffusion in Compressed Supercritical Water. *J. Chem. Phys.*, 74(12):6875–6880, 1981.

[50] Tylisha M. Brown, Peigao Duan, and Phillip E. Savage. Hydrothermal Liquefaction and Gasification of *Nannochloropsis* sp. *Energy Fuels*, 24(6):3639–3646, 6 2010.

[51] NIST Chemistry WebBook, 2016.

[52] Ihsan Barin. *Thermochemical Data of Pure Substances*. VCH Publishers, Inc., New York, 1995.

[53] Greg M. Anderson and David A. Crerar. *Thermodynamics in Geochemistry: The Equilibrium Model*. Oxford University Press, 1993.

[54] Jianli Yu and Phillip E Savage. Catalyst Activity, Stability, and Transformations during Oxidation in Supercritical Water. *Appl. Catal., A*, 31:123–132, 2001.

[55] Anand G. Chakinala, Jithendra K. Chinthaginjala, Kulathuiyer Seshan, Wim P M Van Swaaij, Sascha R A Kersten, and Derk W F Brilman. Catalyst Screening for the Hydrothermal Gasification of Aqueous Phase of Bio-Oil. *Catal. Today*, 195(1):83–92, 2012.

[56] Hemma Zöhrer, Franziska Mayr, and Frdric Vogel. Stability and Performance of Ruthenium Catalysts based on Refractory Oxide Supports in Supercritical Water Conditions. *Energy Fuels*, 27(8):4739–4747, 2013.

[57] Tayier Yunusi, Chao Yang, Wanling Cai, Feng Xiao, Jide Wang, and Xintai Su. Synthesis of MoO_3 Submicron Belts and MoO_2 Submicron Spheres via Polyethylene Glycol-Assisted Hydrothermal Method and their Gas Sensing Properties. *Ceram. Int.*, 39(3):3435–3439, 2013.

[58] A. V. Shishkin, M. Ya. Sokol, and A. A. Vostrikov. Synthesis of MoO_2 Particles during Oxidation of Bulk Molybdenum Samples by Supercritical Water. *Thermophys. Aeromech.*, 20(5):647–650, 2013.

[59] M.-H. Cho, S. a. Park, K.-D. Yang, I. W. Lyo, K. Jeong, S. K. Kang, D.-H. Ko, K. W. Kwon, J. H. Ku, S. Y. Choi, and H. J. Shin. Evolution of Tungsten-Oxide Whiskers Synthesized by a Rapid Thermal-Annealing Treatment. *J. Vac. Sci. Technol., B: Microelectron. Nanometer Struct.–Process., Meas., Phenom.*, 22(3):1084, 2004.

[60] Gang Gu, Bo Zheng, W. Q. Han, Siegmar Roth, and Jie Liu. Tungsten Oxide Nanowires on Tungsten Substrates. *Nano Lett.*, 2(8):849–851, 2002.

[61] Minsoo Kim, Byung Yong Lee, Hyung Chul Ham, Jonghee Han, Suk Woo Nam, Hong-shik Lee, Joo Hoon Park, Sun Choi, and Youhwan Shin. Facile One-Pot Synthesis of Tungsten Oxide (WO_{3-x}) Nanoparticles using Sub and Supercritical Fluids. *J. Supercrit. Fluids*, 111:8–13, 2016.

[62] Makoto Akizuki, Keiji Sano, and Yoshito Oshima. Effect of Supercritical Water on the Stability of WO_X/TiO_2 and NbO_X/TiO_2 Catalysts during Glycerol Dehydration. *J. Supercrit. Fluids*, 113:158–165, 2016.

[63] B. N. Ryzhenko. Technology of Groundwater Quality Prediction: 1. Eh-pH Diagram and Detention Coefficient of Molybdenum and Tungsten in Aqueous Solutions. *Geochem. Int.*, 48(4):407–414, 2010.

[64] Z. Minubayeva and T. M. Seward. Molybdic Acid Ionisation under Hydrothermal Conditions to 300 °C. *Geochim. Cosmochim. Acta*, 74(15):4365–4374, 2010.

[65] Nicole C. Hurtig and Anthony E. Williams-Jones. An Experimental Study of the Solubility of MoO_3 in Aqueous Vapour and Low to Intermediate Density Supercritical Fluids. *Geochim. Cosmochim. Acta*, 136:169–193, 2014.

[66] Kirsten U. Rempel, A. A. Migdisov, and A. E. Williams-Jones. The Solubility and Speciation of Molybdenum in Water Vapour at Elevated Temperatures and Pressures: Implications for Ore Genesis. *Geochim. Cosmochim. Acta*, 70(3):687–696, 2006.

[67] Jeffrey Greeley. Theoretical Heterogeneous Catalysis: Scaling Relationships and Computational Catalyst Design. *Annual Review of Chemical and Biomolecular Engineering*, 7:605–635, 2016.

[68] Joon-Hyung Ahn, Won-Jae Lee, and Ho-Gi Kim. Oxygen Diffusion through RuO_2 Bottom Electrode of Integrated Ferroelectric Capacitors. *Mater. Lett.*, 38(February):250–253, 1999.

[69] Sang Ho Oh, Chan Gyung Park, and Chanro Park. Thermal Stability of RuO_2/Ru Bilayer Thin Film in Oxygen Atmosphere. *Thin Solid Films*, 359:118–123, 2000.

[70] William Costanzo, Roger Hilten, Umakanta Jena, K. C. Das, and James R. Kastner. Effect of low temperature hydrothermal liquefaction on catalytic hydrodenitrogenation of algae biocrude and model macromolecules. *Algal Research*, 13:53–68, 2016.

[71] Morteza Hosseinpour, Abooali Golzary, Mohammad Saber, and Kunio Yoshikawa. Denitrogenation of biocrude oil from algal biomass in high temperature water and formic acid mixture over H + ZSM-5 nanocatalyst. *Fuel*, 206:628–637, 2017.

[72] Ligang Luo, Liyi Dai, and Phillip E. Savage. Catalytic hydrothermal liquefaction of soy protein concentrate. *Energy and Fuels*, 29(5):3208–3214, 2015.

[73] Pei-Qing Yuan, Zhen-Min Cheng, Xiang-Yang Zhang, and Wei-Kang Yuan. Catalytic denitrogenation of hydrocarbons through partial oxidation in supercritical water. *Fuel*, 85(3):367–373, feb 2006.

[74] R. Prins, M. Egorova, A. Röthlisberger, Y. Zhao, N. Sivasankar, and P. Kukula. Mechanisms of hydrodesulfurization and hydrodenitrogenation. *Catalysis Today*, 111(1-2):84–93, 2006.

[75] G Perot. The reactions involved in hydrodenitrogenation. *Catalysis Letters*, 10:447–472, 1991.

[76] O M Ogunsola. Decomposition of isoquinoline and quinoline by supercritical water. *Journal of hazardous materials*, 74(3):187–95, jun 2000.

[77] Jacob G. Dickinson and Phillip E. Savage. Stability and activity of Pt and Ni catalysts for hydrodeoxygenation in supercritical water. *Journal of Molecular Catalysis A: Chemical*, aug 2013.

[78] Tadafumi Adschiri, Ryuji Shibata, Takafumi Sato, Masaru Watanabe, and Kunio Arai. Catalytic Hydrodesulfurization of Dibenzothiophene through Partial Oxidation and a Water Gas Shift Reaction in Supercritical Water. *Industrial & Engineering Chemistry Research*, 37(7):2634–2638, jul 1998.

[79] Neil M Schweitzer, Joshua A Schaidle, Obiefune K Ezekoye, Xiaoqing Pan, Suljo Linic, and Levi T Thompson. High Activity Carbide Supported Catalysts for Water Gas Shift. *Journal of the American Chemical Society*, 133(8):2378–2381, mar 2011.

[80] Maurice H. Waldner, Frank Krumeich, and Frédéric Vogel. Synthetic natural gas by hydrothermal gasification of biomass. Selection procedure towards a stable catalyst and its sodium sulfate tolerance. *Journal of Supercritical Fluids*, 43:91–105, 2007.

[81] Peigao Duan, Xiujun Bai, Yuping Xu, Aiyun Zhang, Feng Wang, Lei Zhang, and Juan Miao. Catalytic upgrading of crude algal oil using platinum/gamma alumina in supercritical water. *Fuel*, 109:225–233, jul 2013.

[82] C G Myers, W H Lang, and P B Welsz. Aging of Platinum Reforming Catalysts. *Industrial & Engineering Chemistry*, 53(4):299–302, 1961.

[83] N.M Rodriguez, P.E Anderson, a Wootsch, U Wild, R Schlögl, and Z Paál. XPS, EM, and Catalytic Studies of the Accumulation of Carbon on Pt Black. *Journal of Catalysis*, 197(2):365–377, jan 2001.

[84] Jennifer N Jocz and Phillip E Savage. Behavior of cholesterol and catalysts in supercritical water. *Energy & Fuels*, 30:7937–7946, 2016.

[85] Courtney A. Young, Patrick R. Taylor, and Corby G. Anderson. *Hydrometallurgy 2008: Proceedings of the Sixth International Symposium.* Society for Mining, Metallurgy, and Exploration, Inc., 2008.

[86] Ingemar Dellien, F M Hall, and Loren G Hepler. Chromium, molybdenum, and tungsten: thermodynamic properties, chemical equilibriums, and standard potentials. *Chemical Reviews*, 76(3):283–310, 1976.

[87] Richard A. Robie, Bruce S. Hemingway, and James R. Fisher. *Thermodynamic Properties of Minerals and Related Substances at 298.15 K and 1 Bar (10e5 Pascals) Pressure and at Higher Temperatures.* United States Government Printing Office, Washington, D.C., 1979.

[88] Scott A. Hayes, Pu Yu, Thomas J. OKeefe, Matthew J. O'Keefe, and James O. Stoffer. The Phase Stability of Cerium Species in Aqueous Systems I. E-pH Diagram for the Ce-HClO$_4$-H$_2$O System. *J. Electrochem. Soc.*, 149:C623–C630, 2002.

[89] S.E. Ziemniak. *Solubility Behavior and Phase Stability of Transition Metal Oxides in Alkaline Hydrothermal Environments.* 2000.

[90] D. A. Sverjensky, E. L. Shock, and H. C. Helgeson. Prediction of the Thermodynamic Properties of Aqueous Metal Complexes to 1000°C and 5 kb. *Geochim. Cosmochim. Acta*, 61:1359–1412, 1997.

[91] S. E. Ziemniak, M. E. Jones, and K. E. S. Combs. Solubility Behavior of Titanium (IV) Oxide in Alkaline Media at Elevated Temperatures. *J. Solution Chem.*, 22:601–623, 1993.

[92] Zarina Minubaeva. *UV Spectroscopic Studies of the Hydrothermal Geochemistry of Molybdenum and Tungsten.* PhD thesis, 2007.

[93] Scott A Wood. Experimental Determination of the Solubility of WO$_{3(s)}$ and the Thermodynamic Properties of H$_2$WO$_{4(aq)}$ in the Range 300-600 °C at 1kbar; Calculation of Scheelite Solubility. *Geochim. Cosmochim. Acta*, 56:1827–1836, 1992.

[94] Everett L. Shock and Harold C. Helgeson. Calculation of the Thermodynamic and Transport Properties of Aqueous Species at High Pressures and Temperatures: Standard Partial Molal Properties of Organic Species. *Geochim. Cosmochim. Acta*, 54:915–945, 1990.